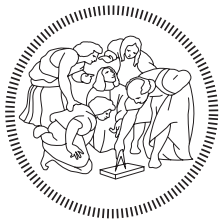

POLITECNICO
MILANO 1863

Three-dimensional physics-based numerical simulations of earthquake ground motion for advanced seismic risk assessment

Advisor:
Prof. Paola F. Antonietti

Co-advisor:
Dr. Ilario Mazzieri

Chair of the Doctoral Program:
Prof. Irene M. Sabadini

Doctoral dissertation of:
Laura Melas

Politecnico di Milano
MOX – Dipartimento di Matematica
Mathematical Models and Methods in Engineering – XXXIII cycle

To my family.

Abstract

An accurate evaluation of seismic hazard, based on suitable modelling of earthquake ground motion prediction, is a key step for the reliable assessment of seismic risk in large urban areas. In recent years, stimulated by the increasing availability of computational resources, physics-based numerical simulations of earthquake ground motion including a full three-dimensional seismic wave propagation model from the source to the site, have gained increasing interest so that they now represent the most promising tool to generate ground shaking scenarios.

In this thesis we develop new mathematical and numerical models for the coupling of the ground motion induced by earthquakes with the induced structural damages of buildings. To model the ground motion induced by seismic waves we employ the elastodynamics equation discretized by the Discontinuous Galerkin Spectral Element method, whereas prediction models of structural damages are based either on empirical laws (fragility curves) or physics-based approaches (linear and non-linear differential models).

To validate the first proposed coupled approach based on fragility curves, we study seismic damages in the Beijing area as a consequence of ground motion scenarios with magnitude in the range 6.5–7.3 M_w. In particular we compute the probability of exceeding a certain damage level conditioned to the earthquake intensity measure. We validate our methodological approach focusing on the specific class of high-rise buildings.

To validate the second proposed approach based on differential models to describe both wave propagation in the underground and its impact on buildings, three-dimensional physics-based scenarios of the 1999 M_w6 Athens earthquake are carried out to study the seismic response of the Acropolis hill and of the Parthenon. In particular we model the main Greek cultural heritage within the framework of the structural analysis.

We also investigate the contact-friction laws that are at the basis of dynamic seismic source modelling and of the description of the interaction between ground and structures to improve the description of the phenomena in realistic applications.

Finally, we present algebraic multigrid solvers for elliptic problems discretized by high order discontinuous Galerkin methods. Algebraic multigrid is an effective technique for solving the linear system of equations stemming from the discretization of partial differential equations.

Acknowledgments

I am thankful to my advisor Prof. Paola F. Antonietti who transferred me the passion for the research, gave me the opportunity and guided me in my PhD experience of these three years.
I also would like to thank my co-advisor Dr. Ilario Mazzieri. From him I learned a lot of knowledge on applied mathematics for earthquake applications. He was always available for research discussions.
I wish also to thank Dr. Carlo Cauzzi who hosted me at ETH Zürich. Thanks to this research exchange I had the opportunity to work in a different university and to enjoy Zürich which is a beautiful, culture-rich, international and friendly city.
I also appreciated the collaborations from both research and teaching points of view and for that I am thanking Profs. Alfio Quarteroni, Marco Verani, Paolo Zunino, Roberto Paolucci, Chiara Smerzini and Dr. Marco Stupazzini.
I acknowledge the Italian Ministry of Education, Universities and Research (MIUR) for having partially supported this research under the SIR (Scientific Independence of young Researchers) starting grant n. RBSI14VT0S (P.I. Prof. P.F. Antonietti).
I am grateful to the research group at TUM in Münich. I thank Prof. Barbara Wohlmuth for the opportunity to fulfil a postdoc position and do research with her group that already welcomed me and is helping me in moving and starting this new experience in this difficult corona crisis situation.

Thanks to my Tender's friends. They were the best office mates that I could desire. Thanks to them, each day in office was enjoyable so that I could not miss a day at my desk (with the exception of the covid lockdown months, but it was not my choice and it was necessary). They were by my side to cheer with me in my good results, but also support me in difficult moments.

I am grateful to my lifelong friends: people with whom you grow up and will always be close in important aspects of life. And thanks to my friends of the swing community: a dance world rich of joy, carefreeness and truly friendship.

My best thanks to my family. To my father Salvatore that has supported and surely will support me for ever even if he is no longer there. To my mother Graziella

that continues to believe in me and encourages me in all my decisions. To Nicola, besides being of my brother, with whom I enjoyed scientific discussion, especially during the covid crisis. Thanks also to my relatives that were close to me in this experience. Among them I am particular thankful to my uncle Alessandro.

Contents

List of Abbreviations

AMG	Algebraic Multigrid
DG	Discontinuous Galerkin
DGSE	Discontinuous Galerkin Spectral Element
FD	Finite Difference
FE	Finite Element
SE	Spectral Element
DS	Damage State
GMM	Ground Motion Model
GMPE	Ground Motion Prediction Equation
I_H	Housner Intensity
IM	Intensity Measure
PBS	Physics-Based Simulations
PGA	Peak Ground Acceleration
PGD	Peak Ground Displacement
PGV	Peak Ground Velocity
PSHA	Probabilistic Seismic Hazard Assessment
SA	Spectral Acceleration
SD	Spectral Displacement
SV	Spectral Velocity
1D	One-Dimensional
2D	Two-Dimensional
3D	Three-Dimensional

Introduction

In the last few decades, losses induced by natural disasters have shown a dramatic increase on a worldwide scale. The reasons are manifold and include the increase in world population, together with the development of new mega-cities with population larger than 2 millions, as well as the development of highly exposed regions and high vulnerability of modern societies and technologies [Smo+04]. Many of these densely populated areas are located in seismic prone regions. The destructive earthquakes of the last decade, such as Chile (Haiti 2010), New Zealand (Canterbury 2010 - 2011), Japan (Tohoku 2011, Kunamoto 2016) and Italy (L'Aquila 2009, Po Plain 2012, Norcia 2016), caused a very high number of victims with losses estimated of the order of several billion dollars. For example, the Haiti earthquake (2010) counts 159.000 fatalities, whereas the overall economic losses caused by the Tohoku 2011 earthquake were estimated to be about 210 billion US dollars with about 15.500 victims (`https://natcatservice.munichre.com`).

The assessment of seismic risk at portfolio, at both urban or regional scale, is a key element for the definition of risk mitigation strategies to mitigate the adverse economic and social effects of earthquakes, the planning and management of emergency response in the aftermath of a disaster event and for the definition of earthquake insurance schemes for risk transfer objectives. A variety of approaches, tools and applications dealing with different components of seismic risk assessment have been proposed, see, e.g., the overview in [Erd17]. In general, the chain of seismic risk assessment involves first the quantification of seismic hazard, then its combination with suitable vulnerability models of structures and facilities and, finally, the prediction of expected losses by incorporating the exposure information. Seismic hazard models provide a quantification of the expected earthquake shaking in a given area in terms of various ground motion Intensity Measure (IM), such as Peak Ground Acceleration (PGA) or acceleration response spectra ordinates (SA). For a structural typology, the direct physical damage can be determined using either suitable fragility/vulnerability relationships providing the probability of damage/loss, conditioned on the level of IM, or a physics-based structural damage

measure. Eventually, economic (direct and indirect) and social (casualties) losses can be estimated as a function of physical damage estimates.

Among the many challenges that a reliable seismic risk assessment poses, the key aspect is the characterization of earthquake ground motion. The goal is to produce estimates of the probability distribution of the ground motion IM as a function of explanatory variables, such as magnitude, source-to-site distance and site conditions, amongst others. An extensive body of approaches exists for this purpose, ranging from Ground Motion Prediction Equations (GMPEs) [Tri76; Dou03; Abr+08; Pow+08], Empirical Green Functions and stochastic methods [Har78; Pav+00; KIP98], to three-dimensional (3D) numerical simulations [Gra96; Moc+07; LD72; Fac+97; KV98; Maz+13], see review in [DA08]. These approaches differ essentially for the amount and detail of input information, as regards both the seismic source and propagation path from the source to the site, and the level of detail of the of output, that can range from only peak values of ground motion to the entire displacement time history.

We next provide some details on each of the most employed approaches to predict earthquake ground motion. GMPEs are statistical regressions on instrumental observations deduced from past earthquakes. Thanks to their simplicity they represent one of the most commonly used approach for ground motion prediction, see [DE16]. Nonetheless, GMPEs suffer from some major limitations, especially when used for earthquake ground motion prediction at urban or regional scale. Indeed they are poorly calibrated in the near-source region of moderate to large earthquakes [PF09] and, as a consequence of ergodic assumption [AA+10], they cannot account for region-, path- and site- specific effects related to the earthquake source, recording site conditions (e.g. complex site effects in case of large sedimentary basins) and source-to-site path. Moreover GMPEs alone cannot provide reliable estimates of the spatial correlation of ground motion, which may be crucial for seismic risk assessment of large urban areas with spatially distributed portfolios or infrastructural systems, see e.g., [JB09; PBB07; Wea+15].

In recent years, boosted by the continuous development of numerical methods together with computational power facilities, there has been an increasing research of numerical methods for the simulation of seismic wave propagation [Bra18; Fra93; OA96; Mad76; Rob96; PMS15; Pao+16; Vil+14; Cha+10; Ant+18b]. Hence, 3D physics-based simulations (referred to as PBS hereafter) have emerged as a powerful and effective tool for earthquake ground motion prediction [Bra18]. PBS are based on either finite difference (FD) methods [Gra96; AKJ68; Vir86; Bay+86; Dab86; KM03; MKH00; MKG14], finite element (FE) methods [LD72; KZ67; Moc+07; Boo72; KZ67] and spectral element (SE) methods [Fac+97; KV98; KT99; KT02a; KT02b; Cha+07] that approximate the solution of the (visco)elastodynamics equation. The output of PBS consists of ground motion time histories reflecting the physics of the seismic wave propagation problem as a whole: from the fault rupture

to the propagation path and local site response. Among all, SE methods have been introduced in computational seismology due to their intrinsic capability of providing highly accurate solutions. To improve geometric flexibility of SE methods and keep low numerical dispersion and dissipation errors, in [Ant+12] Discontinuous Galerkin SE (DGSE) methods have been proposed and analyzed to further enhance the flexibility of SE methods, see also [KD06; Ant+16; Maz+13; AM18; Vil+14; PMS15; Pao+16; Bra18]. Indeed, DGSE methods are well suited for capturing local variations of the physical solution since they feature comparable accuracy of SE methods by keeping the numerical dispersion and dissipation errors low, cf. [Fer+17]. Moreover, they are more flexible than SE methods, because they allow for non-conforming simplicial/hexahedral grids and locally varying polynomial approximation orders [Ant+12]. In particular, the DGSE method based on a domain decomposition approach is described in [Ant+12]. Thanks to this approach the SE is employed in each macro-block and the DG paradigm is applied to their interfaces. This strategy allows to mitigate the high number of the degrees of freedom stemming from the DG discretizations.

In recent years, PBSs have achieved a substantial maturity in the scientific community, so that they can now be embedded within simulation-based seismic hazard assessment frameworks [Gra+11; Bra18; Pao+18; Inf+19] and in the generation of large scale simulation-based seismic risk assessments [Por+11; SP18]. The HayWired Earthquake scenario [DW17; DW18] is an example of cutting-edge evaluation of scenario-based seismic risk from 3D simulations. The physics-based ground shaking scenario of a hypothetical M_w 7 earthquake on the Hayward Fault (San Francisco Bay area, California) provides an estimate of the expected physical and environmental damages resulting from the earthquake shaking. From this scenario it is also possible to obtain insights into social and economic consequences, planning of emergency responses and policy considerations. Recently, Smerzini and Pitilakis [SP18] combined 3D physics-based simulations with the capacity spectrum method to estimate the damage to reinforced concrete buildings in the city of Thessaloniki during the 1978 destructive M_w 6.5 earthquake and to compare it with available post-earthquake damage observations.

The estimation of the seismic risk requires both the knowledge of the seismic hazard and the representation of the seismic quality of the structure: the latter is the objective of the seismic vulnerability assessment methods made through an earthquake scenario [Gue13]. Therefore we are interested to couple ground motion intensity measures with suitable models to predict seismic vulnerability of structures in order to improve seismic risk management. Earthquakes demonstrate the weakness of urban environments relative to the destructive power of these events, however if we better understand them we can use this knowledge to reduce the impact of earthquakes on urban areas. For example, thanks to seismic vulnerability studies it is possible to understand which buildings need eventual reinforcements.

The phase of seismic diagnostic or vulnerability analysis is based on two main approaches, probabilistic or deterministic, [Cal+06; CPB04; Gue13] and it identifies the levels of predicted damage as a function of the typology of construction. The first strategy uses the data collected in sites with past earthquakes to define the probable of damage for a given seismic response parameter leading to the definition of the fragility curve [MA86; RE05; RE03; PKB07; Seo+12; MKS17; BC08; GM13]. On the other hand, the second approach makes use of physics-based seismic risk assessment methods within the structural analysis framework that are governed by differential models based on either linear or non-linear elasticity equations. Most of these techniques are based on the construction and analysis of a mechanical model on the behaviour of the structure subject to seismic shaking [KL18; Mas03; Kap+06; MV12].

In this thesis we aim at proposing and analyzing new coupled numerical models for seismic risk assessment. We develop a method that couples physics-based differential models for ground motion prediction with prediction models of structural damage. To predict the ground motion induced by an earthquake we employ a differential model based on the elastodynamics equations discretized by DGSE methods. This model is then suitably coupled with suitable models to quantify the seismic risk on structures that are based on employing either suitable vulnerability models, (e.g. fragility curves) or the structural analysis. This coupled approach yields an estimation of the predictable damage induced by an earthquake. This information allows us, for example, to quantify the real level of risk, and can guide at reducing the uncertainty related to two of the most important components of seismic risk: the hazard and vulnerability.
More precisely, in the first proposed coupled model, we deal with an approach that combines physics-based elastodynamics differential model for ground shaking prediction with the use of fragility curves for the risk assessment of structural vulnerability. In this way using a deterministic tool for earthquake ground motion prediction based on physical equations rather than empirical methods, we can obtain a more accurate information to assess ground motion hazard. As a result the input for fragility curves could become more reliable and as a consequence the corresponding predictions of possible structural failures. The proposed method is tested considering the metropolitan Beijing high seismicity urban area.
Then, we propose a second fully physics-based approach by considering the differential models for modelling both the earthquake phenomenon and the seismic response of buildings. In particular, with this three-dimensional physics-based model, it is possible to take into account the interactions of the structures with respect to the earthquake ground motion within a multi-scale simulation. In such a way, the measure of the seismic risk level of a building is more accurate. The proposed model is validated considering a "source-site-structure" simulation of the 1999 M_w6 Athens earthquake to investigate the seismic response of the Parthenon, the main cultural

heritage of Greece, and the results are compared with recorded data.
In order to correctly model the earthquake phenomenon, it is important to model several geophysical features, among them there are the topography, material properties of the layers, the geometry of the fault, the magnitude and the seismic source representation. In particular, the seismic source can be described through a kinematic approach by prescribing the slip along the fault or with a dynamic source modeling by introducing physical laws for earthquake spontaneous fault rupture. In the first part of this thesis we adopted a kinematic description, but we are interested in improving the seismic source within its dynamic representation. The advantage of the dynamic source modelling is that it physically describes a phenomenon in a more realistic way, but as a drawback it is much more computationally challenging due to the underlying governing equations, c.f. [And76; DA77; Day82]. Moreover the contact-friction laws that are at the basis of the dynamic fault rupture modeling can be employed to describe the non-linear behavior of the buildings within the framework of the structural analysis.

To conclude, we provide an overview of the contents of each chapter of the thesis.

In Chapter 1 we introduce the physical equations governing seismic wave propagation phenomena together with its mathematical formulation. Then we describe the discretization strategies based on discontinuous Galerkin spectral element methods (for discretization in space) and the leap-frog scheme (for discretization in time) to derive the semi-discrete and algebraic DG formulations, respectively. The proposed method has been proposed in [Ant+12] and implemented in the open source code SPEED (`http://speed.mox.polimi.it`, cf. also [Maz+13]). We also recall the well-posedness and stability results and a priori error bounds for the semi-discrete and fully discrete DG formulations, cf. [Ant+16]. Then we describe the main ground motion intensity measures IM that are at the basis of the earthquake quantification analysis.

In Chapter 2 we propose a new coupled paradigm for seismic risk assessment to yield physics-based damage scenarios, which employs, on the one hand, a rigorous numerical model for the prediction of near-source earthquake ground motion, and on the other, a suitable set of fragility functions for prescribed building typologies to quantify a probabilistic expected buildings damage. Physics-based earthquake scenarios, that are the key ingredients of our approach, exploit the DGSE method revised in Chapter 1. The proposed coupled approach based is expected to provide more accurate, site-specific estimates of earthquake ground motion and, then, of the resulting damage, especially when the coupling of near-field effects and complex site amplification in sedimentary basins may play a key role. Finally, we present an application of the proposed approach focusing on the metropolitan area of Beijing (China). The city of Beijing is located in the proximity of a well-known mapped fault system capable of triggering severe earthquakes of magnitude up to 7.3 M_w. Based on employing our model, we produce maps of seismic damage focusing on

the specific class of high-rise buildings, accounting for a wide set of fault rupture realizations with magnitude in the range 6.5-7.3 M_w. This chapter contains original material and the results are contained in the following publication [Ant+21].

In Chapter 3 we propose a fully physics-based coupled approach where we model both the earthquake ground motion and the built environment with suitable differential equations. To validate the model we focus on the study of the seismic response of the Parthenon during the 1999 M_w 6 Athens earthquake. The simulations have been performed using the high-performance open-source code SPEED (`http://speed.mox.polimi.it`, cf. [Maz+13]) We will provide insights into the seismic wave propagation features of the 1999 Athens earthquake and, hence, contribute to the seismic response investigation of the Acropolis hill and the Parthenon. More precisely, we will validate the 3D model against available recordings for the target event and we will evaluate the observed ground motion and the seismic response of Parthenon during Athens earthquake M_w 6 1999 in terms of amplitude, duration and frequency content. This chapter contains original material and the results will be submitted for possible publication.

In Chapter 4 we consider a more complicated model for the description of the seismic source and interactions among building components after an earthquake, we show theoretical and numerical results for the simulations of dynamic-fault rupture wave propagation based on employing discontinuous Galerkin discretizations. In particular we make use of the variational inequalities principles proposed in [DL76; KO88; MO83]. First we introduce the mathematical model for the dynamic source description; and then we present its variational formulation within the inequality framework. We derive the semi-discrete formulation of the problem with a discontinuous Galerkin discretizations and the algebraic system resulting after using the leap-frog scheme for time integration. We also consider a fixed point iteration to numerically solve the non-linearity stemming from the governing equations. We prove theoretical results for the variational inequality introduced before under suitably simplified hypothesis and then we then prove stability and bounds results for the semi-discrete formulation. Finally, we report some preliminary numerical computations related to a benchmark 2D study test and discuss the achieved results. This chapter contains original material and the results will be submitted for possible publication.

In Conclusions we summarize the achieved results and discuss open problems for future research.

In Appendix A we present multigrid methods for the efficient solution of the linear system of equations stemming from high order discontinuous Galerkin approximations of second order elliptic problems. The goal is to develop an algebraic solver that is both $h-$ and $p-$independent, especially in the high order discontinuous Galerkin setting. Multigrid methods can be viewed as an acceleration of iterative schemes featuring a smoothing property. The smoothing property refers to

an efficient reduction of oscillatory components of the error than the smooth ones. The main idea behind multigrid methods is to project the smooth error modes onto a coarser level where a relaxation will be more effective on all error components. The aim of this Appendix A is to propose new algebraic multigrid methods based on the employment of smoothed aggregation [VMB96] and, following the guideline of [OS11], extend the latter to high order discontinuous discretizations for which standard multigrid approaches cannot be employed because of redundancy of the degrees of freedom associated to the same grid point. This chapter contains original material and the results are contained in the following publication [AM20].

CHAPTER 1

Mathematical and numerical models for three-dimensional physics-based earthquake ground motion

In this chapter we describe the mathematical model and formulate the Discontinuous Galerkin Spectral Element method for the approximation of elastic wave problems in heterogeneous media. Starting from the semi-discrete formulation we analyze the approximation technique from the points of view of accuracy, convergence and stability. We also describe the algebraic formulation that comes from the leap-frog scheme in time. Finally, we introduce the main ground motion intensity measures that are at the basis of the earthquakes study within the framework of the seismic risk analysis.

1.1 Mathematical model

In this section we describe the elastodynamics equation. Let $\Omega \subset \mathbb{R}^3$ be a fixed, polyhedral, open, bounded domain (representing the portion of the ground where we investigate the wave propagation phenomena) and let $\partial\Omega$ be the corresponding boundary that we assume to be sufficiently regular. Moreover let the boundary be decomposed into three disjoint portions Γ_D, Γ_N and Γ_{NR}, where Γ_D is the portion of the boundary where the displacements are assigned, Γ_N is the one where surface loads are imposed and Γ_{NR} is the portion of $\partial\Omega$ where non-reflecting boundary conditions are prescribed. The boundary Γ_{NR} is introduced to avoid unphysical reflections, cf. [Sta88].

Here and in the sequel, vectors are typed with bold letters, while underlined quantities denote tensors. Given a final observation time $T > 0$, we consider the temporal interval $(0, T]$. The dynamic equation for a viscoelastic material leads to

the following system:

$$\begin{cases} \rho\ddot{\mathbf{u}} + 2\rho\xi\dot{\mathbf{u}} - \nabla\cdot\underline{\sigma}(\mathbf{u}) + \rho\xi^2\mathbf{u} = \mathbf{f}, & \text{in } \Omega\times(0,T], \\ \mathbf{u} = \mathbf{0}, & \text{on } \Gamma_D\times(0,T], \\ \underline{\sigma}(\mathbf{u})\mathbf{n} = \mathbf{t}, & \text{on } \Gamma_N\times(0,T], \\ \underline{\sigma}(\mathbf{u})\mathbf{n} = \mathbf{t}^*, & \text{on } \Gamma_{NR}\times(0,T], \\ \mathbf{u} = \mathbf{u}_0, & \text{in } \Omega\times\{0\}, \\ \dot{\mathbf{u}} = \mathbf{u}_1, & \text{in } \Omega\times\{0\}, \end{cases} \tag{1.1}$$

where $\mathbf{u} = \mathbf{u}(\mathbf{x},t)$ is the displacement field, $\underline{\sigma}(\mathbf{u}) = \underline{\sigma}(\mathbf{x},t)$ is the stress tensor, $\rho = \rho(\mathbf{x}) \in L^\infty(\Omega)$ is a strictly positive function describing the material density, $\mathbf{n} = \mathbf{n}(\mathbf{x})$ is the unit outward normal vector to $\partial\Omega$, $\xi = \xi(\mathbf{x}) \geq 0$ is a suitable decay factor with dimension inverse of time that models the dumping effects, and $\mathbf{f} = \mathbf{f}(\mathbf{x},t)$ is a given external load (e.g. a seismic source). On the boundary we impose null displacements on Γ_D, a traction $\mathbf{t} = \mathbf{t}(\mathbf{x},t)$ on Γ_N and, finally, on Γ_{NR} a fictitious traction $\mathbf{t}^* = \mathbf{t}^*(\mathbf{x},t)$, cf. [Sta88; Cas+02]. As initial conditions for the displacement and the velocity, we assign the functions $\mathbf{u}_0 = \mathbf{u}_0(\mathbf{x})$ and $\mathbf{u}_1 = \mathbf{u}_1(\mathbf{x})$, respectively.

We assume a linear constitutive equation for the stress tensor (Hooke's law):

$$\underline{\sigma}(\mathbf{u}) = 2\mu\underline{\varepsilon}(\mathbf{u}) + \lambda\mathrm{tr}(\underline{\varepsilon}(\mathbf{u}))\underline{I}, \tag{1.2}$$

where $\mu = \mu(\mathbf{x}) \in L^\infty(\Omega)$ and $\lambda = \lambda(\mathbf{x}) \in L^\infty(\Omega)$ are the Lamé elastic coefficients, while

$$\underline{\varepsilon}(\mathbf{u}) = \frac{\nabla\mathbf{u} + \nabla\mathbf{u}^T}{2}$$

is the strain tensor, $\underline{I}$ is the identity tensor and $\mathrm{tr}(\cdot)$ is the trace operator.

According to the Hooke's law (1.2) we can relate $\underline{\sigma}$ and $\underline{\varepsilon}$ in the following way

$$\underline{\sigma}(\mathbf{u}) = \underline{D}\,\underline{\varepsilon}(\mathbf{u}),$$

where $\underline{D}$ is the fourth order elasticity tensor. The stiffness tensor $\underline{D}$ is symmetric, positive, definite and bounded over Ω, i.e. it satisfies the following

$$D_{ijkl} = D_{jikl} = D_{ijlk} = D_{klij},$$

where $D_{ijkl} = (\underline{D})_{ijkl}$, and there exists two positive constants D_*, D^* such that

$$0 < D_*\sum_{i,j}^{3} X_{ij}^2 < \sum_{i,j,k,l}^{3} X_{ij}D_{ijkl}X_{kl} < D^*\sum_{i,j}^{3} X_{ij}^2 \quad \forall \underline{X} \neq \underline{0}.$$

We recall that the compressional and shear wave velocities, v_P and v_S respectively, are obtained through the relations

$$v_P = \sqrt{\frac{\lambda+2\mu}{\rho}}, \quad v_S = \sqrt{\frac{\mu}{\rho}}. \tag{1.3}$$

Next we introduce the weak formulation of problem (1.1) that reads: for any $t \in (0,T]$ find $\mathbf{u} = \mathbf{u}(t) \in \mathbf{V} = \{\mathbf{v} \in \mathbf{H}^1(\Omega) : \mathbf{v} = \mathbf{0} \text{ on } \Gamma_D\}$ such that

$$(\rho\, \ddot{\mathbf{u}}, \mathbf{v})_\Omega \,+\, (2\rho\xi\, \dot{\mathbf{u}}, \mathbf{v})_\Omega \,+\, \mathcal{A}(\mathbf{u}, \mathbf{v}) \,+\, (\rho\xi^2 \mathbf{u}, \mathbf{v})_\Omega = \mathcal{F}(\mathbf{v}) \quad \forall \mathbf{v} \in \mathbf{V}, \tag{1.4}$$

where the bilinear form $\mathcal{A} : \mathbf{V} \times \mathbf{V} \to \mathbb{R}^3$ is defined as

$$\mathcal{A}(\mathbf{u}, \mathbf{v}) = (\underline{\sigma}(\mathbf{u}), \underline{\varepsilon}(\mathbf{v}))_\Omega$$

and the linear functional $\mathcal{F} : \mathbf{V} \to \mathbb{R}^3$ as

$$\mathcal{F}(\mathbf{v}) = (\mathbf{f}(t), \mathbf{v})_\Omega \,+\, \langle \mathbf{t}(t), \mathbf{v} \rangle_{\Gamma_N} \,+\, \langle \mathbf{t}^*(t), \mathbf{v} \rangle_{\Gamma_{NR}}.$$

Finally, if $\Gamma_{NR} = \emptyset$ and $\xi = 0$, the above problem is well-posed and its unique solution $\mathbf{u} \in C^0(0,T;\mathbf{V}) \cap C^1(0,T;\mathbf{L}^2(\Omega))$, provided that $\rho \in L^\infty(\Omega)$, $\mathbf{u}_0 \in \mathbf{V}$, $\mathbf{v}_0 \in \mathbf{L}^2(\Omega)$, $\mathbf{f} \in L^2(0,T;\mathbf{L}^2(\Omega))$ and $\mathbf{t} \in L^2(0,T;\mathbf{L}^2(\Gamma_N))$, see for instance [RT83, Theorem 8.3-1].

1.1.1 Seismic source

The seismic source term $\mathbf{f}$ in (1.1) can be modeled in several ways. A possible choice of the seismic input is a point-wise force that acts on a point $\mathbf{x}_0$ in the i-th direction defined as

$$\mathbf{f}(\mathbf{x}, t) = f(t)\delta(\mathbf{x} - \mathbf{x}_0)\mathbf{e}_i,$$

where $f(t)$ is a function of time, $\delta(\cdot)$ is the delta distribution and $\mathbf{e}_i$ is the unit vector in the i-th direction. An example of the function f among different waveforms is the Ricker wavelet defined as

$$f(t) = f_0(1 - 2\pi^2 f_p^2 (t - t_0)^2) e^{-\pi^2 f_p^2 (t-t_0)^2},$$

where f_0 is the amplitude of the wave, f_p is the peak frequency of the signal and t_0 is the reference time.

In many applications the source term is the vertically incident plane wave described by a uniform distribution of body forces along the plane $z = z_0$, i.e.

$$\mathbf{f}(\mathbf{x}, t) = f(t)\delta(z - z_0)\mathbf{e}_i.$$

This seismic input generates a displacement in the i-th direction described by the function

$$\bar{u}_i(\mathbf{x}, t) = \frac{1}{2\rho v} \mathcal{H}(t - \frac{|z - z_0|}{v}) \int_0^{t - \frac{|z-z_0|}{v}} f(\tau)\, d\tau, \tag{1.5}$$

where $\mathcal{H}(\cdot)$ denotes the Heaviside function and v is the wave velocity ($v = v_P, v_S$), see [AW09]. Computing the derivative with respect to time of (1.5) and evaluating the result at $z = z_0$, $f(t)$ can be written as

$$f(t) = 2\rho v \frac{\partial \bar{u}_i}{\partial t}.$$

Finally, the most important choice to describe the seismic source $\mathbf{f}$ in (1.1) is the kinematic finite-fault model expressed in terms of a distribution of double-couple point sources. The body force distribution $\mathbf{f}$ is given by the relation $\mathbf{f}(\mathbf{x}, t) = -\nabla \cdot m(\mathbf{x}, t)$, cf. [Fac+97]. The seismic moment tensor $m(\mathbf{x}, t)$ is defined for $0 \leq t < T$ as, see e.g. [AR02],

$$m_{ij}(\mathbf{x}, t) = \frac{M_0(\mathbf{x}, t)}{V}(s_i \nu_j + s_j \nu_i), \quad i, j = 1, \ldots, 3, \tag{1.6}$$

where $\boldsymbol{\nu}$ and $\mathbf{s}$ are the fault normal and the unit slip vector along the fault, respectively, and $M_0(\mathbf{x}, t)$ is the time history of the moment release at the source point $\mathbf{x}$ inside the elementary volume V.

1.1.2 Absorbing boundary conditions

One of the main aspects in the simulations of seismic wave propagation is the modeling of the absorbing boundary conditions that are introduced to consider the phenomenon in limited domains. Among the many approaches, we describe the absorbing boundary layers by imposing a fictitious traction on Γ_{NR} which consists in a linear combination of space and time derivatives of the displacement. We present the local P3 paraxial condition presented in [Sta88] that provides effective and stable results when $v_P/v_S \leq 2$, as in the applications under consideration. Let $\mathbf{n} = [n_x, n_y, n_z]^T$ be the unit normal vector to Γ_{NR} and $\boldsymbol{\tau}_1 = [\tau_{1,x}, \tau_{1,y}, \tau_{1,z}]^T$, $\boldsymbol{\tau}_2 = [\tau_{2,x}, \tau_{2,y}, \tau_{2,z}]^T$ a couple of mutually orthogonal unit vectors that lie on the plane tangent to the boundary, then the P3 paraxial absorbing conditions read as

$$\begin{cases} \dfrac{\partial}{\partial \mathbf{n}}(\mathbf{u} \cdot \mathbf{n}) = -\dfrac{1}{v_P}\dfrac{\partial}{\partial t}(\mathbf{u} \cdot \mathbf{n}) + \dfrac{v_S - v_P}{v_P}\left[\dfrac{\partial}{\partial \boldsymbol{\tau}_1}(\mathbf{u} \cdot \boldsymbol{\tau}_1) + \dfrac{\partial}{\partial \boldsymbol{\tau}_2}(\mathbf{u} \cdot \boldsymbol{\tau}_2)\right], \\ \dfrac{\partial}{\partial \mathbf{n}}(\mathbf{u} \cdot \boldsymbol{\tau}_1) = -\dfrac{1}{v_S}\dfrac{\partial}{\partial t}(\mathbf{u} \cdot \boldsymbol{\tau}_1) + \dfrac{v_S - v_P}{v_P}\dfrac{\partial}{\partial \boldsymbol{\tau}_1}(\mathbf{u} \cdot \mathbf{n}), \\ \dfrac{\partial}{\partial \mathbf{n}}(\mathbf{u} \cdot \boldsymbol{\tau}_2) = -\dfrac{1}{v_S}\dfrac{\partial}{\partial t}(\mathbf{u} \cdot \boldsymbol{\tau}_2) + \dfrac{v_S - v_P}{v_P}\dfrac{\partial}{\partial \boldsymbol{\tau}_2}(\mathbf{u} \cdot \mathbf{n}). \end{cases} \tag{1.7}$$

We denote as $\underline{\sigma}^* = \underline{\sigma}^*(\mathbf{u})$ the stress on the absorbing boundary in the local coordinate system $(\boldsymbol{\tau}_1, \boldsymbol{\tau}_2, \mathbf{n})$. Therefore we have

$$\begin{cases} \underline{\sigma}^*_{\boldsymbol{\tau}_1,\boldsymbol{\tau}_1} = (\lambda+2\mu)\dfrac{\partial}{\partial \boldsymbol{\tau}_1}(\mathbf{u}\cdot\boldsymbol{\tau}_1) + \lambda\left[\dfrac{\partial}{\partial \boldsymbol{\tau}_2}(\mathbf{u}\cdot\boldsymbol{\tau}_2) + \dfrac{\partial}{\partial \mathbf{n}}(\mathbf{u}\cdot\mathbf{n})\right], \\ \underline{\sigma}^*_{\boldsymbol{\tau}_2,\boldsymbol{\tau}_2} = (\lambda+2\mu)\dfrac{\partial}{\partial \boldsymbol{\tau}_2}(\mathbf{u}\cdot\boldsymbol{\tau}_2) + \lambda\left[\dfrac{\partial}{\partial \boldsymbol{\tau}_1}(\mathbf{u}\cdot\boldsymbol{\tau}_1) + \dfrac{\partial}{\partial \mathbf{n}}(\mathbf{u}\cdot\mathbf{n})\right], \\ \underline{\sigma}^*_{\mathbf{n},\mathbf{n}} = (\lambda+2\mu)\dfrac{\partial}{\partial \mathbf{n}}(\mathbf{u}\cdot\mathbf{n}) + \lambda\left[\dfrac{\partial}{\partial \boldsymbol{\tau}_1}(\mathbf{u}\cdot\boldsymbol{\tau}_1) + \dfrac{\partial}{\partial \boldsymbol{\tau}_2}(\mathbf{u}\cdot\boldsymbol{\tau}_2)\right], \\ \underline{\sigma}^*_{\boldsymbol{\tau}_2,\mathbf{n}} = \mu\left[\dfrac{\partial}{\partial \mathbf{n}}(\mathbf{u}\cdot\boldsymbol{\tau}_2) + \dfrac{\partial}{\partial \boldsymbol{\tau}_2}(\mathbf{u}\cdot\mathbf{n})\right], \\ \underline{\sigma}^*_{\boldsymbol{\tau}_1,\mathbf{n}} = \mu\left[\dfrac{\partial}{\partial \mathbf{n}}(\mathbf{u}\cdot\boldsymbol{\tau}_1) + \dfrac{\partial}{\partial \boldsymbol{\tau}_1}(\mathbf{u}\cdot\mathbf{n})\right], \\ \underline{\sigma}^*_{\boldsymbol{\tau}_1,\boldsymbol{\tau}_2} = \mu\left[\dfrac{\partial}{\partial \boldsymbol{\tau}_2}(\mathbf{u}\cdot\boldsymbol{\tau}_1) + \dfrac{\partial}{\partial \boldsymbol{\tau}_1}(\mathbf{u}\cdot\boldsymbol{\tau}_2)\right]. \end{cases} \tag{1.8}$$

By combining (1.7) and (1.8), the traction term $\mathbf{t}^* = [t^*_{\boldsymbol{\tau}_1}, t^*_{\boldsymbol{\tau}_2}, t^*_{\mathbf{n}}] = \underline{\sigma}^*(\mathbf{u})\mathbf{n}$ in the local coordinate system $(\boldsymbol{\tau}_1, \boldsymbol{\tau}_2, \mathbf{n})$ reads as

$$\begin{bmatrix} t^*_{\boldsymbol{\tau}_1} \\ t^*_{\boldsymbol{\tau}_2} \\ t^*_{\mathbf{n}} \end{bmatrix} = \begin{bmatrix} \frac{\mu(2v_P - v_S)}{v_S}\frac{\partial}{\partial \boldsymbol{\tau}_1}(\mathbf{u}\cdot\mathbf{n}) - \frac{\mu}{v_S}\frac{\partial}{\partial t}(\mathbf{u}\cdot\boldsymbol{\tau}_1) \\ \frac{\mu(2v_P - v_S)}{v_S}\frac{\partial}{\partial \boldsymbol{\tau}_2}(\mathbf{u}\cdot\mathbf{n}) - \frac{\mu}{v_S}\frac{\partial}{\partial t}(\mathbf{u}\cdot\boldsymbol{\tau}_2) \\ \frac{\lambda v_S + 2\mu(v_P - v_S)}{v_S}\left[\frac{\partial}{\partial \boldsymbol{\tau}_2}(\mathbf{u}\cdot\boldsymbol{\tau}_1) + \frac{\partial}{\partial \boldsymbol{\tau}_1}(\mathbf{u}\cdot\boldsymbol{\tau}_2)\right] - \frac{\lambda+2\mu}{v_S}\frac{\partial}{\partial t}(\mathbf{u}\cdot\mathbf{n}) \end{bmatrix}. \tag{1.9}$$

Finally, the expression of $\mathbf{t}^*$ in the global coordinate system can be recovered by writing the normal and the tangential derivatives as

$$\begin{aligned} \frac{\partial}{\partial \mathbf{n}} &= \frac{\partial}{\partial x}n_x + \frac{\partial}{\partial y}n_y + \frac{\partial}{\partial z}n_z, \\ \frac{\partial}{\partial \boldsymbol{\tau}_1} &= \frac{\partial}{\partial x}\tau_{1,x} + \frac{\partial}{\partial y}\tau_{1,y} + \frac{\partial}{\partial z}\tau_{1,z}, \\ \frac{\partial}{\partial \boldsymbol{\tau}_2} &= \frac{\partial}{\partial x}\tau_{2,x} + \frac{\partial}{\partial y}\tau_{2,y} + \frac{\partial}{\partial z}\tau_{2,z}, \end{aligned}$$

and then projecting the resulting vector on the global coordinate system by

$$\mathbf{t}^*(\mathbf{x}, t) = \begin{bmatrix} t^*_x \\ t^*_y \\ t^*_z \end{bmatrix} = \begin{bmatrix} \tau_{1,x} & \tau_{2,x} & n_x \\ \tau_{1,y} & \tau_{2,y} & n_y \\ \tau_{1,z} & \tau_{2,z} & n_z \end{bmatrix} \begin{bmatrix} t^*_{\boldsymbol{\tau}_1} \\ t^*_{\boldsymbol{\tau}_2} \\ t^*_{\mathbf{n}} \end{bmatrix}. \tag{1.10}$$

In particular, in [Cas+02] it is possible to find a description on how to choose the vectors $(\boldsymbol{\tau}_1, \boldsymbol{\tau}_2)$.

1.2 Numerical discretization

Following [Ant+12], see [Ant+18a] for a review, we introduce the DGSE space discretization to problem (1.4) based on a domain decomposition approach. At

the first level, we subdivide Ω into K non-overlapping regions Ω_k, $k = 1, \ldots, K$, such that $\Omega = \cup_{k=1}^{K} \Omega_k$, and we denote by $\mathcal{S}$ the collection of the interfaces between subdomains. Note that this (macro) decomposition can be geometrically non-conforming. Then problem (1) is solved in each Ω_k together with transmission conditions at the interface between the sub-domains that are encoded in the scheme. Then, within each subdomain Ω_k, we construct a grid $\mathcal{T}_{h_k}$ made of hexahedral or tetrahedral elements E_k^l, with diameter h_k^l, and assign a polynomial approximation degree $N_k \geq 1$. We suppose that each $E_k^l \in \Omega_k$ is the image through the map $\mathbf{F}_k^l : \hat{E} \to E_k^l$ of the unit reference hexahedron or the unit reference tetrahedron $\hat{E}$. Notice that mesh generation is performed independently on each subdomain and also the local polynomial degree N_k can vary subdomainwise. We define $\mathcal{T}_h$ to be the union of the (independently generated) grids $\mathcal{T}_{h_k}$, and collect all the element faces (here a face is the non empty interior of the intersection of two neighboring hexahedral or tetrahedral elements that belong to $\mathcal{T}_h$) that lie on the interface $\mathcal{S}$ in the set $\mathcal{F}_h$. Problem (1.4) is then discretized on each subdomain Ω_k with a SE method of degree N_k and at the interfaces $\mathcal{F}_h$ the DG paradigm is employed. We introduce the space $\mathbf{V}_{h_k}^{N_k}(\Omega_k) = \{\mathbf{v} \in \mathbf{C}^0(\overline{\Omega}_k) : \mathbf{v}|_{E_k^l} \circ \mathbf{F}_k^l \in [\mathbb{M}^{N_k}(\hat{E})]^3 \quad \forall E_k^l \in \mathcal{T}_{h_k}\}$, where $\mathbb{M}^{N_k}(\hat{E})$ is either the space $\mathbb{Q}^{N_k}(\hat{E})$ of polynomials of degree N_k in each coordinate direction on $\hat{E}$, if $\hat{E}$ is the unit reference cube, or $\mathbb{P}^{N_k}(\hat{E})$ of polynomials of total degree at most N_k on $\hat{E}$, if $\hat{E}$ is the reference tetrahedron. Then, denoting by $\mathbf{V}_{DG}$ the discrete space of function that are piecewise continuous polynomials of degree N_k in each coordinate direction on each subdomain Ω_k, i.e. $\mathbf{V}_{DG} = \{\mathbf{v} \in \mathbf{L}^2(\Omega), \mathbf{v} = \mathbf{0} \text{ on } \Gamma_D : \mathbf{v}|_{\Omega_k} \in \mathbf{V}_{h_k}^{N_k}(\Omega_k),\ k = 1, \ldots, K\}$, and that can be discontinuous at the interface $\mathcal{S}$, the semi-discrete DGSE formulation reads as follows: for any $t \in (0, T]$, find $\mathbf{u}_h = \mathbf{u}_h(t) \in \mathbf{V}_{DG}$ such that

$$\begin{aligned}(\rho\ddot{\mathbf{u}}_h, \mathbf{v})_{\mathcal{T}_h} + (2\rho\xi\dot{\mathbf{u}}_h, \mathbf{v})_{\mathcal{T}_h} + \mathcal{A}_h(\mathbf{u}_h, \mathbf{v}) + (\rho\xi^2\mathbf{u}, \mathbf{v})_{\mathcal{T}_h} \\ = (\mathbf{f}(t), \mathbf{v})_{\mathcal{T}_h} + \langle \mathbf{t}(t), \mathbf{v}\rangle_{\mathcal{F}_h^N} + \langle \mathbf{t}^*(t), \mathbf{v}\rangle_{\mathcal{F}_h^{NR}},\end{aligned} \tag{1.11}$$

for any $\mathbf{v} \in \mathbf{V}_{DG}$, where

$$\mathcal{A}_h(\mathbf{u}, \mathbf{v}) = (\underline{\sigma}(\mathbf{u}), \underline{\varepsilon}(\mathbf{v}))_{\mathcal{T}_h} - \langle \{\underline{\sigma}(\mathbf{u})\}, [\![\mathbf{v}]\!]\rangle_{\mathcal{F}_h^I} - \langle [\![\mathbf{u}]\!], \{\underline{\sigma}(\mathbf{v})\}\rangle_{\mathcal{F}_h^I} + \langle \eta [\![\mathbf{u}]\!], [\![\mathbf{v}]\!]\rangle_{\mathcal{F}_h^I} \tag{1.12}$$

and $(\cdot,\cdot)_{\mathcal{T}_h}$/ $\langle \cdot, \cdot\rangle_{\mathcal{F}_h^b}$, $b = I, N, NR$, denote the $\mathbf{L}^2(\mathcal{T}_h)$/ $\mathbf{L}^2(\mathcal{F}_h^b)$ respectively, inner products defined as

$$(\mathbf{w}, \mathbf{v})_{\mathcal{T}_h} = \sum_{E \in \mathcal{T}_h} (\mathbf{w}, \mathbf{v})_E, \qquad \langle \mathbf{w}, \mathbf{v}\rangle_{\mathcal{F}_h^b} = \sum_{F \in \mathcal{F}_h^b} \langle \mathbf{w}, \mathbf{v}\rangle_F.$$

For any two neighbouring regions $\Omega_{k^\pm}$ that share a face $F \in \mathcal{F}_h$ we denote with $\mathbf{v}^\pm$ and $\underline{\tau}^\pm$ the traces of (regular enough) vector- and tensor-valued functions $\mathbf{v}$ and $\underline{\tau}$ on $\Omega_{k^\pm}$, respectively. We also denote with $\mathbf{n}^\pm$ the unit normal vector to F pointing

outward to $\Omega_{k^\pm}$. We define the averages $\{\cdot\}$ and jumps $[\![\cdot]\!]$ operators (see [Arn+01; Ant+18a]) as

$$\begin{aligned} \{\mathbf{v}\} &= \frac{1}{2}(\mathbf{v}^+ + \mathbf{v}^-), \qquad [\![\mathbf{v}]\!] = \mathbf{v}^+ \otimes \mathbf{n}^+ + \mathbf{v}^- \otimes \mathbf{n}^-, \\ \{\underline{\tau}\} &= \frac{1}{2}(\underline{\tau}^+ + \underline{\tau}^-), \qquad [\![\underline{\tau}]\!] = \underline{\tau}^+ \cdot \mathbf{n}^+ + \underline{\tau}^- \cdot \mathbf{n}^-, \end{aligned} \tag{1.13}$$

where $\mathbf{a} \otimes \mathbf{b} \in \mathbb{R}^{3\times 3}$ is the tensor with entries $(\mathbf{a} \otimes \mathbf{b})_{ij} = a_i b_j$, $i, j = 1, 2, 3$, for all $\mathbf{a}, \mathbf{b} \in \mathbb{R}^3$. On each face $F \in \mathcal{F}_h$ shared by two elements $E^+ \subset \Omega_{k^+}$ and $E^- \subset \Omega_{k^-}$ the penalty parameter η is defined as

$$\eta = \alpha\{\lambda + 2\mu\}_A \frac{\mathtt{N}^2}{\mathtt{h}}, \tag{1.14}$$

where $\{q\}_A = 2q^+q^-/(q^+ + q^-)$ is the harmonic average of the quantity q across F, α is a (large enough) positive constant to be properly chosen [Arn82; Arn+01; ER07], and $\mathtt{N}$ and $\mathtt{h}$ are defined on each face $F \in \mathcal{F}_h$ as $\mathtt{N} = \max\{N_{k^+}, N_{k^-}\}$ and $\mathtt{h} = \min\{h_{k^+}, h_{k^-}\}$.

1.3 Stability and error analysis of the semi-discrete formulation

The main goal of this section is to prove some results for the DG semi-discrete formulation (1.11), [Ant+12; Ant+18a]. We first introduce some notations and technical tools to state the main results. In particular, for the sake of presentation, we consider $\Gamma_D = \partial\Omega$ and $\Gamma_{NR}, \Gamma_N = \emptyset$.

To carry out the analysis, we suppose that local bounded variation assumption on the mesh-size and the polynomial degree holds, i.e. $h_{k^+} \lesssim h_{k^-} \lesssim h_{k^+}$ and $N_{k^+} \lesssim N_{k^-} \lesssim N_{k^+}$ for any pair of neighboring elements $\Omega_{k^\pm}$, cf. [PS02] for example. In addition we also assume that for any element $E \in \mathcal{T}_h$ and for any face $F \subset \partial K$, it holds $h_K \lesssim h_F$, see [PS02; GHH07]. We remark that this last assumption can be relaxed, cf. [AM18; CGH14; AFV20].

1.3.1 Well-posedness of the discontinuous Galerkin formulation

Lemma 1.1. *For any polynomial* $\mathbf{v}$ *of degree* $N_k \geq 1$ *over* $E \in \mathcal{T}_{h_k}$ *there hold*

$$\begin{aligned} |\mathbf{v}|_{m,E} &\lesssim \left(\frac{N_k^2}{h_k}\right)^{m-s} |\mathbf{v}|_{s,E} \quad 0 \leq s \leq m, \\ ||\mathbf{v}||_{0,F} &\lesssim \left(\frac{N_k^2}{h_k}\right)^{1/2} ||\mathbf{v}||_{0,E} \quad \forall F \subset \partial E. \end{aligned}$$

From the above lemma, by summation on all the elements E in each Ω_k, it holds the following.

Lemma 1.2. *For any polynomial v of degree $N_k \geq 1$ over Ω_k there hold*

$$|\mathbf{v}|_{m,\Omega_k} \lesssim \left(\frac{N_k^2}{h_k}\right)^{m-s} |\mathbf{v}|_{s,\Omega_k} \quad 0 \leq s \leq m,$$
$$||\mathbf{v}||_{0,F} \lesssim \left(\frac{N_k^2}{h_k}\right)^{1/2} ||\mathbf{v}||_{0,\Omega_k} \quad \forall F \in \mathcal{F}_h^I, F \subset \partial\Omega_k.$$

See [Agm65; Bre04; Can+06; Sch98; STW11] for further details and proofs. We next introduce the following (discretization parameters dependent) norms

$$||\mathbf{v}||_{DG}^2 = ||\underline{D}^{1/2}\underline{\varepsilon}(\mathbf{v})||_{0,\mathcal{T}_h}^2 + ||\eta^{1/2}[\![\mathbf{v}]\!]||_{0,\mathcal{F}_h^I}^2 \quad \forall \mathbf{v} \in \mathbf{H}^1(\mathcal{T}_h) \cap \mathbf{V}_{DG},$$
$$|||\mathbf{v}|||_{DG}^2 = ||\mathbf{v}||_{DG}^2 + ||\eta^{-1/2}\{\underline{D\varepsilon}(\mathbf{v})\}||_{0,\mathcal{F}_h^I}^2 \quad \forall \mathbf{v} \in \mathbf{H}^2(\mathcal{T}_h).$$

The norms $||\cdot||_{DG}$ and $|||\cdot|||_{DG}$ are equivalent when restricted to the space $\mathbf{V}_{DG}$. It can be proved by employing the trace-inverse inequality of Lemma 1.2.

Moreover we consider the following results.

Lemma 1.3. *The following inequality holds*

$$||\eta^{-1/2}\{\underline{\sigma}(\mathbf{v})\}||_{0,\mathcal{F}_h^I}^2 \lesssim \frac{1}{\alpha}||\underline{D}^{1/2}\underline{\varepsilon}(\mathbf{v})||_{0,\mathcal{T}_h}^2 \quad \forall \mathbf{v} \in \mathbf{V}_{DG}, \tag{1.15}$$

where α is the stability parameter appearing in the definition of the penalization function (1.14)*.*

Proof. Let $F \in \mathcal{F}_h^I$ be an interior face shared by two neighboring elements $\Omega_{k^\pm}$. Using the definition of the average operator it clearly holds

$$||\eta^{-1/2}\{\underline{\sigma}(\mathbf{v})\}||_{0,F}^2 \lesssim ||\eta^{-1/2}\{\underline{\sigma}(\mathbf{v}^+)\}||_{0,F}^2 + ||\eta^{-1/2}\{\underline{\sigma}(\mathbf{v}^-)\}||_{0,F}^2. \tag{1.16}$$

Recalling that $\underline{\sigma}(\mathbf{v}^\pm) = \underline{D\varepsilon}(\mathbf{v}^\pm)$, it is therefore enough to show

$$||\eta^{-1/2}\underline{\sigma}(\mathbf{v}^\pm)||_{0,F}^2 = ||\eta^{-1/2}\underline{D\varepsilon}(\mathbf{v}^\pm)||_{0,F}^2 \lesssim \frac{1}{\alpha}||\underline{D}^{1/2}\underline{\varepsilon}(\mathbf{v})||_{0,\Omega_{k^\pm}}^2, \tag{1.17}$$

since the thesis then follows by summing over all the interior faces $F \in \mathcal{F}_h^I$. Using the definition of the penalization function (1.14), the local bounded variation property, together with the trace-inverse inequality in Lemma 1.2 we have

$$||\eta^{-1/2}\underline{D\varepsilon}(\mathbf{v}^\pm)||_{0,F}^2 \lesssim \frac{1}{\alpha}\frac{\min\{h_{k^+}, h_{k^-}\}}{\max\{N_{k^+}^2, N_{k^-}^2\}}||\underline{D}^{1/2}\underline{\varepsilon}(\mathbf{v}^\pm)||_{0,F}^2 \lesssim \frac{1}{\alpha}||\underline{D}^{1/2}\underline{\varepsilon}(\mathbf{v})||_{0,\Omega_{k^\pm}}^2, \tag{1.18}$$

where hidden constant depends on the material properties through the quantity $||\underline{D}||_\infty/\{\underline{D}\}_H$. □

Let us introduce the following (mesh dependent) energy norm

$$||\mathbf{u}_h(t)||_{\mathcal{E}}^2 = ||\rho^{1/2}\dot{\mathbf{u}}_h(t)||_{0,\mathcal{T}_h}^2 + ||\rho^{1/2}\xi\mathbf{u}_h(t)||_{0,\mathcal{T}_h}^2 + ||\mathbf{u}_h(t)||_{DG}^2 \quad t \in (0,T]. \tag{1.19}$$

.

Lemma 1.4. *For any* $\mathbf{V}_{DG}$ *it holds*

$$||\mathbf{v}||_{\mathcal{E}}^2 - 2\langle\{\underline{\sigma}(\mathbf{v})\}, [\![\mathbf{v}]\!]\rangle_{\mathcal{F}_h^I} \lesssim ||\mathbf{v}||_{\mathcal{E}}^2, \tag{1.20a}$$

$$||\mathbf{v}||_{\mathcal{E}}^2 - 2\langle\{\underline{\sigma}(\mathbf{v})\}, [\![\mathbf{v}]\!]\rangle_{\mathcal{F}_h^I} \gtrsim ||\mathbf{v}||_{\mathcal{E}}^2. \tag{1.20b}$$

The second bound holds provided the stability parameter α *appearing in the definition of the penalization function* (1.14) *is chosen large enough.*

Proof. We prove the first bound with the Cauchy-Schwarz inequality, Lemma 1.3 and the definition of $||\cdot||_{\mathcal{E}}$-norm.

$$\begin{aligned} ||\mathbf{v}||_{\mathcal{E}}^2 - 2\langle\{\underline{\sigma}(\mathbf{v})\}, [\![\mathbf{v}]\!]\rangle_{\mathcal{F}_h^I} &\lesssim ||\mathbf{v}||_{\mathcal{E}}^2 + ||\eta^{-1/2}\{\underline{\sigma}(\mathbf{v})\}||_{0,\mathcal{F}_h^I} ||\eta^{1/2}[\![\mathbf{v}]\!]||_{0,\mathcal{F}_h^I} \\ &\lesssim ||\mathbf{v}||_{\mathcal{E}}^2 + \left(\frac{1}{\alpha}||\underline{D}^{1/2}\underline{\varepsilon}(\mathbf{v})||_{0,\mathcal{T}_h}^2\right)^{1/2} ||\mathbf{v}||_{DG} \\ &\lesssim ||\mathbf{v}||_{\mathcal{E}}^2 + ||\mathbf{v}||_{DG}^2 \lesssim ||\mathbf{v}||_{\mathcal{E}}^2. \end{aligned}$$

To find the second bound, it is sufficient to show that

$$||\mathbf{v}||_{DG}^2 - 2\langle\{\underline{\sigma}(\mathbf{v})\}, [\![\mathbf{v}]\!]\rangle_{\mathcal{F}_h^I} \gtrsim ||\mathbf{v}||_{DG}^2. \tag{1.21}$$

Indeed using definition of $||\mathbf{v}||_{\mathcal{E}}^2$ we have

$$\begin{aligned} ||\mathbf{v}||_{\mathcal{E}}^2 - 2\langle\{\underline{\sigma}(\mathbf{v})\}, [\![\mathbf{v}]\!]\rangle_{\mathcal{F}_h^I} &= ||\rho^{1/2}\dot{\mathbf{v}}||_{0,\mathcal{T}_h}^2 + ||\rho^{1/2}\xi\mathbf{v}||_{0,\mathcal{T}_h}^2 + ||\mathbf{v}||_{DG}^2 - 2\langle\{\underline{\sigma}(\mathbf{v})\}, [\![\mathbf{v}]\!]\rangle_{\mathcal{F}_h^I} \\ &\gtrsim ||\rho^{1/2}\dot{\mathbf{v}}||_{0,\mathcal{T}_h}^2 + ||\rho^{1/2}\xi\mathbf{v}||_{0,\mathcal{T}_h}^2 + ||\mathbf{v}||_{DG}^2 = ||\mathbf{v}||_{\mathcal{E}}^2. \end{aligned} \tag{1.22}$$

Therefore, we next show that (1.21) holds provided that the stability parameter α appearing in the definition of the penalization function η (1.14) is chosen large enough. To this aim, we observe that by using the Cauchy-Schwartz and Young inequalities we have, for any positive number β,

$$\begin{aligned} \langle\{\underline{\sigma}(\mathbf{v})\}, [\![\mathbf{v}]\!]\rangle_{\mathcal{F}_h^I} &\leq ||\eta^{-1/2}\{\underline{\sigma}(\mathbf{v})\}||_{0,\mathcal{F}_h^I} ||\eta^{1/2}[\![\mathbf{v}]\!]||_{0,\mathcal{F}_h^I} \\ &\leq \frac{1}{\beta}||\eta^{-1/2}\{\underline{\sigma}(\mathbf{v})\}||_{0,\mathcal{F}_h^I}^2 + \beta||\eta^{1/2}[\![\mathbf{v}]\!]||_{0,\mathcal{F}_h^I}^2 \end{aligned}$$

Therefore, from the definition of the DG norm $||\mathbf{v}||_{DG}$ it follows

$$\begin{aligned} &||\mathbf{v}||_{DG}^2 - 2\langle\{\underline{\sigma}(\mathbf{v})\}, [\![\mathbf{v}]\!]\rangle_{\mathcal{F}_h^I} \\ &\quad\geq ||\underline{D}^{1/2}\underline{\varepsilon}(\mathbf{v})||_{0,\mathcal{T}_h}^2 + ||\eta^{1/2}[\![\mathbf{v}]\!]||_{0,\mathcal{F}_h^I}^2 - \frac{1}{\beta}||\eta^{-1/2}\{\underline{\sigma}(\mathbf{v})\}||_{0,\mathcal{F}_h^I}^2 - \beta||\eta^{1/2}[\![\mathbf{v}]\!]||_{0,\mathcal{F}_h^I}^2 \\ &\quad\geq \left(1 - \frac{C}{\alpha\beta}\right)||\underline{D}^{1/2}\underline{\varepsilon}(\mathbf{v})||_{0,\mathcal{T}_h}^2 + (1-\beta)||\eta^{1/2}[\![\mathbf{v}]\!]||_{0,\mathcal{F}_h^I}^2 \gtrsim ||\mathbf{v}||_{DG}^2 \end{aligned}$$

where the last step follows from Lemma 1.3, with C denoting the hidden constant. Then (1.21) follows by choosing, for example, $\beta = 1/2$ and $\alpha \geq 4C$. □

Remark 1.1. The minimum value of penalty parameter α in the penalty function (1.14) is a function of the constant of the inverse inequality estimate that depends on the dimension of the problem and the shape of the elements employed in the discretization of the domain [WH03]. In [ER07], computable bounds of the threshold penalty parameter on triangular and tetrahedral meshes are provided in the case of a second-order elliptic problem. In practice, the numerical value $\alpha = 10$ guarantees stability (and therefore convergence) of symmetric interior penalty Galerkin methods.

Lemma 1.5. *The bilinear form* $\mathcal{A}_h(\cdot,\cdot) : \mathbf{V}_{DG} \times \mathbf{V}_{DG} \to \mathbb{R}$ *defined as in* (1.12) *satisfies*

$$|\mathcal{A}_h(\mathbf{w},\mathbf{v})| \lesssim ||\mathbf{w}||_{DG}||\mathbf{v}||_{DG}, \quad \mathcal{A}_h(\mathbf{v},\mathbf{v}) \gtrsim ||\mathbf{v}||^2_{DG}, \quad \forall \mathbf{v},\mathbf{w} \in \mathbf{V}_{DG},$$

where the second estimate holds provided that the parameter α *appearing in the definition of the stabilization function cf.* (1.14) *is chosen sufficiently large. Moreover,*

$$|\mathcal{A}_h(\mathbf{w},\mathbf{v})| \lesssim |||\mathbf{w}|||_{DG}||\mathbf{v}||_{DG}, \quad \forall \mathbf{w} \in \mathbf{H}^2(\mathcal{T}_h), \forall \mathbf{v} \in \mathbf{V}_{DG}.$$

Proof. Taking into account of the equivalence between the $|||\cdot|||_{DG}$ and $||\cdot||_{DG}$-norms, the continuity properties follow from the definition of the $|||\cdot|||_{DG}$-norm by applying the Cauchy-Schwartz and trace inequality. Finally, it is possible to prove the coercivity estimate with the definition of the $||\cdot||_{DG}$-norm and the results (1.21) in Lemma 1.4. □

1.3.2 Stability

In this section we present a stability analysis of the semi-discrete formulation (1.11) in the (mesh dependent) energy norm defined in (1.19). We remark that for $t = 0$ we have

$$||\mathbf{u}_h(0)||^2_{\mathcal{E}} = ||\rho^{1/2}\mathbf{v}_{0,h}||^2_{0,\mathcal{T}_h} + ||\rho^{1/2}\xi\mathbf{u}_{0,h}||^2_{0,\mathcal{T}_h} + ||\mathbf{u}_{0,h}||^2_{DG},$$

where $\mathbf{u}_{0,h}, \mathbf{v}_{0,h} \in \mathbf{V}_{DG}$ are suitable approximations of the initial data $\mathbf{u}_0$ and $\mathbf{u}_1$, respectively.

First we provide some technical tools useful to prove results in next sections, cf. [Qua14; Ant+18a]. We recall the following integration by parts formula

$$\int_0^t (\mathbf{u},\dot{\mathbf{v}})_* d\tau = (\mathbf{u}(t),\mathbf{v}(t))_* - (\mathbf{u}(0),\mathbf{v}(0))_* - \int_0^t (\dot{\mathbf{u}},\mathbf{v})_* d\tau \tag{1.23}$$

where $\mathbf{u},\mathbf{v}$ are regular enough and $(\cdot,\cdot)_*$ denotes any scalar product.

We also introduce the Gronwall's lemma.

Lemma 1.6 (Gronwall)**.** *Let $\beta(t) \in L^1(0,T)$ and $\varphi(t) \in C^0(0,T)$ non-negative functions such that*

$$\varphi(t)^2 \leq \gamma + \int_0^t \beta(\tau)\varphi(\tau)d\tau \quad \forall t \in [0,T], \tag{1.24}$$

where γ is a non-negative constant. Then

$$\varphi(t) \leq \sqrt{\gamma} + \int_0^t \beta(\tau)d\tau \quad \forall t \in [0,T]. \tag{1.25}$$

Theorem 1.1 (Stability)**.** *Let, for any time $t \in (0,T]$ and for a sufficiently large penalty parameter α in* (1.14)*, $\mathbf{u}_h(t) \in \mathbf{V}_{DG}$ be the solution of problem* (1.11)*. If $\mathbf{f} \in L^2(0,T;\mathbf{L}^2(\Omega))$, then*

$$||\mathbf{u}_h(t)||_{\mathcal{E}} \lesssim ||\mathbf{u}_h(0)||_{\mathcal{E}} + \int_0^t ||\mathbf{f}(\tau)||_{0,\Omega}\, d\tau, \quad 0 < t \leq T.$$

Proof. By taking $\mathbf{v} = \dot{\mathbf{u}}_h$ in (1.11), we obtain

$$\begin{aligned}(\rho\ddot{\mathbf{u}}_h, \dot{\mathbf{u}}_h)_{\mathcal{T}_h} &+ (2\rho\xi\dot{\mathbf{u}}_h, \dot{\mathbf{u}}_h)_{\mathcal{T}_h} + (\underline{\sigma}(\mathbf{u}_h), \underline{\varepsilon}(\dot{\mathbf{u}}_h))_{\mathcal{T}_h} - \langle\{\underline{\sigma}(\mathbf{u}_h)\}, [\![\dot{\mathbf{u}}_h]\!]\rangle_{\mathcal{F}_h^I} \\ &- \langle[\![\mathbf{u}_h]\!], \{\underline{\sigma}(\dot{\mathbf{u}}_h)\}\rangle_{\mathcal{F}_h^I} + \langle\eta\,[\![\mathbf{u}_h]\!], [\![\dot{\mathbf{u}}_h]\!]\rangle_{\mathcal{F}_h^I}, + (\rho\xi^2\mathbf{u}_h, \dot{\mathbf{u}}_h)_{\mathcal{T}_h} = (\mathbf{f}, \dot{\mathbf{u}}_h)_{\mathcal{T}_h},\end{aligned}$$

that is

$$\frac{1}{2}\frac{d}{dt}\left(||\mathbf{u}_h||_{\mathcal{E}}^2 - 2\langle\{\underline{\sigma}(\mathbf{u}_h)\}, [\![\mathbf{u}_h]\!]\rangle_{\mathcal{F}_h^I}\right) + 2||\rho^{1/2}\xi^{1/2}\dot{\mathbf{u}}_h||_{0,\mathcal{T}_h}^2 = (\mathbf{f}, \dot{\mathbf{u}}_h)_{\mathcal{T}_h}.$$

Integrating the above inequality over the time interval $(0,t)$ we have

$$\begin{aligned}||\mathbf{u}_h(t)||_{\mathcal{E}}^2 &- 2\langle\{\underline{\sigma}(\mathbf{u}_h(t))\}, [\![\mathbf{u}_h(t)]\!]\rangle_{\mathcal{F}_h^I} + 4\int_0^t ||\rho^{1/2}\xi^{1/2}\dot{\mathbf{u}}_h(\tau)||_{0,\mathcal{T}_h}^2 d\tau \\ &= ||\mathbf{u}_h(0)||_{\mathcal{E}}^2 - 2\langle\{\underline{\sigma}(\mathbf{u}_h(0))\}, [\![\mathbf{u}_h(0)]\!]\rangle_{\mathcal{F}_h^I} + 2\int_0^t (\mathbf{f}(\tau), \dot{\mathbf{u}}_h(\tau))_{\mathcal{T}_h}\, d\tau.\end{aligned}$$

Since $4\int_0^t ||\rho^{1/2}\xi^{1/2}\dot{\mathbf{u}}_h(\tau)||_{0,\mathcal{T}_h}^2 d\tau \geq 0$, then

$$\begin{aligned}||\mathbf{u}_h(t)||_{\mathcal{E}}^2 &- 2\langle\{\underline{\sigma}(\mathbf{u}_h(t))\}, [\![\mathbf{u}_h(t)]\!]\rangle_{\mathcal{F}_h^I} \\ &\leq ||\mathbf{u}_h(0)||_{\mathcal{E}}^2 - 2\langle\{\underline{\sigma}(\mathbf{u}_h(0))\}, [\![\mathbf{u}_h(0)]\!]\rangle_{\mathcal{F}_h^I} + 2\int_0^t (\mathbf{f}(\tau), \dot{\mathbf{u}}_h(\tau))_{\mathcal{T}_h}\, d\tau.\end{aligned}$$

From Lemma 1.4 we get

$$\begin{aligned}||\mathbf{u}_h||_{\mathcal{E}}^2 - 2\langle\{\underline{\sigma}(\mathbf{u}_h)\}, [\![\mathbf{u}_h]\!]\rangle_{\mathcal{F}_h^I} &\gtrsim ||\mathbf{u}_h||_{\mathcal{E}}^2, \\ ||\mathbf{u}_h(0)||_{\mathcal{E}}^2 - 2\langle\{\underline{\sigma}(\mathbf{u}_h(0))\}, [\![\mathbf{u}_h(0)]\!]\rangle_{\mathcal{F}_h^I} &\lesssim ||\mathbf{u}_h(0)||_{\mathcal{E}}^2,\end{aligned}$$

where the first bound holds provided that the stability parameter α appearing in the definition of the penalization function (1.14) is chosen large enough. Then

$$||\mathbf{u}_h(t)||_{\mathcal{E}}^2 \lesssim ||\mathbf{u}_h(0)||_{\mathcal{E}}^2 + 2\int_0^t (\mathbf{f}(\tau), \dot{\mathbf{u}}_h(\tau))_{\mathcal{T}_h}\, d\tau.$$

The Cauchy-Schwarz inequality leads to

$$2\int_0^t (\mathbf{f}(\tau),\dot{\mathbf{u}}_h(\tau))_{\mathcal{T}_h}\,d\tau \lesssim \int_0^t ||\mathbf{f}(\tau)||_{0,\mathcal{T}_h}||\rho^{1/2}\dot{\mathbf{u}}_h(\tau)||_{0,\mathcal{T}_h}\,d\tau \leq \int_0^t ||\mathbf{f}(\tau)||_{0,\Omega}||\mathbf{u}_h||_{\mathcal{E}}\,d\tau.$$

The thesis follows based on employing the Gronwall's lemma. □

1.3.3 Semi-discrete error estimates

Lemma 1.7 ([BS87b, Lemma 4.5])**.** *For any function* $\mathbf{v}$ *such that* $\mathbf{v}|_{\Omega_k} \in \mathbf{H}^{s_k}(\Omega_k)$, $s_k \geq 0$, $k = 1,\ldots,K$, *there exists* $\mathbf{v}_I \in \mathbf{V}_{DG}$ *such that*

$$\sum_{\Omega_k} ||\mathbf{v}-\mathbf{v}_I||^2_{r,\Omega_k} \lesssim \sum_{\Omega_k} \frac{h_k^{2m_k-2r}}{N_k^{2s_k-2r}}||\mathbf{v}||^2_{s_k,\Omega_k}, \quad \forall r, 0 \leq r \leq s_k,$$

$$\sum_{\Omega_k} ||\mathbf{v}-\mathbf{v}_I||^2_{0,\partial\Omega_k} \lesssim \sum_{\Omega_k} \frac{h_k^{2m_k-1}}{N_k^{2s_k-1}}||\mathbf{v}||^2_{s_k,\Omega_k},$$

$$\sum_{\Omega_k} ||\nabla(\mathbf{v}-\mathbf{v}_I)||^2_{0,\partial\Omega_k} \lesssim \sum_{\Omega_k} \frac{h_k^{2m_k-3}}{N_k^{2s_k-3}}||\mathbf{v}||^2_{s_k,\Omega_k},$$

where $m_k = \min(s_k, N_k+1)$.

Based on standard DG techniques, the following preliminary bound holds.

Lemma 1.8. *For any function* $\mathbf{v}$ *such that* $\mathbf{v}|_{\Omega_k} \in \mathbf{H}^{s_k}(\Omega_k)$, $s_k \geq 2$, $k = 1,\ldots,K$, *there exists* $\mathbf{v}_I \in \mathbf{V}_{DG}$ *such that*

$$|||\mathbf{v}-\mathbf{v}_I|||^2_{DG} \lesssim \sum_{\Omega_k} \frac{h_k^{2m_k-2}}{N_k^{2s_k-3}}||\mathbf{v}||^2_{s_k,\Omega_k}, \tag{1.26}$$

where $m_k = \min(s_k, N_k+1)$. *Moreover, if in addition* $\mathbf{v}|_{\Omega_k}, \dot{\mathbf{v}}|_{\Omega_k} \in \mathbf{H}^{s_k}(\Omega_k)$, $s_k \geq 2$, $k = 1,\ldots,K$, *then*

$$||\mathbf{v}-\mathbf{v}_I||^2_{\mathcal{E}} \lesssim \sum_{\Omega_k} \frac{h_k^{2m_k-2}}{N_k^{2s_k-3}}\left(||\dot{\mathbf{v}}||^2_{s_k,\Omega_k} + ||\mathbf{v}||^2_{s_k,\Omega_k}\right). \tag{1.27}$$

Proof. We first show (1.26). With this aim, use Lemma 1.7 to bound each contribution appearing in the definition of the DG norm $|||\cdot|||^2_{DG}$.

$$||\underline{D}^{1/2}\underline{\varepsilon}(\mathbf{v}-\mathbf{v}_I)||^2_{0,\mathcal{T}_h} \lesssim \sum_{\Omega_k} \frac{h_k^{2m_k-2}}{N_k^{2s_k-2}}||\mathbf{v}||^2_{s_k,\Omega_k},$$

$$||\eta^{1/2}[\![\mathbf{v}-\mathbf{v}_I]\!]||^2_{0,\mathcal{F}_h^I} \lesssim \sum_{\Omega_k} \frac{h_k^{2m_k-2}}{N_k^{2s_k-3}}||\mathbf{v}||^2_{s_k,\Omega_k},$$

$$||\eta^{-1/2}\{\underline{D\varepsilon}(\mathbf{v}-\mathbf{v}_I)\}||^2_{0,\mathcal{F}_h^I} \lesssim \sum_{\Omega_k} \frac{h_k^{2m_k-2}}{N_k^{2s_k-1}}||\mathbf{v}||^2_{s_k,\Omega_k}.$$

This yields

$$|||\mathbf{v}-\mathbf{v}_I|||_{DG}^2 \lesssim \sum_{\Omega_k} \frac{h_k^{2m_k-2}}{N_k^{2s_k-3}} \left(\frac{1}{N_k}+1+\frac{1}{N_k^2}\right) ||\mathbf{v}||_{s_k,\Omega_k}^2 \lesssim \sum_{\Omega_k} \frac{h_k^{2m_k-2}}{N_k^{2s_k-3}} ||\mathbf{v}||_{s_k,\Omega_k}^2.$$

Next we show (1.27). We recall the definition of energy norm and employ again the interpolation estimates of Lemma 1.7 to get

$$\begin{aligned}
||\rho^{1/2}(\dot{\mathbf{v}}-\dot{\mathbf{v}}_I)||_{0,\mathcal{T}_h}^2 &\lesssim \sum_{\Omega_k} \frac{h_k^{2m_k}}{N_k^{2s_k}} ||\dot{\mathbf{v}}||_{s_k,\Omega_k}^2,\\
||\rho^{1/2}\xi(\mathbf{v}-\mathbf{v}_I)||_{0,\mathcal{T}_h}^2 &\lesssim \sum_{\Omega_k} \frac{h_k^{2m_k}}{N_k^{2s_k}} ||\mathbf{v}||_{s_k,\Omega_k}^2,\\
||\mathbf{v}-\mathbf{v}_I||_{DG}^2 &\lesssim \sum_{\Omega_k} \frac{h_k^{2m_k-2}}{N_k^{2s_k-3}} ||\mathbf{v}||_{s_k,\Omega_k}^2.
\end{aligned}$$

Finally, summing up the above contributions we obtain

$$\begin{aligned}
||\mathbf{v}-\mathbf{v}_I||_{\mathcal{E}}^2 &\lesssim \sum_{\Omega_k} \frac{h_k^{2m_k-2}}{N_k^{2s_k-3}} \left(\frac{h_k^2}{N_k^3} ||\dot{\mathbf{v}}||_{s_k,\Omega_k}^2 + \frac{h_k^2}{N_k^3} ||\mathbf{v}||_{s_k,\Omega_k}^2 + ||\mathbf{v}||_{s_k,\Omega_k}^2\right)\\
&\lesssim \sum_{\Omega_k} \frac{h_k^{2m_k-2}}{N_k^{2s_k-3}} \left(||\dot{\mathbf{v}}||_{s_k,\Omega_k}^2 + ||\mathbf{v}||_{s_k,\Omega_k}^2\right).
\end{aligned}$$

□

Theorem 1.2 (A-priori error estimate in the energy norm)**.** *Assume that, for any time $t \in [0,T]$, the exact solution $\mathbf{u}(t)$ of problem* (1.4) *together with its two first temporal derivatives satisfy $\mathbf{u}(t)|_{\Omega_k}, \dot{\mathbf{u}}(t)|_{\Omega_k}, \ddot{\mathbf{u}}(t)|_{\Omega_k} \in \mathbf{H}^{s_k}(\Omega_k)$, $k=1,\dots,K$, $s_k \geq 2$. Let $\mathbf{u}_h$ be the corresponding solution of the semi-discrete DG formulation given in* (1.11)*, with a sufficiently large penalty parameter α in the definition of the stabilization function* (1.14)*. Then,*

$$\begin{aligned}
\sup_{t\in[0,T]} ||\mathbf{e}_h(t)||_{\mathcal{E}}^2 \lesssim \sup_{t\in[0,T]} &\left\{ \sum_{\Omega_k} \frac{h_k^{2m_k-2}}{N_k^{2s_k-3}} \left(||\dot{\mathbf{u}}||_{s_k,\Omega_k}^2 + ||\mathbf{u}||_{s_k,\Omega_k}^2\right)\right\}\\
&+ \int_0^T \sum_{\Omega_k} \frac{h_k^{2m_k-2}}{N_k^{2s_k-3}} \left(||\ddot{\mathbf{u}}||_{s_k,\Omega_k}^2 + ||\dot{\mathbf{u}}||_{s_k,\Omega_k}^2\right) dt.
\end{aligned}$$

Proof. The discrete formulation (1.11) is strongly consistent, that is the exact solution $\mathbf{u}$ of (1.4) satisfies equation (1.11) for any time $t \in (0,T]$:

$$(\rho\,\ddot{\mathbf{u}},\mathbf{v})_{\mathcal{T}_h} + (2\rho\xi\,\dot{\mathbf{u}},\mathbf{v})_{\mathcal{T}_h} + \mathcal{A}_h(\mathbf{u},\mathbf{v}) + (\rho\xi^2\,\mathbf{u},\mathbf{v})_{\mathcal{T}_h} = \mathcal{F}_h(\mathbf{v}) \quad \forall \mathbf{v} \in \mathbf{V}_{DG}.$$

Subtracting (1.11) from the above identity and setting $\mathbf{e} = \mathbf{u} - \mathbf{u}_h$, we obtain the error equation

$$(\rho\,\ddot{\mathbf{e}}, \mathbf{v})_{\mathcal{T}_h} + (2\rho\xi\,\dot{\mathbf{e}}, \mathbf{v})_{\mathcal{T}_h} + \mathcal{A}_h(\mathbf{e}, \mathbf{v}) + (\rho\xi^2\,\mathbf{e}, \mathbf{v})_{\mathcal{T}_h} = \mathbf{0} \quad \forall \mathbf{v} \in \mathbf{V}_{DG}.$$

We next decompose the error as $\mathbf{e} = \mathbf{e}_I - \mathbf{e}_h$, with $\mathbf{e}_I = \mathbf{u} - \mathbf{u}_I$ and $\mathbf{e}_h = \mathbf{u}_h - \mathbf{u}_I$, $\mathbf{u}_I \in \mathbf{V}_{DG}$ being the interpolant defined as in Lemma 1.7, and rewrite the above identity as

$$\begin{aligned}(\rho\,\ddot{\mathbf{e}}_h, \mathbf{v})_{\mathcal{T}_h} + (2\rho\xi\,\dot{\mathbf{e}}_h, \mathbf{v})_{\mathcal{T}_h} + \mathcal{A}_h(\mathbf{e}_h, \mathbf{v}) + (\rho\xi^2\,\mathbf{e}_h, \mathbf{v})_{\mathcal{T}_h} \\ = (\rho\,\ddot{\mathbf{e}}_I, \mathbf{v})_{\mathcal{T}_h} + (2\rho\xi\,\dot{\mathbf{e}}_I, \mathbf{v})_{\mathcal{T}_h} + \mathcal{A}_h(\mathbf{e}_I, \mathbf{v}) + (\rho\xi^2\,\mathbf{e}_I, \mathbf{v})_{\mathcal{T}_h} \quad \forall \mathbf{v} \in \mathbf{V}_{DG}.\end{aligned}$$

By taking as test function $\mathbf{v} = \dot{\mathbf{e}}_h$, we get

$$\begin{aligned}(\rho\,\ddot{\mathbf{e}}_h, \dot{\mathbf{e}}_h)_{\mathcal{T}_h} + (2\rho\xi\,\dot{\mathbf{e}}_h, \dot{\mathbf{e}}_h)_{\mathcal{T}_h} + \mathcal{A}_h(\mathbf{e}_h, \dot{\mathbf{e}}_h) + (\rho\xi^2\,\mathbf{e}_h, \dot{\mathbf{e}}_h)_{\mathcal{T}_h} \\ = (\rho\,\ddot{\mathbf{e}}_I, \dot{\mathbf{e}}_h)_{\mathcal{T}_h} + (2\rho\xi\,\dot{\mathbf{e}}_I, \dot{\mathbf{e}}_h)_{\mathcal{T}_h} + \mathcal{A}_h(\mathbf{e}_I, \dot{\mathbf{e}}_h) + (\rho\xi^2\,\mathbf{e}_I, \dot{\mathbf{e}}_h)_{\mathcal{T}_h},\end{aligned}$$

that is

$$\begin{aligned}&\frac{1}{2}\frac{d}{dt}\left(||\rho^{1/2}\dot{\mathbf{e}}_h||^2_{0,\mathcal{T}_h} + ||\rho^{1/2}\xi\mathbf{e}_h||^2_{0,\mathcal{T}_h} + ||\mathbf{e}_h||^2_{DG} - 2\langle\{\underline{\sigma}(\mathbf{e}_h)\}, [\![\mathbf{e}_h]\!]\rangle_{\mathcal{F}_h^I}\right) \\ &\quad + 2||\rho^{1/2}\xi^{1/2}\dot{\mathbf{e}}_h||^2_{0,\mathcal{T}_h} = (\rho\,\ddot{\mathbf{e}}_I, \dot{\mathbf{e}}_h)_{\mathcal{T}_h} + (2\rho\xi\,\dot{\mathbf{e}}_I, \dot{\mathbf{e}}_h)_{\mathcal{T}_h} + \mathcal{A}_h(\mathbf{e}_I, \dot{\mathbf{e}}_h) + (\rho\xi^2\,\mathbf{e}_I, \dot{\mathbf{e}}_h)_{\mathcal{T}_h}.\end{aligned}$$

Using the definition of the energy norm and the Cauchy-Schwarz inequality to bound the terms on the right hand side we obtain

$$\begin{aligned}&\frac{1}{2}\frac{d}{dt}\left(||\mathbf{e}_h||^2_{\mathcal{E}} - 2\langle\{\underline{\sigma}(\mathbf{e}_h)\}, [\![\mathbf{e}_h]\!]\rangle_{\mathcal{F}_h^I}\right) + 2||\rho^{1/2}\xi^{1/2}\dot{\mathbf{e}}_h||^2_{0,\mathcal{T}_h} \\ &\qquad \le ||\dot{\mathbf{e}}_I||_{\mathcal{E}}||\mathbf{e}_h||_{\mathcal{E}} + 2||\rho^{1/2}\xi^{1/2}\dot{\mathbf{e}}_I||_{0,\mathcal{T}_h}||\rho^{1/2}\xi^{1/2}\dot{\mathbf{e}}_h||_{0,\mathcal{T}_h} \\ &\qquad + \mathcal{A}_h(\mathbf{e}_I, \dot{\mathbf{e}}_h) + (\rho\xi^2\,\mathbf{e}_I, \dot{\mathbf{e}}_h)_{\mathcal{T}_h}.\end{aligned}$$

Thanks to the Young's inequality we have that $2||\rho^{1/2}\xi^{1/2}\dot{\mathbf{e}}_I||_{0,\mathcal{T}_h}||\rho^{1/2}\xi^{1/2}\dot{\mathbf{e}}_h||_{0,\mathcal{T}_h} \le ||\rho^{1/2}\xi^{1/2}\dot{\mathbf{e}}_I||^2_{0,\mathcal{T}_h} + ||\rho^{1/2}\xi^{1/2}\dot{\mathbf{e}}_h||^2_{0,\mathcal{T}_h}$ and therefore the above bound can be rewritten as

$$\begin{aligned}&\frac{1}{2}\frac{d}{dt}\left(||\mathbf{e}_h||^2_{\mathcal{E}} - 2\langle\{\underline{\sigma}(\mathbf{e}_h)\}, [\![\mathbf{e}_h]\!]\rangle_{\mathcal{F}_h^I}\right) + ||\rho^{1/2}\xi^{1/2}\dot{\mathbf{e}}_h||^2_{0,\mathcal{T}_h} \\ &\qquad \le ||\dot{\mathbf{e}}_I||_{\mathcal{E}}||\mathbf{e}_h||_{\mathcal{E}} + ||\rho^{1/2}\xi^{1/2}\dot{\mathbf{e}}_I||^2_{0,\mathcal{T}_h} + \mathcal{A}_h(\mathbf{e}_I, \dot{\mathbf{e}}_h) + (\rho\xi^2\,\mathbf{e}_I, \dot{\mathbf{e}}_h)_{\mathcal{T}_h}.\end{aligned}$$

Observing that $||\rho^{1/2}\xi^{1/2}\dot{\mathbf{e}}_h||_{0,\mathcal{T}_h} \ge 0$ and integrating in time between 0 and t, and using that $\mathbf{e}_h(0) = \mathbf{u}_h(0) - \mathbf{u}_I(0) = \mathbf{0}$, it follows

$$\begin{aligned}\frac{1}{2}\left(||\mathbf{e}_h||^2_{\mathcal{E}} - 2\langle\{\underline{\sigma}(\mathbf{e}_h)\}, [\![\mathbf{e}_h]\!]\rangle_{\mathcal{F}_h^I}\right) \le \int_0^t ||\dot{\mathbf{e}}_I||_{\mathcal{E}}||\mathbf{e}_h||_{\mathcal{E}}\,d\tau + \int_0^t ||\rho^{1/2}\xi^{1/2}\dot{\mathbf{e}}_I||^2_{0,\mathcal{T}_h}\,d\tau \\ + \int_0^t \mathcal{A}_h(\mathbf{e}_I, \dot{\mathbf{e}}_h)\,d\tau + \int_0^t (\rho\xi^2\,\mathbf{e}_I, \dot{\mathbf{e}}_h)_{\mathcal{T}_h}\,d\tau.\end{aligned}$$

Employing Lemma 1.4 we obtain

$$\begin{aligned}\frac{1}{2}||\mathbf{e}_h||_{\mathcal{E}}^2 \leq \int_0^t ||\dot{\mathbf{e}}_I||_{\mathcal{E}}||\mathbf{e}_h||_{\mathcal{E}}\,d\tau + \int_0^t ||\rho^{1/2}\xi^{1/2}\dot{\mathbf{e}}_I||_{0,\mathcal{T}_h}^2\,d\tau \\ + \int_0^t \mathcal{A}_h(\mathbf{e}_I,\dot{\mathbf{e}}_h)\,d\tau + \int_0^t (\rho\xi^2\,\mathbf{e}_I,\dot{\mathbf{e}}_h)_{\mathcal{T}_h}\,d\tau.\end{aligned} \tag{1.28}$$

We next estimate the last two terms on the right hand side. For the first one, the integration by parts formula together with the observation that $\mathbf{e}_h(0) = \mathbf{u}_h(0) - \mathbf{u}_I(0) = \mathbf{0}$, and Lemma 1.5 lead to

$$\begin{aligned}\int_0^t \mathcal{A}_h(\mathbf{e}_I,\dot{\mathbf{e}}_h)\,d\tau =& \mathcal{A}_h(\mathbf{e}_I(t),\mathbf{e}_h(t)) - \mathcal{A}_h(\mathbf{e}_I(0),\mathbf{e}_h(0)) - \int_0^t \mathcal{A}_h(\dot{\mathbf{e}}_I,\mathbf{e}_h)\,d\tau \\ &\lesssim |||\mathbf{e}_I|||_{DG}||\mathbf{e}_h||_{DG} + \int_0^t |||\dot{\mathbf{e}}_I|||_{DG}||\mathbf{e}_h||_{DG}\,d\tau \\ &\lesssim |||\mathbf{e}_I|||_{DG}||\mathbf{e}_h||_{\mathcal{E}} + \int_0^t |||\dot{\mathbf{e}}_I|||_{DG}||\mathbf{e}_h||_{\mathcal{E}}\,d\tau,\end{aligned} \tag{1.29}$$

where in the last step we have used the definition of the energy norm. Analogously, for the second term

$$\begin{aligned}\int_0^t (\rho\xi^2\,\mathbf{e}_I,\dot{\mathbf{e}}_h)_{\mathcal{T}_h}\,d\tau =& (\rho\xi^2\,\mathbf{e}_I(t),\mathbf{e}_h(t))_{\mathcal{T}_h} - (\rho\xi^2\,\mathbf{e}_I(0),\mathbf{e}_h(0))_{\mathcal{T}_h} - \int_0^t (\rho\xi^2\,\dot{\mathbf{e}}_I,\mathbf{e}_h)_{\mathcal{T}_h}\,d\tau \\ &\lesssim ||\mathbf{e}_I||_{\mathcal{E}}||\mathbf{e}_h||_{\mathcal{E}} + \int_0^t ||\dot{\mathbf{e}}_I||_{\mathcal{E}}||\mathbf{e}_h||_{\mathcal{E}}\,d\tau.\end{aligned} \tag{1.30}$$

By substituting the above two bounds (1.29) and (1.30) in (1.28) we get

$$\begin{aligned}\frac{1}{2}||\mathbf{e}_h||_{\mathcal{E}}^2 &\lesssim \int_0^t ||\dot{\mathbf{e}}_I||_{\mathcal{E}}||\mathbf{e}_h||_{\mathcal{E}}\,d\tau + \int_0^t ||\rho^{1/2}\xi^{1/2}\dot{\mathbf{e}}_I||_{0,\mathcal{T}_h}^2\,d\tau + |||\mathbf{e}_I|||_{DG}||\mathbf{e}_h||_{\mathcal{E}} \\ &+ \int_0^t |||\dot{\mathbf{e}}_I|||_{DG}||\mathbf{e}_h||_{\mathcal{E}}\,d\tau + ||\mathbf{e}_I||_{\mathcal{E}}||\mathbf{e}_h||_{\mathcal{E}} + \int_0^t ||\dot{\mathbf{e}}_I||_{\mathcal{E}}||\mathbf{e}_h||_{\mathcal{E}}\,d\tau \\ &= (||\mathbf{e}_I||_{\mathcal{E}} + |||\mathbf{e}_I|||_{DG})||\mathbf{e}_h||_{\mathcal{E}} + \int_0^t ||\rho^{1/2}\xi^{1/2}\dot{\mathbf{e}}_I||_{0,\mathcal{T}_h}^2\,d\tau \\ &+ \int_0^t (||\dot{\mathbf{e}}_I||_{\mathcal{E}} + |||\dot{\mathbf{e}}_I|||_{DG})\,||\mathbf{e}_h||_{\mathcal{E}}\,d\tau.\end{aligned}$$

From the Young's inequality, it follows

$$\begin{aligned}(||\mathbf{e}_I||_{\mathcal{E}} + |||\mathbf{e}_I|||_{DG})||\mathbf{e}_h||_{\mathcal{E}} &\leq \delta(||\mathbf{e}_I||_{\mathcal{E}} + |||\mathbf{e}_I|||_{DG})^2 + \frac{1}{\delta}||\mathbf{e}_h||_{\mathcal{E}}^2 \\ &\leq 2\delta(||\mathbf{e}_I||_{\mathcal{E}}^2 + |||\mathbf{e}_I|||_{DG}^2) + \frac{1}{\delta}||\mathbf{e}_h||_{\mathcal{E}}^2\end{aligned} \tag{1.31}$$

and therefore, we can therefore chose $\delta = 4C$ being C the hidden constant in (1.31) and obtain

$$\begin{aligned}\frac{1}{4}||\mathbf{e}_h||_{\mathcal{E}}^2 \lesssim& ||\mathbf{e}_I||_{\mathcal{E}}^2 + |||\mathbf{e}_I|||_{DG}^2 + \int_0^t ||\rho^{1/2}\xi^{1/2}\dot{\mathbf{e}}_I||_{0,\mathcal{T}_h}^2\,d\tau \\ &+ \int_0^t (||\dot{\mathbf{e}}_I||_{\mathcal{E}} + |||\dot{\mathbf{e}}_I|||_{DG})\,||\mathbf{e}_h||_{\mathcal{E}}\,d\tau.\end{aligned}$$

By applying the Gronwall's lemma we get

$$||\mathbf{e}_h||^2_{\mathcal{E}} \lesssim \gamma + \int_0^t \left(||\dot{\mathbf{e}}_I||^2_{\mathcal{E}} + |||\dot{\mathbf{e}}_I|||^2_{DG} \right) d\tau$$

with

$$\gamma = \sup_{t\in[0,T]} \left\{ ||\mathbf{e}_I||^2_{\mathcal{E}} + |||\mathbf{e}_I|||^2_{DG} + \int_0^t ||\rho^{1/2}\xi^{1/2}\dot{\mathbf{e}}_I||^2_{0,\mathcal{T}_h} \, d\tau \right\}.$$

The interpolation estimates of Lemmas 1.7 and 1.8 lead to

$$\gamma \lesssim \sup_{t\in[0,T]} \left\{ \sum_{\Omega_k} \frac{h_k^{2m_k-2}}{N_k^{2s_k-3}} \left(||\dot{\mathbf{u}}||^2_{s_k,\Omega_k} + ||\mathbf{u}||^2_{s_k,\Omega_k} + \int_0^t ||\dot{\mathbf{u}}||^2_{s_k,\Omega_k} \, d\tau \right) \right\},$$

$$||\dot{\mathbf{e}}_I||^2_{\mathcal{E}} + |||\dot{\mathbf{e}}_I|||^2_{DG} \lesssim \sum_{\Omega_k} \frac{h_k^{2m_k-2}}{N_k^{2s_k-3}} \left(||\ddot{\mathbf{u}}||^2_{s_k,\Omega_k} + ||\dot{\mathbf{u}}||^2_{s_k,\Omega_k} \right).$$

Therefore we obtain

$$\sup_{t\in[0,T]} ||\mathbf{e}_h(t)||^2_{\mathcal{E}} \lesssim \sup_{t\in[0,T]} \left\{ \sum_{\Omega_k} \frac{h_k^{2m_k-2}}{N_k^{2s_k-3}} \left(||\dot{\mathbf{u}}||^2_{s_k,\Omega_k} + ||\mathbf{u}||^2_{s_k,\Omega_k} + \int_0^t ||\dot{\mathbf{u}}||^2_{s_k,\Omega_k} \, d\tau \right) \right\}$$
$$+ \int_0^T \sum_{\Omega_k} \frac{h_k^{2m_k-2}}{N_k^{2s_k-3}} \left(||\ddot{\mathbf{u}}||^2_{s_k,\Omega_k} + ||\dot{\mathbf{u}}||^2_{s_k,\Omega_k} \right) dt$$

and the proof is complete. □

1.4 Fully discrete formulation

The algebraic version of (1.11) can be obtained by: (i) introducing a basis $\{\mathbf{\Psi}\}_{i=1,...,N_h}$ for the finite element space $\mathbf{V}_{DG}$; (ii) expressing $\mathbf{u} \in \mathbf{V}_{DG}$ as linear combination of the shape functions, i.e. $\mathbf{u}(\mathbf{x},t) = \sum_{i=1}^{N_h} \mathbf{U}_j(t)\mathbf{\Psi}_j(\mathbf{x})$; and (iii) choosing $\mathbf{v} = \mathbf{\Psi}_i$ for any $i = 1, ..., N_h$. The resulting system has the following structure

$$\mathsf{M}\ddot{\mathbf{U}}(t) + \mathsf{C}\dot{\mathbf{U}}(t) + \mathsf{A}\mathbf{U}(t) = \mathbf{F}(t), \quad t \in (0,T], \tag{1.32}$$

together with initial conditions $\mathbf{U}(0) = \mathbf{u}_{0,h}$ and $\dot{\mathbf{U}}(0) = \mathbf{v}_{0,h}$, being $\mathbf{u}_{0,h}$ and $\mathbf{v}_{0,h}$ suitable approximation in $\mathbf{V}_{DG}$ of the initial data $\mathbf{u}_0$ and $\mathbf{u}_1$. In (1.32), the vector $\mathbf{U}(t) \in \mathbb{R}^{N_h}$ contains the unknown expansion coefficients in the chosen basis, i.e. $\mathbf{U}_j(t) = \mathbf{u}(\mathbf{x}_j, t)$. The mass, damping, and stiffness matrices are defined as

$$\begin{aligned}
\mathsf{M}_{ij} &= (\rho\mathbf{\Psi}_j, \mathbf{\Psi}_i)_{\mathcal{T}_h}, && i,j = 1, ..., N_h, \\
\mathsf{C}_{ij} &= (2\rho\xi\mathbf{\Psi}_j, \mathbf{\Psi}_i)_{\mathcal{T}_h}, && i,j = 1, ..., N_h \\
\mathsf{A}_{ij} &= \mathcal{A}_h(\mathbf{\Psi}_j, \mathbf{\Psi}_i) + (\rho\xi^2\mathbf{\Psi}_j, \mathbf{\Psi}_i)_{\mathcal{T}_h}, && i,j = 1, ..., N_h,
\end{aligned}$$

respectively. Finally, the right-hand side $\mathbf{F}(t)$ has the following expression

$$\mathbf{F}_i(t) = (\mathbf{f}(t), \mathbf{\Psi}_i)_{\mathcal{T}_h} + \langle \mathbf{t}(t), \mathbf{\Psi}_i \rangle_{\mathcal{F}_h^N} + \langle \mathbf{t}^*(t), \mathbf{\Psi}_i \rangle_{\mathcal{F}_h^{NR}}, \qquad i = 1, ..., N_h.$$

Notice that the choice of the basis functions $\{\mathbf{\Psi}_i\}$ for the spectral element space $\mathbf{V}_{DG}$ reflects on the structure of system (1.32). To span the discrete space we consider tensor product nodal Lagrangian functions associated to the tensor product of the Gauss-Legendre-Lobatto (GLL) interpolating points [Can+06] for hexaedral elements. Instead when we employ tetrahedral elements, we use modal boundary adapted basis [KS13; SK95]. This in turn gives a diagonal structure to the matrices M and C that can be effectively exploited for the time integration scheme. Indeed, to integrate (1.32) in time we proceed as follows. We subdivide the time interval $(0, T]$ into N_T time slabs of length $\Delta t = T/N_T$ and we denote by $\mathbf{U}^k$ the approximation of $\mathbf{U}$ at time $t^k = k\Delta t$, i.e. $\mathbf{U}^k \approx \mathbf{U}(t_k)$, $k = 0, ..., N_T$. Given $\mathbf{U}^0 = \mathbf{U}(0)$ and $\mathbf{V}^0 = \dot{\mathbf{U}}(0)$, to solve system (1.32) we use the leap-frog scheme:

$$\left(\mathsf{M} + \frac{\Delta t}{2}\mathsf{C}\right)\mathbf{U}^{n+1} = \left(2\mathsf{M} - \Delta t^2\mathsf{A}\right)\mathbf{U}^n - \left(\mathsf{M} - \frac{\Delta t}{2}\mathsf{C}\right)\mathbf{U}^{n-1} + \Delta t^2\mathbf{F}^n, \qquad n = 1, \ldots, N_T - 1, \tag{1.33}$$

with

$$\mathsf{M}\mathbf{U}^1 = \left(\mathsf{M} - \frac{\Delta t^2}{2}\mathsf{A}\right)\mathbf{U}^0 + \left(\Delta t\mathsf{M} - \frac{\Delta t^2}{2}\mathsf{C}\right)\mathbf{V}^0 + \frac{\Delta t^2}{2}\mathbf{F}^0.$$

By taking advantage of the structure of M and C we can easily invert the system $\mathsf{M} + \frac{\Delta t}{2}\mathsf{C}$ in (1.33). We recall that the leap-frog scheme (1.33) is explicit and second order accurate, therefore to ensure the numerical stability the Courant-Friedrichs-Lewy (CFL) condition has to be satisfied, see e.g., [QV94; Can+07].

1.5 Analysis of dispersion, dissipation and numerical stability

In this section we report the main results obtained in [Ant+12; MR12; Fer+17; Ant+18a] related to dispersion, dissipation and stability properties of the semi- and fully-discrete numerical scheme introduced previously.

1.5.1 Dispersion and dissipation errors

The dispersion measures the phase lag between the numerical wave and the physical one, whereas the dissipation effect is the misfit between amplitude waves (cf. Figure 1.1). In general, a traveling physical wave in a homogeneous isotropic three-dimensional elastic medium can be decomposed into compressional and shear waves: the pressure wave (P-wave) introduces a particles displacement in the same direction of the propagating wave, while and the shear wave (S-wave) in a plane transversal to the propagating wave. Indeed for the latter, one can introduce a horizontal component (SH-wave), inducing a transversal motion on a horizontal plane containing the wave direction, and a vertical component (SV-wave), inducing a motion on a plane perpendicular to the wave direction, cf. [AR02; She09].

The Von Neumann analysis (see [Coh02; Hug87]) investigates the properties of the

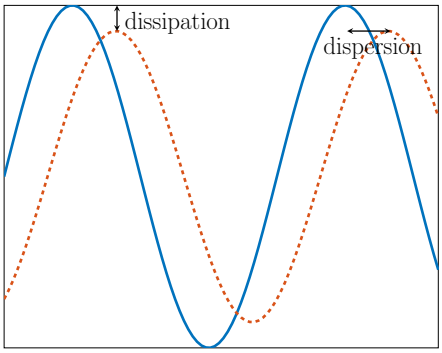

Figure 1.1: Example of a travelling wave (blue solid line) and its numerical approximation (orange dashed line).

numerical solutions, in term of dispersion and dissipation errors, when approximating a plane wave $\mathbf{u}(\mathbf{x},t) = \mathbf{A}e^{i(\mathbf{k}\cdot\mathbf{x}-\omega t)}$ propagating in an unbounded domain. $\mathbf{A} = [A_1, A_2, A_3]^T \in \mathbb{R}^3$ is the amplitude vector of the wave, ω is the angular frequency, $\mathbf{k} = 2\pi L(\cos(\vartheta)\cos(\varphi), \sin(\vartheta)\cos(\varphi), \sin(\varphi))$ represents the wave number vector, being L the wave length, ϑ and φ the angles between the propagating direction and the coordinate axes.

Dispersion analysis

As a measure of the phase-lag one can consider the relative dispersion errors

$$e_P = \frac{v_{P,h}}{v_P} - 1, \quad e_S = \frac{v_{S,h}}{v_S} - 1,$$

where v_P and v_S are the P- and S-wave velocities (1.3), whereas $v_{P,h}$ and $v_{S,h}$ are the corresponding numerical wave velocities whose expression is given by

$$v_{P,h} = \frac{h\omega_{P,h}}{2\pi\delta}, \quad v_{S,h} = \frac{h\omega_{S,h}}{2\pi\delta},$$

where $\delta = h/(NL)$ is the sampling ratio, i.e., δ^{-1} is the number of interpolation points per wavelength, h is the mesh size, N is the polynomial degree and $\omega_{P,h}$ and $\omega_{S,h}$ are the numerical angular frequencies for the P-wave and the S-wave, respectively.
Results in [Fer+17] show how the computed dispersion errors behave w.r.t. the polynomial degree N, the sampling ratio δ, the time step Δt and the angles of incidence ϑ, φ for both hexaedral and tetrahedral grids.
More specifically:

1. the computed dispersion errors on tetrahedral meshes are greater than the corresponding ones computed on hexahedral meshes;

2. the semi-discrete DGSE formulation shows negligible dispersion errors (i.e. $e_P, e_S \leq 10^{-6}$), provided that the polynomial degree $N \geq 4$ and more than 5 (10 respectively) points per wavelength are employed when hexahedral (tetrahedral respectively) grids are considered;

3. the leap-frog time integration scheme does not introduce any further significant dispersion errors to those arising from space discretization. Indeed, the error curves behave like the ones obtained in the semi-discrete case until the time discretization error becomes dominant.

Dissipation analysis

For the dissipation analysis, the amplitude of the numerical displacement is studied. For this purpose, the unitary plane wave with amplitude $|e^{i(\mathbf{k}\cdot\mathbf{x}-\omega t)}| = e^{t\mathrm{Im}(\omega)}$ is considered. Since for the physical wave it holds $\mathrm{Im}(\omega) = 0$, its amplitude is equal to 1 for all time t. On the other hand, for the numerical wave in general $\mathrm{Im}(\omega_h) \neq 0$. Therefore the scheme is non dissipative when $\mathrm{Im}(\omega_h) = 0$ and dissipative if $\mathrm{Im}(\omega_h) < 0$. From numerical studies in [Fer+17], it follows that

1. the semi-discrete DGSE formulation does not suffer from dissipation error;

2. the leap-frog time integration scheme does not introduce any further significant dissipation error to those arising from space discretization. Therefore also the fully-discrete formulation does not suffer from dissipation error.

1.5.2 Numerical stability

In this section we recall the stability properties of the fully discrete scheme (1.33), cf. [Ant+12; Fer+17; Ant+18a]. As already mentioned previously, the leap-frog scheme is stable provided that the time step Δt satisfies the CFL condition

$$\Delta t \leq C_{CFL} \frac{h}{v_P N^2}, \tag{1.34}$$

where h is the mesh size, N is the polynomial degree, v_P is the velocity of the pressure wave and the C_{CFL} constant depends on penalty parameter α in (1.14), more precisely it can be proved that $C_{CFL} \propto \alpha^{-1/2}$, see [Ant+12; Maz12].

1.6 Ground Motion Intensity Measures

In the previous sections we presented the mathematical model and its numerical discretization to find the solution of the seismic wave propagation problem. Since in the seismic risk analysis framework we are mainly interested in the physics-measurements of the earthquakes, we need to introduce specific formulas that are able to compute this data.

The ground motion intensity measure IM provides a quantification of the seismic event. Typical choices to quantify the IM are the Peak Ground Acceleration (PGA), the Peak Ground Velocity (PGV), the Spectral Acceleration (SA), the Spectral Displacement (SD), or an integral measure of ground shaking, such as the Housner intensity (I_H) [LC07; Hou52].
The Peak Ground measures are computed through their maximum absolute value w.r.t. time. For example, the Peak Ground Velocity (PGV) is defined as $PGV = \max_t |v(t)|$, where $v(t)$ is the velocity time history. In a similar way the Peak Ground Displacement (PGD) or the Peak Ground Acceleration (PGA) can be described.
Spectral quantities are defined through the solution of the vibratory motion of the damped single-degree-of-freedom given by

$$\begin{cases} y(t) = x(t) - u(t) \\ m\ddot{y}(t) + c\dot{y}(t) + ky(t) = -m\ddot{u}(t) \end{cases},$$

where $x(t)$ and $u(t)$ are the absolute displacements of the oscillator and of the support, respectively, and $y(t)$ represents the relative displacement of the oscillator w.r.t. the support, see Figure 1.2. The parameters m, c and k denote the mass, elasticity constant and damping of the system, respectively. The system depends on the natural period $T = 2\pi/\omega$ and damping ratio $\zeta = c/(2m\omega)$, where $\omega = \sqrt{k/m}$ is the circular frequency of the oscillator. Then the spectral displacement is defined

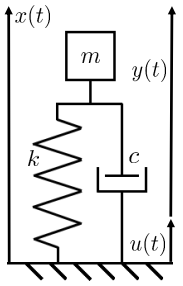

Figure 1.2: A schematic of a simple spring–mass–damper system used to model the 1-D damped vibrating system.

as the maximum relative displacement response $y(t)$, subjected to a prescribed acceleration $\ddot{u}(t)$ at the base, for a given vibration period T and damping ratio ζ, i.e. $SD(T, \zeta) = \max_t |y(t)|$. With similar arguments we can introduce the velocity and acceleration response spectral ordinates, that are Spectral Velocity (SV) and Spectral Acceleration (SA), respectively. SV and SA are defined as the maximum relative velocity and maximum absolute acceleration, respectively, i.e. $SV(T, \zeta) = \max_t |\dot{y}(t)|$ and $SA(T, \zeta) = \max_t |\ddot{x}(t)|$. Moreover the spectral values introduced are related by the period of interest, that is $SV = (T/2\pi)SD$ and $SA = (T/2\pi)^2 SD$.
As natural consequence of the spectral values, we introduce the Housner intensity

defined as the integral of the elastic velocity spectrum between $0.1s$ and $2.5s$, i.e.:

$$I_H(\zeta) = \int_{0.1}^{2.5} SV(T, \zeta)\, dT$$

where T, ζ are the parameters of the structure and SV is the spectral velocity spectrum.
In our applications, cf. Chapters 2 and 3, we will consider the Peak Ground Velocity (PGV) and the Spectral Displacement (SD). They are computed by considering their 2D generalization by means of the geometric mean of their horizontal components, i.e. the intensity measure is computed as $IM = \sqrt{IM_{x_1} IM_{x_2}}$ where IM_{x_k}, $k = 1, 2$, represent the 1D-intensity measure $IM = SD, PGV$ associated to each horizontal component.

CHAPTER 2

Seismic risk assessment based on coupled three-dimensional physics-based simulations and fragility curves models

In this chapter we describe a mathematical and numerical approach that combines physics-based simulated ground motion caused by earthquakes with fragility functions to model the structural damages induced to buildings. To simulate earthquake ground motion we use the discontinuous Galerkin spectral element method to solve a three-dimensional differential model at regional scale describing the propagation of seismic waves through the earth layers up to the surface. Selected intensity measures, retrieved from the synthetic time histories, are then employed as input for a vulnerability model based on fragility functions, in order to predict building damage scenarios at urban scale. The main features and effectiveness of the proposed numerical approach are tested on the Beijing metropolitan area.

2.1 A new coupled approach for seismic risk assessment based on three-dimensional physics-based numerical simulations and fragility functions

For a specific asset, seismic risk is computed by convolution of hazard with vulnerability. Conventionally, the probability of damage is estimated on the basis of the total probability theorem, as follows:

$$P(DS \geq d_s) = \int P(DS \geq d_s | IM = \mathtt{im}) f_{IM}(\mathtt{im})\, d\mathtt{im} \tag{2.1}$$

where $P(DS \geq d_s | IM = \mathtt{im})$ represents the probability of exceeding a certain damage level (or state) conditioned on the intensity measure $IM = \mathtt{im}$, i.e., the

fragility function expressing the complementary cumulative distribution function for DS conditional to IM, while $f_{IM}(\texttt{im})$ is the probability density function of the given IM. In the most comprehensive context of performance-based earthquake engineering, $f_{IM}(\texttt{im})$ is derived from the seismic hazard curve at a site (given the annual probability of exceedance as a function of the given IM) computed through a Probabilistic Seismic Hazard Assessment (PSHA), and (2.1) allows to compute the annual probability of exceedance of a given loss metric (e.g. monetary losses or damage state, the latter being related to losses through correlations of damage with repair or replacement costs). In deterministic risk calculations, the risk is computed for a single ground shaking scenario without computing the convolution integral of (2.1).

The key element of the comprehensive methodological approach proposed in this chapter (see Figure 2.1 for a schematic representation) is the characterization of seismic ground shaking and of its spatial variability through 3D physics-based numerical models of earthquakes. These earthquake scenarios are based on solving approximately a differential problem modeling the displacement of a (visco)elastic medium subjected to an external excitation source. The numerical method employed to approximate the displacement field is the DGSE method proposed in [Ant+12] and implemented in the open source code SPEED (`http://speed.mox.polimi.it`, cf. also [Maz+13]). Besides being verified in a number of benchmarks, see [Maz+13; AM18], SPEED has been proven successful to simulate real earthquakes, such as the 2009 April 6th L'Aquila, Central Italy [Eva+17], the 2011 February 22nd Christchurch, New Zealand [Gui+11], the 2012 May 29th Po Plain, Northern Italy [PMS15], the 1978 June 20th Volvi, Northern Greece [SPH17], the 1915 January 15th Marsica [Pao+16].

Each numerical simulation provides as output, at any site of interest, the full waveform of ground motion compatible with the source rupture process (causative fault, magnitude M_w, hypocenter location, fault slip distribution, etc..), the source-to-site path and the local geological conditions. Note that, for a given magnitude M_w, multiple realizations are simulated to account for the aleatory uncertainty associated with the fault rupture process, in terms of slip distribution, hypocenter location and kinematic source parameters (e.g. rupture velocity and rise time). For the sake of clarity, in the following the term *scenario* will be used to refer to a set of earthquakes on a given fault characterized by a prescribed magnitude M_w, while *footprint* is used to denote the specific realization (i.e. in terms of co-seismic slip distribution across the fault and hypocenter location) within a given scenario. From the synthetic waveform, the associated ground motion IM can be computed, depending on the class of structures/infrastructures at risk, provided that the simulated ground motion is *broadband*, i.e., it is sufficiently accurate in a broad frequency range of interest for the seismic response of structures. Once the selected IM is computed, it is used as input to the fragility functions for the target

class of structures to compute the probability of exceedance of a given damage state.

The methodological approach implemented in this work allows to compute seismic risk estimates at two different levels.

1. At the first level ($L1$), deterministic seismic risk estimates, i.e. $P(DS \geq d_s|IM = \texttt{im})$, are provided for representative earthquake footprints computed through a single numerical simulation.

2. At the second level ($L2$), based on equation (2.1), seismic risk estimates are computed for a given earthquake scenario with prescribed magnitude M_w, i.e. $P(DS \geq d_s|scenario)$, exploiting a statistically significant set of earthquake footprints, from which the probability distribution of ground motion can be computed. This implies that, for any site of interest, the probability distribution of earthquake shaking, i.e., the term $f_{IM}(\texttt{im})$ in (2.1) can be computed from the N footprints of the given earthquake scenario.

For the latter approach, in order to evaluate $P(DS \geq d_s)$, we have to compute the integral in (2.1). This can be evaluated numerically by means of Gaussian quadrature formula. Note that under specific hypothesis it is possible to calculate analytically the value of the integral in (2.1). In our case, for the mathematical description of $P(DS \geq d_s|IM = \texttt{im})$ we refer to Section 2.2 (see (2.3)), whereas we assume that IM is log-normally distributed with probability density function given by

$$f_{IM}(\texttt{im}) = \frac{1}{\texttt{im}} \frac{1}{\sigma_{im}\sqrt{2\pi}} \exp\left(-\frac{1}{2\sigma_{im}^2}\left(\ln\frac{\texttt{im}}{\mu_{im}}\right)^2\right), \tag{2.2}$$

where μ_{im} and σ_{im} are the median and logarithmic standard deviation.

In this chapter, we are mainly interested in the methodological chain for seismic risk assessment via PBS, so that we do not explicitly account for specific exposure models of the region under study. This means that, as output, we provide risk estimates for any site of the model that contains a prescribed building typology. Furthermore, only physical damage predictions are provided, overlooking the computation of economic and/or social losses. The three main ingredients of the proposed methodological approach of Figure 2.1, are a rigorous numerical model for the prediction of near-source earthquake ground motion (Section 1.1), a quantification of ground motion intensity measures (Section 1.6) and suitable fragility functions for prescribed building typologies (Section 2.2).

The chapter is organized as follows. The fragility functions for the vulnerability model to be coupled with PBSs are discussed in Sections 2.2. Then in Sections 2.3 and 2.4, we present an application of the proposed approach focusing on the metropolitan area of Beijing (China). The city of Beijing is located in the proximity of a well-known mapped fault system capable of triggering severe earthquakes of magnitude up to 7.3 M_w. Based on employing our model, we produce maps of

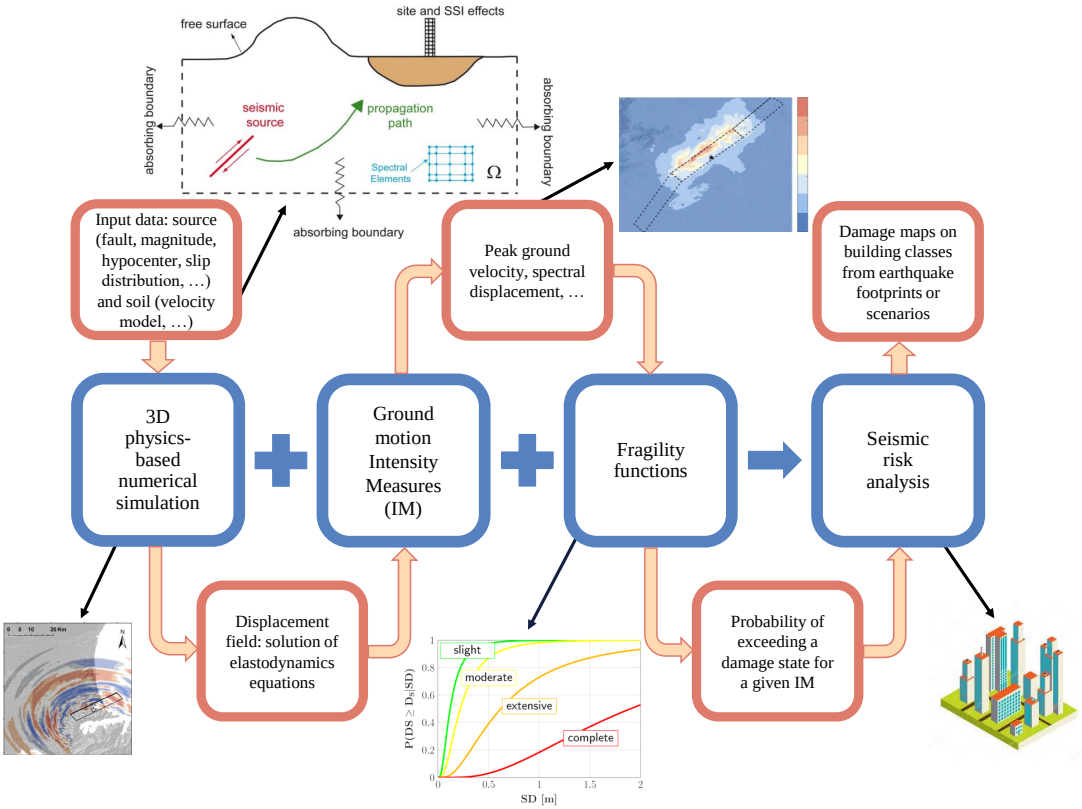

Figure 2.1: A methodological approach for seismic risk assessment based on 3D PBS and fragility models.

seismic damage focusing on the specific class of high-rise buildings, accounting for a wide set of fault rupture realizations with magnitude in the range 6.5-7.3 M_w.

2.2 Fragility models

The fragility function is a key component of the chain for seismic risk assessment, as it measures the probability of exceeding certain performance (or design) criteria as a function of the level of seismic input intensity, see (2.1). In general, the fragility function is defined as the conditional probability of a given damage state (or measure) DS exceeding a threshold d_s, given a value of the ground motion intensity measure $IM = \texttt{im}$, i.e.

$$\text{FC}(\texttt{im}, d_s) = P(DS \geq d_s | IM = \texttt{im}),$$

where $P(A|B)$ is the conditional probability of A given B, cf. [MKS17; SK96]. The most common form of a seismic fragility function is the log-normal cumulative

distribution function [Shi+00; Ell01], given by

$$\mathrm{FC}(\mathtt{im}, d_s) = \varphi\left(\frac{1}{\sigma_s} \ln \frac{\mathtt{im}}{\mu_s}\right), \tag{2.3}$$

where φ is the standard Gaussian cumulative distribution function, μ_s is the median value of the distribution and σ_s is its logarithmic standard deviation for each damage state d_s, $s = 1, \ldots, N$. The log-normal distribution is typically used because: (i) it fits a variety of structural component failure data, as well as non-structural failure data and building collapse by Incremental Dynamic Analyses performed on numerical structural models, see [PKB07]; (ii) it has a strong theoretical basis, being positive definite and fully defined by measures of the first and second statistical moments. The parameters μ_s and σ_s can be evaluated with the use of the maximum likelihood estimation [Shi+00; Sey+10; Zen10; MKS17] or with the linear regression method [GES08; JME12; BS08; MKS17].

As an illustrative example, in Figure 2.2, we show the family of fragility functions for high-rise buildings (height below 200 m and low seismic design code) developed by Wu et al. [WWY13] as a function of spectral displacement SD, cf. Section 1.6.

In Figure 2.2 fragility functions are given for the following damage states: Normal Operation (d_1 = NO), Immediate Occupancy (d_2 = IO), Life Safe (d_3 = LS), Collapse Prevention (d_4 = CP). Each function is represented by a log-normal probability distribution, see Equation (2.3), therefore it is fully described, for each damage state d_s, by the pair (μ_s, σ_s) reported in Table 2.1.

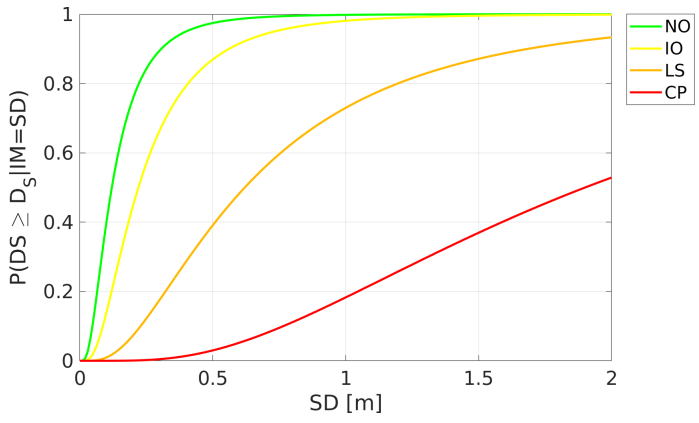

Figure 2.2: Fragility functions for high-rise buildings – height below 200 meters and low seismic design code – according to Wu et al. (2013), where SD is the spectral displacement.

Table 2.1: Median Spectral Displacement, μ_s (in meters), and logarithmic standard deviation, σ_s, for damage states d_s as retrieved from the fragility functions proposed by Wu et al. (2013) for high-rise buildings with height below 200 meters and low seismic design code.

s	Damage State	d_s	μ_s (m)	σ_s
1	Normal Operation	NO	0.12	0.73
2	Immediate Occupancy	IO	0.22	0.73
3	Life Safe	LS	0.62	0.78
4	Collapse Prevention	CP	1.90	0.71

2.3 Earthquake ground motion prediction in the metropolitan area of Beijing

To apply the methodological approach described in Section 2.1, we consider the metropolitan area of Beijing. Beijing is situated on a large sedimentary basin and, with its more than 20 million inhabitants and strong urbanization, is one of the many megacities around the world highly exposed to the seismic threat. From an historical point of view Beijing was severely affected by seismic events [GLS83], such as the Sanhe-Pinggu earthquake in 1679, with an estimated magnitude 8. In this work, we are interested in investigating the potential rupture of two relevant, well-known seismogenic structures, namely, the Shunyi-Qianmen-Liangxiang and the Nanyuan-Tongxian faults, crossing the metropolitan area of Beijing. Being capable to generate earthquakes up to magnitude 7.3, these faults represent, in fact, a significant threat to the city.

The proximity to these faults along with the complex geological configuration makes the large urban area of Beijing an interesting case study, where non-standard approaches are needed for a more accurate characterization of strong ground motion. To this end, a 3D physics-based numerical model of the Beijing metropolitan area was constructed to simulate a large set of earthquake scenarios originating along these faults with magnitude varying from 6.5 to 7.3. Then, seismic risk estimates were obtained by combining these earthquake ground shaking scenarios with fragility functions for high-rise buildings, the latter ones being an important component of the entire building stock of the city.

Even if some studies adopted physics-based numerical simulation [Din+04] or tried to explicitly model in full 3D the detailed shape of the alluvial basin of Beijing [Gao+04], to our knowledge, none of the previous investigations have considered a large number of earthquake scenarios occurring along the two aforementioned faults. Furthermore, in those studies, no attempt was made to use synthetic ground motion scenarios to generate seismic damage scenarios for specific building typologies existing in this hazardous area.

As already pointed out by Xiong et al. [Xio+19], our synthetic seismograms obtained via wave propagation simulation might be used as input for dynamic response history analyses of buildings requiring the entire time history rather than IM values, as recently done by Xu et al. and Lu et al. [Xu+19; Lu+19].

2.3.1 Set-up of the three-dimensional numerical model

The 3D computational domain for the Beijing area was set up considering the following input data: (i) the topography model, (ii) the seismic fault whose rupture is modelled using a kinematic representation, (iii) the 3D subsoil structure accounting for the variable thickness of the sedimentary basin and the 3D velocity profiles, cf. [Ant+18a]. The topography model was built from freely-available digital elevation dataset of CGIAR-CSI for the Beijing area (downloaded from the website `http://srtm.csi.cgiar.org`). The data have a resolution of approximately 90×90 m, for north-south and east-west directions.
Among the relevant seismic sources (i.e. Shunyi-Qianmen-Liangxian, SQL, and Nanyuan-Tongxian, NT, faults), for sake of presentation, herein we investigate earthquake rupture scenarios occurring only along the SQL fault system which crosses the central Beijing area. It is a normal quasi-vertical (the dip angle is about 80°) fault consisting of three main segments with different strike angles. The total fault length is about 90 km and it can produce events up to M_w 7.3. In Table 2.2 we report the parameters of the SQL fault, as implemented in our computational model.

Table 2.2: Geometric parameters of the Shunyi-Qianmen-Liangxiang fault. Fault origin indicates the vertex of the fault at zero strike and dip.

Segment	L_{max}	W_{max}	Strike	Dip	Top Depth	Fault Origin
	$[km]$	$[km]$	(°)	(°)	$[m]$	$(Lat\,[°N],\ Lon[°E])$
North	24.9	30	44	80	38.8	(40.02, 116.52)
Middle	29.7	30	48	80	51.9	(39.84, 116.27)
South	35.6	30	30	80	31.7	(39.56, 116.07)

As regards the 3D soil model, it was constructed by merging data regarding both the geologic structure of the alluvial basin, see Figure 2.3 (top left), and the spatial distribution of $V_{s,30}$ (weighted average shear wave velocity in the top 30 m), cf. Figure 2.3 (top right) and [AW09]. The former was derived from the digitalization of the model proposed in [Gao+04], while the latter was adapted from `https://earthquake.usgs.gov/data/vs30`. In particular, given z_{top} and z_{sed}, that represent the projection of a generic point with coordinate z into the surface and the sediment base, respectively, we have considered for the first layer (0 to 2 km

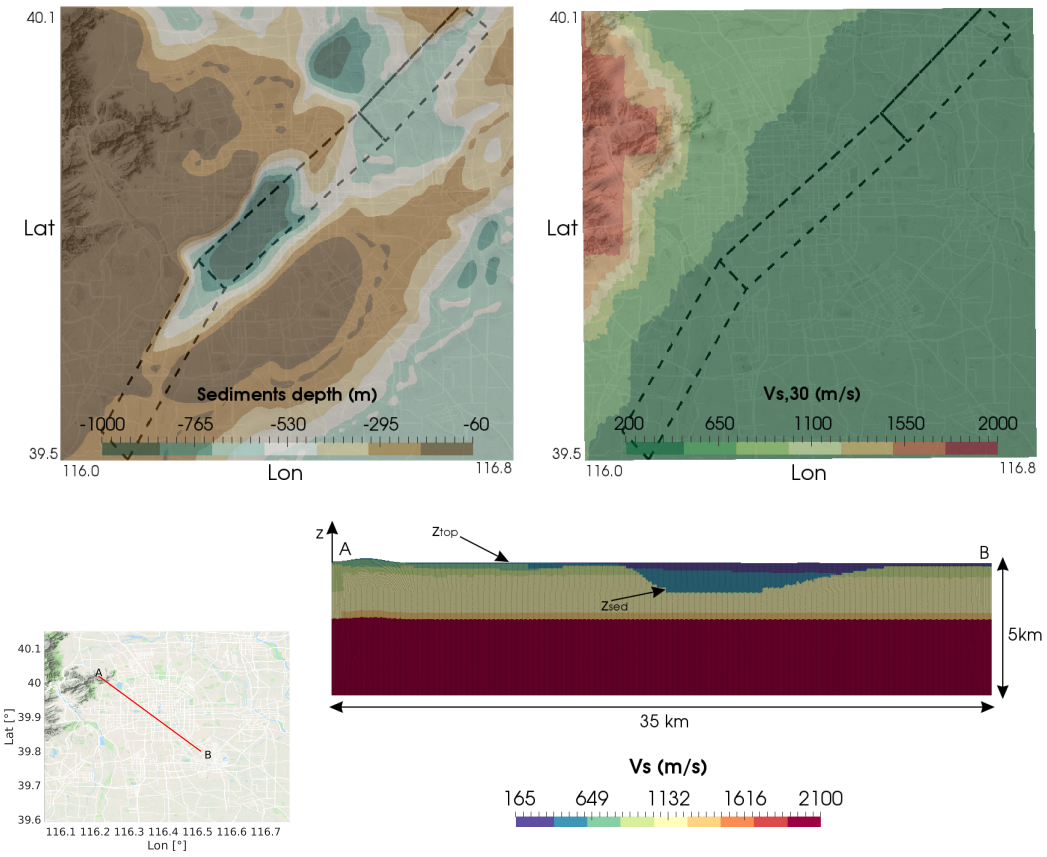

Figure 2.3: Sediment thickness (top left) and $V_{s,30}$ model (top right). Black rectangles represent the surface projection of the considered Shunyi-Qianmen-Liangxiang (SQL) fault. Bottom: geologic cross-section $A - B$ (see map on the left) showing the distribution of $v_s(z)$ for the first layer 0-2 km (right).

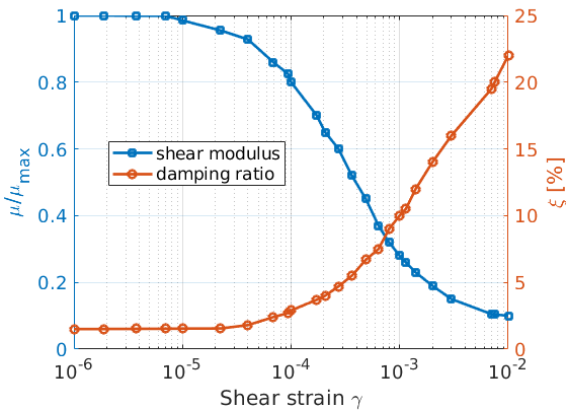

Figure 2.4: Normalized shear modulus μ and damping ratio ξ as a function of shear strain γ, adopted for the alluvium shallow materials in the Beijing basin.

depth) the following properties, cf. Figure 2.3 (bottom),

$$v_s = \begin{cases} V_{s,30} + 5\sqrt{|z - z_{top}|}, & \text{for } V_{s,30} \geq 600\, m/s, \\ V_{s,30} + 10\sqrt{|z - z_{top}|}, & \text{for } V_{s,30} < 600\, m/s,\ z \geq z_{sed}, \\ 800 + 10\sqrt{|z - z_{top}|}, & \text{for } V_{s,30} < 600\, m/s,\ z < z_{sed}, \end{cases} \tag{2.4}$$

$$v_p = \begin{cases} 1.6 v_s, & \text{for } V_{s,30} \geq 600\, m/s, \\ 1.6 v_s, & \text{for } V_{s,30} < 600\, m/s,\ z \geq z_{sed}, \\ 2000 + 15\sqrt{|z - z_{top}|}, & \text{for } V_{s,30} < 600\, m/s,\ z < z_{sed}, \end{cases} \tag{2.5}$$

where the velocity profiles are in m/s. Similarly, we defined the soil density in kg/m^3 as follows

$$\rho = \begin{cases} 1800 + 5\sqrt{|z - z_{top}|}, & \text{for } V_{s,30} \geq 600\, m/s, \\ 1530 + 5\sqrt{|z - z_{top}|}, & \text{for } V_{s,30} < 600\, m/s,\ z \geq z_{sed}, \\ 1800 + 5\sqrt{|z - z_{top}|}, & \text{for } V_{s,30} < 600\, m/s,\ z < z_{sed}. \end{cases} \tag{2.6}$$

In addition, we consider a non-linear soil behaviour of the soft soil deposits ($V_{s,30} \leq 400\ m/s$ and $z_{top} - 300 \leq z \leq z_{top}\ m$). We remark that the algorithm presented in Section 1.1 can be straightforwardly generalized to the case of a nonlinear soil model as the one we are considering for the Beijing application, cf. [PSZ07; SPI09]. The latter is a 3D generalization of the classical $\mu - \gamma$ and $\xi - \gamma$ curves used within 1D linear-equivalent approaches, see, e.g., [Kra96], where γ is the 1D shear strain. At each time step of the analysis the shear modulus μ and the viscous damping ξ are updated on the basis of the maximum deformation achieved at each element of the model. In particular, referring to the Mohr's circle, the maximum shear deformation γ_{max} is evaluated at each grid node from the principal strains ε_I, ε_{II} and ε_{III}, as follows

$$\gamma_{max}(\mathbf{x}, t) = \max\left[|\varepsilon_I(\mathbf{x}, t) - \varepsilon_{II}(\mathbf{x}, t)|, |\varepsilon_I(\mathbf{x}, t) - \varepsilon_{III}(\mathbf{x}, t)|, |\varepsilon_{II}(\mathbf{x}, t) - \varepsilon_{III}(\mathbf{x}, t)|\right].$$

This value, averaged on each mesh element, defines update shear modulus μ and damping ratio ξ at each time step, following a material stress-strain ($\mu - \gamma$) and a damping-strain ($\xi - \gamma$) curve, respectively. In practice, at the generic position $\mathbf{x}$ and generic instant of time t a scalar measure of shear strain amplitude γ is computed, then this value is introduced in the $\mu - \gamma$ and $\xi - \gamma$ curves, and finally the corresponding parameters are updated for the following timestep. Therefore, unlike the classical linear-equivalent approach, the initial values of the dynamic soil properties are recovered at the end of the excitation, i.e. when the displacement wave field, and consequently γ_{max}, is close to zero. An example of modulus reduction

Table 2.3: Horizontally stratified crustal model, from Gao et al. (2014).

Layer	Depth $[km]$	$v_s\,[m/s]$	$v_p\,[m/s]$	$\rho\,[kg/m^3]$	$\xi\,[mHz]$
1	0 – 2		see (2.4) – (2.6)		$15\pi/v_s$
2	2 – 4	2100	3500	2200	22.44
3	4 – 12	3400	6000	2760	13.86
4	12 – 30	3500	6200	2810	13.46

$\mu - \gamma$ and damping $\xi - \gamma$ curves used for the shallow soil materials are reported in Figure 2.4.

Dynamic properties for the underlying bedrock layers (depth $> 2\ km$), assumed to be horizontally stratified, have been assigned in accordance with [Gao+04], see Table 2.3. The computational domain was built by considering all the information above and extends over an area of $70 \times 70\ km^2$ down to $30\ km$ depth (see Figure 2.5).

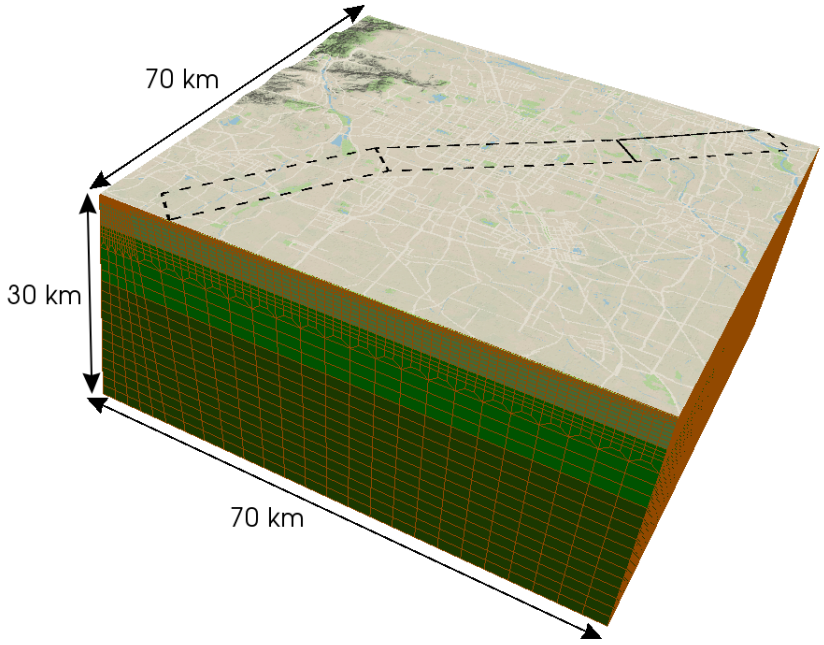

Figure 2.5: 3D computational model for the Beijing area with indication of the SQL fault.

In order to correctly simulate by SPEED the earthquake ground motion up to a maximum frequency $f = 1.5\ Hz$, we built a conforming mesh with size of 150 m on the top surface, of 600 m at 4 km depth and reaching 1800 m in the underlying layers. In particular the model consists of 859.677 hexahedral elements and, by using a fourth order polynomial approximation degree $N = 4$, it has approximately 160 million degrees of freedom. Then we fixed the total observation time

$T = 30\ s$ and we used a time step $\Delta t = 0.001\ s$. The walltime for each simulation is around 12 hours on 512 cores on the Marconi cluster at CINECA, Italy (`http://www.cineca.it/en/content/marconi`).

To capture the variability of earthquake ground motion resulting from different fault ruptures along the SQL fault, a set of 30 footprints was performed by varying the moment magnitude M_w, from a minimum of 6.5 up to a maximum of 7.3, the location of the hypocenter, the kinematic slip distribution on the fault and the rupture area location. A summary of the simulated seismic footprints, grouped according to the three magnitude levels (i.e. scenario), is provided in Table 2.4.

Table 2.4: Summary of PBSs. Simulated footprints for each earthquake scenario with given M_w.

Scenario: M_w	Simulated footprints	Rupture area ($km \times km$)
6.5	15	24×12
6.9	10	36×18
7.3	5	54×24

Remark 2.1. The relatively reduced number of simulations for M_w7.3 scenario is essentially driven by the fact that computational resources are limited. Therefore we decide to consider a number of simulations for each scenario proportional to the probability of its event. For example an earthquake scenario with M_w6.5 happens more likely than the one with M_w7.3. This is the criteria that we use to decide the number of footprints for each scenario.
Keeping that in mind, the scenarios have been chosen, on the one hand, striving to adequately cover the variability of the ground motion and, on the other, adopting as "rule of thumb" what has been already found in other publications, see e.g. [Vil+14]. Obviously, the ambition is to increase the number of simulations available nevertheless this latter will be always limited by computational resources. Therefore it is fundamental to steer the simulation process selecting the set of scenarios that is best suited to explore the ground motion variability [Stu+20].

The main kinematic parameters of the slip distributions for a given fault and a given earthquake magnitude were chosen by considering probability distributions ensuring that the resulting scenario variability is not affected by systematic bias in the input parameters. In order to produce a number of random slip distributions, a pre-processing Matlab toolboox was defined: given a fault type and a target magnitude M_w, the program computes the fault length (L), the fault width (W), the maximum displacement (MD) and the average displacement (AD) of the slip distribution according to the Wells and Coppersmith [WC94] relations. Moreover, the hypocenter position is defined at run-time randomly, using a Gaussian distribution with mean depth equal to 10 km and standard deviation equal to 2 km. Then, the

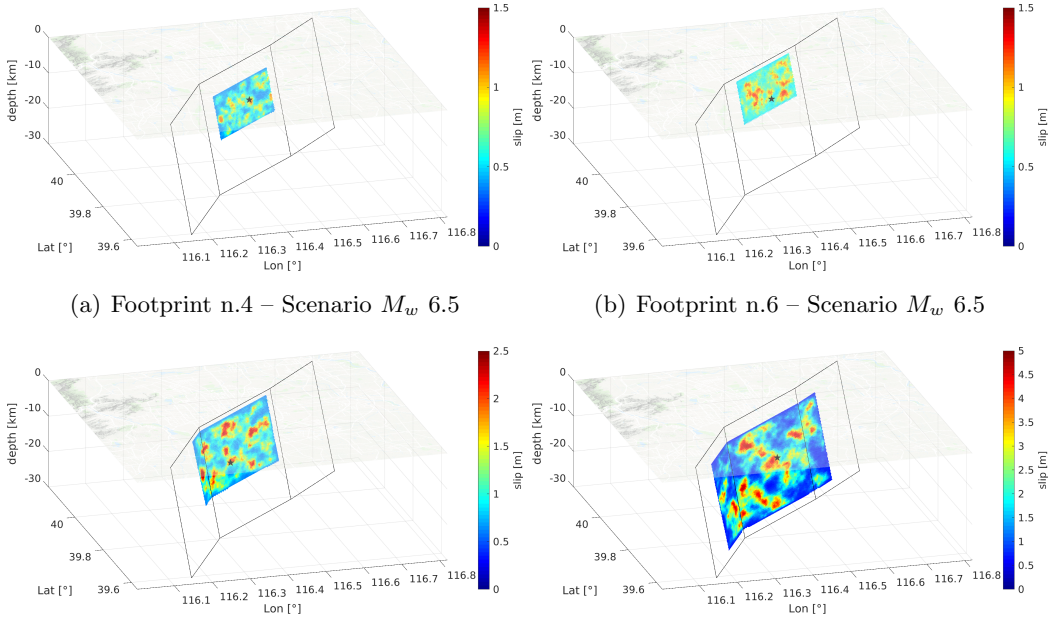

(a) Footprint n.4 – Scenario M_w 6.5

(b) Footprint n.6 – Scenario M_w 6.5

(c) Footprint n.8 – Scenario M_w 6.9

(d) Footprint n.1 – Scenario M_w 7.3

Figure 2.6: Distribution of the slip pattern along the fault and hypocenter location (black star) for four selected footprints corresponding to earthquake scenarios with M_w 6.5, 6.9 and 7.3.

relative position of the rupture fault is obtained by assuming a Weibull distribution with parameters defined according to [Cau+08]. For each scenario kinematic slip distribution, rupture time and rise time are directly generated by the model of Schmedes et al. [SAL12]. The resulting outputs are then read by the SPEED code and at run-time applied to the discretization nodes. In the following we will consider different rupture realizations for four selected footprints, namely n.4 and n.6 for scenario M_w 6.5, n.8 for scenario M_w 6.9 and n.1 for scenario M_w 7.3. As an example, Figure 2.6 shows the fault rupture realizations considered for four selected footprints which will considered in further details in the following.

2.3.2 Results of three-dimensional physics-based scenarios and comparison with ground motion prediction equations

In the following, some representative results of the 3D physics-based numerical simulations will be discussed with emphasis on the characterization of earthquake ground motion. Figure 2.7 shows some snapshots of the velocity wave field (modulus of horizontal components) for the footprint n.4 – scenario M_w 6.5. Interestingly, two large pulses, pointing south-west and north-east with respect to the epicenter and almost aligned along the surface projection of the top segment of the fault, are clearly visible. These pulses can be observed also in the velocity time histories,

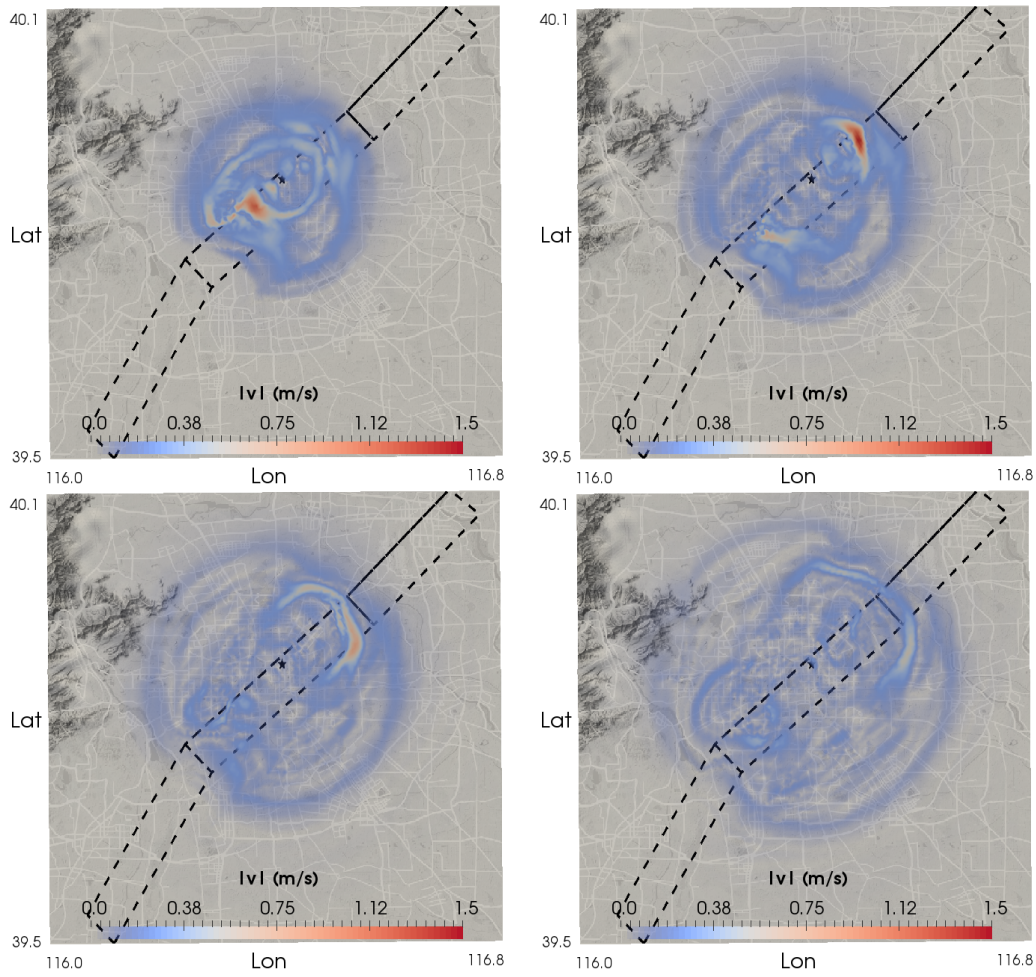

Figure 2.7: Snapshots of the velocity wave field obtained for footprint n.4 with M_w 6.5, cf. Table 2.4. Top-left: $t = 7\ s$, top-right: $t = 8\ s$, bottom-left: $t = 9\ s$, bottom-right: $t = 10\ s$.

East-West (EW) component, illustrated in Figure 2.8 for 7 representative sites, more specifically at stations 2, 3 and 4, lying above the surface projection of the fault.

As already proposed by Villani et al. [Vil+14], for each scenario the first statistical moments obtained for the relevant ground motion parameters from the population of synthetic signals (at the sites of interest) can be computed, and used in the same way as one would use the median and the standard deviation of a classical GMPE. Figure 2.9 (left column) shows the map of the median values (first statistical moment) of the peak ground velocity (maximum absolute value w.r.t. time of velocity, PGV, geometric mean of horizontal components, cf. Section 1.6), computed from all set of simulated footprints for each scenario magnitude: M_w 6.5 (top), M_w 6.9 (middle) and M_w 7.3 (bottom), cf. Table 2.4. The right column of Figure 2.9 compares the median PGV, obtained by the numerical simulation

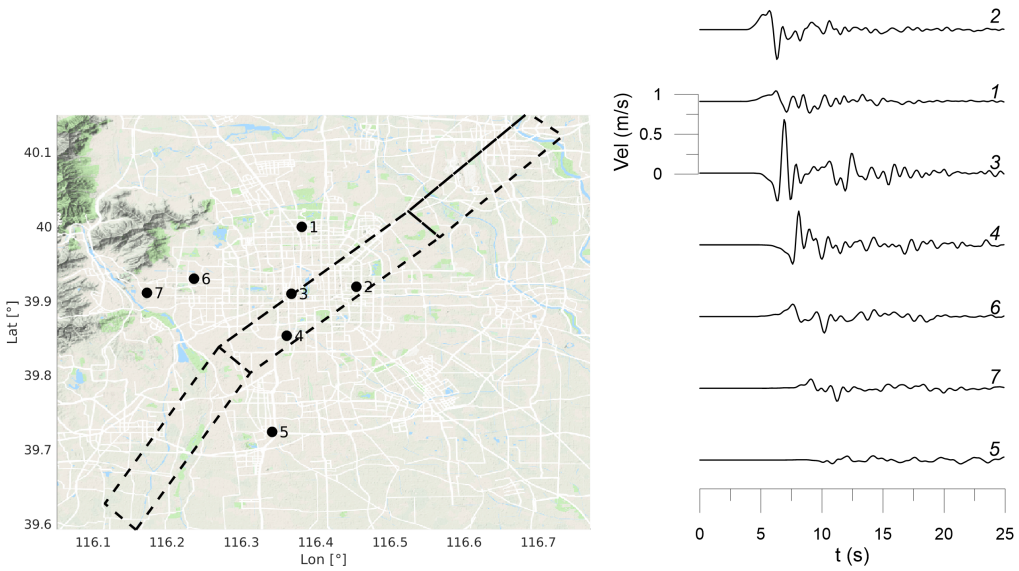

Figure 2.8: Velocity time histories (low-pass filter at 1.5 Hz), footprint n.4 – scenario M_w 6.5, East-West (EW) component, at 7 representative sites of the model.

against the one based on the GMPE proposed by Cauzzi et al. [Cau+15a], referred to as CAEA15 hereafter. For simplicity, the GMPE was calculated assuming an average $V_{s,30}$ equal to 235 m/s, being this value relatively constant throughout the whole metropolitan area of Beijing. Consistently to the chosen GMPE, the metric adopted for the comparison is the closest distance to the fault rupture (R_{rupt}). Note that, for scenario M_w 7.3, the minimum rupture distances are larger than the ones for other scenarios, because of the larger depth of the rupture area.
It is worth to highlight that the results obtained by PBS present an overall good agreement with the prediction of the GMPE. However, PBS produce median peak ground values systematically higher at short distances from the fault (typically for R_{rupt} less than around 5 km) and generally lower at longer distances. Furthermore, the standard deviation computed from our site-specific simulations tends to be smaller than the corresponding one obtained based on employing CAEA15, as the latter is increased because of the ergodic assumption, applied to site-generic applications of earthquake ground motion modeling.

2.4 Seismic risk assessment for high-rise buildings

In this section the numerical simulations obtained in Section 2.3 are coupled with fragility functions to generate seismic damage scenarios for the buildings in the urban area of Beijing. In this work, we focus on a special class of buildings: the so-called super high-rise buildings with height over 100 m, cf. [Moe+11; Kaz+14]. For

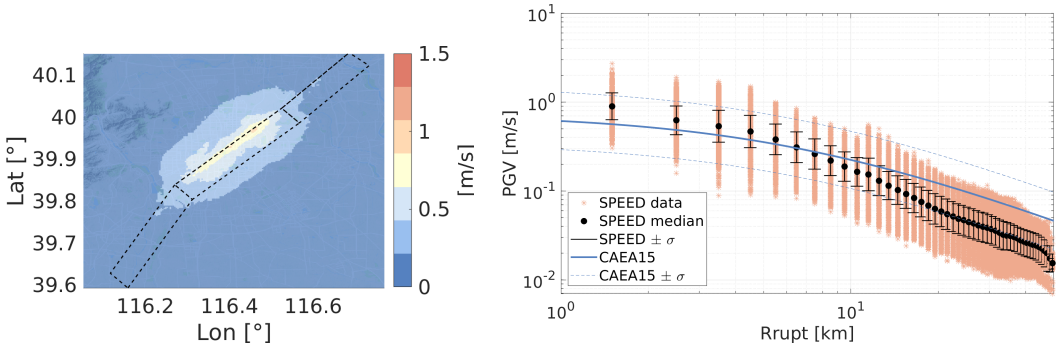

(a) All Scenarios – M_w 6.5

(b) All Scenarios – M_w 6.5

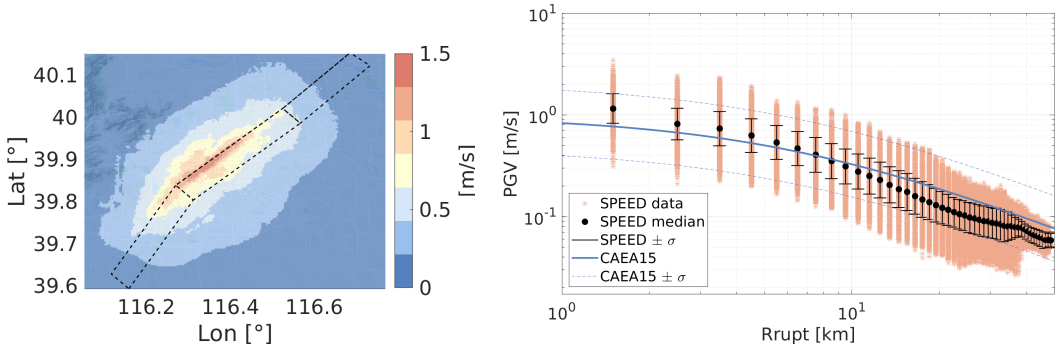

(c) All Scenarios – M_w 6.9

(d) All Scenarios – M_w 6.9

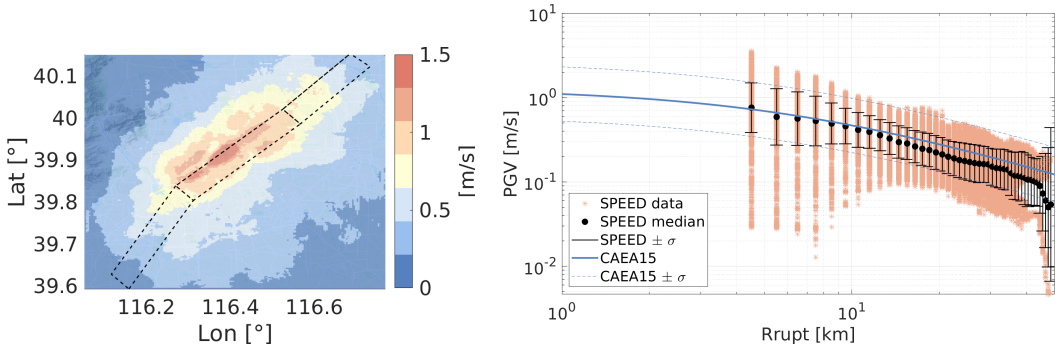

(e) All Scenarios – M_w 7.3

(f) All Scenarios – M_w 7.3

Figure 2.9: Left column: Median PGV (geometric mean of horizontal components) maps obtained by considering all footprints for scenarios with M_w 6.5 (top), M_w 6.9 (middle) and M_w 7.3 (bottom). Right column: comparison with the GMPE by Cauzzi et al. (2015), (CAEA15) against physics-based scenarios. Pink stars show PGV simulated at each receiver for each individual footprint, while black dots represent the median and the bar the dispersion around that value.

this purpose, the results of PBS, introduced in previous Section, are combined with the fragility functions developed by Wu et al. [WWY13] specifically for Chinese high-rise buildings. For simplicity, results will be only provided in terms of seismic damage assessment, while the extension to comprehensive seismic risk evaluation including fatality and/or loss assessment is beyond the scope of this work.

Starting from the published data regarding more than 50 high-rise buildings, Wu et al. [WWY13] developed regression analyses between the maximum storey drift ratios and the response spectral displacement for high-rise buildings located in China. Fragility functions were then proposed for different categories of high-rise buildings, depending on the building height (above 200 m and below 200 m) and the level of seismic design code (low, moderate and high), and for the following damage states: Normal Operation (NO), Immediate Occupancy (IO), Life Safe (LS), Collapse Prevention (CP). These four classes can be described in terms of damage levels as follows: NO = very light, IO = light, LS = moderate and CP = severe, cf. FEMA273 [Cou97]. In our analysis, without loss of generality, we focus on the category of high-rise buildings with height below 200 m and low prescriptions levels for seismic design, see Figure 2.2 and Table 2.1 in Section 2.2.
Considering buildings with height of approximately 100 m, for which, on average, a fundamental period of vibration of $3s$ can be defined based on statistical analysis of vibration properties of Chinese high-rise buildings [XXL14], spectral displacement (SD) at $3s$ with damping ratio 5% was assumed as a ground motion proxy for the fragility functions. In our framework SD is the maximum relative displacement response w.r.t. time of the building w.r.t. the ground. It is computed as geometric mean of the spectral displacement associated to each horizontal component, cf. Section 1.6.

Figure 2.10 shows the probability of exceeding the LS damage state as a function of R_{rupt}, for the four previously selected footprints corresponding to three scenarios (M_w 6.5, 6.9 and 7.3). Note that these plots show footprints-based estimates, therefore they provide the probability of exceedance of damage state LS, conditioned to the value of IM attained at any site of the model, i.e. $P(DS \geq \text{LS}|IM)$. Pink stars represent $P(DS \geq \text{LS}|IM)$ for all the receivers included in our computational model within a given distance bin, while the black dots and bars show the corresponding mean and $\pm\sigma$ values, respectively. Results obtained from the PBS are compared with those obtained employing the median and $16/84^{th}$ percentiles values of $SD(3s)$ provided by CAEA15. Consistently with the previous comment on ground motion, the probability of LS damage state differs significantly at short distances: PBS estimates provides remarkable higher values compared to the GMPE based one. At around 10 km distance the discrepancy tends to vanish also due to the fact that 3 footprints out of the 4 selected, are clearly showing an almost negligible probability associated to this specific damage state.

In Figure 2.11 we report the probability of exceeding the different damage states,

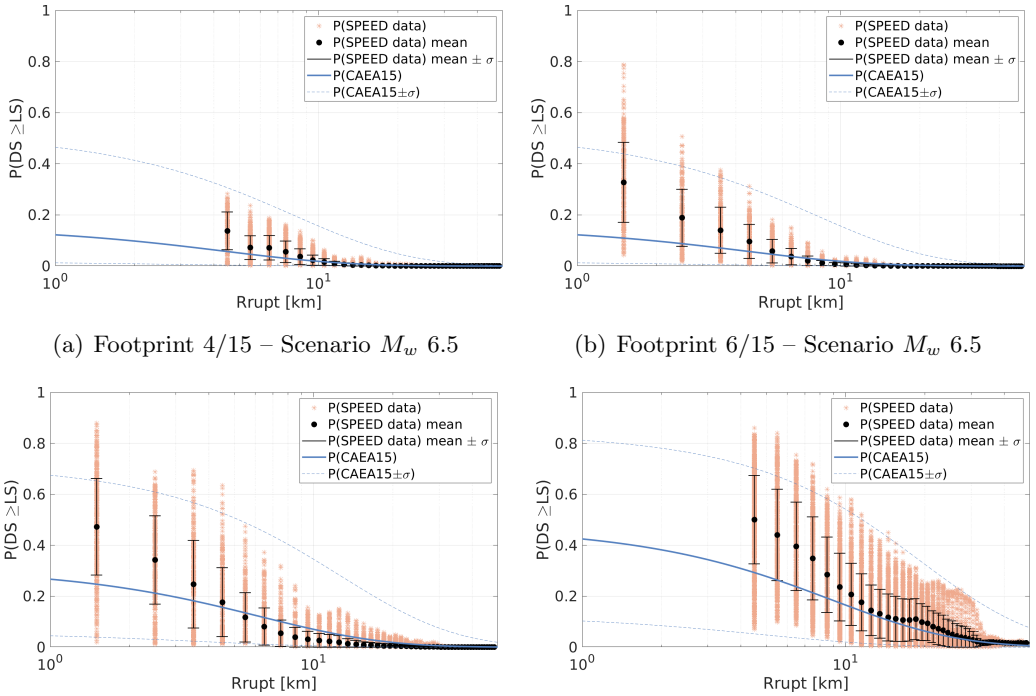

(a) Footprint 4/15 – Scenario M_w 6.5

(b) Footprint 6/15 – Scenario M_w 6.5

(c) Footprint 8/10 – Scenario M_w 6.9

(d) Footprint 1/5 – Scenario M_w 7.3

Figure 2.10: Probability of exceeding damage state (DS) greater than or equal to Life Safe (LS) versus the closest distance to the fault rupture (R_{rupt}). Pink stars denote the $P(DS \geq \text{LS}|IM)$ for each simulated receiver within the Beijing area, while filled black dots and bars represent the corresponding mean and standard deviation.

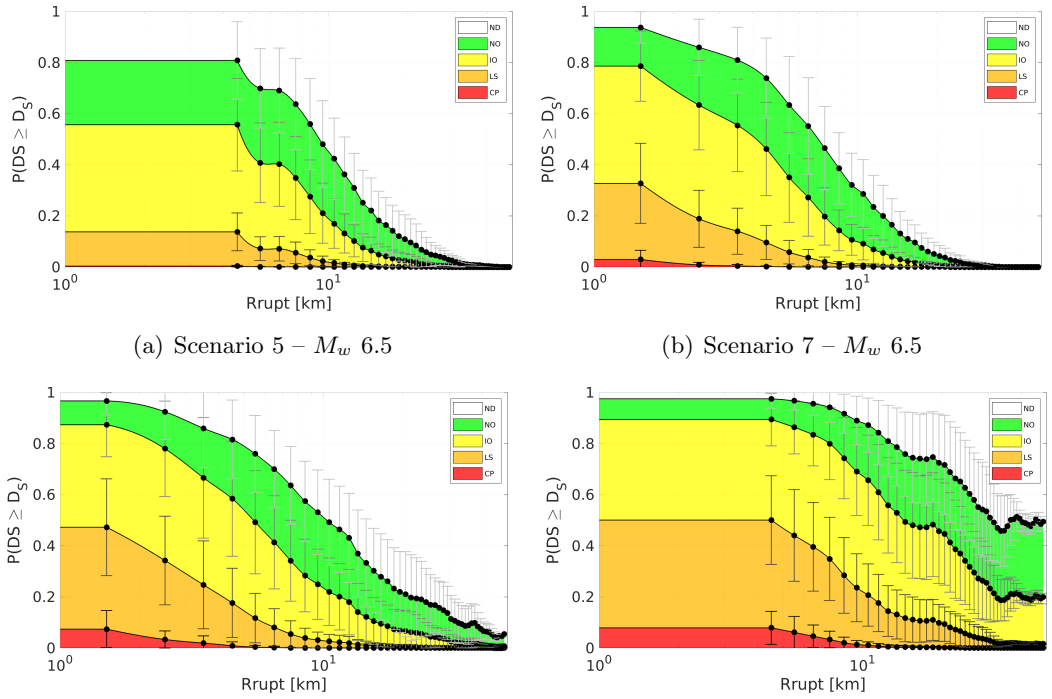

(a) Scenario 5 – M_w 6.5

(b) Scenario 7 – M_w 6.5

(c) Scenario 21 – M_w 6.9

(d) Scenario 22 – M_w 7.3

Figure 2.11: Probability of exceeding all Damage States (DS) as a function of R_{rupt}: white – No Damage (ND), green – Normal Operation (NO), yellow – Immediate Occupancy (IO), orange – Life Safe (LS) and red – Collapse Prevention (CP). Filled black dots: mean; bars: standard deviation.

specifically, white – No Damage (ND), green – Normal Operation (NO), yellow – Immediate Occupancy (IO), orange – Life Safe (LS) and red – Collapse Prevention (CP), as a function of R_{rupt}, for the 4 selected footprints. The plot interestingly shows, on the one hand, a very steep reduction of the mean damage state probabilities and, on the other, an impressively stable trend of the dispersion around the mean value. Particularly because of the latter fact, it is important to consider PBS, aiming at explaining this variability from a physical point of view and to spatially correlate it to the fault rupture. In a nutshell, these preliminary analyses show that in the near-field region a systematic bias between GMPE and PBS can be observed, and that the probability of exceeding two critical damage levels (LS and CP) is very significant.

Given the location of the Shunyi-Qianmen-Liangxiang fault, a rather large portion of the metropolitan area of Beijing falls in this near-field range. In Tables 2.5 and 2.6, for the four selected footprints, the probability associated to each performance level is depicted as a pie chart where the different colors denote the damage states, specifically, white – No Damage (ND), green – Normal Operation (NO), yellow – Immediate Occupancy (IO), orange – Life Safe (LS) and red – Collapse

Prevention (CP). We observe the following: starting from footprint n.4 (M_w 6.5) the dominating effects are null and slight damages (colors white and green), while footprint n.1 (M_w 7.3) shows a predominance of significant and severe damages up to collapse (colors yellow, orange and red). Furthermore, comparing results obtained for the different sites, it is evident that sites 2, 3 and 4, located on the surface projection of the fault, show, across all footprints, the most dangerous damage estimates.

So far, seismic risk scenarios were generated for specific earthquake footprints in a deterministic way ($L1$ risk analysis), focusing on the analysis of the damage distribution as a function of the distance from the causative fault. Finally, to shed light on the potential use of 3D PBS within probabilistic frameworks for seismic risk assessment, the conditional probability $P(DS \geq d_s|scenario)$ was computed by the convolution integral of equation (2.1) according to the procedure proposed in Section 2.1 ($L2$ risk analysis).

For the sake of brevity, we focus here on the earthquake scenario with magnitude M_w 6.5, for any site of the model, the probability of different damage states was derived by taking into account all 15 earthquake footprints simulated for this scenario (see Table 2.4). This means that, under the assumption of a log-normal probability density function for $SD(3s)$ (see equation (2.2)), $\mu_{SD(3s)}$ and $\sigma_{SD(3s)}$ are estimated, for the selected scenario, from the corresponding set of footprints by using the maximum likelihood method. Then, in order to be able to compare PBS and CAEA15 results, we need to attribute $\mu_{SD(3s)}$ and $\sigma_{SD(3s)}$ to a log-normal base 10 distribution. The median $\mu_{SD(3s)}$ does not change, whereas $\sigma_{SD(3s)}$ becomes $\sigma_{\log_{10} SD(3s)}$. The computed results along with the SQL fault obtained at the 7 sites under consideration are shown in Table 2.7 in terms of $\mu_{SD(3s)}$, $\sigma_{\log_{10} SD(3s)}$ and $P(DS = d_s|M_w\,6.5)$ for the different damage states. Figure 2.12 illustrates the spatial distribution of damage probabilities $P(DS \geq d_s|M_w\,6.5)$ obtained by means of PBS. In order to highlight the differences that may arise adopting GMPEs, Table 2.8 shows the analogous results obtained using CAEA15 for the same scenario earthquake. Note that top rows of both Tables 2.7 and 2.8 illustrate the map of $\mu_{SD(3s)}$, $\sigma_{\log_{10} SD(3s)}$ from PBS and CAEA15, respectively. From the comparison of these maps, it is clear that: (i) median values from PBS show a steep gradient of the ground motion predicted in the proximity of the fault due to the coupling of source rupture effects with complex site effects in the Beijing basin; (ii) σ values from PBS tend to be smaller, on average, than the ones from CAEA15 as the former are site-specific (i.e. ergodic assumption is removed, see [AA+10]); furthermore, PBS produce dispersion values characterised by a strong spatial dependency, which cannot, or can only partially, be accounted for in GMPEs.

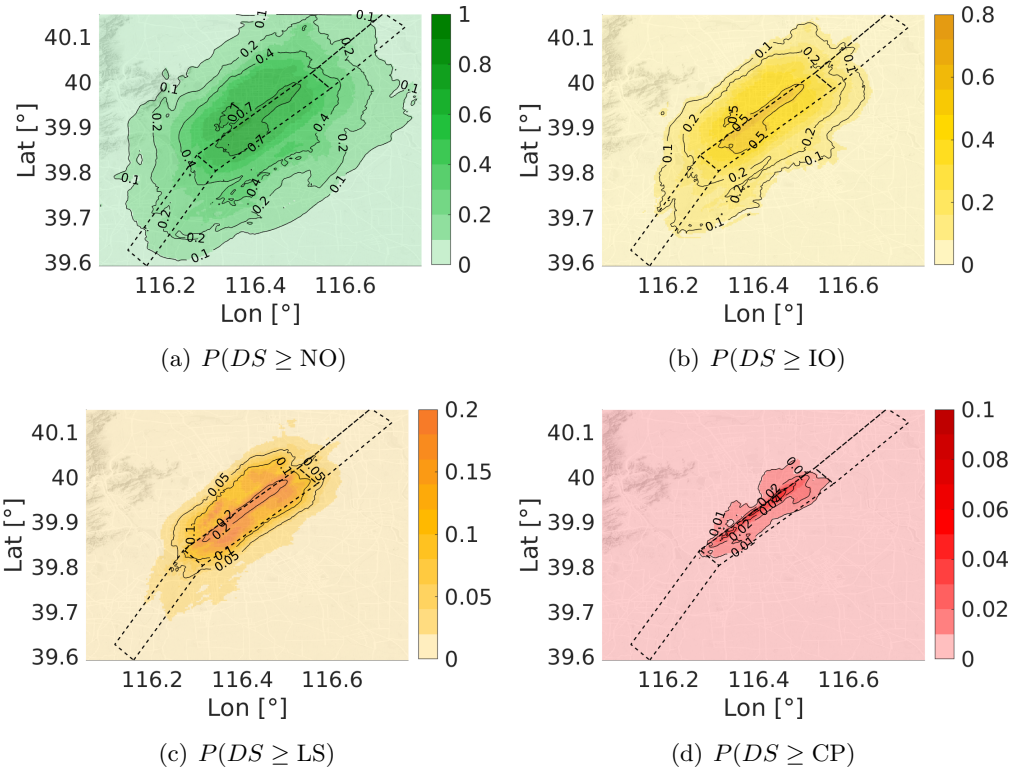

(a) $P(DS \geq \text{NO})$ (b) $P(DS \geq \text{IO})$

(c) $P(DS \geq \text{LS})$ (d) $P(DS \geq \text{CP})$

Figure 2.12: Seismic damage maps for high-rise buildings, in terms of $P(DS \geq d_s|M_w\ 6.5)$, accounting for all footprints corresponding to a scenario earthquake with M_w 6.5.

2.5 Concluding remarks

In this work we have introduced a simple and effective approach for seismic risk assessment which couples 3D physics-based scenarios (PBSs) and fragility functions in order to obtain risk estimate. This approach uses PBSs as an alternative to standard empirical approaches, based on Ground Motion Prediction Equations (GMPEs). The latter may provide inaccurate results, especially in the near-field of an earthquake, because the number of records might be not sufficient to satisfactorily constrain the expected site-specific ground motion spatial distribution, including peculiar effects, such as directivity or spatial correlation of the ground motion. For this reason, instead of GMPEs, we proposed a mathematical framework that exploits PBSs by solving the wave propagation problem. Once a relatively large set of synthetic scenarios was generated, we combined suitable ground motion intensity measures with classical fragility functions in order to finally evaluate the seismic risk for any specific class of buildings. As a case study of the proposed approach, the large metropolitan area of Beijing was considered, the seismic hazard of which is governed by the Shunyi-Qianmen-Liangxiang and Nanyuan-Tongxian

faults. For this purpose, a set of PBSs was obtained with magnitudes ranging from a minimum of 6.5 M_w up to a maximum of 7.3 M_w; the location of hypocenter, the slip patterns and other parameters have been systematically varied, aiming at covering, as much as possible, the variability of seismic shaking, associated with the different ruptures that might realistically take place in the future. The potential consequences of such scenarios have been investigated, focusing on the structural response of the high-rise building class, particularly relevant in Beijing. To this end, we adopted fragility functions explicitly calibrated for the Chinese building stock.

Our analysis suggest that PBSs can be successfully adopted for seismic risk assessment purposes. The comparison of our results with similar ones obtained by GMPEs highlighted that systematic differences take place especially in the near-field region. Considering the fact that GMPEs tend to lack of calibration data in this area and that PBSs are intrinsically physically constrained, we conclude that the PBS methodology may be complementary to GMPEs when the seismogenic structure that governs local seismic hazard is known and a sufficiently accurate 3D model of the local geology may be constructed.

Table 2.5: Damage predictions for selected earthquake footprints and selected locations in the Beijing area. For each footprint (left: n.4 – M_w 6.5 and right: n.6 – M_w 6.5) and each location (from 1 to 7) we report: 1) maps in terms of SD at $T = 3\ s$; 2) values of PGV and $SD(3s)$ and 3) pie charts showing $P(DS = d_s)$, with colors denoting the different damage states (white: no damages – ND; green: very light damages, normal operation – NO; yellow: light damages, immediate occupancy – IO; orange: moderate damages, life safe – LS; red: severe damages, collapse prevention – CP).

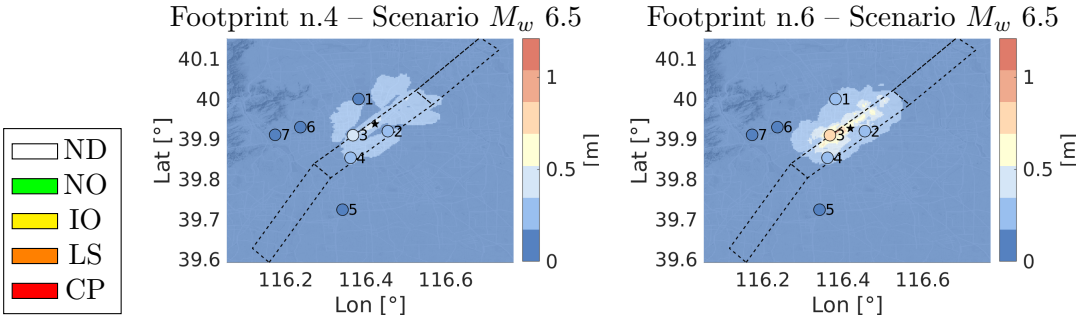

Location ID	R_{rupt} $[km]$	PGV $[m/s]$	$SD(3s)$ $[m]$	DS [%]	R_{rupt} $[km]$	PGV $[m/s]$	$SD(3s)$ $[m]$	DS [%]
1	9	0.23	0.15		7	0.31	0.22	
2	6	0.39	0.18		4	0.47	0.29	
3	5	0.81	0.35		1	2.10	0.81	
4	6	0.47	0.21		4	0.55	0.28	
5	16	0.09	0.10		16	0.10	0.07	
6	11	0.16	0.07		10	0.16	0.09	
7	14	0.10	0.04		13	0.10	0.05	

Table 2.6: Damage predictions for selected earthquake footprints and selected locations in the Beijing area. For each footprint (left: n.8 – M_w 6.9 and right: n.1 – M_w 7.3) and each location (from 1 to 7) we report: 1) maps in terms of SD at $T = 3$ s; 2) values of PGV and $SD(3s)$ and 3) pie charts showing $P(DS = d_s)$, with colors denoting the different damage states (white: no damages – ND; green: very light damages, normal operation – NO; yellow: light damages, immediate occupancy – IO; orange: moderate damages, life safe – LS; red: severe damages, collapse prevention – CP).

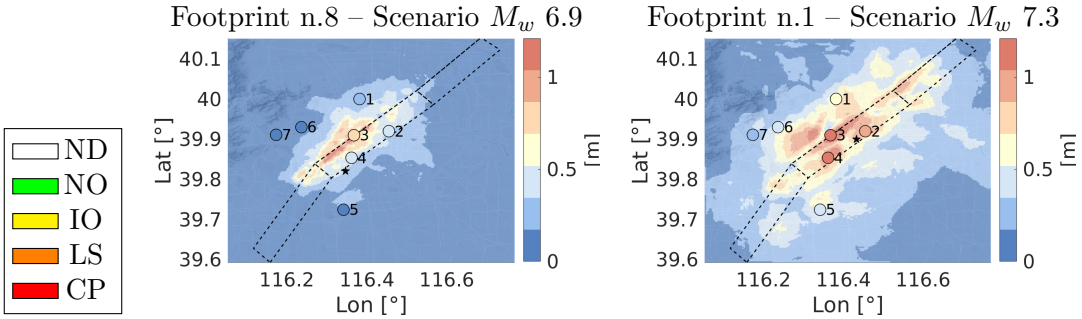

Location ID	R_{rupt} $[km]$	PGV $[m/s]$	$SD(3s)$ $[m]$	DS [%]	R_{rupt} $[km]$	PGV $[m/s]$	$SD(3s)$ $[m]$	DS [%]
1	7	0.39	0.25		8	1.32	0.67	
2	4	0.68	0.41		5	1.86	1.04	
3	1	1.75	0.84		4	3.10	1.26	
4	4	0.67	0.49		5	1.38	1.04	
5	11	0.20	0.16		12	0.55	0.51	
6	10	0.25	0.10		11	0.78	0.43	
7	12	0.18	0.08		13	0.56	0.28	

Table 2.7: Damage predictions for selected locations in Beijing area, considering all footprints for earthquake scenario with M_w 6.5. For each location (from 1 to 7), the first statistical moments of $SD(3s)$, i.e. $(\mu_{SD(3s)}, \sigma_{\log_{10} SD(3s)})$, along with the pie charts of damage probabilities, are shown. Colors for damage states are white: no damages – ND; green: very light damages, normal operation – NO; yellow: light damages, immediate occupancy – IO; orange: moderate damages, life safe – LS; red: severe damages, collapse prevention – CP.

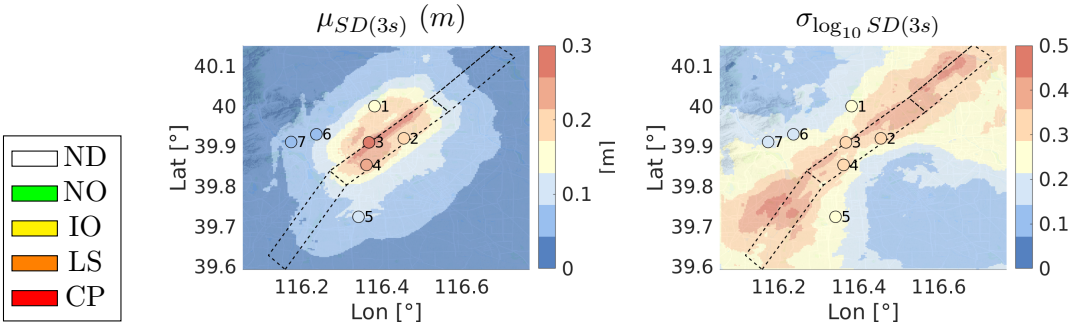

ID	1	2	3	4
$\mu_{SD(3s)}$ (m)	0.16	0.19	0.29	0.24
$\sigma_{\log_{10} SD(3s)}$	0.22	0.31	0.31	0.30
DS	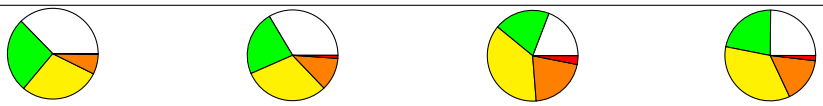			

ID	5	6	7
$\mu_{SD(3s)}$ (m)	0.09	0.08	0.05
$\sigma_{\log_{10} SD(3s)}$	0.24	0.19	0.21
DS			

Table 2.8: Damage predictions for selected locations in Beijing area, considering GMPE predictions (CAEA15) for earthquake scenario with M_w 6.5. For each location (from 1 to 7), the first statistical moments of $SD(3s)$, i.e. $(\mu_{SD(3s)}, \sigma_{\log_{10} SD(3s)})$, along with the pie charts of damage probabilities, are shown. Colors for damage states are white: no damages – ND; green: very light damages, normal operation – NO; yellow: light damages, immediate occupancy – IO; orange: moderate damages, life safe – LS; red: severe damages, collapse prevention – CP.

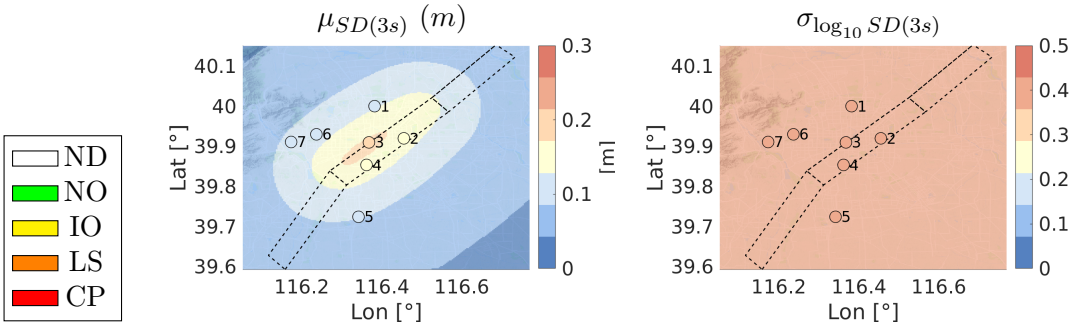

ID	1	2	3	4
$\mu_{SD(3s)}$ (m)	0.12	0.15	0.18	0.16
$\sigma_{\log_{10} SD(3s)}$	0.36	0.36	0.36	0.36
DS				

ID	5	6	7
$\mu_{SD(3s)}$ (m)	0.09	0.11	0.10
$\sigma_{\log_{10} SD(3s)}$	0.36	0.36	0.36
DS	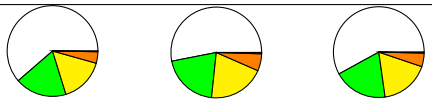		

CHAPTER 3

Seismic risk assessment based on three-dimensional physics-based simulations with coupled ground motion and structural analysis models

In this chapter, we present a seismic risk assessment strategy based on physics-based scenarios that model both earthquakes and build environment. The differential model is discretized in space based on employing the discontinuous Galerkin spectral element method coupled with a leap-frog time integration scheme for the solution of seismic wave propagation problems in three-dimensional realistic geological configurations (see Chapter 1). As output of the proposed coupled approach, we provide physical seismic response predictions for the building typology that is in the computation model.

3.1 Three-dimensional physics-based simulations by coupling earthquake and building models for seismic risk analysis

Understanding the physics of earthquakes and predicting their impacts on the human and natural environment is of crucial importance for delineating seismic risk reduction strategies. Nowadays, the most employed approaches to predict ground motion are: (i) empirical models, (e.g. ground motion prediction equations) and (ii) physics-based approaches (e.g. numerical methods to approximate differential models describing the expected ground motion), cf. [DA08]. In this application we focus on approach (ii) which, boosted by the continuous development of computer facili-

ties, is the most advanced strategy for the prediction of earthquake dynamics. The spectral element (SE) method nowadays is among the most popular techniques in computational seismology due to its capability of providing fast and highly accurate solutions [KV98]. Discontinuous Galerkin spectral element formulation (DGSE) has been proposed and analyzed for the elastodynamics equation to allow for variable mesh size h and polynomial approximation degree p, cf. [Ant+12], making it well suited for capturing local variations of the physical solution. Moreover the DGSE methods preserve the same accuracy of SE approaches while improving their flexibility by using non-conforming grids and different local approximation degrees in the numerical model. Based on the DGSE method, in the recent years, three-dimensional (3D) physics-based simulations have been employed for the study of real earthquake ground motion (e.g. Po Plain, L'Aquila) [Eva+17; PMS15] and recently for seismic risk scenarios in large urban areas [Pao+14; Ant+21]. However, accounting for multi-scale nature of earthquakes within a single model poses challenging demands on computational methods and resources due to the coexistence of very different spatial scales, from a few tens of kilometers, with reference to the seismic fault, up to a few meters, or even less when considering some structural elements.

In order to correctly simulate the earthquakes and the built environment via physics-based scenarios, we propose to couple suitable differential models for seismic ground motion and building structures. To model the ground motion of the earthquakes, we consider the elastodynamics equations presented in Chapter 1. On the other hand, we want to introduce suitable differential models for the description of the structures. Here we propose two of them. The first model for the structural analysis is based on the assumption that the building has full elastic behaviour and therefore it can be described with the same model of Chapter 1 with suitable transmission condition for its interaction with the ground. A second different set of equations is based on the fact that the structure has a non-linear behaviour due to its seismic response after an earthquake, but also because it can be modelled by few blocks that are in contact with each other. For this description, we can adopt suitable contact-friction laws (see later Chapter 4). In Figure 3.1 we show an illustrative schematic representation of the proposed coupled approaches for the seismic risk assessment based on three-dimensional physics-based models for earthquakes and structural analysis. Thanks to the proposed approaches, numerical simulations provide as output the full waveform of ground motion compatible with the source rupture process, the source-to-site path and the local geological conditions, but also with the seismic response of the built environment.

To validate the proposed approach, we present three-dimensional physics-based numerical simulations of the 1999 M_w6 Athens (Greece) earthquake. The three-dimensional numerical model includes the surface topography of the region of Attica, a kinematic earthquake source description, and the major geological features

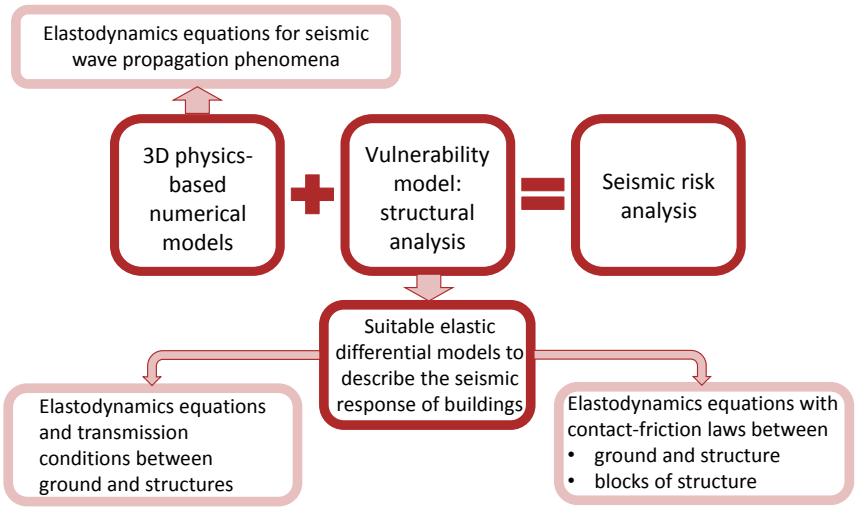

Figure 3.1: A methodological approach for seismic risk assessment based on earthquake simulations and structural analysis.

of the region, including the most important geological units in the metropolitan area of Athens. Suitable models of the Acropolis hill and of the Parthenon are included in the computational domain. As first level of investigation, we consider the simplest differential model fully based on elastodynamics equations, cf. Chapter 1, for both the ground motion and structural analysis with suitable transmission conditions. In particular, at the interface between ground and structure, we impose a weak continuity condition on the displacement $\mathbf{u}$ and enforce strongly continuous tractions $\underline{\sigma}$, that is $[\![\mathbf{u}]\!] = \mathbf{0}$ and $[\![\underline{\sigma}]\!] = \mathbf{0}$, respectively. Here $[\![\cdot]\!]$ denotes the jump of a quantity across a given interface, see (1.13). In this application we demonstrate the ability of three-dimensional discontinuous Galerkin spectral element numerical simulations to jointly study multi-scale engineering-seismology problems, comprising the earthquake source, complex wave propagation paths, and interaction with the built environment.

Remark 3.1. The ambition of the last part of the thesis is to introduce and code in SPEED the contact-friction laws within the structural analysis. This model features many challenges both mathematically and computationally (e.g. to handle with non-linearities and variational inequalities, higher computational costs, see later Chapter 4). For this reason, for the Athens case we considered simplified equations to model buildings that are the so-called transmission conditions. These laws act like suitable DG conditions across the interface, and they have been analyzed and suitably coded in SPEED (e.g. simplified modeling of the interaction between the Acropolis and the Parthenon).

The chapter is organized as follows. In Section 3.2 the 3D physics-based numerical simulations of the 1999 Athens earthquake (M_w6) are presented with the

numerical description of the geophysical and geological models. Finally in Section 3.3 we give a summary of the results achieved and propose improvements as future work.

3.2 Numerical modeling of the seismic response of the Acropolis and the Parthenon under the M_w6.0 Athens (Greece) 1999 earthquake

On September 7, 1999 at 14:56:50 (local time) an earthquake of magnitude M_w6 struck Attica region (Greece) within a few kilometers from the center of the city of Athens. This event was unexpected because no important earthquakes were recorded before, therefore this area was considered to have a very low seismicity [Pap+97; MDL89]. Although the earthquake magnitude was moderate, the intensity reached IX as major damage was observed, especially in the north–northwest part of the city, close to the earthquake rupture. 143 people were killed, more than 2000 were injured and over a hundred ordinary buildings collapsed. On the other hand, historical monuments were nearly untouched except for small displacements observed at some columns [TZ00; Pap+00a; Rou+03; Ana+99; Pap+00b; Gaz01]. The Acropolis of Athens, a worldwide renowned symbol of the cultural and historical heritage of Greece within the context of western civilization, hosts the Parthenon, one the most important surviving buildings of Classical Greece, generally considered the apotheosis of the Doric order. Within the last two decades extensive restoration and conservation works have been carried out in the Acropolis of Athens, focusing on the Parthenon, that also include a seismic monitoring network.

In this section, we investigate the fully-coupled seismic response of the Acropolis hill and the Parthenon during the Athens 1999 M_w6 earthquake, by means of a multi-scale approach. In particular we consider a kinematic model of the earthquake source, the crustal structure, the major geological features of the Athens area, the geometry of the Acropolis hill and a simplified model of the Parthenon. The final aim of this study is to develop a numerical model well suited for source-site-structure 3D numerical simulations of the seismic response of the Parthenon during the 1999 M_w6 Athens earthquake. The simulations will be performed using the high-performance open-source code SPEED (`http://speed.mox.polimi.it`, cf. also [Maz+13]), which is based on high-order discontinuous Galerkin spectral element methods on hexahedral/tetrahedral meshes. SPEED can accurately simulate large-scale seismic events by including a kinematic source model suitable to predict both far and near-field ground motions, an arbitrary complex propagation path throughout the crustal layers, up to the dynamic response of structures. In this work we will provide insights into the seismic wave propagation features in the 1999 Athens earthquake including the Acropolis hill and the Parthenon. To validate

the model, we will compare our synthetic results with available recordings in terms of amplitude, duration and frequency content.

3.2.1 Numerical simulations of the 1999 Athens earthquake

In this section we present physics-based simulations of the ground shaking generated in Athens (Greece) by the M_w6 earthquake occurred on September 7 1999 in the proximity of the metropolitan area (see `https://esm-db.eu/#/event/GR-1999-0001`) based on employing the model introduced in Chapter 1. The numerical model comprises the earthquake source, the crustal layering, the major geological features of the Athenian basin, the Acropolis and a simplified model of the Parthenon. The complexity of the problem at hand required adopting a multi-scale approach. In particular all the components of the numerical model were designed to account for: (i) the large variations of the characteristic dimensions of the computational mesh across the computational domain which encompasses the source region and the city of Athens (Attica region $45km \times 39km \times 30km$, Athens city $1.2km \times 1.4km \times 0.6km$ and Acropolis hill area $580m \times 380m \times 40m$, cf. also Figure 3.4); and (ii) the need of propagating relatively high frequencies through the computational domain in order to study the dominant features of the site response of the Acropolis and the Parthenon. The simulations have been carried out based on employing the open-source software SPEED (`http://speed.mox.polimi.it`, cf. also [Maz+13]) which can handle sharp changes of the mesh size and locally varying polynomial approximation orders [Ant+12] and allows a highly flexible description of the spatial variation of geophysical properties of the geo-materials [Pel+10]. Thanks to the flexibility of DG methods, we were able to relax the meshing constraints typical of SE approaches and build a computational domain that takes into account for the different geological features and large scale variations of the considered region, especially for the geometrical accuracy of the Acropolis hill and the Parthenon.

A first set of simulation was carried out to ensure that the large-scale regional model assembled for this study could yield results consistent with the previous findings of [Cau+15b], who investigated the seismic response of the Acropolis using a local model and high-frequency ($f_{max} = 30Hz$) plane-wave excitations. Encouraged by the good outcome of this sanity check, we proceeded with two advanced numerical simulations of the 1999 Athens earthquake: (a) the first focuses on the ground shaking across the metropolitan area including the Acropolis hill; (b) the second focuses on the Acropolis and the Parthenon.

3.2.2 Numerical model of the source process, regional crustal properties and geological setting

We adopted the kinematic representation of the seismic fault proposed in [Rou+03], where broadband seismograms recorded at regional distances are used to estimate

the source features of the Athens 1999 M_w 6 mainshock, occurred on 7 September 1999. The earthquake had a normal faulting style, and most likely occurred on the Fili fault [PPG02], one of the major tectonic features in the area [Gan+04]. In our study the total fault length and width are considered to be about $25km$. The average slip across the rupture area is $0.16m$, while the maximum slip approaches $1m$ in the proximity of the hypocenter (Figure 3.2). The rise time is equal to $0.3s$, while the rupture velocity is $2.7km/s$. Strike, dip and rake of the fault plane are 115°, 57°, −80° respectively. Consistent with [Rou+03], we use the hypocenter location of [Pap+00a], at $8km$ depth. The geophysical properties of the 1D layered regional crustal model are the same used by [GB04] and [TZ00]. The shear-wave velocity increases with depth, from $1.5km/s$ at the free surface to $3.6km/s$ at the bottom of the numerical model. The free surface of the model follows the regional geomorphology, smoothed starting from Shuttle Radar Topography Mission (SRTM) 1 Arc-Second ($30m$) global data. Water bodies are not included. Since a detailed representation of the complexity of the geological and seismotectonic settings of the regions of Attika and Athens is beyond the scope of this study, the model comprises only the dominant regional geological features, besides those crucial to the development of the case study at hand. In the Athens metropolitan area the model includes simplified representations of the Athenian Schist formation - a slightly metamorphosed series of Cretaceous marls and shales with lenses of sandstone and limestone - and of the recent deposits of the Athens basin, along with a high-resolution model of the limestone outcrop of the Acropolis. The geometry of the contact between recent deposits and bedrock was obtained from [KS00]. The extent of the Athenian Schist formation was derived merging information from [KS00; Arg+13] and the 1:50,000 geological map of Greece (Athinai, Piraieus sheet). Our representation of the Athens Schist formation is necessarily gross and only aims at representing the overall footprint of the formation and its likely depth in the metropolitan area. The Acropolis hill is a block of late Cretaceous limestone resting on the Athenian Schist. The Acropolis ridge is well approximated by an ellipse elongated in the EW direction with major axis length $\sim 250m$ and minor axis length $\sim 150m$. The hill is characterized by very steep topography on the northern, eastern and southern edges, where the geomorphology is dominated by a $30-35m$ thick limestone outcrop and the average slope of the hill flanks exceeds 30°. Large portions of the Acropolis are covered by anthropic infill overlaying the limestone unit. The anthropic infill unit was not included in the model because the dominant frequencies ($> 10Hz$, see [Cau+15a]) of its dynamic response are beyond the maximum frequency for which the computational grid was designed. The Parthenon and its foundation are made of porous-stone blocks with dry masonry structure, cf. [KE13]. The geophysical properties of the geomaterials as included in the numerical model are given in Table 3.2. Each ID block number of the computational model refers to a geophysical layer in which we assign the material and numerical parameters, see also Figure 3.4.

In particular, given z_q, $q = 0, 1, 2, 3$, that represent the projection of a generic point with coordinate z into the topografical surface, outcrop of the Acropolis, the Athenian basin and Schist, respectively, the properties of the first layer are described in Table 3.1 and Figure 3.3, where the different velocity profiles are in m/s and the soil density in kg/m^3.

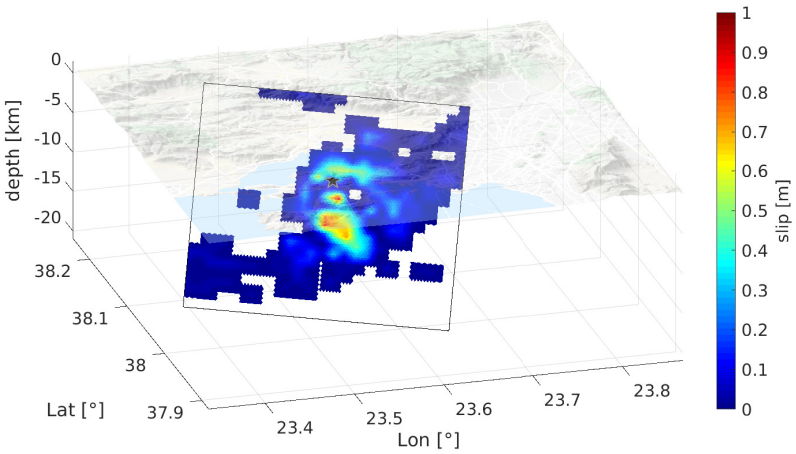

Figure 3.2: Distribution of the slip amplitude values on the fault plane after [Rou+03] and location of the hypocenter (star) after [Pap+00a].

Table 3.1: Properties of the first layer.

Sublayer	$v_s\,[m/s]$	$v_p\,[m/s]$	$\rho\,[kg/m^3]$
$z_1 < z \leq z_0,\ z \leq z_3$	1500	2670	2500
$z_2 < z \leq z_0$	380	760	1800
$z_3 < z \leq z_0,\ z \leq z_1,\ z \leq z_2$	700	1250	2300

As mentioned in the previous sections, we carried out two main numerical simulations of the 1999 Athens earthquake: (a) the first focuses on the ground shaking across the metropolitan area including the Acropolis hill; (b) the second focuses on the Acropolis and the Parthenon.

Simulation of 1999 Athens earthquake M_w6 ground motion

In order to be able to propagate accurately waves with a frequency content up to $f_{max} = 5Hz$, we built a non-conforming mesh with size of $5 - 20m$ on the Acropolis hill, and of $70m$ in the metropolitan area of Athens. Outside the city and in the source region, the mesh size ranges from $200 - 300m$ within the topmost layer to $700m$ at depth, see Figure 3.4. The model consists of 1.319.941 hexahedral elements and, by using a polynomial approximation degree N_k varying from 1 to 4 (Tables 3.2 and 3.3), it has 253.599.612 degrees of freedom. We fixed the total observation

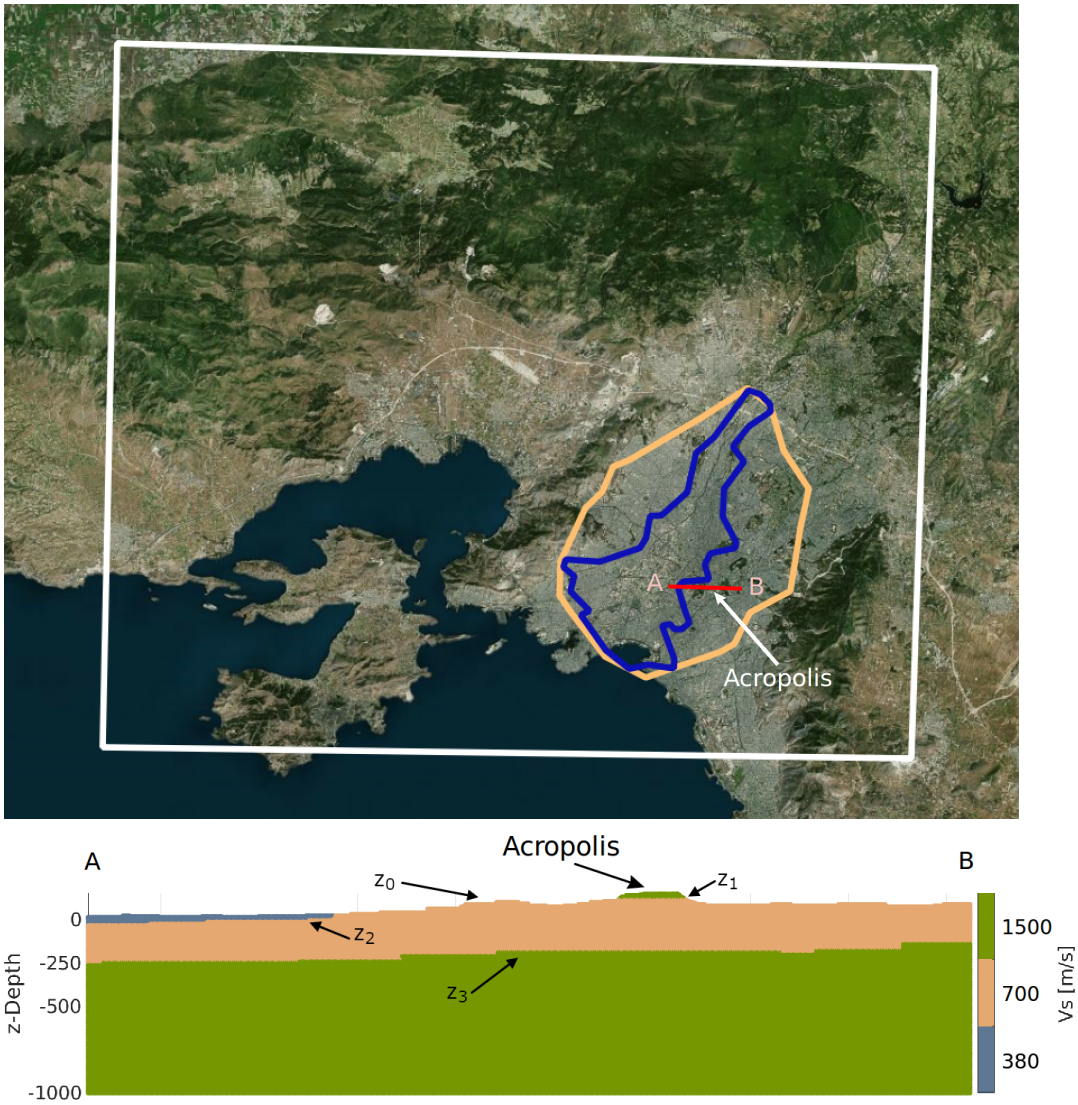

Figure 3.3: Top: digital terrain model encompassing the geographic extent of the simulations. The white lines delimit the computational area. The orange and blue curves represent the simplified boundaries of the Athens Schist and alluvial deposits, obtained as described in the text. Bottom: vertical cross-section along the East-West (EW) direction (see horizontal red line $A - B$ in top figure). z_q, $q = 0, 1, 2, 3$ represent the surfaces that delimit the sublayers with different material properties (z_1 outcrops of the Acropolis, z_2 and z_3 denote the Athenian basin and Schist (blue and orange curves on top), respectively.

time $T = 30s$ and we used a time step $\Delta t = 10^{-4}s$ with $C_{CFL} = 0.1702$ (see (1.34)). The wall-time for the simulation was around 50 hours on 1024 cores on the Marconi cluster at CINECA, Italy (`https://www.hpc.cineca.it/hardware/marconi`).

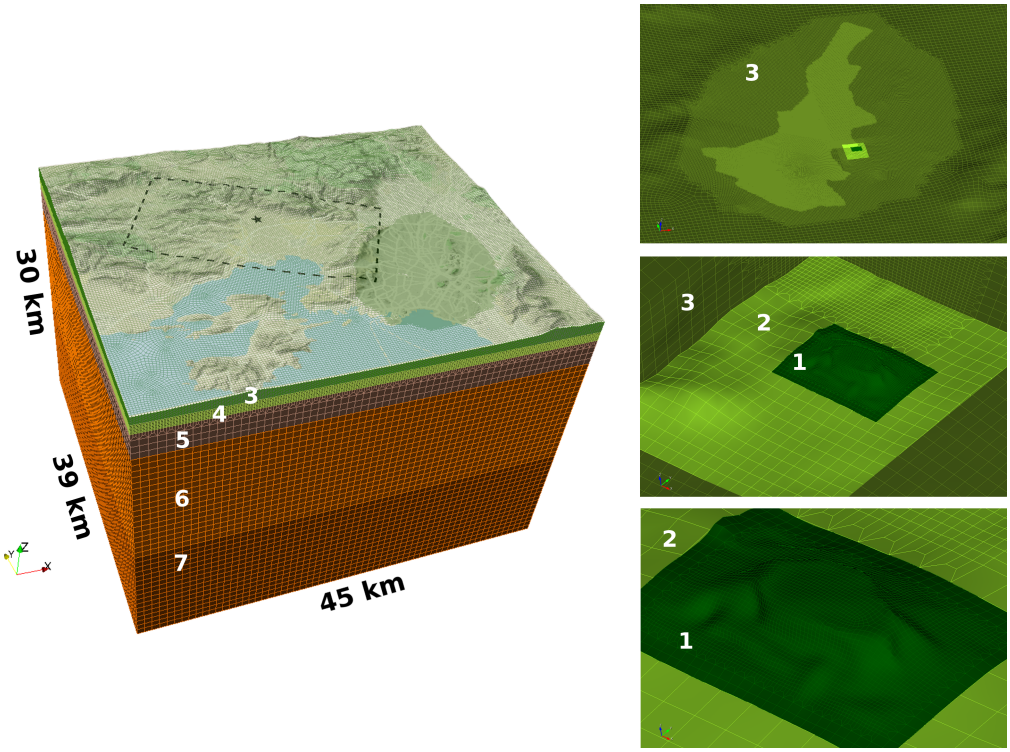

Figure 3.4: 3D computational model for the Attika region with indication of the surface projection of the Fili fault and of the epicentre of the 1999 Athens earthquake, (left) and zoom on the Athens metropolitan area and Acropolis hill (right). Numbers denote ID blocks, see Tables 3.2 and 3.3.

Seismic response of the Parthenon under the 1999 M_w 6 earthquake

In the second simulation we considered the previous computational model with the following simplification: homogeneous geophysical properties for the topmost layer ($v_s = 1500m/s$, $v_p = 2670m/s$ and $\rho = 2500kg/m^3$) with constant mesh size of $300m$. Then we integrated a simplified model of the Parthenon using a non-conforming mesh with size of $0.5m$ (Figure 3.5 and Table 3.4). The numerical model of this simulation has 738.109 hexahedral elements and, by choosing a first order polynomial degree for the computational mesh of the Parthenon $N_k = 1$, it has 127.900.548 degrees of freedom. The time step was $\Delta t = 10^{-5}s$ with $C_{CFL} = 0.1157$ (see (1.34)). In this case the wall-time for the simulation was around 210 hours on 512 cores on the Galileo and Marconi–100 cluster at CINECA, Italy (`https://www.hpc.cineca.it/hardware/marconi100`, `https://www.hpc.cineca.it/hardware/galileo`).

Table 3.2: Horizontally stratified crustal model.

Layer	ID Block	Depth $[km]$	$v_s\,[m/s]$	$v_p\,[m/s]$	$\rho\,[kg/m^3]$	$\xi\,[\mathrm{m}Hz]$
1	1–3	top – 1	see Table 3.1	see Table 3.1	see Table 3.1	$50\pi/v_s$
2	4	1 – 2	2500	4450	2500	62.83
3	5	2 – 5	3200	5700	2840	49.09
4	6	5 – 18	3370	6000	2900	46.61
5	7	18 – 30	3600	6400	2980	43.63

Layer	ID Block	$h_k\,[m]$	N_k
1	1–3	see Table 3.3	see Table 3.3
2	4	200 – 300	4
3	5	700	4
4	6	700	4
5	7	700	4

Table 3.3: Horizontally stratified crustal model: zoom on first layer.

ID Block	$h_k\,[m]$	N_k
1	5 – 20	1
2	65	2
3	70 – 300	4

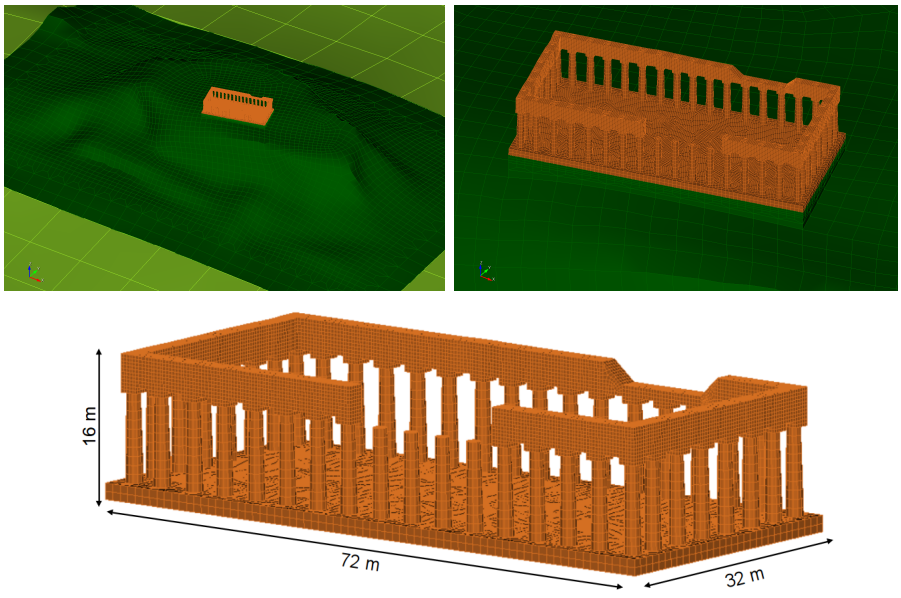

Figure 3.5: 3D computational meshes of the Acropolis hill and the Parthenon.

Table 3.4: Mesh size (h_k) and elastic properties of the Parthenon modelled as a single geophysical unit.

$h_k\,[m]$	N_k	$v_s\,[m/s]$	$v_p\,[m/s]$	$\rho\,[kg/m^3]$	$\xi\,[\mathrm{m}Hz]$
0.5	1	600	1000	2450	261.80

3.2.3 Numerical results and comparison with records

In the following, the results of the 3D physics-based numerical simulations will be discussed with emphasis on the characterization of earthquake ground motion and the seismic response of the Acropolis hill and its Parthenon.

Simulation of 1999 Athens earthquake M_w6 ground motion

Figure 3.6 (top panel) depicts the spatial distribution of peak ground velocity (PGV, maximum of the two orthogonal horizontal components) generated by simulation (a), along with the surface projection of the ruptured fault (dashed polygon) and the epicentre (star). The largest PGV values approach $46cm/s$ in the source area and decrease to a few cm/s across the metropolitan area. On the Acropolis hill, the simulated PGV values are $6.5\,cm/s$. The figure shows the locations of seven strong-motion accelerographs operating at the time of the event. Information about these stations as retrieved from the Engineering Strong Motion Database (`https://esm-db.eu`) is given in Table 3.5, including the recorded PGV values.

Figure 3.6 (mid panel) shows the macroseismic intensity levels (I) obtained from the synthetic PGV values and the largely used ground-motion conversion equation of [FM10], i.e.:

$$I = 5.11 + 2.35 * \log_{10}(PGV[cm/s]). \tag{3.1}$$

The bottom panel of Figure 3.6 shows the macroseismic intensity ShakeMap available in the global earthquake atlas of the United States Geological Survey (USGS) at `https://earthquake.usgs.gov/earthquakes/eventpage/iscgem1655758/shakemap/intensity`. There is a good match between the maximum intensity values yielded by simulation (a) and the USGS ShakeMap, while the spatial distribution of intensity shows some discrepancies that can be mainly attributed to the following issues. (i) The geology of the area was necessarily simplified in the numerical model; in particular the geometry of the as-modelled Schist formation is clearly controlling the spatial distribution of synthetic intensities in the metropolitan area. (ii) The intensity distribution in the USGS ShakeMap is mainly constrained by felt reports and field observations which may be affected by local site amplification effects. In spite of these limitation, the overall agreement between the synthetic intensities and the USG ShakeMap demonstrates the soundness of the simulations as input to seismic hazard an risk studies in the area of Athens.

The soundness of the predictive tool is further corroborated by the comparison with the global empirical ground motion model (GMM) CEA15 [Cau+15a], as shown in Figure 3.7. The physics-based synthetic (PBS) *PGV* values are color-coded according to the surface geology at the location of the synthetic receivers (the free surface nodes of the numerical mesh): green–limestone (L), orange–Athenian Schist (AS), blue–Athenian alluvial basin deposits (AB). We used $v_{s,30} = 1500m/s$ for the GMM, i.e., the v_s of the topmost layer of the crustal structure and of the Athens limestone. Consistent with the chosen GMM, the closest distance to the fault rupture (R_{rupt}) is used on the x-axis of Figure 3.7. The agreement with the GMM is remarkable, especially in the near-field region ($R_{rupt} \lesssim 20km$), where PBS and GMMs often tend to disagree. The comparison remains very good at larger distances: the rate of attenuation seems to be the same for the synthetics and the GMM; the median values of the PBS show a rather constant offset w.r.t. the GMM and are always within the standard deviation $\pm\sigma$ bounds of the GMM.

Table 3.5: List of stations in the area of Athens and comparison of *PGV* values from ShakeMap and SPEED simulation.

ID	Station code	Lat (°)	Lon (°)	Elevation $[m]$	Geology
1	ATH2	38.0176	23.7890	167.3	Athenian schist – limestone
2	ATH3	37.9724	23.7053	22.4	alluvium
3	ATH4	37.9951	23.7383	105.0	alluvium
4	ATHA	38.0008	23.7735	170.3	Athenian schist
5	DMKA	37.9970	23.8210	291.9	limestone
6	SGMA	37.9755	23.7353	89.0	Athenian schist
7	SPLB	38.0040	23.7103	45.8	alluvium

ID	Station code	ShakeMap *PGV* $[cm/s]$	SPEED *PGV* $[cm/s]$
1	ATH2	8.4	3.0
2	ATH3	15.9	4.8
3	ATH4	8.9	5.7
4	ATHA	7.4	4.2
5	DMKA	2.4	1.7
6	SGMA	13.6	4.9
7	SPLB	21.5	8.1

The comparison of the synthetic waveforms generated by simulation (a) with the actual recordings of the 1999 Athens earthquake poses some challenges due to the characteristics of the contemporary strong-motion monitoring infrastructure and associated data / metadata. The exact start time of the recordings is unknown, as are the actual orientation and polarity of the orthogonal horizontal components of the accelerographs. In spite of these difficulties, we propose in Figure 3.8 a comparison at station SGMA, located on the Athenian Schist formation in the iconic

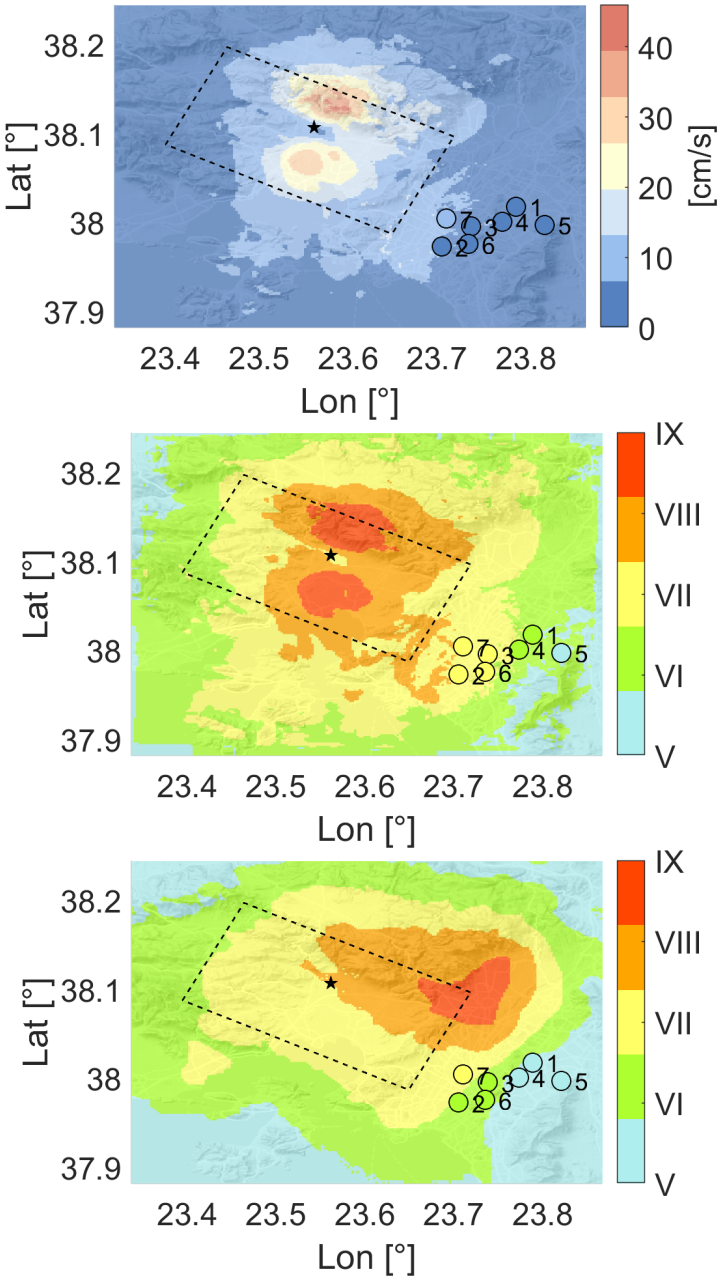

Figure 3.6: Synthetic peak ground velocity (PGV, top panel), synthetic macroseismic intensity (I, middle panel), ShakeMap intensity (I, bottom panel) computed / obtained as described in the text.

Syntagma Square. All data were filtered in the range $[.5 - 5]Hz$ using a causal Butterworth filter with order $N_f = 3$; the recorded data retrieved by the Engineering Strong-Motion Database were delayed by $1.1s$. The comparison is overall satisfactory, since the synthetics seem to capture well the orientation and polarity at the onset of ground shaking – the signature of the fault mechanism – and the

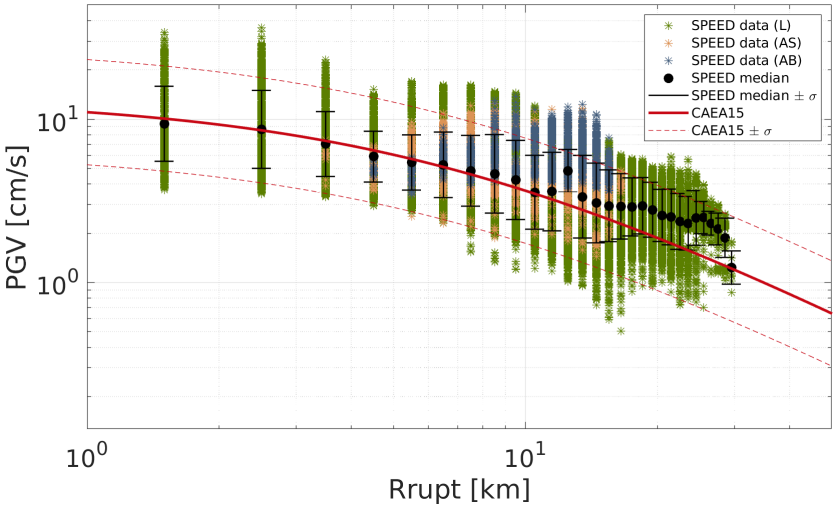

Figure 3.7: Synthetic peak ground velocity (PGV, top panel) values compared with the empirical ground motion model of CEA15 [Cau+15a] as explained in the text. Colored stars refer to PGV values at each receiver with assigned material properties: green–limestone (L), orange–Athenian Schist (AS), blue–Athenian alluvial basin deposits (AB).

dominant periods / frequencies of the recorded data both in the time and frequency domains. The recorded peak amplitudes are larger on the horizontal components, most likely due to amplification induced by small-scale geological features that are not included in the numerical models. The comparison between the synthetic and the recorded data further improves if the low-cut of the filters is set to $1Hz$, not shown here for brevity. The comparison of the Fourier Amplitude Spectra (FAS) of the vertical components hints a stronger vertical attenuation than in the numerical models, or a lower quality factor Q_P.

Seismic response of the Parthenon under the 1999 M_w 6 earthquake

Simulation (b) was devoted to jointly modelling the Athens 1999 earthquake and the shaking induced by the earthquake to the Parthenon. The Acropolis of Athens is monitored with a local network of strong-motion accelerographs operated by the Institute of Geodynamics, National Observatory of Athens (NOA-IG), in collaboration with the Acropolis Restoration Service (YSMA). The array consists of 10 strong-motion sensors (Guralp CMG-5TD) recording in continuous mode on 24-bit digitisers, sampling the main geological units constituting the Acropolis and including two sites devoted to monitoring monumental elements of the Parthenon (Table 3.6). In particular, stations C and B are located respectively at the crest and base of a marble column pertaining to the northern colonnade of the Parthenon. Even if the Acropolis array was not yet operational in 1999, the abundant recordings

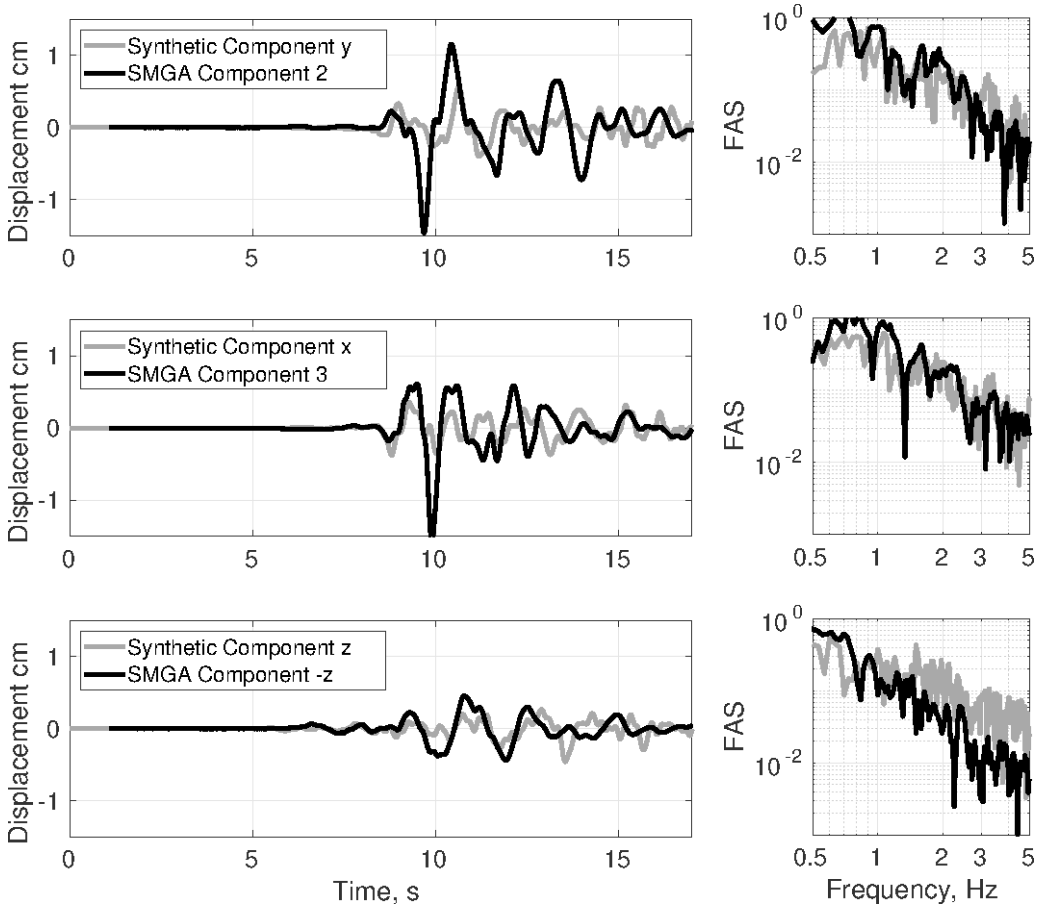

Figure 3.8: Comparison of synthetic and recorded data at station SGMA (Syntagma Square ID 6) on Athenian Schist. Waveform data processed as described in the text. LHS panels: time-domain displacement waveforms; RHS panels: Fourier Amplitude Spectra (FAS).

of earthquakes and ambient vibration acquired since its installation allow empirically assessing the key features of the seismic response of the Acropolis and the Parthenon, as e.g. in [Cau+15b]. Figure 3.9 shows the spectral ratios between station C and B. The thick curve shows the ratio (geometric mean of the horizontal components) as computed in [Cau+15b] based on local earthquakes and ambient vibrations; the dashed curve is the ratio obtained from numerical simulation (b). The dominant frequencies at $\sim 1.5 - 2Hz$ of the empirical seismic response of the northern colonnade are well captured by the simulation, although the amplitude of the empirical spectral ratio is higher. Given the drastic simplifications adopted in this to model the Parthenon as a homogenous continuous geophysical unit, this result is quite remarkable and encouraging towards future refinements.

Table 3.6: List of stations on the Acropolis hill.

Station code	Lat (°)	Lon (°)	Elevation $[m]$	Location	Geology
ACRA	37.9716	23.7277	152.2	free-field	limestone
ACRB	37.9716	23.7265	159.8	Parthenon basement	porous stone blocks on limestone
ACRC	37.9716	23.7265	173.6	Parthenon N colonnade	(-)
ACRD	37.9712	23.7272	151.6	free-field	limestone – anthropic infill
ACRE	37.9718	23.7279	154.6	free-field	limestone
ACRF	37.9723	23.7262	148.9	free-field	limestone
ACRG	37.9721	23.7249	113.7	free-field	Athenian schist
ACRH	37.9719	23.7249	137.7	free-field	limestone
ACRI	37.9714	23.7266	155.1	Parthenon basement	porous stone blocks on limestone
ACRJ	37.9711	23.7273	130.8	free-field	limestone

3.3 Concluding remarks

In this work we presented and validated on a real test case a numerical model for complex multi-scale engineering-seismology problems, including soil-structure interaction.

The simulations are based on a DGSE method and carried out based on employing the open source code SPEED. SPEED is based on discontinuous Galerkin spectral element method, suitable for handling non-matching grids as well as variable approximation orders. This approach can accommodate sharp geophysical discontinuities and / or complicated geometrical settings, which often occur in engineering wave propagation problems. The proposed application to the Athens 1999 earth-

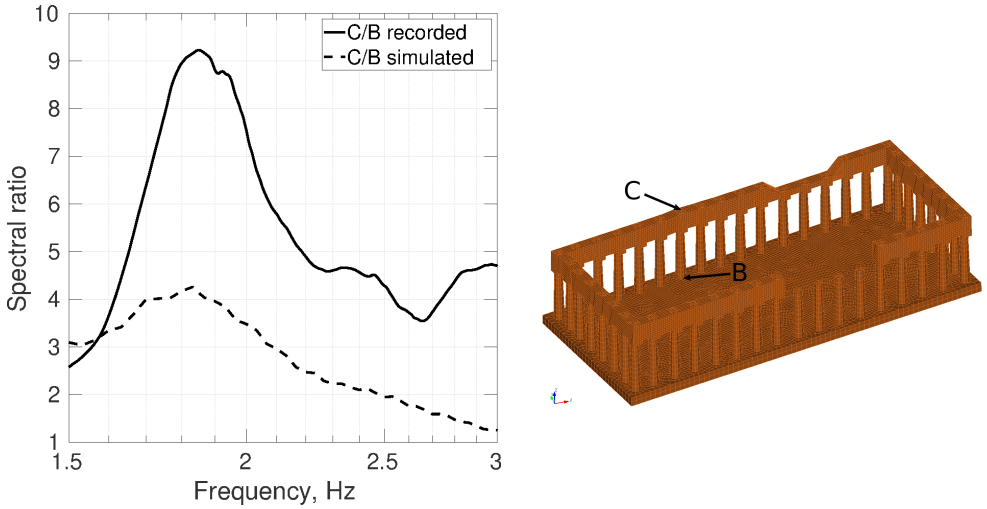

Figure 3.9: Comparison of the recorded and simulated spectral ratios at two stations (C, B) located respectively at the crest and base of a marble column pertaining to the northern colonnade of the Parthenon.

quake showed that SPEED offers major advantages for modeling multi-scale seismic scenarios, by relaxing constraints imposed by standard conforming SE methods and, therefore, reducing the simulation costs while attaining high order accuracy as typical of spectral element methods. To accomplish the multi-physics feature of the problem under investigation, we described the Athens 1999 $M_w 6$ earthquake with a set of simulations to capture all the main features.

Indeed, by taking into account for the need of propagation at high frequencies, the different geological features and the geometrical accuracy of the model (e.g. Acropolis hill and the Parthenon), in our simulations we choose small mesh size/large polynomial degree for the DG approximations and therefore a very small Δt due to the CFL condition. In order to reduce the computational costs related to that condition and be able to propagate the phenomenon up to $30Hz$, necessary to investigate the seismic response of the Acropolis hill, it is possible to consider space-time DG discretizations [AMM20] that relax the choice of the time step. Further development to improve the description of the seismic phenomenon in a more accurate way could be the contact-friction laws that model the dynamic fault spontaneous rupture and the non-linear seismic response of the buildings, in our case of the Parthenon. This new model is currently under investigation.

The proposed validation test case demonstrates the effectiveness of seismic simulations within the framework of the seismic risk mitigation strategies for the cultural heritage.

CHAPTER 4

Simulation of seismic wave propagation problems with contact-friction laws by discontinuous Galerkin discretizations

In this chapter we describe the formulation, the numerical analysis and the implementation of contact-friction laws that are at the basis of dynamic seismic source modelling and of the description of the non-linear interaction between ground and structures. Suitable contact-friction laws are incorporated within the elastodynamics model and the discontinuous Galerkin method is adopted for the semidiscrete approximation. The convergence analysis of the resulting semidiscrete formulation is presented. A wide set of verification tests for a spontaneous dynamic rupture test case have been carried out and the results have been compared with the numerical data available in the literature.

4.1 Contact-friction laws in elastodynamics models

Physics-based modelling of dynamic fault rupture and non-linear behaviour of the structures is of crucial importance in seismic risk applications. Indeed, the representation of the seismic source is one of the main key ingredients when describing seismic wave propagation phenomena, whereas an improvement of the description of the buildings is fundamental within the seismic structural analysis. In the literature there are two main descriptions of the seismic source for earthquake applications: kinematic representation of the fault rupture and dynamic source modelling. In Chapter 1 we have shown the kinematic representation of the fault rupture (see

(1.6)) that is then employed in the applications presented in Chapters 2 and 3. Here we address the dynamic source modelling which is based on the coupling of contact-friction laws with the elastodynamics equations, c.f. [And76; DA77; Day82]. On the other hand, at the best of our knowledge, the contact-friction laws within the seismic vulnerability models have not been addressed so far and they can describe the non-linear behaviour of the buildings within the structural analysis framework, cf. Chapter 3.

Within the computational seismology framework, many numerical methods have been adopted to simulate the dynamic fault rupture. Since this model is based on the coupling of elastodynamics equations and contact-friction laws, we observe that the numerical approaches that are presented in literature have the same drawbacks when solving the elastodynamics equations for seismic propagation phenomena. Indeed, numerical methods employed for dynamic rupture simulations have shown that, for example, the FD method is accurate but cannot be employed efficiently in complex geophysical settings (see [And73; And99; Day82; EDM09; MOA98; Moc+07; Day+05; DD06; Dal12]). The FE method are geometrically flexible, but they are very dispersive for wave propagation problems since they have low-order accuracy (see [Hug+76; AHH01; OAN98; OAN00; GMK08]). Moreover FD and FE methods that describe the fault discontinuity by adding the discontinuity terms at grid nodes are called traction-at-split-node (TSN) methods, c.f. [DD07; And73; And99; Day77; Day82]. Instead the SE methods provide highly-accurate solutions, but they suffer geometric limitations due to the fact that are based on hexaedral elements, c.f. [Amp02; KLA08; VFA06; KLA08; Gal+14; FV05]. Finally, DGSE methods, as already mentioned before, are both accurate and flexible and have been employed to simulate the spontaneous dynamic rupture in a successful way, see [PAK09; Pue+07; Pue+08; DK06; KD06; Käs+07; KMD07; Pel+12; KI05; KHP08; TT02].

From the mathematical point of view, at the best of our knowledge, the dynamic fault rupture modelling with its mathematical and numerical analysis has not been addressed so far within the discontinuous Galerkin framework. Moreover, solving and analyzing the dynamic-fault rupture problem is a challenging task due to the non-linear nature of its governing equations. In literature there is a number of theoretical and numerical analysis related to contact, friction and contact-friction problems that can be the basis of our study.

The main theoretical results for the class of contact-friction problems in the elasticity and elastodynamics setting were established by Duvaut and Lions [DL76] within the framework of variational inequalities. See also [Hla+88; EJK05; Lau02] for an overview. The numerical analysis based on the variational inequality principles within a finite element framework can be found, for example, in [MO83; KO88; Lau02; Woh11; COK82; TP82; Pan79; LK79; Pan77; Sew69; Kal79].

The most employed methods to solve numerically the problem of contact-friction within the framework of elasticity and elastodynamics that can be found in literature

are the following.

1. Penalty methods make use of penalty parameters to transform a set of inequalities into a non-linear equation, c.f. [MO83; KO88; KS81; OK82b; OK82a].

2. Mixed methods are based on Lagrange multipliers that represent the normal and tangential stress on the contact boundary, see e.g. [HH06; BeHW07; HW12; SWW15; AMR14; HW05; HW12; HMW07; HSW08; BD18].

3. The Nitsche method treats the boundary or interface conditions in a weak sense, c.f. [Nit71; Cho+19; Cho14; Cho+17; CMR18; CEP20].

In the following we introduce the mathematical model based on the elastodynamics equations supplemented with the contact-friction laws that govern the dynamic fault rupture and non-linear behaviour of constructions. We present its variational formulation within the inequality framework, c.f. [DL76; KO88; MO83], and show theoretical and numerical results for the simulations of dynamic-fault rupture wave propagation by non-conforming discontinuous Galerkin discretizations, c.f. [Ant+12].

The chapter is organized as follows. In the following we introduce the mathematical model for the dynamic source description and non-linear behaviour of structures. Then we present its variational formulation within the inequality framework. In addition we provide theoretical results for the variational inequality introduced before under suitable simplified hypothesis. In Section 4.2 we derive the semi- and fully-discrete formulations; space-discretization is based on the discontinuous Galerkin discretizations whereas the leap-frog scheme is employed to integrate in time. We also introduce a suitable method to solve the non-linearity in the governing equations. In Section 4.3 we present the theoretical stability and error estimates for the semi-discrete formulation. In Section 4.4 we report some numerical computations carried out on a benchmark 2D test case of seismic dynamic rupture problem. Finally, in Section 4.5 we discuss the achieved results and we draw some conclusions.

4.1.1 Statement of the problem and governing equations

Let $\Omega \subset \mathbb{R}^d$, $d = 2, 3$, be a fixed polygonal bounded domain and let $\partial\Omega$ be the corresponding boundary that we assume to be sufficiently regular. We suppose that Ω is subdivided into two connected subdomains Ω^+ and Ω^- by the internal planar surface Γ_C, that represents the fault surface across where displacement discontinuities are allowed. Moreover let the external boundary $\partial\Omega$ be decomposed into three disjoint portions Γ_D, Γ_N and Γ_{NR}, where Γ_D, $|\Gamma_D| > 0$, is the portion of the boundary where the displacements are assigned, Γ_N is the one where surface loads are imposed and on Γ_{NR} are set non-reflecting boundary conditions to avoid unphysical reflections.

Given a final observation time $T > 0$, we consider the temporal interval $(0, T]$ and the dynamic equation for an elastic material with contact-friction laws leads to the following system:

$$\begin{cases} \rho\ddot{\mathbf{u}} - \nabla \cdot \underline{\sigma}(\mathbf{u}) = \mathbf{f}, & \text{in } \Omega \times (0,T], \\ \mathbf{u} = \mathbf{0}, & \text{on } \Gamma_D \times (0,T], \\ \underline{\sigma}(\mathbf{u})\mathbf{n} = \mathbf{t}, & \text{on } \Gamma_N \times (0,T], \\ \underline{\sigma}(\mathbf{u})\mathbf{n} = \mathbf{t}^*, & \text{on } \Gamma_{NR} \times (0,T], \\ [u]_N = 0, & \\ \sigma_N \leq 0, & \text{on } \Gamma_C \times (0,T], \\ |\boldsymbol{\sigma}_T| \leq -\mu_f \sigma_N, & \\ \mathbf{u} = \mathbf{u}_0, & \text{in } \Omega \times \{0\}, \\ \dot{\mathbf{u}} = \mathbf{u}_1, & \text{in } \Omega \times \{0\}. \end{cases} \tag{4.1}$$

As before, the quantity $\rho = \rho(\mathbf{x}) \in L^\infty(\Omega)$ is a strictly positive function describing the material density, $\mathbf{u} = \mathbf{u}(\mathbf{x}, t)$ is the displacement field, $\underline{\sigma}(\mathbf{u}) = \underline{\sigma}(\mathbf{x}, t)$ is the stress tensor, $\mathbf{n} = \mathbf{n}(\mathbf{x})$ is the unit outward normal vector to $\partial\Omega$ and $\mathbf{f} = \mathbf{f}(\mathbf{x}, t)$ is a given external load. On the boundary we impose null displacements on Γ_D, a traction $\mathbf{t} = \mathbf{t}(\mathbf{x}, t)$ on Γ_N and a fictitious traction $\mathbf{t}^* = \mathbf{t}^*(\mathbf{x}, t)$ on Γ_{NR} introduced to avoid unphysical reflections on the artificial boundaries, see [Sta88; Ant+18a]. Moreover we impose contact-friction conditions on Γ_C. We assume that the fault is made of a single smooth surface with continuous normal vector $\mathbf{n}$. Implicit in this definition is that the interface Γ_C can be described as two surfaces, Γ_C^+ and Γ_C^-, in frictional contact: each geometric point $\mathbf{x}$ located on Γ_C corresponds to two material points $\mathbf{x}^\pm$ located on each side of the fault, cf. Figure 4.1. We define the orientation of $\mathbf{n}$ as going from Γ_C^+ to Γ_C^- and the displacements on each material side of the fault as

$$\mathbf{u}^\pm = \mathbf{u}(\mathbf{x}^\pm).$$

The displacement discontinuity (slip) across Γ_C is denoted by

$$[\mathbf{u}] = \mathbf{u}^+ - \mathbf{u}^-.$$

The normal and tangential components of $[\mathbf{u}]$ are defined as

$$[u]_N = [\mathbf{u}] \cdot \mathbf{n} = u_N^+ - u_N^-, \tag{4.2}$$

$$[\mathbf{u}]_T = [\mathbf{u}] - [u]_N \mathbf{n} = \mathbf{u}_T^+ - \mathbf{u}_T^-, \tag{4.3}$$

respectively. With these conventions $[u]_N$ is negative for separation and positive for penetration between the two fault sides. Similar definitions are adopted for velocities $\dot{\mathbf{u}}$ and accelerations $\ddot{\mathbf{u}}$.

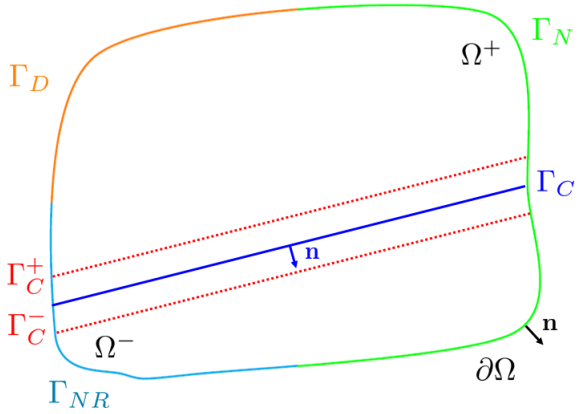

Figure 4.1: Illustrative geometry, the fault interface $\Gamma_C = \partial\bar{\Omega}^+ \cap \partial\bar{\Omega}^-$ with $\Omega = \Omega^+ \cup \Omega^-$. The normal vector to the surface Γ_C^+, pointing towards Γ_C^-, is denoted by $\mathbf{n}$.

We observe that we can write the slip, the slip-rate on the fault in the following form:

$$\mathbf{v} = \mathbf{v}_T + v_N \mathbf{n}, \quad v_N = \mathbf{v} \cdot \mathbf{n},$$

respectively.

The tractions acting on each side of the fault are denoted by

$$\boldsymbol{\sigma}^{\pm} = \pm \underline{\sigma}(\mathbf{u}^{\pm})\mathbf{n},$$

for which it follows that $\boldsymbol{\sigma} = \boldsymbol{\sigma}^+ = -\boldsymbol{\sigma}^-$ and $\boldsymbol{\sigma} = \sigma_N \mathbf{n} + \boldsymbol{\sigma}_T$. The normal and tangential components of $\boldsymbol{\sigma}$, denoted as σ_N and $\boldsymbol{\sigma}_T$, respectively, are defined as in (4.2)–(4.3) respectively. Here, σ_N is negative for compression and positive for tension. With the notation introduced before, mixed interface conditions are prescribed on the fault: friction and contact laws relate $\boldsymbol{\sigma}$ to $[\mathbf{u}]$, $[\dot{\mathbf{u}}]$ or to other variables describing the fault state. The friction and contact conditions apply to the total fields, including the initial values for fault stress, slip and state variables. The normal components of $\boldsymbol{\sigma}$ and $[\mathbf{u}]$, i.e. σ_N and $[u]_N$, respectively, are typically related by unilateral contact conditions, also known as Signorini conditions. These imply no interpenetration of the two fault sides and vanishing normal stress on open faults. In our study we only consider the case of no opening faults, i.e. $[u]_N = 0$. On the other hand, the tangential components are related by friction conditions that imply that shear tractions are bounded by frictional strength proportional to normal tractions. The friction coefficient $\mu_f \geq 0$ can depend on $|[\mathbf{u}]_T|$, $|[\dot{\mathbf{u}}]_T|$ or on other fault state variables, such as normal stress or thermal and mechanical quantities, cf. [Biz+01]. In the case of linear slip-weakening the following friction law is considered, see e.g. [PR73; Ida72],

$$\mu_f(\mathbf{u}) = \mu_s - (\mu_s - \mu_d) \min(|[\mathbf{u}]_T|/D_c, 1), \tag{4.4}$$

where $|[\mathbf{u}]_T|$ is called the slip length. When $|[\mathbf{u}]|$ is large the friction coefficient μ_f drops linearly from the static value μ_s to the dynamic value μ_d over the critical slip distance D_c. The linear slip weakening friction law (4.4) is capable of modeling initial rupture, arrest of sliding and reactivation of slip. In particular the condition $|\boldsymbol{\sigma}_T| \leq -\mu_f \sigma_N$ can be formulated as

$$\begin{cases} |\boldsymbol{\sigma}_T| < -\mu_f \sigma_N \implies [\dot{\mathbf{u}}]_T = \mathbf{0} \\ |\boldsymbol{\sigma}_T| = -\mu_f \sigma_N \implies \exists \gamma > 0 : [\dot{\mathbf{u}}]_T = -\gamma \boldsymbol{\sigma}_T \end{cases}. \tag{4.5}$$

Finally, as initial conditions for the displacement and the velocity we assign the functions $\mathbf{u}_0 = \mathbf{u}_0(\mathbf{x})$ and $\mathbf{u}_1 = \mathbf{u}_1(\mathbf{x})$, respectively. Moreover we assume to have linear elasticity (Hooke's law) for the constitutive equation $\underline{\sigma}(\mathbf{u}) = \underline{D}\,\underline{\varepsilon}(\mathbf{u})$, cf. Section 1.1.

Remark 4.1. In this chapter, for the sake of simplicity, we are addressing the elastodynamics equation without the damping term that was in the model problem introduced in Chapter 1. Further developments in the future include considering visco-elastic materials and suitably generalizing the contact-friction laws.

4.1.2 Variational formulation

In this section we present the variational inequality associated to problem (4.1) following the main results obtained by Duvaut and Lions [DL76] within the framework of contact-friction equations. We introduce the product space $\mathbf{V} = \{\mathbf{v} = (\mathbf{v}^+, \mathbf{v}^-) \in \mathbf{V}^+ \otimes \mathbf{V}^-\}$, where the spaces $\mathbf{V}^\pm$ are defined by $\mathbf{V}^\pm = \{\mathbf{v} \in \mathbf{H}^1(\Omega^\pm) : \mathbf{v} = \mathbf{0} \text{ on } \Gamma_D \cap \partial\Omega^\pm\}$. Therefore the variational formulation of problem (4.1) reads: find $\mathbf{u}(t) \in \mathbf{V}$, for any $t \in (0, T]$, such that

$$\begin{aligned} (\rho\, \ddot{\mathbf{u}}(t), \mathbf{v} - \dot{\mathbf{u}}(t))_\Omega + \mathcal{B}(\mathbf{u}(t), \mathbf{v} - \dot{\mathbf{u}}(t)) + \mathcal{P}(\mathbf{u}(t), \mathbf{v} - \dot{\mathbf{u}}(t)) \\ + \mathcal{J}(\mathbf{u}(t), \mathbf{v}) - \mathcal{J}(\mathbf{u}(t), \dot{\mathbf{u}}(t)) \geq \mathcal{F}(\mathbf{v} - \dot{\mathbf{u}}(t)) \quad \forall \mathbf{v} \in \mathbf{V}, \end{aligned} \tag{4.6}$$

where

$$\begin{aligned} \mathcal{B}(\mathbf{u}, \mathbf{v}) &= (\underline{\sigma}(\mathbf{u}), \underline{\varepsilon}(\mathbf{v}))_\Omega + \langle \eta_N [u]_N, [v]_N \rangle_{\Gamma_C}, \\ \mathcal{P}(\mathbf{u}, \mathbf{v}) &= \langle -\sigma_N(\mathbf{u}), [v]_N \rangle_{\Gamma_C}, \\ \mathcal{J}(\mathbf{u}, \mathbf{v}) &= \langle -\mu_f(\mathbf{u}) \sigma_N(\mathbf{u}), |[\mathbf{v}]_T| \rangle_{\Gamma_C}, \\ \mathcal{F}(\mathbf{v}) &= (\mathbf{f}(t), \mathbf{v})_\Omega + \langle \mathbf{t}(t), \mathbf{v} \rangle_{\Gamma_N} + \langle \mathbf{t}^*(t), \mathbf{v} \rangle_{\Gamma_{NR}}. \end{aligned}$$

Here $(\cdot, \cdot)_D$ and $\langle \cdot, \cdot \rangle_{\partial D}$ denote $\mathbf{L}^2(D)$ and $\mathbf{L}^2(\partial D)$ inner products, respectively. Moreover $\eta_N > 0$ is a parameter introduced to penalize the normal discontinuity of the displacements in the formulation. The variational inequality introduced (4.6) follows from

$$\begin{aligned} (\rho\, \ddot{\mathbf{u}}(t), \mathbf{v} - \dot{\mathbf{u}}(t))_\Omega + \mathcal{B}(\mathbf{u}(t), \mathbf{v} - \dot{\mathbf{u}}(t)) - \mathcal{F}(\mathbf{v} - \dot{\mathbf{u}}(t)) \\ = \langle \sigma_N, [v]_N \rangle_{\Gamma_C} - \langle \sigma_N, [\dot{u}(t)]_N \rangle_{\Gamma_C} + \langle \boldsymbol{\sigma}_T, [\mathbf{v}]_T \rangle_{\Gamma_C} - \langle \boldsymbol{\sigma}_T, [\dot{\mathbf{u}}(t)]_T \rangle_{\Gamma_C}, \end{aligned}$$

where we have integrated by parts the governing equations after multiplication by a test function $\mathbf{v} = \mathbf{v} - \dot{\mathbf{u}}$. Then, by adding and subtracting $\mathcal{P}(\mathbf{u}, \mathbf{v} - \dot{\mathbf{u}}(t))$, $\mathcal{J}(\mathbf{u}(t), \mathbf{v})$, $-\mathcal{J}(\mathbf{u}(t), \dot{\mathbf{u}}(t))$, we obtain

$$\begin{aligned}
(\rho\,\ddot{\mathbf{u}}(t), \mathbf{v} - \dot{\mathbf{u}}(t))_\Omega \,+\, \mathcal{B}(\mathbf{u}(t), \mathbf{v} - \dot{\mathbf{u}}(t)) \,+\, \mathcal{P}(\mathbf{u}, \mathbf{v} - \dot{\mathbf{u}}(t)) \\
\quad +\, \mathcal{J}(\mathbf{u}(t), \mathbf{v}) \,-\, \mathcal{J}(\mathbf{u}(t), \dot{\mathbf{u}}(t)) \,-\, \mathcal{F}(\mathbf{v} - \dot{\mathbf{u}}(t)) \\
= \langle \sigma_N, [v]_N \rangle_{\Gamma_C} \,-\, \langle \sigma_N, [\dot{u}(t)]_N \rangle_{\Gamma_C} \,+\, \langle \boldsymbol{\sigma}_T, [\mathbf{v}]_T \rangle_{\Gamma_C} \,-\, \langle \boldsymbol{\sigma}_T, [\dot{\mathbf{u}}(t)]_T \rangle_{\Gamma_C} \\
\quad +\, \mathcal{P}(\mathbf{u}, \mathbf{v} - \dot{\mathbf{u}}(t)) \,+\, \mathcal{J}(\mathbf{u}(t), \mathbf{v}) \,-\, \mathcal{J}(\mathbf{u}(t), \dot{\mathbf{u}}(t)) \\
= \langle \boldsymbol{\sigma}_T, [\mathbf{v}]_T \rangle_{\Gamma_C} \,-\, \langle \boldsymbol{\sigma}_T, [\dot{\mathbf{u}}(t)]_T \rangle_{\Gamma_C} \\
\quad -\, \langle \mu_f(\mathbf{u})\sigma_N, |[\mathbf{v}]_T| \rangle_{\Gamma_C} \,+\, \langle \mu_f(\mathbf{u})\sigma_N, |[\dot{\mathbf{u}}(t)]_T| \rangle_{\Gamma_C} \,\geq 0.
\end{aligned}$$

Indeed, if $|\boldsymbol{\sigma}_T| < -\mu_f \sigma_N$ then $[\dot{\mathbf{u}}]_T = \mathbf{0}$ (see (4.5)). Therefore it follows:

$$\begin{aligned}
\boldsymbol{\sigma}_T \cdot [\mathbf{v}]_T \,-\, \boldsymbol{\sigma}_T \cdot [\dot{\mathbf{u}}(t)]_T - \mu_f \sigma_N |[\mathbf{v}]_T| \,+\, \mu_f \sigma_N |[\dot{\mathbf{u}}(t)]_T| \\
= \boldsymbol{\sigma}_T \cdot [\mathbf{v}]_T \,-\, \mu_f \sigma_N |[\mathbf{v}]_T| \\
\geq -\,|\boldsymbol{\sigma}_T| \cdot |[\mathbf{v}]_T| \,-\, \mu_f \sigma_N |[\mathbf{v}]_T| \\
= (-|\boldsymbol{\sigma}_T| \,-\, \mu_f \sigma_N) |[\mathbf{v}]_T| \,\geq 0.
\end{aligned}$$

If $|\boldsymbol{\sigma}_T| = -\mu_f \sigma_N$ then $\exists \gamma > 0 : [\dot{\mathbf{u}}]_T = -\gamma \boldsymbol{\sigma}_T$, (see (4.5)), therefore it follows:

$$\begin{aligned}
\boldsymbol{\sigma}_T \cdot [\mathbf{v}]_T \,-\, \boldsymbol{\sigma}_T \cdot [\dot{\mathbf{u}}(t)]_T \,-\, \mu_f \sigma_N |[\mathbf{v}]_T| \,+\, \mu_f \sigma_N |[\dot{\mathbf{u}}(t)]_T| \\
= \boldsymbol{\sigma}_T \cdot [\mathbf{v}]_T \,+\, \gamma |\boldsymbol{\sigma}_T|^2 \,-\, \sigma_N (|[v]_N| \,+ \mu_f |[\mathbf{v}]_T|) + \mu_f \gamma \sigma_N |\boldsymbol{\sigma}_T| \\
\geq -\,|\boldsymbol{\sigma}_T| \cdot |[\mathbf{v}]_T| \,+\, \gamma |\boldsymbol{\sigma}_T|^2 \,-\, \sigma_N (|[v]_N| \,+ \mu_f |[\mathbf{v}]_T|) + \mu_f \gamma \sigma_N |\boldsymbol{\sigma}_T| \\
= \,(-\,|\boldsymbol{\sigma}_T| \,-\, \mu_f \sigma_N) \cdot |[\mathbf{v}]_T| \,+\, \gamma |\boldsymbol{\sigma}_T|\,(|\boldsymbol{\sigma}_T| \,+\, \mu_f \sigma_N) = 0.
\end{aligned}$$

4.1.3 Regularized variational problem

In this section we introduce the regularized variational formulation of problem (4.6) as done, e.g., in [DL76; KO88; MO83]. The first step is to consider a convex and Gateaux differentiable regularization of the functional $\mathcal{J}$, defined as follows

$$\mathcal{J}^\varepsilon(\mathbf{u}, \mathbf{v}) = \langle -\mu_f(\mathbf{u})\sigma_N(\mathbf{u}), \psi_\varepsilon([\mathbf{v}]_T) \rangle_{\Gamma_C},$$

where ε is a real positive parameter with $\mathcal{J}^\varepsilon \to \mathcal{J}$ as $\varepsilon \to 0$ and where

$$\psi_\varepsilon(\mathbf{v}) = \begin{cases} |\mathbf{v}| - \dfrac{\varepsilon}{2} & \text{if } |\mathbf{v}| > \varepsilon, \\ \dfrac{1}{2\varepsilon}|\mathbf{v}|^2 & \text{if } |\mathbf{v}| < \varepsilon, \end{cases} \tag{4.7}$$

where $|\cdot|$ is the Euclidean norm. Therefore the regularized version of problem (4.6) reads: for any $t \in (0, T]$, find $\mathbf{u}_\varepsilon(t) \in \mathbf{V}$, such that

$$(\rho\,\ddot{\mathbf{u}}_\varepsilon(t), \mathbf{v})_\Omega \,+\, \mathcal{B}(\mathbf{u}_\varepsilon(t), \mathbf{v}) \,+\, \mathcal{P}(\mathbf{u}_\varepsilon(t), \mathbf{v}) \,+\, \langle \mathcal{K}^\varepsilon(\mathbf{u}_\varepsilon(t), \dot{\mathbf{u}}_\varepsilon(t)), \mathbf{v} \rangle \,=\, \mathcal{F}(\mathbf{v}) \quad \forall \mathbf{v} \in \mathbf{V}, \tag{4.8}$$

where

$$\langle \mathcal{K}^{\varepsilon}(\mathbf{u},\mathbf{w}),\mathbf{v}\rangle = \langle -\mu_f(\mathbf{u})\sigma_N(\mathbf{u}), \varphi_{\varepsilon}([\mathbf{w}]_T,[\mathbf{v}]_T)\rangle_{\Gamma_C},$$

and

$$\varphi_{\varepsilon}(\mathbf{w},\mathbf{v}) = \frac{\mathbf{v}\cdot\mathbf{w}}{|\mathbf{w}|}\begin{cases} 1 & \text{if } |\mathbf{w}|>\varepsilon, \\ \dfrac{|\mathbf{w}|}{\varepsilon} & \text{if } |\mathbf{w}|<\varepsilon. \end{cases} \tag{4.9}$$

Here $\langle \mathcal{K}^{\varepsilon}(\mathbf{u}_{\varepsilon}(t),\dot{\mathbf{u}}_{\varepsilon}(t)),\mathbf{v}\rangle$ is the Gateaux derivative of $\mathcal{J}^{\varepsilon}$ at $(\mathbf{u}_{\varepsilon}(t),\dot{\mathbf{u}}_{\varepsilon}(t))$ in the direction $\mathbf{v}$. Since we have introduced the Gateaux differentiable functional $\mathcal{J}^{\varepsilon}$, the variational formulation of the regularized problem is now an equation and not an inequality as in (4.6) was. For more details see [DL76; MO83].

4.1.4 Analysis of the continuous variational formulation

In this section we briefly provide some results of the variational problems (4.6) and (4.8), cf. [DL76; MO83; II02; CCR09]. We assume to have $\sigma_N = F_N$ on Γ_C assigned, with $F_N \leq 0$, and $\mu_f = \mu_f(\mathbf{x},t)$. Moreover, for the sake of presentation, we consider $|\Gamma_D| = \partial\Omega$ and $\Gamma_N, \Gamma_{NR} = \emptyset$. Therefore the variational formulation of problem (4.1) becomes: find $\mathbf{u}(t) \in \mathbf{V}$, for any $t \in (0,T]$, such that

$$(\rho\,\ddot{\mathbf{u}}(t),\mathbf{v}-\dot{\mathbf{u}}(t))_{\Omega} + \mathcal{B}(\mathbf{u}(t),\mathbf{v}-\dot{\mathbf{u}}(t)) + \mathcal{J}(\mathbf{v}) - \mathcal{J}(\dot{\mathbf{u}}(t)) \geq \mathcal{F}(\mathbf{v}-\dot{\mathbf{u}}(t)) \quad \forall \mathbf{v}\in\mathbf{V} \tag{4.10}$$

where

$$\mathcal{B}(\mathbf{u},\mathbf{v}) = (\underline{\sigma}(\mathbf{u}),\underline{\varepsilon}(\mathbf{v}))_{\Omega} + \langle \eta_N[u]_N,[v]_N\rangle_{\Gamma_C},$$

$$\mathcal{J}(\mathbf{v}) = \langle -\mu_f F_N, |[\mathbf{v}]_T|\rangle_{\Gamma_C}, \tag{4.11}$$

and

$$\mathcal{F}(\mathbf{v}) = (\mathbf{f}(t),\mathbf{v})_{\Omega} + \langle F_N(t),[v]_N\rangle_{\Gamma_C}.$$

The regularized reduced variational formulation of problem (4.10) reads: find $\mathbf{u}_{\varepsilon}(t) \in \mathbf{V}$, for any $t \in (0,T]$, such that

$$(\rho\,\ddot{\mathbf{u}}_{\varepsilon}(t),\mathbf{v})_{\Omega} + \mathcal{B}(\mathbf{u}_{\varepsilon}(t),\mathbf{v}) + \langle \mathcal{K}^{\varepsilon}(\dot{\mathbf{u}}_{\varepsilon}(t)),\mathbf{v}\rangle = \mathcal{F}(\mathbf{v}) \quad \forall \mathbf{v}\in\mathbf{V} \tag{4.12}$$

where

$$\mathcal{J}^{\varepsilon}(\mathbf{v}) = \langle -\mu_f F_N, \psi_{\varepsilon}([\mathbf{v}]_T)\rangle_{\Gamma_C}, \tag{4.13}$$

$$\langle \mathcal{K}^{\varepsilon}(\mathbf{w}),\mathbf{v}\rangle = \langle -\mu_f F_N, \varphi_{\varepsilon}([\mathbf{w}]_T,[\mathbf{v}]_T)\rangle_{\Gamma_C}.$$

4.1.5 Well-posedness of the formulation

The space $\mathbf{V}$ is equipped with the norm:

$$||\mathbf{v}||^2_{\mathcal{B}} = ||D^{1/2}\underline{\varepsilon}(\mathbf{v})||^2_{0,\Omega} + ||\eta_N^{1/2}[v]_N||^2_{0,\Gamma_C}.$$

Remark 4.2. By employing Poincaré and Korn's inequalities it holds:

$$||\mathbf{v}||_{0,\Omega} \lesssim ||\nabla \mathbf{v}||_{0,\Omega} \lesssim ||D^{1/2}\underline{\varepsilon}(\mathbf{v})||_{0,\Omega} \lesssim ||\mathbf{v}||_{\mathcal{B}}. \tag{4.14}$$

As a consequence of the properties of the elasticity tensor, Cauchy-Schwarz, Poincaré's and Korn's inequalities, the bilinear form $\mathcal{B}(\cdot,\cdot)$ can be shown to have the following properties:

- continuity: $\mathcal{B}(\mathbf{u},\mathbf{v}) \lesssim ||\mathbf{u}||_{\mathcal{B}}||\mathbf{v}||_{\mathcal{B}}\ \forall \mathbf{u},\mathbf{v} \in \mathbf{V}$.
- coercivity: $\mathcal{B}(\mathbf{v},\mathbf{v}) \gtrsim ||\mathbf{v}||^2_{\mathcal{B}}\ \forall \mathbf{v} \in \mathbf{V}$.

In the following we consider the energy norm of the problem given by:

$$||\mathbf{v}||^2_{\mathcal{E}} = ||\rho^{1/2}\dot{\mathbf{v}}||_{0,\Omega} + ||\mathbf{v}||^2_{\mathcal{B}}. \tag{4.15}$$

The main approach to prove existence and uniqueness of the solution of problem (4.10) employs the following theorem from convex analysis and variational inequality, cf. [OK79; COK82; KO88].

Proposition 4.1. *Let* $\mathbf{X}$ *be a reflexive Banach space. Moreover let* $\mathcal{J}^\varepsilon : \mathbf{X} \to \mathbb{R}$ *be a convex and Gateaux-differentiable functional and let* $\mathcal{K}^\varepsilon : \mathbf{X} \to \mathbb{R}$ *be its derivative. Then it holds:*

$$\langle \mathcal{K}^\varepsilon(\mathbf{u}), \mathbf{v}-\mathbf{u}\rangle \leq \mathcal{J}^\varepsilon(\mathbf{v}) - \mathcal{J}^\varepsilon(\mathbf{u}) \quad \forall \mathbf{u},\mathbf{v} \in \mathbf{X}.$$

Remark 4.3. Proposition 4.1 holds for the choice $\mathbf{X} = \mathbf{V}$ and $\mathcal{J}^\varepsilon(\cdot)$, $\mathcal{K}^\varepsilon(\cdot)$ defined in (4.13), cf. [COK82; MO83; KO88].

There hold the following results, cf. [DL76; MO83].

Theorem 4.1 ([DL76, Theorem 5.7])**.** *Let us assume that the data posses the following regularity:* $\mathbf{f}, \dot{\mathbf{f}}, \ddot{\mathbf{f}} \in L^2(0,T;\mathbf{L}^2(\Omega))$, $F_N, \dot{F}_N, \ddot{F}_N \in L^2(0,T;L^2(\Gamma_C))$, $-\mu_f F_N \in L^\infty(\Gamma_C)$ *be given and independent of time,* $\mathbf{u}_0 \in \mathbf{H}^2(\Omega)\cap\mathbf{V}$, $[u_0]_N = 0$ *on* Γ_C, $\mathbf{u}_1 \in \mathbf{H}^1(\Omega)$, $[\mathbf{u}_1]_T = 0$ *on* Γ_C, $\langle \boldsymbol{\sigma}_{0T}, [\mathbf{v}]_T\rangle_{\Gamma_C} = 0\ \forall \mathbf{v} \in \mathbf{V}$. *In addition, let* $\Gamma_N, \Gamma_{NR} = \emptyset$. *Then, there exists one and only one solution* $\mathbf{u}$ *of problem* (4.10). *Moreover,*

$$\mathbf{u}, \dot{\mathbf{u}} \in L^\infty(0,T;\mathbf{V}) \quad \textit{and} \quad \ddot{\mathbf{u}} \in L^\infty(0,T;\mathbf{L}^2(\Omega)).$$

Remark 4.4. The following property holds for the functional $\mathcal{K}^\varepsilon$ defined in (4.13):

$$\langle \mathcal{K}^\varepsilon(\mathbf{w},\mathbf{w})\rangle = \langle -\mu_f F_N, \varphi_\varepsilon([\mathbf{w}]_T,[\mathbf{w}]_T)\rangle_{\Gamma_C} \geq 0 \quad \forall \mathbf{w} \in \mathbf{V}.$$

Indeed $-\mu_f F_N \geq 0$ and

$$\varphi_\varepsilon(\mathbf{w},\mathbf{w}) = \frac{\mathbf{w}\cdot\mathbf{w}}{|\mathbf{w}|}\begin{cases} 1 & \text{if } |\mathbf{w}| > \varepsilon, \\ \dfrac{|\mathbf{w}|}{\varepsilon} & \text{if } |\mathbf{w}| < \varepsilon, \end{cases} = \begin{cases} |\mathbf{w}| & \text{if } |\mathbf{w}| > \varepsilon, \\ \dfrac{|\mathbf{w}|^2}{\varepsilon} & \text{if } |\mathbf{w}| < \varepsilon, \end{cases} \geq 0.$$

Theorem 4.2 ([MO83, Theorem 2.3])**.** *Let* $\mathbf{u}$ *be the solution of the variational inequality* (4.10) *and let* $\mathbf{u}_\varepsilon$ *be the solution of the regularized problem* (4.12)*. Then there exists a constant* $K > 0$ *independent of* ε *and* t *such that, for every* $t \in [0, T]$*,*

$$||\mathbf{u}_\varepsilon(t) - \mathbf{u}(t)||^2_{\mathcal{E}} = ||\rho^{1/2}(\dot{\mathbf{u}}_\varepsilon(t) - \dot{\mathbf{u}}(t))||^2_{0,\Omega} + ||\mathbf{u}_\varepsilon(t) - \mathbf{u}(t)||^2_{\mathcal{B}} \leq K\varepsilon. \tag{4.16}$$

Remark 4.5. The estimate (4.16) implies that

$$\mathbf{u}_\varepsilon \to \mathbf{u} \text{ strongly in } L^\infty(0, T; \mathbf{V}),$$

$$\dot{\mathbf{u}}_\varepsilon \to \dot{\mathbf{u}} \text{ strongly in } L^\infty(0, T; \mathbf{L}^2(\Omega)),$$

cf. [MO83].

4.2 Numerical approximation

In this section we describe the numerical approximation of the variational formulation (4.8). We make use of discontinuous Galerkin methods for space discretizations coupled with the leap-frog scheme for time integration. For the sake of presentation we suppose that $\Omega \subset \mathbb{R}^2$ is a convex polygonal domain. Moreover we assume that $\Gamma_N, \Gamma_{NR} = \emptyset$. The proposed formulation and related results can be easily extended in the three-dimensional case.

4.2.1 Discontinuous Galerkin approximation

Here we introduce the DG semi-discrete formulation of problem (4.8) for the spontaneous earthquake rupture propagation on a pre-existing fault surface Γ_C embedded in an elastic polyhedral domain Ω. For the sake of presentation, the surface Γ_C separates the domain Ω into two sub-domains Ω^+ and Ω^-, that is $\Gamma_C = \partial\bar{\Omega}^+ \cap \partial\bar{\Omega}^-$. The fault Γ_C is represented by a (regular) interface composed of two matching geometrical surfaces Γ_C^+ and Γ_C^- in contact. See Figure 4.2.

We consider a shape-regular partition $\mathcal{T}_{h_\pm}$ of $\Omega^\pm$ into disjoint open triangular or quadrilateral elements $E^\pm$ such that $\Omega^\pm = \cup_{E^\pm \in \mathcal{T}_{h_\pm}} E^\pm$. For a given mesh $\mathcal{T}_{h_\pm}$, we define the mesh size of the partition as $h_\pm = \max_{E^\pm \in \mathcal{T}_{h_\pm}} h_{E^\pm}$ with $h_{E^\pm} = \text{diam}(E^\pm)$ and assign a polynomial approximation degree $N_\pm \geq 1$. We define $\mathcal{T}_h$ to be the union of the grids $\mathcal{T}_{h_\pm}$ and its mesh size is $h = \max(h_+, h_-)$. We collect all the interior (boundary, respectively) edges in the set $\mathcal{F}_h^I$ ($\mathcal{F}_h^B$, respectively) and set $\mathcal{F}_h = \mathcal{F}_h^I \cup \mathcal{F}_h^B$. In particular, $\mathcal{F}_h^B = \mathcal{F}_h^D \cup \mathcal{F}_h^C$, where $\mathcal{F}_h^b = \mathcal{F}_h^B \cap \Gamma_b$, $b = D, C$, contains respectively all Dirichlet and contact-friction boundary edges. Implicit in this definition is the fact that $\Gamma_C^\pm$ can be described by different (non matching) meshes. In Figure 4.2 we show an illustrative example.

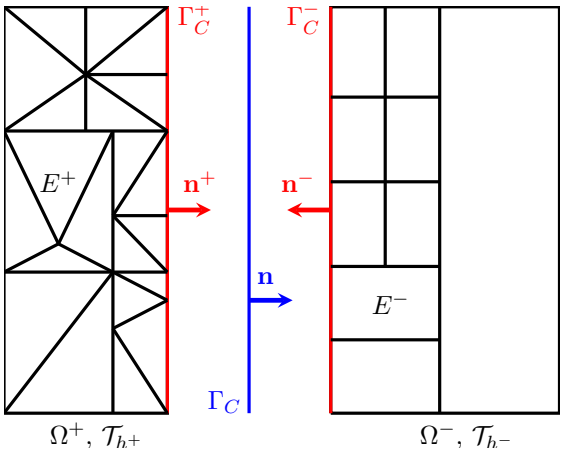

Figure 4.2: Illustrative geometry and mesh partition $\mathcal{T}_{h^\pm}$, the fault interface $\Gamma_C = \partial\bar{\Omega}^+ \cap \partial\bar{\Omega}^-$ with $\Omega = \Omega^+ \cup \Omega^-$. Each subdomain $\Omega^\pm$ is meshed independently. The normal vector to the surface Γ_C^+, pointing towards Γ_C^-, is denoted by $\mathbf{n}$.

We assume to have a bounded local variation property, cf. Chapter 1. In addition, for the sake of simplicity we also assume that, for any element $E \in \mathcal{T}_h$ and for any face $F \in \partial E$, it holds $h_E \lesssim h_F$, cf. Chapter 1. This last condition can be relaxed, cf. [CGH14; AM18; AFV20].

We introduce the space $\mathbf{V}_{h_\pm}^{N_\pm}(\Omega^\pm) = \{\mathbf{v} \in \mathbf{L}^2(\Omega^\pm), \mathbf{v} = \mathbf{0} \text{ on } \partial\Omega^\pm \cap \Gamma_D : \mathbf{v}|_{E^\pm} \in [\mathbb{P}^{N_\pm}(E^\pm)]^2 \quad \forall E^\pm \in \mathcal{T}_{h_\pm}\}$, where $\mathbb{P}^N(E)$ is the space of polynomials of total degree at most N on E. Then we define the space $\mathbf{V}_{DG}$ as $\mathbf{V}_{DG} = \mathbf{V}_{h_+}^{N^+}(\Omega^+) \otimes \mathbf{V}_{h_-}^{N^-}(\Omega^-)$. The semi-discrete DG formulation reads as follows: for any $t \in (0, T]$, find $\mathbf{u}_h = \mathbf{u}_h(t) \in \mathbf{V}_{DG}$ such that

$$(\rho\, \ddot{\mathbf{u}}_h, \mathbf{v}_h)_{\mathcal{T}_h} + \mathcal{B}_h(\mathbf{u}_h, \mathbf{v}_h) + \mathcal{P}(\mathbf{u}_h, \mathbf{v}_h) + \mathcal{K}_h^\varepsilon(\mathbf{u}_h, \dot{\mathbf{u}}_h, \mathbf{v}_h) = \mathcal{F}(\mathbf{v}_h) \quad \forall \mathbf{v}_h \in \mathbf{V}_{DG} \tag{4.17}$$

with

$$\begin{aligned}\mathcal{B}_h(\mathbf{u}, \mathbf{v}) = (\underline{\sigma}(\mathbf{u}) : \underline{\varepsilon}(\mathbf{v}))_{\mathcal{T}_h} - \langle \{\underline{\sigma}(\mathbf{u})\}, [\![\mathbf{v}]\!] \rangle_{\mathcal{F}_h^I} - \langle [\![\mathbf{u}]\!], \{\underline{\sigma}(\mathbf{v})\} \rangle_{\mathcal{F}_h^I} \\ + \langle \eta\, [\![\mathbf{u}]\!], [\![\mathbf{v}]\!] \rangle_{\mathcal{F}_h^I} + \langle \eta_N\, [u]_N, [v]_N \rangle_{\mathcal{F}_h^C}\end{aligned} \tag{4.18}$$

where we have used the short-hand notation $(\mathbf{w}, \mathbf{v})_{\mathcal{T}_h} = \sum_{E \in \mathcal{T}_h} (\mathbf{w}, \mathbf{v})_E$ and $\langle \mathbf{w}, \mathbf{v} \rangle_{\mathcal{F}_h^b} = \sum_{F \in \mathcal{F}_h^b} \langle \mathbf{w}, \mathbf{v} \rangle_F$, $b = I, C$, and

$$\mathcal{K}_h^\varepsilon(\mathbf{u}, \dot{\mathbf{u}}, \mathbf{v}) = \langle -\mu_f(\mathbf{u}) \sigma_N(\mathbf{u}), \varphi_\varepsilon([\dot{\mathbf{u}}]_T, [\mathbf{v}]_T) \rangle_{\mathcal{F}_h^C}. \tag{4.19}$$

For any two neighbouring elements $E_{i,j}$ that share a face $F \in \mathcal{F}_h$ we denote with $\mathbf{v}_{i,j}$ and $\boldsymbol{\tau}_{i,j}$ the traces of (regular enough) vector- and tensor-valued functions

$\mathbf{v}$ and $\boldsymbol{\tau}$ on $E_{i,j}$, respectively. We also denote with $\mathbf{n}_{i,j}$ the unit normal vector to F pointing outward to $E_{i,j}$. Averages $\{\cdot\}$ and jumps $[\![\cdot]\!]$ operators (see [Arn+01]) are defined as in (1.13).

On each face $F \in \mathcal{F}_h$ shared by two elements E_i and E_j the penalty parameter η is defined as

$$\eta = \alpha\{\lambda + 2\mu\}_A \frac{\mathtt{N}^2}{\mathtt{h}}, \tag{4.20}$$

where $\{q\}_A = 2q^+q^-/(q^+ + q^-)$ is the harmonic average of the quantity q across F, α is a (large enough) positive constant to be properly chosen, and $\mathtt{N}$ and $\mathtt{h}$ are defined on each face $F \in \mathcal{F}_h$ as $\mathtt{N} = \max\{N_i, N_j\}$ and $\mathtt{h} = \min\{h_i, h_j\}$.

4.2.2 Algebraic formulation

In this section we introduce the algebraic formulation of problem (4.17). Let $\{\boldsymbol{\Phi}_i\}_{i=1}^{N_{dof}} = \{\boldsymbol{\Phi}_i^1, \boldsymbol{\Phi}_i^2\}_{i=1}^{N_{dof}}$ be a set of basis functions for the finite element space $\mathbf{V}_{DG}$, where N_{dof} is the number of degrees of freedom for each component of the problem and $\boldsymbol{\Phi}^1 = (\Phi_i, 0)^T$ and $\boldsymbol{\Phi}^2 = (0, \Phi_i)^T$ for $i = 1, \ldots, N_{dof}$. We write the function $\mathbf{u} \in \mathbf{V}_{DG}$ as a linear combination of the basis functions, i.e.,

$$\mathbf{u}(\mathbf{x}, t) = \sum_{j=1}^{N_{dof}} \boldsymbol{\Phi}_j^1(\mathbf{x}) U_j^1(t) + \boldsymbol{\Phi}_j^2(\mathbf{x}) U_j^2(t),$$

with $U_j^1, U_j^2 \in \mathbb{R}$, $j = 1, \ldots, N_{dof}$. Then we write equation (4.17) for any test function $\{\boldsymbol{\Phi}_i\}_{i=1}^{N_{dof}}$ and we obtain the following non-linear system of ordinary differential equations

$$\mathsf{M}\ddot{\mathbf{U}} + \mathbf{K}(\mathbf{U}, \dot{\mathbf{U}}) + \mathsf{A}\mathbf{U} = \mathbf{F}, \tag{4.21}$$

where $\mathbf{U}$, $\dot{\mathbf{U}}$ and $\ddot{\mathbf{U}}$ are the vectors of expansion coefficients of the displacement, velocity and acceleration, respectively. The mass and stiffness matrices are defined as

$$\mathsf{M}_{ij} = (\rho\boldsymbol{\Phi}_j, \boldsymbol{\Phi}_i)_{\mathcal{T}_h} \quad i, j = 1, \ldots, N_{dof},$$

$$\mathsf{A}_{ij} = \mathcal{B}_h(\boldsymbol{\Phi}_j, \boldsymbol{\Phi}_i) + \mathcal{P}(\boldsymbol{\Phi}_j, \boldsymbol{\Phi}_i) \quad i, j = 1, \ldots, N_{dof},$$

respectively, and $\mathbf{F}$ is the vector of the external load defined as

$$\mathbf{F}_i = (\mathbf{f}, \boldsymbol{\Phi}_i)_{\mathcal{T}_h} + (\mathbf{t}, \boldsymbol{\Phi}_i)_{\mathcal{F}_h^N} + (\mathbf{t}^*, \boldsymbol{\Phi}_i)_{\mathcal{F}_h^{NR}} \quad i = 1, \ldots, N_{dof}.$$

In (4.21) $\mathbf{K}$ is the vector of the friction forces on Γ_C defined as

$$\mathbf{K}_i(\mathbf{U}, \dot{\mathbf{U}}) = \mathcal{K}_h^{\varepsilon}(\mathbf{u}, \dot{\mathbf{u}}, \boldsymbol{\Phi}_i) \quad i = 1, \ldots, N_{dof}.$$

4.2.3 Time integration scheme

In this section we briefly describe the time integration scheme adopted to find the numerical solution of the semi-discrete problem (4.21). To approximate in time the non-linear equation, we proceed as proposed in [MO83]. We first subdivide the time interval $(0, T]$ into N_T subintervals of length $\Delta t = T/N_T$. Then we set $t_n = n\Delta t$, $n = 0, \dots, N_T$ and denote by $\mathbf{U}^n/\dot{\mathbf{U}}^n/\ddot{\mathbf{U}}^n$ the numerical approximation of $\mathbf{U}(t_n)/\dot{\mathbf{U}}(t_n)/\ddot{\mathbf{U}}(t_n)$, respectively, for any $n = 0, \dots, N_T$. We consider the Leap-Frog scheme:

$$\ddot{\mathbf{U}}^n = -\ddot{\mathbf{U}}^{n-1} + \frac{2}{\Delta t}(\dot{\mathbf{U}}^n - \dot{\mathbf{U}}^{n-1}),$$

$$\mathbf{U}^n = \mathbf{U}^{n-1} + \Delta t\dot{\mathbf{U}}^{n-1} + \frac{1}{2}\Delta t^2\ddot{\mathbf{U}}^{n-1}.$$

Applying the Leap-Frog method, to solve the system (4.21) where the unknown is the velocity, we obtain

$$\frac{2}{\Delta t}\mathsf{M}\dot{\mathbf{U}}^n + \mathbf{K}(\mathbf{U}^n, \dot{\mathbf{U}}^n) = \mathbf{F}_*^n \tag{4.22}$$

with

$$\mathbf{F}_*^n = \mathbf{F}^n + \mathsf{M}\left(\ddot{\mathbf{U}}^{n-1} + \frac{2}{\Delta t}\dot{\mathbf{U}}^{n-1}\right) - \mathsf{A}\left(\mathbf{U}^{n-1} + \Delta t\dot{\mathbf{U}}^{n-1} + \frac{1}{2}\Delta t^2\ddot{\mathbf{U}}^{n-1}\right).$$

Equation (4.22) is, of course, nonlinear since $\mathbf{K}(\mathbf{U}^n, \dot{\mathbf{U}}^n)$ depends on the solution $\mathbf{U}^n, \dot{\mathbf{U}}^n$.

At each time-step we solve the non-linear equation (4.22) by employing a semi-implicit method. When $t = 0$ we have $\mathbf{U}^0 = \mathbf{U}(0)$, $\dot{\mathbf{U}}^0 = \dot{\mathbf{U}}(0)$, suitable approximations in $\mathbf{V}_{DG}$ of the initial data $\mathbf{u}_0$ and $\mathbf{u}_1$. We find the initial acceleration by solving

$$\mathsf{M}\ddot{\mathbf{U}}^0 + \mathbf{K}(\mathbf{U}^0, \dot{\mathbf{U}}^0) + \mathsf{A}\mathbf{U}^0 = \mathbf{F}^0.$$

Then for $t > 0$, we solve for each step in time the non linear equation given by (4.22). To solve the non-linearity of the algebraic system, we employ a fixed-point iteration and we stop it by employing suitable stopping criteria (e.g. tolerance *tol* on residual and maximum number of iterations N_{max}). See Algorithm 1.

We recall that the leap-frog method is explicit and is stable if the Courant-Friedrichs-Lewy (CFL) condition is satisfied, i.e. $\Delta t \leq C_{CFL}(p)h/c_P$, where $C_{CFL} \in (0, 1)$ is a constant depending on the parameters involved in the model and the polynomial degree and h is the mesh size, see e.g., [AM18].

4.3 Analysis of the semi-discrete formulation

In this section we address the analysis of the semi-discrete formulation following [Ant+18a; Ant+16]. First we introduce the DG semi-discrete formulation of the

Algorithm 1 Pseudocode to solve the non-linear system advancing on time steps iteration

for all t_n, $n = 1, \dots, N_T$ **do**
  Compute $\mathbf{U}^n$ with Leap-Frog's formulas ▷ $n-th$ step in time
  $i = 0$
  $\dot{\mathbf{U}}^n_{(0)} = \dot{\mathbf{U}}^{n-1}$ ▷ Initialization
  while $||\mathbf{K}(\mathbf{U}^n, \dot{\mathbf{U}}^n_{(i+1)}) - \mathbf{K}(\mathbf{U}^n, \dot{\mathbf{U}}^n_{(i)})|| < tol$ & $i < N_{max}$ **do**
    Find $\dot{\mathbf{U}}^n_{(i+1)}$, solution of ▷ $i-th$ iteration for non-linearity

$$\frac{2}{\Delta t}\mathsf{M}\dot{\mathbf{U}}^n_{(i+1)} + \mathbf{K}(\mathbf{U}^n, \dot{\mathbf{U}}^n_{(i)}) = \mathbf{F}^n_*$$

    $i = i + 1$
  end while
  Set $\dot{\mathbf{U}}^n = \dot{\mathbf{U}}^n_{(i)}$
  Compute $\ddot{\mathbf{U}}^n$ with Leap-Frog's formulas ▷ $n-th$ step in time
end for

regularized variational formulation of the simplified problem (4.12) by employing the space discretization technique presented in Section 4.2. Then the DG formulation of problem (4.12) reads: for any $t \in (0, T]$ find $\mathbf{u}_h = \mathbf{u}_h(t) \in \mathbf{V}_{DG}$ such that

$$(\rho\, \ddot{\mathbf{u}}_h, \mathbf{v}_h)_{\mathcal{T}_h} + \mathcal{B}_h(\mathbf{u}_h, \mathbf{v}_h) + \mathcal{K}^\varepsilon_h(\dot{\mathbf{u}}_h, \mathbf{v}_h) = \mathcal{F}(\mathbf{v}_h) \quad \forall \mathbf{v}_h \in \mathbf{V}_{DG} \tag{4.23}$$

with

$$\mathcal{K}^\varepsilon_h(\dot{\mathbf{u}}, \mathbf{v}) = \langle -\mu_f F_N, \varphi_\varepsilon([\dot{\mathbf{u}}]_T, [\mathbf{v}]_T)\rangle_{\mathcal{F}^C_h}, \tag{4.24}$$

being the Gateaux-derivative of

$$\mathcal{J}^\varepsilon_h(\mathbf{v}) = \langle -\mu_f F_N, \psi_\varepsilon([\mathbf{v}]_T)\rangle_{\mathcal{F}^C_h}. \tag{4.25}$$

We introduce the following (discretization parameters dependent) norms

$$||\mathbf{v}||^2_{DG} = ||D^{1/2}\varepsilon(\mathbf{v})||^2_{0,\mathcal{T}_h} + ||\eta^{1/2}[\![\mathbf{v}]\!]||^2_{0,\mathcal{F}^I_h} + ||\eta_N^{1/2}[v]_N||^2_{0,\mathcal{F}^C_h} \quad \forall \mathbf{v} \in \mathbf{H}^1(\mathcal{T}_h) \cap \mathbf{V}_{DG},$$

$$|||\mathbf{v}|||^2_{DG} = ||\mathbf{v}||^2_{DG} + ||\eta^{-1/2}\{D\varepsilon(\mathbf{v})\}||^2_{0,\mathcal{F}^I_h} \quad \forall \mathbf{v} \in \mathbf{H}^2(\mathcal{T}_h).$$

By employing the trace-inverse inequality of Lemma 1.1, it can be shown that the norms $||\cdot||_{DG}$ and $|||\cdot|||_{DG}$ are equivalent when restricted to the space $\mathbf{V}_{DG}$.

The following results ensure the stability and a-priori error estimate of the DG formulation (4.23).

Lemma 4.1. *The bilinear form* $\mathcal{B}_h(\cdot,\cdot) : \mathbf{V}_{DG} \times \mathbf{V}_{DG} \to \mathbb{R}$ *defined as in* (4.18) *satisfies*

$$|\mathcal{B}_h(\mathbf{w}, \mathbf{v})| \lesssim ||\mathbf{w}||_{DG}||\mathbf{v}||_{DG}, \quad \mathcal{B}_h(\mathbf{v}, \mathbf{v}) \gtrsim ||\mathbf{v}||^2_{DG} \quad \forall \mathbf{v}, \mathbf{w} \in \mathbf{V}_{DG},$$

where the second estimate holds provided that the parameter α appearing in the definition of the stabilization function cf. (4.20) *is chosen sufficiently large. Moreover,*

$$|\mathcal{B}_h(\mathbf{w},\mathbf{v})| \lesssim |||\mathbf{w}|||_{DG}||\mathbf{v}||_{DG} \quad \forall \mathbf{w} \in \mathbf{H}^2(\mathcal{T}_h)\, \forall \mathbf{v} \in \mathbf{V}_{DG}.$$

Proof. Taking into account of the equivalence between the $|||\cdot|||_{DG}$ and $||\cdot||_{DG}$-norms, the continuity properties follow from the definition of the $|||\cdot|||_{DG}$-norm by applying the Cauchy-Schwarz and trace inequality. Finally, it is possible to prove the coercivity estimate with the definition of the $||\cdot||_{DG}$-norm and a results analogous to (1.21) in Lemma 1.4.

Proposition 4.2. *Let $\mathcal{J}_h^\varepsilon : \mathbf{V}_{DG} \to \mathbb{R}$ be defined as in* (4.25)*. It follows that $\mathcal{J}_h^\varepsilon$ is a convex and Gateaux-differentiable functional and $\mathcal{K}_h^\varepsilon : \mathbf{V}_{DG} \to \mathbb{R}$ is its derivative* (4.24)*. Moreover it holds:*

$$\mathcal{K}_h^\varepsilon(\mathbf{u}, \mathbf{v}-\mathbf{u}) \leq \mathcal{J}_h^\varepsilon(\mathbf{v}) - \mathcal{J}_h^\varepsilon(\mathbf{u}) \quad \forall \mathbf{u}, \mathbf{v} \in \mathbf{V}_{DG}.$$

Proof. (Sketch.) Following similar arguments presented in [COK82; MO83; KO88], we proceed as follows. By straightforward calculations we verify that $\psi_\varepsilon(\mathbf{v})$ in (4.7) is continuous, convex and $\psi_\varepsilon(\mathbf{u}+\vartheta\mathbf{v}) \in C^1[0,1]$ for any $\mathbf{u}, \mathbf{v} \in \mathbf{V}_{DG}$. Then, it follows that $\mathcal{J}_h^\varepsilon$ is a convex and Gateaux-differentiable functional, cf. [KO88, Theorem 3.6]. Finally, we apply Proposition 4.1 to get the final bound result. □

Remark 4.6. The following property holds for the functional $\mathcal{K}_h^\varepsilon$ defined in (4.24):

$$\mathcal{K}_h^\varepsilon(\mathbf{w},\mathbf{w}) = \langle -\mu_f F_N, \varphi_\varepsilon([\mathbf{w}]_T, [\mathbf{w}]_T)\rangle_{\Gamma_C} \geq 0 \quad \forall \mathbf{w} \in \mathbf{V}_{DG}.$$

This results can be proved with same arguments introduced in Remark 4.4.

4.3.1 Stability

In this section we present a stability analysis of the semi-discrete formulation (4.23) in the following (mesh dependent) energy norm

$$||\mathbf{u}_h(t)||_{\mathcal{E}}^2 = ||\rho^{1/2}\dot{\mathbf{u}}_h(t)||_{0,\mathcal{T}_h}^2 + ||\mathbf{u}_h(t)||_{DG}^2 \quad t \in (0,T]. \tag{4.26}$$

For $t = 0$ we have

$$||\mathbf{u}_h(0)||_{\mathcal{E}}^2 = ||\rho^{1/2}\mathbf{v}_{0,h}||_{0,\mathcal{T}_h}^2 + ||\mathbf{u}_{0,h}||_{DG}^2,$$

where $\mathbf{u}_{0,h}, \mathbf{v}_{0,h} \in \mathbf{V}_{DG}$ are suitable approximations of the initial data $\mathbf{u}_0$ and $\mathbf{u}_1$, respectively. To prove the following theorem we consider the outline of the results given in [Ant+18a; Ant+16] and Remark 4.6.

Theorem 4.3 (Stability)**.** *For any time $t \in (0,T]$ and for a sufficiently large penalty parameter α in* (4.20)*, let $\mathbf{u}_h(t) \in \mathbf{V}_{DG}$ be the solution of problem* (4.23)*. If $\mathbf{f} \in L^2(0,T;\mathbf{L}^2(\Omega))$ and $F_N \in L^2(0,T;\mathbf{L}^2(\Gamma_C))$, then*

$$||\mathbf{u}_h(t)||_{\mathcal{E}} \lesssim ||\mathbf{u}_h(0)||_{\mathcal{E}} + \int_0^t (||\mathbf{f}(\tau)||_{0,\Omega} + ||F_N(\tau)||_{0,\Gamma_C})\, d\tau, \quad 0 < t \leq T.$$

Proof. By taking $\mathbf{v} = \dot{\mathbf{u}}_h$ in (4.23), we obtain

$$\begin{aligned}(\rho\ddot{\mathbf{u}}_h, \dot{\mathbf{u}}_h)_{\mathcal{T}_h} + (\underline{\sigma}(\mathbf{u}_h), \underline{\varepsilon}(\dot{\mathbf{u}}_h))_{\mathcal{T}_h} - \langle\{\underline{\sigma}(\mathbf{u}_h)\}, [\![\dot{\mathbf{u}}_h]\!]\rangle_{\mathcal{F}_h^I} - \langle[\![\mathbf{u}_h]\!], \{\underline{\sigma}(\dot{\mathbf{u}}_h)\}\rangle_{\mathcal{F}_h^I} \\ + \langle\eta\,[\![\mathbf{u}_h]\!], [\![\dot{\mathbf{u}}_h]\!]\rangle_{\mathcal{F}_h^I} + \langle\eta_N\,[u_h]_N, [\dot{u}_h]_N\rangle_{\mathcal{F}_h^C} + \mathcal{K}_h^{\varepsilon}(\dot{\mathbf{u}}_h, \dot{\mathbf{u}}_h) \\ = (\mathbf{f}, \dot{\mathbf{u}}_h)_{\mathcal{T}_h} + \langle F_N, [\dot{u}_h]_N\rangle_{\mathcal{F}_h^C},\end{aligned}$$

that is

$$\frac{1}{2}\frac{d}{dt}\left(||\mathbf{u}_h||_{\mathcal{E}}^2 - 2\langle\{\underline{\sigma}(\mathbf{u}_h)\}, [\![\mathbf{u}_h]\!]\rangle_{\mathcal{F}_h^I}\right) + \mathcal{K}_h^{\varepsilon}(\dot{\mathbf{u}}_h, \dot{\mathbf{u}}_h) = (\mathbf{f}, \dot{\mathbf{u}}_h)_{\mathcal{T}_h} + \langle F_N, [\dot{u}_h]_N\rangle_{\mathcal{F}_h^C}, \tag{4.27}$$

where we have used the definition of the energy norm (4.26). Moreover we consider that from Remark 4.6, by taking $\mathbf{w} = \mathbf{u}_h(\tau)$ for all $\tau \in [0,t]$, $t < T$, it holds

$$\int_0^t \mathcal{K}_h^{\varepsilon}(\dot{\mathbf{u}}_h(\tau), \dot{\mathbf{u}}_h(\tau))\, d\tau \geq 0. \tag{4.28}$$

Integrating the equation (4.27) over the time interval $(0,t)$ and considering (4.28), we have

$$\begin{aligned}||\mathbf{u}_h(t)||_{\mathcal{E}}^2 - 2\langle\{\underline{\sigma}(\mathbf{u}_h(t))\}, [\![\mathbf{u}_h(t)]\!]\rangle_{\mathcal{F}_h^I} \\ \leq ||\mathbf{u}_h(0)||_{\mathcal{E}}^2 - 2\langle\{\underline{\sigma}(\mathbf{u}_h(0))\}, [\![\mathbf{u}_h(0)]\!]\rangle_{\mathcal{F}_h^I} \\ + 2\int_0^t (\mathbf{f}(\tau), \dot{\mathbf{u}}_h(\tau))_{\mathcal{T}_h}\, d\tau + 2\int_0^t \langle F_N(\tau), [\dot{u}_h]_N(\tau)\rangle_{\mathcal{F}_h^C}\, d\tau.\end{aligned}$$

From Lemma 1.4 we get

$$\begin{aligned}||\mathbf{u}_h||_{\mathcal{E}}^2 - 2\langle\{\sigma(\mathbf{u}_h)\}, [\![\mathbf{u}_h]\!]\rangle_{\mathcal{F}_h^I} \gtrsim ||\mathbf{u}_h||_{\mathcal{E}}^2, \\ ||\mathbf{u}_h(0)||_{\mathcal{E}}^2 - 2\langle\{\sigma(\mathbf{u}_h(0))\}, [\![\mathbf{u}_h(0)]\!]\rangle_{\mathcal{F}_h^I} \lesssim ||\mathbf{u}_h(0)||_{\mathcal{E}}^2,\end{aligned}$$

where the first bound holds provided that the stability parameter α appearing in the definition of the penalization function (4.20) is chosen large enough. Then

$$||\mathbf{u}_h(t)||_{\mathcal{E}}^2 \lesssim ||\mathbf{u}_h(0)||_{\mathcal{E}}^2 + 2\int_0^t (\mathbf{f}(\tau), \dot{\mathbf{u}}_h(\tau))_{\mathcal{T}_h}\, d\tau + 2\int_0^t \langle F_N(\tau), [\dot{u}_h]_N(\tau)\rangle_{\mathcal{F}_h^C}\, d\tau.$$

The Cauchy-Schwarz inequality leads to

$$2\int_0^t (\mathbf{f}(\tau), \dot{\mathbf{u}}_h(\tau))_{\mathcal{T}_h}\, d\tau \lesssim \int_0^t ||\mathbf{f}(\tau)||_{0,\mathcal{T}_h} ||\rho^{1/2}\dot{\mathbf{u}}_h(\tau)||_{0,\mathcal{T}_h}\, d\tau \leq \int_0^t ||\mathbf{f}(\tau)||_{0,\Omega} ||\mathbf{u}_h||_{\mathcal{E}}\, d\tau.$$

The Cauchy-Schwarz and trace inequalities leads to

$$2\int_0^t \langle F_N(\tau), [\dot{u}_h]_N(\tau)\rangle_{\mathcal{F}_h^C}\, d\tau \lesssim \int_0^t ||F_N(\tau)||_{0,\mathcal{F}_h^C} ||\rho^{1/2}\ddot{\mathbf{u}}_h(\tau)||_{0,\mathcal{F}_h^C}\, d\tau$$
$$\lesssim \int_0^t ||F_N(\tau)||_{0,\Gamma_C} ||\rho^{1/2}\ddot{\mathbf{u}}_h(\tau)||_{0,\mathcal{T}_h}\, d\tau \lesssim \int_0^t ||F_N(\tau)||_{0,\Gamma_C} ||\mathbf{u}_h||_{\mathcal{E}}\, d\tau$$

The thesis follows based on employing the Gronwall's lemma.

4.3.2 Semi-discrete error estimates

In this section we derive a priori error estimates for the semi-discrete problem (4.23) in the energy norm (4.26) following the outline given in [Ant+18a; Ant+16]. We start by recalling some useful interpolation estimates, cf. [BS87a].

Lemma 4.2. *For any function* $\mathbf{v}$ *such that* $\mathbf{v}|_E \in \mathbf{H}^{s_E}(E), s_E \geq 0, E \in \mathcal{T}_h$, *there exists* $\mathbf{v}_I \in \mathbf{V}_{DG}$ *such that*

$$||\mathbf{v}-\mathbf{v}_I||_{r,E}^2 \lesssim \frac{{h_E}^{2m_E-2r}}{N_E^{2s_E-2r}} ||\mathbf{v}||_{s_E,E}^2, \quad \forall r, 0 \leq r \leq s_E,$$
$$||\mathbf{v}-\mathbf{v}_I||_{0,\partial E}^2 \lesssim \frac{{h_E}^{2m_E-1}}{N_E^{2s_E-1}} ||\mathbf{v}||_{s_E,E}^2,$$
$$||\nabla(\mathbf{v}-\mathbf{v}_I)||_{0,\partial E}^2 \lesssim \frac{{h_E}^{2m_E-3}}{N_E^{2s_E-3}} ||\mathbf{v}||_{s_E,E}^2,$$

where $m_E = \min(s_E, N_E+1)$.
Therefore, by summing over all the elements $E \in \mathcal{T}_h$ *and* $F \in \mathcal{F}_h$, *it follows that for any function* $\mathbf{v}$ *such that* $\mathbf{v}|_{\mathcal{T}_{h_\pm}} \in \mathbf{H}^{s_\pm}(\mathcal{T}_{h_\pm}), s_\pm \geq 0$, *there exists* $\mathbf{v}_I \in \mathbf{V}_{DG}$ *such that*

$$||\mathbf{v}-\mathbf{v}_I||_{r,\mathcal{T}_h}^2 \lesssim \sum_{\mathcal{T}_{h_\pm}} \frac{h_\pm^{2m_\pm-2r}}{N_\pm^{2s_\pm-2r}} ||\mathbf{v}||_{s_\pm,\mathcal{T}_{h_\pm}}^2, \quad \forall r, 0 \leq r \leq s_\pm,$$
$$||\mathbf{v}-\mathbf{v}_I||_{0,\mathcal{F}_h^I}^2 \lesssim \sum_{\mathcal{T}_{h_\pm}} \frac{h_\pm^{2m_\pm-1}}{N_\pm^{2s_\pm-1}} ||\mathbf{v}||_{s_\pm,\mathcal{T}_{h_\pm}}^2,$$
$$||\mathbf{v}-\mathbf{v}_I||_{0,\mathcal{F}_h^C}^2 \lesssim \sum_{\substack{E^\pm \in \mathcal{T}_{h_\pm},\\ \partial E^\pm \cap \mathcal{F}_h^C \neq \emptyset}} \frac{h_\pm^{2m_\pm-1}}{N_\pm^{2s_\pm-1}} ||\mathbf{v}||_{s_\pm,\mathcal{T}_{h_\pm}}^2 \lesssim \sum_{\mathcal{T}_{h_\pm}} \frac{h_\pm^{2m_\pm-1}}{N_\pm^{2s_\pm-1}} ||\mathbf{v}||_{s_\pm,\mathcal{T}_{h_\pm}}^2,$$
$$||\nabla(\mathbf{v}-\mathbf{v}_I)||_{0,\mathcal{F}_h^I}^2 \lesssim \sum_{\mathcal{T}_{h_\pm}} \frac{h_\pm^{2m_\pm-3}}{N_\pm^{2s_\pm-3}} ||\mathbf{v}||_{s_\pm,\mathcal{T}_{h_\pm}}^2,$$

where $m_\pm = \min(s_\pm, N_\pm+1)$.

The previous estimates are employed to prove the following interpolation bounds.

Lemma 4.3. *For any function* $\mathbf{v}$ *such that* $\mathbf{v}|_{\mathcal{T}_{h_\pm}} \in \mathbf{H}^{s_\pm}(\mathcal{T}_{h_\pm}), s_\pm \geq 2$*, there exists* $\mathbf{v}_I \in \mathbf{V}_{DG}$ *such that*

$$|||\mathbf{v} - \mathbf{v}_I|||_{DG}^2 \lesssim \sum_{\mathcal{T}_{h_\pm}} \frac{h_\pm^{2m_\pm - 2}}{N_\pm^{2s_\pm - 3}} ||\mathbf{v}||_{s_\pm, \mathcal{T}_{h_\pm}}^2 \tag{4.29}$$

where $m_\pm = \min(s_\pm, N_\pm + 1)$*. Moreover, if in addition* $\mathbf{v}|_{\mathcal{T}_{h_\pm}}, \dot{\mathbf{v}}|_{\mathcal{T}_{h_\pm}} \in \mathbf{H}^{s_\pm}(\mathcal{T}_{h_\pm}), s_\pm \geq 2$*, then*

$$||\mathbf{v} - \mathbf{v}_I||_{\mathcal{E}}^2 \lesssim \sum_{\mathcal{T}_{h_\pm}} \frac{h_\pm^{2m_\pm - 2}}{N_\pm^{2s_\pm - 3}} \left(||\dot{\mathbf{v}}||_{s_\pm, \mathcal{T}_{h_\pm}}^2 + ||\mathbf{v}||_{s_\pm, \mathcal{T}_{h_\pm}}^2 \right). \tag{4.30}$$

Proof. We first show (4.29). With this aim, we use Lemma 4.2 to bound each contribution appearing in the definition of the DG norm $|||\cdot|||_{DG}^2$:

$$\begin{aligned}
||D^{1/2}\varepsilon(\mathbf{v} - \mathbf{v}_I)||_{0,\mathcal{T}_h}^2 &\lesssim \sum_{\mathcal{T}_{h_\pm}} \frac{h_\pm^{2m_\pm - 2}}{N_\pm^{2s_\pm - 2}} ||\mathbf{v}||_{s_\pm, \mathcal{T}_{h_\pm}}^2, \\
||\eta^{1/2}[\![\mathbf{v} - \mathbf{v}_I]\!]||_{0,\mathcal{F}_h^I}^2 &\lesssim \sum_{\mathcal{T}_{h_\pm}} \frac{h_\pm^{2m_\pm - 2}}{N_\pm^{2s_\pm - 3}} ||\mathbf{v}||_{s_\pm, \mathcal{T}_{h_\pm}}^2, \\
||\eta_N^{1/2}[\mathbf{v} - \mathbf{v}_I]_N||_{0,\mathcal{F}_h^C}^2 &\lesssim \sum_{\mathcal{T}_{h_\pm}} \frac{h_\pm^{2m_\pm - 1}}{N_\pm^{2s_\pm - 1}} ||\mathbf{v}||_{s_\pm, \mathcal{T}_{h_\pm}}^2, \\
||\eta^{-1/2}\{D\varepsilon(\mathbf{v} - \mathbf{v}_I)\}||_{0,\mathcal{F}_h^I}^2 &\lesssim \sum_{\mathcal{T}_{h_\pm}} \frac{h_\pm^{2m_\pm - 2}}{N_\pm^{2s_\pm - 1}} ||\mathbf{v}||_{s_\pm, \mathcal{T}_{h_\pm}}^2.
\end{aligned}$$

This yields

$$\begin{aligned}
|||\mathbf{v} - \mathbf{v}_I|||_{DG}^2 &\lesssim \sum_{\mathcal{T}_{h_\pm}} \frac{h_\pm^{2m_\pm - 2}}{N_\pm^{2s_\pm - 3}} \left(\frac{1}{N_\pm} + 1 + \frac{1}{N_\pm^2} + \frac{h_\pm}{N_\pm} \right) ||\mathbf{v}||_{s_\pm, \mathcal{T}_{h_\pm}}^2 \\
&\lesssim \sum_{\mathcal{T}_{h_\pm}} \frac{h_\pm^{2m_\pm - 2}}{N_\pm^{2s_\pm - 3}} ||\mathbf{v}||_{s_\pm, \mathcal{T}_{h_\pm}}^2.
\end{aligned}$$

Next we show (4.30). We recall the definition of energy norm and employ again the interpolation estimates of Lemma 4.2 to get

$$\begin{aligned}
||\rho^{1/2}(\dot{\mathbf{v}} - \dot{\mathbf{v}}_I)||_{0,\mathcal{T}_h}^2 &\lesssim \sum_{\mathcal{T}_{h_\pm}} \frac{h_\pm^{2m_\pm}}{N_\pm^{2s_\pm}} ||\dot{\mathbf{v}}||_{s_\pm, \mathcal{T}_{h_\pm}}^2, \\
||\mathbf{v} - \mathbf{v}_I||_{DG}^2 &\lesssim \sum_{\mathcal{T}_{h_\pm}} \frac{h_\pm^{2m_\pm - 2}}{N_\pm^{2s_\pm - 3}} ||\mathbf{v}||_{s_\pm, \mathcal{T}_{h_\pm}}^2.
\end{aligned}$$

Finally, summing up the above contributions we obtain

$$||\mathbf{v}-\mathbf{v}_I||^2_{\mathcal{E}} \lesssim \sum_{\mathcal{T}_{h_\pm}} \frac{h_\pm^{2m_\pm-2}}{N_\pm^{2s_\pm-3}} \left(\frac{h_\pm^2}{N_\pm^3} ||\dot{\mathbf{v}}||^2_{s_\pm,\mathcal{T}_{h_\pm}} + ||\mathbf{v}||^2_{s_\pm,\mathcal{T}_{h_\pm}} \right)$$
$$\lesssim \sum_{\mathcal{T}_{h_\pm}} \frac{h_\pm^{2m_\pm-2}}{N_\pm^{2s_\pm-3}} \left(||\dot{\mathbf{v}}||^2_{s_\pm,\mathcal{T}_{h_\pm}} + ||\mathbf{v}||^2_{s_\pm,\mathcal{T}_{h_\pm}} \right).$$

□

Theorem 4.4 (A-priori error estimate in the energy norm)**.** *Assume that, for any time $t \in [0,T]$, the exact solution $\mathbf{u}(t) = \mathbf{u}_\varepsilon(t)$ of problem (4.12) together with its two first temporal derivatives satisfy $\mathbf{u}(t)|_{\mathcal{T}_{h_\pm}}, \dot{\mathbf{u}}(t)|_{\mathcal{T}_{h_\pm}}, \ddot{\mathbf{u}}(t)|_{\mathcal{T}_{h_\pm}} \in \mathbf{H}^{s_\pm}(\mathcal{T}_{h_\pm})$, $s_\pm \geq 2$. Let $\mathbf{u}_h$ be the corresponding solution of the semidiscrete DG formulation given in (4.23), with a sufficiently large penalty parameter α in the definition of the stabilization function (4.20). Then,*

$$\sup_{t\in[0,T]} ||\mathbf{e}_h(t)||^2_{\mathcal{E}} \lesssim \sup_{t\in[0,T]} \left\{ \sum_{\mathcal{T}_{h_\pm}} \frac{h_\pm^{2m_\pm-2}}{N_\pm^{2s_\pm-3}} ||\mathbf{u}||^2_{s_\pm,\mathcal{T}_{h_\pm}} \right\} + \int_0^T \sum_{\mathcal{T}_{h_\pm}} \frac{h_\pm^{m_\pm-1/2}}{N_\pm^{s_\pm-1/2}} ||\dot{\mathbf{u}}||_{s_\pm,\mathcal{T}_{h_\pm}} dt$$
$$+ \int_0^T \sum_{\mathcal{T}_{h_\pm}} \frac{h_\pm^{2m_\pm-2}}{N_\pm^{2s_\pm-3}} \left(||\ddot{\mathbf{u}}||^2_{s_\pm,\mathcal{T}_{h_\pm}} + ||\dot{\mathbf{u}}||^2_{s_\pm,\mathcal{T}_{h_\pm}} \right) dt$$

Proof. The discrete formulation (4.23) is strongly consistent, that is the exact solution $\mathbf{u}$ of (4.12) satisfies equation (4.23) for any time $t \in (0,T]$

$$(\rho\,\ddot{\mathbf{u}},\mathbf{v})_{\mathcal{T}_h} + \mathcal{B}_h(\mathbf{u},\mathbf{v}) + \mathcal{K}_h^\varepsilon(\dot{\mathbf{u}},\mathbf{v}) = \mathcal{F}_h(\mathbf{v}) \quad \forall \mathbf{v} \in \mathbf{V}_{DG}$$

Subtracting (4.23) from the above identity and setting $\mathbf{e} = \mathbf{u} - \mathbf{u}_h$, we obtain the error equation

$$(\rho\,\ddot{\mathbf{e}},\mathbf{v})_{\mathcal{T}_h} + \mathcal{B}_h(\mathbf{e},\mathbf{v}) + \mathcal{K}_h^\varepsilon(\dot{\mathbf{u}},\mathbf{v}) - \mathcal{K}_h^\varepsilon(\dot{\mathbf{u}}_h,\mathbf{v}) = \mathbf{0} \quad \forall \mathbf{v} \in \mathbf{V}_{DG}$$

We next decompose the error as $\mathbf{e} = \mathbf{e}_I - \mathbf{e}_h$, with $\mathbf{e}_I = \mathbf{u} - \mathbf{u}_I$ and $\mathbf{e}_h = \mathbf{u}_h - \mathbf{u}_I$, $\mathbf{u}_I \in \mathbf{V}_{DG}$ being the interpolant defined as in Lemma 4.2, and rewrite the above identity as

$$(\rho\,\ddot{\mathbf{e}}_h,\mathbf{v})_{\mathcal{T}_h} + \mathcal{B}_h(\mathbf{e}_h,\mathbf{v}) = (\rho\,\ddot{\mathbf{e}}_I,\mathbf{v})_{\mathcal{T}_h} + \mathcal{B}_h(\mathbf{e}_I,\mathbf{v}) + \mathcal{K}_h^\varepsilon(\dot{\mathbf{u}},\mathbf{v}) - \mathcal{K}_h^\varepsilon(\dot{\mathbf{u}}_h,\mathbf{v}) \quad \forall \mathbf{v} \in \mathbf{V}_{DG}$$

By taking as test function $\mathbf{v} = \dot{\mathbf{e}}_h$, we get

$$(\rho\,\ddot{\mathbf{e}}_h,\dot{\mathbf{e}}_h)_{\mathcal{T}_h} + \mathcal{B}_h(\mathbf{e}_h,\dot{\mathbf{e}}_h) = (\rho\,\ddot{\mathbf{e}}_I,\dot{\mathbf{e}}_h)_{\mathcal{T}_h} + \mathcal{B}_h(\mathbf{e}_I,\dot{\mathbf{e}}_h) + \mathcal{K}_h^\varepsilon(\dot{\mathbf{u}},\dot{\mathbf{e}}_h) - \mathcal{K}_h^\varepsilon(\dot{\mathbf{u}}_h,\dot{\mathbf{e}}_h),$$

that is

$$\frac{1}{2}\frac{d}{dt}\left(||\rho^{1/2}\dot{\mathbf{e}}_h||^2_{0,\mathcal{T}_h} + ||\mathbf{e}_h||^2_{DG} - 2\langle\{\underline{\sigma}(\mathbf{e}_h)\},[\![\mathbf{e}_h]\!]\rangle_{\mathcal{F}_h^I} \right)$$
$$= (\rho\,\ddot{\mathbf{e}}_I,\dot{\mathbf{e}}_h)_{\mathcal{T}_h} + \mathcal{B}_h(\mathbf{e}_I,\dot{\mathbf{e}}_h) + \mathcal{K}_h^\varepsilon(\dot{\mathbf{u}},\dot{\mathbf{e}}_h) - \mathcal{K}_h^\varepsilon(\dot{\mathbf{u}}_h,\dot{\mathbf{e}}_h).$$

Using the definition of the energy norm we obtain

$$\frac{1}{2}\frac{d}{dt}\left(||\mathbf{e}_h||_{\mathcal{E}}^2 - 2\langle\{\underline{\sigma}(\mathbf{e}_h)\},[\![\mathbf{e}_h]\!]\rangle_{\mathcal{F}_h^I}\right) = (\rho\,\ddot{\mathbf{e}}_I,\dot{\mathbf{e}}_h)_{\mathcal{T}_h} + \mathcal{B}_h(\mathbf{e}_I,\dot{\mathbf{e}}_h) + \mathcal{K}_h^\varepsilon(\dot{\mathbf{u}},\dot{\mathbf{e}}_h) - \mathcal{K}_h^\varepsilon(\dot{\mathbf{u}}_h,\dot{\mathbf{e}}_h).$$

Integrating in time between 0 and t, using the Cauchy-Schwarz inequality to bound the term $(\rho\,\ddot{\mathbf{e}}_I,\dot{\mathbf{e}}_h)_{\mathcal{T}_h}$ and that $\mathbf{e}_h(0)=\mathbf{u}_h(0)-\mathbf{u}_I(0)=\mathbf{0}$, we get

$$\frac{1}{2}\left(||\mathbf{e}_h||_{\mathcal{E}}^2 - 2\langle\{\underline{\sigma}(\mathbf{e}_h)\},[\![\mathbf{e}_h]\!]\rangle_{\mathcal{F}_h^I}\right) \le \int_0^t ||\dot{\mathbf{e}}_I||_{\mathcal{E}}||\mathbf{e}_h||_{\mathcal{E}}\,d\tau + \int_0^t \mathcal{B}_h(\mathbf{e}_I,\dot{\mathbf{e}}_h)\,d\tau + \int_0^t (\mathcal{K}_h^\varepsilon(\dot{\mathbf{u}},\dot{\mathbf{e}}_h) - \mathcal{K}_h^\varepsilon(\dot{\mathbf{u}}_h,\dot{\mathbf{e}}_h))\,d\tau.$$

Employing Lemma 1.4 we obtain

$$\frac{1}{2}||\mathbf{e}_h||_{\mathcal{E}}^2 \le \int_0^t ||\dot{\mathbf{e}}_I||_{\mathcal{E}}||\mathbf{e}_h||_{\mathcal{E}}\,d\tau + \int_0^t \mathcal{B}_h(\mathbf{e}_I,\dot{\mathbf{e}}_h)\,d\tau + \int_0^t (\mathcal{K}_h^\varepsilon(\dot{\mathbf{u}},\dot{\mathbf{e}}_h) - \mathcal{K}_h^\varepsilon(\dot{\mathbf{u}}_h,\dot{\mathbf{e}}_h))\,d\tau. \tag{4.31}$$

We next estimate the last two terms on the right hand side. For the first one, the integration by parts formula together with the observation that $\mathbf{e}_h(0)=\mathbf{u}_h(0)-\mathbf{u}_I(0)=\mathbf{0}$, and Lemma 4.1 lead to

$$\begin{aligned}\int_0^t \mathcal{B}_h(\mathbf{e}_I,\dot{\mathbf{e}}_h)\,d\tau &= \mathcal{B}_h(\mathbf{e}_I(t),\mathbf{e}_h(t)) - \mathcal{B}_h(\mathbf{e}_I(0),\mathbf{e}_h(0)) - \int_0^t \mathcal{B}_h(\dot{\mathbf{e}}_I,\mathbf{e}_h)\,d\tau\\ &\lesssim |||\mathbf{e}_I|||_{DG}||\mathbf{e}_h||_{DG} + \int_0^t |||\dot{\mathbf{e}}_I|||_{DG}||\mathbf{e}_h||_{DG}\,d\tau\\ &\lesssim |||\mathbf{e}_I|||_{DG}||\mathbf{e}_h||_{\mathcal{E}} + \int_0^t |||\dot{\mathbf{e}}_I|||_{DG}||\mathbf{e}_h||_{\mathcal{E}}\,d\tau,\end{aligned} \tag{4.32}$$

where in the last step we have used the definition of the energy norm. For the second term in (4.31) we have (considering that it is linear w.r.t. second argument)

$$\begin{aligned}\mathcal{K}_h^\varepsilon(\dot{\mathbf{u}},\dot{\mathbf{e}}_h) - \mathcal{K}_h^\varepsilon(\dot{\mathbf{u}}_h,\dot{\mathbf{e}}_h) &= \mathcal{K}_h^\varepsilon(\dot{\mathbf{u}},\dot{\mathbf{u}}_h \pm \dot{\mathbf{u}} - \dot{\mathbf{u}}_I) - \mathcal{K}_h^\varepsilon(\dot{\mathbf{u}}_h,\dot{\mathbf{u}}_h - \dot{\mathbf{u}}_I)\\ &= \mathcal{K}_h^\varepsilon(\dot{\mathbf{u}},\dot{\mathbf{u}}_h - \dot{\mathbf{u}}) + \mathcal{K}_h^\varepsilon(\dot{\mathbf{u}}_h,\dot{\mathbf{u}}_I - \dot{\mathbf{u}}_h) - \mathcal{K}_h^\varepsilon(\dot{\mathbf{u}},\dot{\mathbf{u}}_I - \dot{\mathbf{u}})\\ &\le \mathcal{J}_h^\varepsilon(\dot{\mathbf{u}}_h) - \mathcal{J}_h^\varepsilon(\dot{\mathbf{u}}) + \mathcal{J}_h^\varepsilon(\dot{\mathbf{u}}_I) - \mathcal{J}_h^\varepsilon(\dot{\mathbf{u}}_h) + |\mathcal{K}_h^\varepsilon(\dot{\mathbf{u}},\dot{\mathbf{u}}_I - \dot{\mathbf{u}})|\\ &\le |\mathcal{J}_h^\varepsilon(\dot{\mathbf{u}}_I) - \mathcal{J}_h^\varepsilon(\dot{\mathbf{u}})| + \sum_{F\in\mathcal{F}_h^C}\int_F g\frac{|[\dot{\mathbf{u}}]_T\cdot[\dot{\mathbf{u}}_I-\dot{\mathbf{u}}]_T|}{|[\dot{\mathbf{u}}]_T|}\\ &\lesssim ||g||_{0,\mathcal{F}_h^C}||\dot{\mathbf{u}}_I-\dot{\mathbf{u}}||_{0,\mathcal{F}_h^C} \lesssim ||\dot{\mathbf{u}}_I-\dot{\mathbf{u}}||_{0,\mathcal{F}_h^C}.\end{aligned}$$

To obtain that result we have used: the convexity and Gateaux differentiability of $\mathcal{J}_h^\varepsilon$,the definition of $\mathcal{K}_h^\varepsilon(\dot{\mathbf{u}},\mathbf{v})$, in particular the fact that $0\le\psi_\varepsilon(\mathbf{w})\le 1$, and the Cauchy-Schwarz inequality. Therefore for the second argument of the right-hand side in (4.31) it holds

$$\int_0^t (\mathcal{K}_h^\varepsilon(\dot{\mathbf{u}},\dot{\mathbf{e}}_h) - \mathcal{K}_h^\varepsilon(\dot{\mathbf{u}}_h,\dot{\mathbf{e}}_h))\,d\tau \lesssim \int_0^t ||\dot{\mathbf{e}}_I||_{0,\mathcal{F}_h^C}\,d\tau. \tag{4.33}$$

By substituting the above two bounds (4.32) and (4.33) in (4.31) we get

$$\begin{aligned}\frac{1}{2}||\mathbf{e}_h||_{\mathcal{E}}^2 \lesssim & \int_0^t ||\dot{\mathbf{e}}_I||_{\mathcal{E}}||\mathbf{e}_h||_{\mathcal{E}}\,d\tau + |||\mathbf{e}_I|||_{DG}||\mathbf{e}_h||_{\mathcal{E}} \\ & + \int_0^t |||\dot{\mathbf{e}}_I|||_{DG}||\mathbf{e}_h||_{\mathcal{E}}\,d\tau + \int_0^t ||\dot{\mathbf{e}}_I||_{0,\mathcal{F}_h^C}\,d\tau \\ & = |||\mathbf{e}_I|||_{DG}||\mathbf{e}_h||_{\mathcal{E}} + \int_0^t ||\dot{\mathbf{e}}_I||_{0,\mathcal{F}_h^C}\,d\tau + \int_0^t \left(||\dot{\mathbf{e}}_I||_{\mathcal{E}} + |||\dot{\mathbf{e}}_I|||_{DG}\right)||\mathbf{e}_h||_{\mathcal{E}}\,d\tau.\end{aligned}$$

From the Young's inequality, it follows

$$\frac{1}{2}||\mathbf{e}_h||_{\mathcal{E}}^2 \lesssim \delta|||\mathbf{e}_I|||_{DG}^2 + \frac{1}{\delta}||\mathbf{e}_h||_{\mathcal{E}}^2 + \int_0^t ||\dot{\mathbf{e}}_I||_{0,\mathcal{F}_h^C}\,d\tau + \int_0^t \left(||\dot{\mathbf{e}}_I||_{\mathcal{E}} + |||\dot{\mathbf{e}}_I|||_{DG}\right)||\mathbf{e}_h||_{\mathcal{E}}\,d\tau \tag{4.34}$$

and therefore we can chose $\delta = 4C$, being C the hidden constant in (4.34), and obtain

$$\frac{1}{4}||\mathbf{e}_h||_{\mathcal{E}}^2 \lesssim |||\mathbf{e}_I|||_{DG}^2 + \int_0^t ||\dot{\mathbf{e}}_I||_{0,\mathcal{F}_h^C}\,d\tau + \int_0^t \left(||\dot{\mathbf{e}}_I||_{\mathcal{E}} + |||\dot{\mathbf{e}}_I|||_{DG}\right)||\mathbf{e}_h||_{\mathcal{E}}\,d\tau.$$

By applying the Gronwall's lemma 1.6 we get

$$||\mathbf{e}_h||_{\mathcal{E}}^2 \lesssim |||\mathbf{e}_I|||_{DG}^2 + \int_0^t ||\dot{\mathbf{e}}_I||_{0,\mathcal{F}_h^C}\,d\tau + \int_0^t \left(||\dot{\mathbf{e}}_I||_{\mathcal{E}}^2 + |||\dot{\mathbf{e}}_I|||_{DG}^2\right)\,d\tau.$$

The interpolation estimates of Lemma 4.2 and Lemma 4.3 lead to

$$\begin{aligned}|||\mathbf{e}_I|||_{DG}^2 &\lesssim \sum_{\mathcal{T}_{h_\pm}} \frac{h_\pm^{2m_\pm-2}}{N_\pm^{2s_\pm-3}}||\mathbf{u}||_{s_\pm,\mathcal{T}_{h_\pm}}^2, \\ ||\dot{\mathbf{e}}_I||_{0,\mathcal{F}_h^C} &\lesssim \sum_{\mathcal{T}_{h_\pm}} \frac{h_\pm^{m_\pm-1/2}}{N_\pm^{s_\pm-1/2}}||\dot{\mathbf{u}}||_{s_\pm,\mathcal{T}_{h_\pm}}, \\ ||\dot{\mathbf{e}}_I||_{\mathcal{E}}^2 + |||\dot{\mathbf{e}}_I|||_{DG}^2 &\lesssim \sum_{\mathcal{T}_{h_\pm}} \frac{h_\pm^{2m_\pm-2}}{N_\pm^{2s_\pm-3}}\left(||\ddot{\mathbf{u}}||_{s_\pm,\mathcal{T}_{h_\pm}}^2 + ||\dot{\mathbf{u}}||_{s_\pm,\mathcal{T}_{h_\pm}}^2\right).\end{aligned}$$

Therefore we obtain

$$\begin{aligned}\sup_{t\in[0,T]} ||\mathbf{e}_h(t)||_{\mathcal{E}}^2 \lesssim \sup_{t\in[0,T]} & \left\{\sum_{\mathcal{T}_{h_\pm}} \frac{h_\pm^{2m_\pm-2}}{N_\pm^{2s_\pm-3}}||\mathbf{u}||_{s_\pm,\mathcal{T}_{h_\pm}}^2\right\} + \int_0^T \sum_{\mathcal{T}_{h_\pm}} \frac{h_\pm^{m_\pm-1/2}}{N_\pm^{s_\pm-1/2}}||\dot{\mathbf{u}}||_{s_\pm,\mathcal{T}_{h_\pm}}\,dt \\ & + \int_0^T \sum_{\mathcal{T}_{h_\pm}} \frac{h_\pm^{2m_\pm-2}}{N_\pm^{2s_\pm-3}}\left(||\ddot{\mathbf{u}}||_{s_\pm,\mathcal{T}_{h_\pm}}^2 + ||\dot{\mathbf{u}}||_{s_\pm,\mathcal{T}_{h_\pm}}^2\right)dt\end{aligned}$$

and the proof is complete. □

4.4 Numerical results

In this section we present preliminary numerical tests. For the dynamic fault-rupture problems, no analytical solution exists to be used as reference one for the validation. For this reason we consider a 2D version of the benchmark problem for spontaneous rupture propagation of the Southern California Earthquake Center (SCEC). The original 3D SCEC test (TPV3) was proposed by Harris et al. [Har+04] and its 2D analogue is described and used as validation test in [PAK09; KLA08; Roj+08].
We consider a straight fault of length $30\,km$ embedded in a homogeneous elastic body with material properties $\rho = 2670\,kg/m^3$, $v_P = 6000\,m/s$ and $v_S = 3464\,m/s$. The center of the fault is characterized by a nucleation patch of $3\,km$ with higher initial shear stress. The initial stress field and frictional parameters of the LSW law are given in Table 4.1.

Table 4.1: Parameters describing the fault rupture segment for the SCEC test case

Parameter	Nucleation zone	Outside Nucleation zone
Initial shear traction σ_T (MPa)	81.6	70
Initial normal stress $-\sigma_N$ (MPa)	120	120
Static friction coefficient μ_s	0.677	0.677
Dynamic friction coefficient μ_d	0.525	0.525
Critical slip distance D_c (m)	0.4	0.4

To perform the simulations we use a large computational domain of size $72 \times 72\,km$ with absorbing boundary conditions. Beyond the fault segment, the rupture does not occur. In agreement with our model, the horizontal segment of the fault subdivide the domain Ω in two subdomains $\Omega^{\pm}$. The fault plane is then subdivided in different portions in which we assign the rupture conditions in agreement with Table 4.1. Figure 4.3 shows a sketch of the 2D SCEC spontaneous rupture problem.

All meshes are made by unstructured triangles, for the sake of simplicity with regular mesh spacing forced along the fault plane. The mesh is gradually refined nearby the rupture area of the fault ($h^{\pm}_{min}$), while it remains coarse near the boundary ($h^{\pm}_{max}$). We test our model for the solution of the proposed problem on different computational domains with mesh size $h^{\pm}_{min}$ ranging from $400m$ to $1500m$, while $h^{\pm}_{max} \approx 1500m$ is fixed. We have employed different orders, from $N^{\pm} = 1$ to 4. In all the simulations, we consider the same discretization parameters on both partitions $\mathcal{T}_{h^{\pm}}$ and $\Delta t = 10^{-4}s$. Moreover we fix $\varepsilon = 10^{-4}$ in (4.19). In particular, due to the high computational cost of the numerical problem, we consider Algorithm 1 with 1 maximum number of iterations and a tolerance of $tol = 10^{-6}$.

The first results that we propose are a comparison of the slip rate $|[\dot{\mathbf{u}}]_T|$ and traction $\boldsymbol{\sigma}_T$ solutions for the reference point $Q = (7500m, 0m)$ that lies on the fault

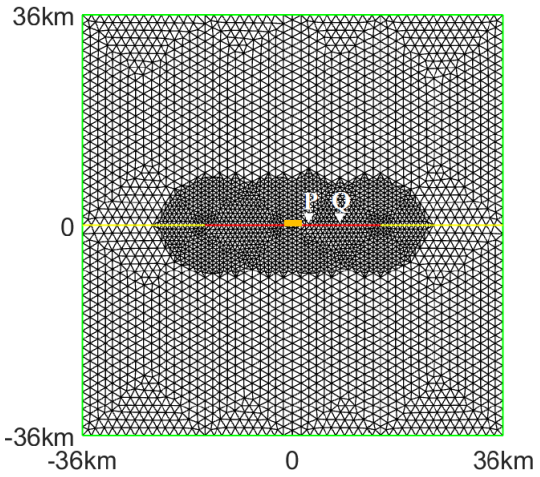

Figure 4.3: Sketch of 2D domain for SCEC problem. Yellow, orange and red: segment fault. Orange: nucleation, red: rupture, yellow: plane of fault where no rupture occurs.

(see Figure 4.3) and obtained with our method, cf. Section 4.2. In Figure 4.4 we show the profile of the solutions for fixed degree polynomial $N = 3$ and two different mesh parameters $h_{min} \approx 400, 1500m$. In Figure 4.5 there are the solutions obtained with fixed mesh parameter $h_{min} \approx 800m$ and two choices of polynomial degree $N = 2, 4$. From the results presented in Figures 4.4 and 4.5, we observe a good agreement of the behavior of the solutions w.r.t. the numerical parameters. We also perform a set of simulations by varying the parameter ε in (4.9) that represents a threshold to regularize the absolute value near zero value, therefore we select $\varepsilon = 10^{-2}, 10^{-4}, 10^{-6}$. The results are shown in Figure 4.6. We observe that for larger regularization parameters ε (and within the range of reasonable values), then the main peak values of the slip rate $|[\dot{\mathbf{u}}]_T|$ and traction $\boldsymbol{\sigma}_T$ are larger and slightly shifted in time.

A second set of results in which we are interested is the physical behaviour of the solution. For this reason we show in Figure 4.7 the two profile of the slip rate and traction quantities for two different points that lie on the fault, that are $P = (2500m, 0m)$ and $Q = (7500m, 0m)$. We can observe that the main peaks of the solutions arrives first in P and then in Q. This is in agreement with the spontaneous rupture propagation phenomenon in which we expect that the rupture starts from nucleation and propagates from all other points of the fault domain. Therefore we observe a coherent direction of rupture propagation.

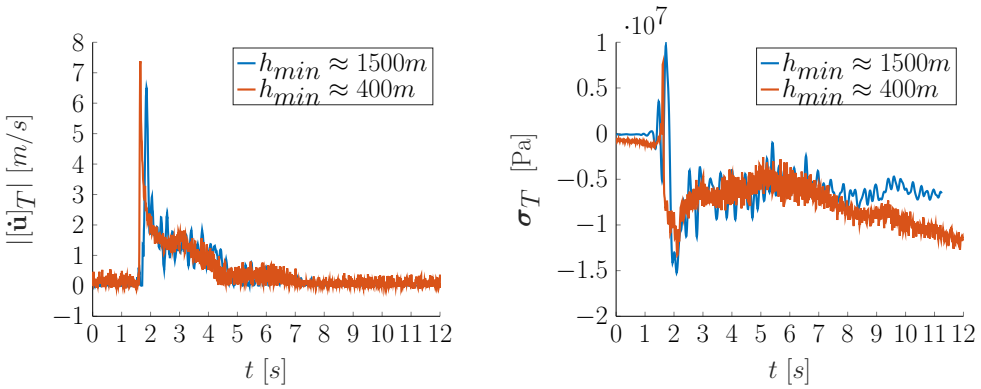

Figure 4.4: Comparison of slip rate $|[\dot{\mathbf{u}}]_T|$ and traction $\boldsymbol{\sigma}_T$ solutions of the proposed method (see Section 4.2) for fixed polynomial degree $N = 3$ and mesh size of $h_{min} \approx 1500, 400m$.

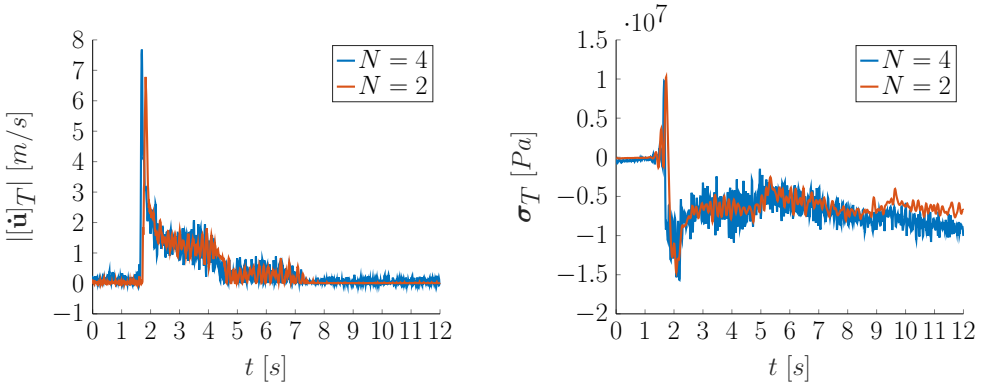

Figure 4.5: Comparison of slip rate $|[\dot{\mathbf{u}}]_T|$ and traction $\boldsymbol{\sigma}_T$ solutions of the proposed method (see Section 4.2) for fixed grid mesh size $h_{min} \approx 800m$ and polynomial degree $N = 2, 4$.

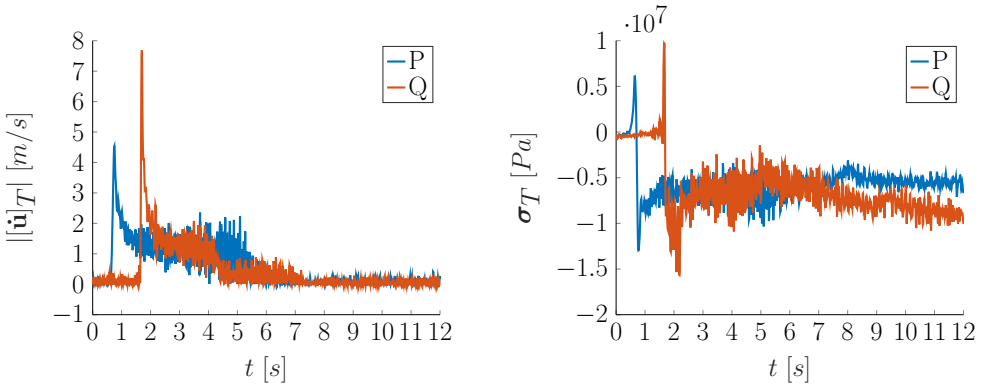

Figure 4.7: Evaluation of slip rate $|[\dot{\mathbf{u}}]_T|$ and traction $\boldsymbol{\sigma}_T$ solutions of the proposed method (see Section 4.2) with fixed $N = 4$ and $h_{min} \approx 800m$ at two different points on the fault plane: $P = (2500m, 0m)$ and $Q = (7500m, 0m)$.

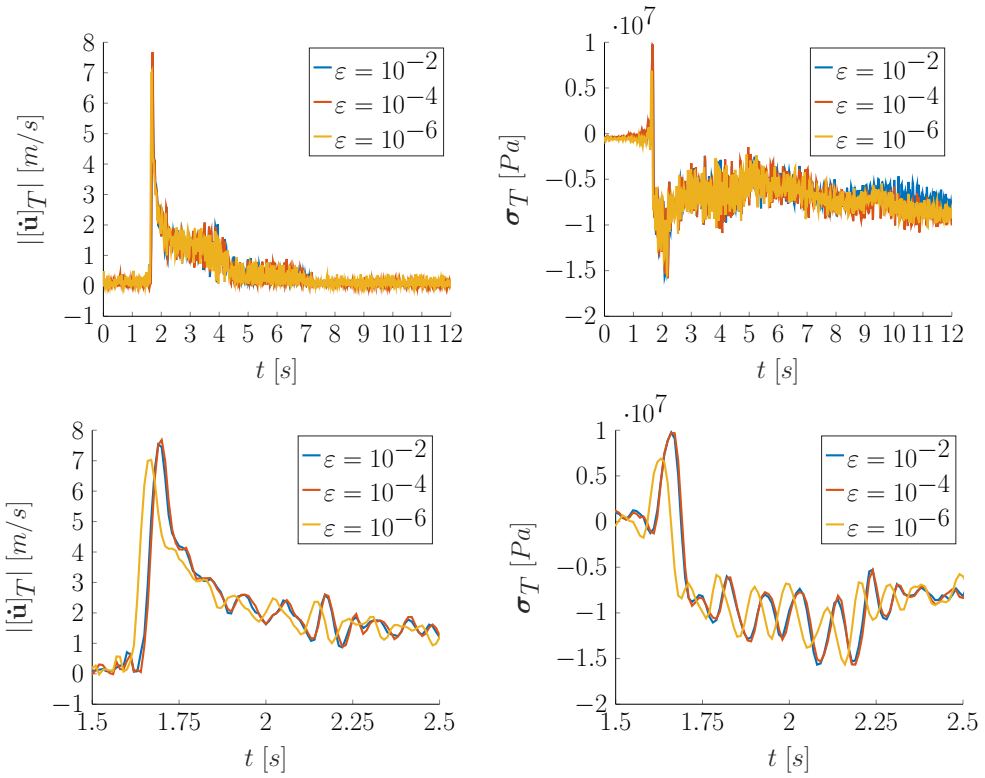

Figure 4.6: Comparison of slip rate $|[\dot{\mathbf{u}}]_T|$ and traction $\boldsymbol{\sigma}_T$ solutions of the proposed method (see Section 4.2) for fixed grid mesh size $h_{min} \approx 800m$, polynomial degree $N = 4$ and $\varepsilon = 10^{-2}, 10^{-4}, 10^{-6}$.

Finally, we compare our results with ones in literature of [Pue+08].[1] In Figure 4.8 we represent the reference solutions at point $Q = (7500m, 0m)$ of slip rate and traction of literature w.r.t. the one obtained with our proposed method, cf. Section 4.2. We can appreciate the same behavior which is approximately in good agreement.

[1]This data were kindly provided by Josep de la Puente, one of the authors of the cited work.

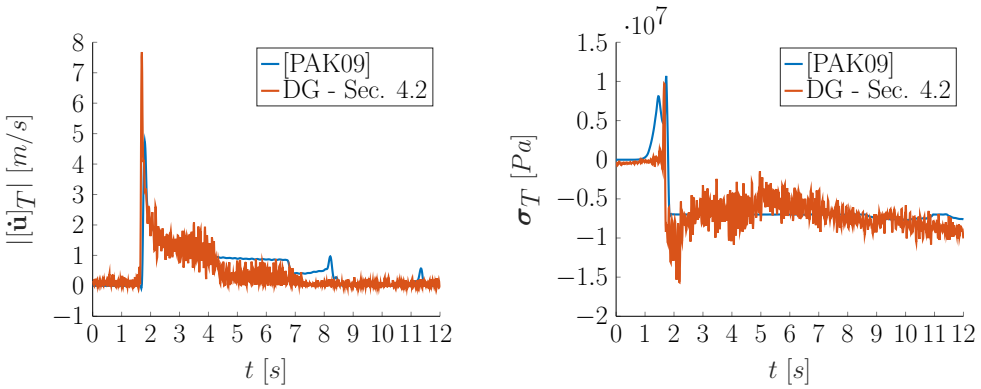

Figure 4.8: Comparison of slip rate $|[\dot{\mathbf{u}}]_T|$ and traction $\boldsymbol{\sigma}_T$ solutions of the proposed method (see Section 4.2) w.r.t. the literature ([PAK09]).

From our preliminary results, we observe that we are able to capture the spontaneous rupture phenomenon. In order to correctly validate our contact-friction model with the reference solution available in literature [PAK09], we are going to investigate suitable ways to improve physically the proposed models. Moreover, due to the need of accurate solutions for the spontaneous rupture problems, we would like to improve the quality of the proposed solver (e.g. increasing the polynomial degree or the number of iterations in the time algorithm) by keeping low the computational costs.

4.5 Concluding remarks

In this chapter we addressed the main mathematical aspects of the contact-friction laws in elastodynamics models. We first described the governing equations of the dynamical fault rupture and non-linear behaviour of buildings. Then we provided the variational formulation within the inequality framework. We derived the semi-discrete discontinuous Galerkin formulation and then we carried out the well-possdness, stability and convergence analysis. Then, after a leap-frog scheme for the integration in time, we described the algorithm to solve the non-linear fully-discrete formulation. Finally, we proposed a set of numerical tests to demonstrate the effectiveness of our proposed model to simulate the dynamic source phenomena. Possible further improvements include a suitable adaptation of physical laws in our model w.r.t. the validation test in consideration, new algorithms to solve accurately the numerical problem by keeping low the computational cost. Moreover it is of interest considering new validation tests with different properties of the fault (e.g. inclination, general shape-curve), but also to consider case studies within the structural analysis and, finally, to extend the model in 3D and consider real applications.

Conclusions

In this thesis we presented advanced models for the seismic risk assessment in case of both large urban areas and cultural heritages. The novelty of the proposed methods consists of employing three-dimensional physics-based numerical simulations to determine earthquake ground motion instead of more standard empirical approaches. The project is truly interdisciplinary since it required the numerical developments of high performance mathematical computing tools and the evaluations of seismic actions and of structural vulnerability for risk assessment.

We developed a first approach where we propose to employ physics-based three-dimensional wave propagation models to simulate earthquake ground motion time histories, which can then be used to provide the key input for fragility curves of different structural types and to quantify seismic risk. 3D simulations are obtained by solving the wave propagation problem with discontinuous Galerkin spectral element methods. Then we employ the synthetic scenarios as input for vulnerability models, in our case for the fragility curves. Since 3D numerical simulations can provide a more detailed picture of the seismic event, e.g. characterization of the ground motion in the near-field of an earthquake, this allows a more reliable risk analysis. The proposed coupled approach has been tested considering the high seismicity Beijing metropolitan area focusing on the the class of high-rise building. This application demonstrates the capability of the combination of 3D physics-based scenarios with suitable vulnerability models to yield an accurate seismic risk assessment.

As second approach we considered three-dimensional physics-based description for both the ground motion and the building behavior under a seismic event. For that purpose we made use of the discontinuous Galerin spectral element methods implemented in the high-performance code SPEED to handle the 3D modeling of complex multi-scale engineering-seismology problems, including soil-structure interaction. This approach can be more accurate than the one presented before, but it requires more computational effort. However it may be the only possibility for structures that are unique, for example in the case of cultural heritage for which fragility curves are not available. To show the ability of the proposed approach we

presented the application of the Athens 1999 earthquake in which we investigated the seismic response of the Parthenon. The proposed application study, despite the simplifications, demonstrates the effectiveness of seismic simulations within the framework of the seismic risk mitigation strategies for the cultural heritage.

As we could experienced from previous applications, physics-based simulations can provide a complete picture of the seismic wave propagation phenomenon and can be the basis to construct the description of a seismic scenario for the risk analysis. In order to improve the models introduced before, we would like to describe in a more realistic way the earthquakes and the behavior of the buildings. For that reason we consider the elastodynamics equation with the contact-friction laws that are at the basis of both the dynamic source modelling and the interactions of the main blocks that compose a structure. We shown a theoretical analysis of the introduced model and then the discontinuous Galerkin approximations have been adopted to discretize the problem. Convergence and numerical error estimates are investigated. It has also been proposed a 2D validation test for a spontaneous dynamic rupture.

Future developments that arise from the work carried out in this thesis are the following.

- After the validation of the proposed methodological approach based on the coupling of three-dimensional physics-based scenarios and fragility curves, it would be of great interest to apply it for the seismic risk assessment in high seismicity Italian urban areas, e.g. L'Aquila and Sulmona.

- The simulations performed on the Athens 1999 (Mw6) earthquake showed encouraging results. However we would need to propagate relatively higher frequencies through the computational domain in order to capture the dominant features of the site response of the Acropolis ($30Hz$). For that reason the model should be improved by considering, for example, the contact-friction laws that better describe the seismic source w.r.t. high frequency and a discontinuous Galerkin approximation in time to reduce the computational cost that comes from CFL condition in problems with high frequencies. Moreover in order to improve the structural description of the Parthenon, we should describe it as composed by blocks with different material properties and that can move one w.r.t. the other governed by a suitable generalization of the contact-friction laws.

- As mentioned before, in three-dimensional realistic cases the use of contact-friction laws would be of great interest. For that reason we should extend the proposed algebraic development from 2D up to 3D and then employ it to perform physics-based simulations.

- In order to improve the physics-based description of earthquakes phenomena, we should adopt suitable nonlinear elasticity models or elasto-acoutstic cou-

plings in presence of water ([ABM19; ABM20; Ant+20]). In specif the latter method could be employed in our case of the Athens earthquake.

- In each of the test cases for which we applied the different proposed techniques, we numerically observed a very high computational cost. For that reason, the development of a fast and robust solver would improve the performance to get the numerical solution. Therefore in Appendix A we investigate algebraic multigrid methods for linear systems arising from high-order nodal discontinous Galerkin approximations of elliptic problems. In future the proposed approach should be extended to elasticity and elastodynamics equations.

APPENDIX A

Algebraic multigrid schemes for high-order discontinuous Galerkin methods

The numerical solution of partial differential equations is of fundamental importance in the description of phenomena in Engineering and Applied Science. An obvious demand that arises is the high accuracy of the numerical solution of the mathematical model, and therefore highly efficient arbitrarily accurate numerical techniques are needed.

The mathematical models and applications introduced in the previous chapters are governed by the elastodynamics equations with the discontinuous Galerkin (DG) approximations. They require accurate solutions against a large computational cost. Therefore an efficient solver for these problems is needed. Here, to start in simple and ideal conditions, we want to propose an investigation of the efficient algebraic multigrid (AMG) methods for the 2D-Laplace problem with DG schemes. Then the proposed study can be at the basis of future developments that possibly include the solution of the elastodynamics equations with the AMG solvers.

Therefore here we present algebraic multigrid methods for the efficient solution of the linear system of equations stemming from high-order discontinuous Galerkin discretizations of second-order elliptic problems. For discontinuous Galerkin methods standard multigrid approaches cannot be employed because of redundancy of the degrees of freedom associated to the same grid point. We present new aggregation procedures and test them on extensive two-dimensional numerical experiments that demonstrate that the proposed AMG method is uniformly convergent with respect to all the discretization parameters, namely the mesh-size and the polynomial approximation degree.

A.1 Introduction to algebraic multigrid schemes for discontinuous Galerkin methods

High-order discontinuous Galerkin (DG) methods are widely employed for the numerical solution of partial differential equations because of their flexibility in dealing with non-conforming grids and elementwise varying approximation orders, see, e.g. [Riv08; HW08; DPE12] for an overview on DG methods.
In this work we focus on multigrid methods and present a new algebraic multigrid iterative scheme for the efficient solution of the linear system of equations stemming from high-order discontinuous Galerkin finite element approximations of second order elliptic differential equations. Since the pioneer work of Gopalakrishnan and Kanschat [GK03], multigrid methods for discontinuous Galerkin finite element discretizations of partial differential equations have been intensively studied.
The first developments of geometric multigrid methods for low-order, i.e. linear, discontinuous Galerkin methods can be found in [GK03; RH05; BZ05; Dob+06; BO07; BCS09; Bre+11; Bas+12; BBC14]. Multigrid techniques coupling geometric and p-multigrid approaches have also been studied, cf. [HA06; HA08; MHA10]. Recently, new hp-multigrid schemes for high-order discontinuous Galerkin discretizations have been proposed and analyzed, cf. [ASV15; Ant+17; AP18; Ant+ a]. Algebraic multigrid techniques for matrices stemming from low-order discontinuous Galerkin finite element discretizations of elliptic equations can be found in [PLMH09; BBS12; Sch12]. The first scalable algebraic multigrid method for high-order discontinuous Galerkin discretizations of the Poisson operator is developed by Olson and Schroder [OS11]. It assumes the access to mesh points in order to perform the first step of coarsening, therefore employing a geometric information. To the best of our knowledge, purely algebraic multigrid methods for high-order discontinuous Galerkin discretizations have not been addressed so far. Indeed the work by Prill et al. [PLMH09] requires the knowledge of the grid in order to build all the aggregates, Olson and Schroder [OS11] assume the access to the mesh information for the first coarsening step and the method of Bastian et al. [BBS12] requires that the natural embedding operator is provided. More precisely, the AMG method proposed by Olson and Schroder [OS11] is a quasi-purely algebraic multigrid because it employs the geometric assumptions only for the first aggregation step.
In this chapter we present a new algebraic multigrid method for the efficient solution of the linear systems of equations stemming from high-order discontinuous Galerkin approximations of second-order elliptic problems. We modify the first step of coarsening of the AMG method of Olson and Schroder [OS11] within an algebraic framework proposing a block-aggregation scheme applied to the finest level. For the coarse levels we employ the classical aggregation of Vaněk et al. [VMB96] following the guideline given in [OS11]. With these steps our algorithm is fully algebraic

because it employs only the entries of the matrix. We demonstrate that for the proposed AMG iterative scheme convergence is achieved independently of both the discretization parameters, namely the mesh-size and the polynomial approximation degree, making the method well suited for both low- and high-order DG approximations.
The remaining part of the chapter is organized as follows. In Section A.2 we introduce the model problem and its discontinuous Galerkin discretization. In Section A.3 we propose our algebraic multigrid method based on smoothed aggregation and extend it to high-order discontinuous discretizations. In Section A.4 we present extensive numerical experiments to investigate the efficiency and robustness of our method. In Section A.5 we give a summary of the achieved results and we draw some remarks.

A.2 Model problem and its discontinuous Galerkin discretization

In this section we present the model problem and its discontinuous Galerkin discretization. Throughout the chapter we use the standard notation for Sobolev spaces, cf. [Ada75]. Let $\Omega \subset \mathbb{R}^2$ be a bounded polygonal domain and let $\mathbf{n}$ be the unit outward normal vector to the boundary $\partial\Omega$. For a given function $f \in L^2(\Omega)$ and a given $g \in H^{\frac{1}{2}}(\partial\Omega)$, we consider the weak formulation of the Poisson problem subject to essential boundary conditions: find $u \in V = \{v \in H^1(\Omega)\colon\ u = g \text{ on } \partial\Omega\}$ such that

$$\int_\Omega \nabla u \cdot \nabla v \, d\Omega = \int_\Omega f v \, d\Omega \quad \forall v \in H_0^1(\Omega). \tag{A.1}$$

Now we describe the numerical solution of (A.1) based on employing the discontinuous finite element method. We begin by constructing a conforming mesh $\mathcal{T}_h$ of the domain $\Omega \subset \mathbb{R}^2$ made of non-overlapping shape-regular triangles/quads of diameter h_K, and set $h = \max_K h_K$. We assume that each K is the affine map of a fixed master element $\widehat{K}$, i.e. $K = F_K(\widehat{K})$, where $\widehat{K}$ is either the unit reference simplex $\widehat{T} = \{(x, y) : x, y \geq 0,\ x + y \leq 1\}$ or the reference square $\widehat{Q} = (-1, 1)^2$. Let $\mathcal{E}_I$ be the set of interior edges of the mesh $\mathcal{T}_h$, $\mathcal{E}_B$ the set of boundary edges and $\mathcal{E}{=}\mathcal{E}_I \cup \mathcal{E}_B$ the set of all edges. Let $e \in \mathcal{E}_I$ shared by two neighbouring elements $K^\pm$, for (regular enough) scalar and vector-valued functions v and $\boldsymbol{\tau}$, respectively, we define the averages and jumps as

$$\{\!\{v\}\!\} = \frac{1}{2}(v^+ + v^-) \qquad [\![v]\!] = v^+\mathbf{n}^+ + v^-\mathbf{n}^-$$

$$\{\!\{\boldsymbol{\tau}\}\!\} = \frac{1}{2}(\boldsymbol{\tau}^+ + \boldsymbol{\tau}^-) \qquad [\![\boldsymbol{\tau}]\!] = \boldsymbol{\tau}^+ \cdot \mathbf{n}^+ + \boldsymbol{\tau}^- \cdot \mathbf{n}^-$$

where $\mathbf{n}^\pm$ is the unit normal vector to e pointing outward to $K^\pm$, and $v^\pm$ and $\boldsymbol{\tau}^\pm$ are the traces of the functions v and $\boldsymbol{\tau}$ on $K^\pm$, cf. [Arn+01]. If $e \in \mathcal{E}_B$ belongs to the

boundary $\partial\Omega$ we extend these definition as follows $\{\!\{v\}\!\} = v$, $[\![v]\!] = v\mathbf{n}$, $\{\!\{\boldsymbol{\tau}\}\!\} = \boldsymbol{\tau}$ and $[\![\boldsymbol{\tau}]\!] = \boldsymbol{\tau} \cdot \mathbf{n}$, cf. [Arn+01]. Let V_{hp} be a family of finite dimensional spaces defined as

$$V_{hp} = \{v \in L^2(\Omega) : v \circ F_K \in \mathbb{M}_p(\widehat{K}) \quad \forall K \in \mathcal{T}_h\},$$

where $\mathbb{M}_p(\widehat{K})$ is either the space $\mathbb{P}_p(\cdot)$ of polynomials of degree lower than or equal to $p \geq 1$ on $\widehat{K}$ if $\widehat{K} \equiv \widehat{T}$ is the reference triangle, or the space $\mathbb{Q}_p(\cdot)$ of all tensor-product polynomials on $\widehat{K}$ of degree p in each coordinate direction if $\widehat{K} \equiv \widehat{Q}$ is the reference square. The space V_{hp} is equipped with the norm

$$|v|^2_{DG} = \sum_{K \in \mathcal{T}_h} |\nabla v|^2_{L^2(K)} + \sum_{e \in \mathcal{E}} |\sqrt{\gamma_e}[\![v]\!]|^2_{L^2(e)},$$

where, for a given penalty parameter $\sigma^e > 0$, γ_e is defined edgewise as $\gamma_e = \sigma^e p^2/|e|$, $|e|$ being the length of the edge e.
Next we define the bilinear form $\mathcal{A} : V_{hp} \times V_{hp} \to \mathbb{R}$ as

$$\begin{aligned}\mathcal{A}(u,v) = &\sum_{K \in \mathcal{T}_h} \int_K \nabla u \cdot \nabla v \, d\Omega - \sum_{e \in \mathcal{E}} \int_e \{\!\{\nabla u\}\!\} \cdot [\![v]\!] \, d\gamma \\ &- \sum_{e \in \mathcal{E}} \int_e \{\!\{\nabla v\}\!\} \cdot [\![u]\!] \, d\gamma + \sum_{e \in \mathcal{E}} \gamma_e \int_e [\![u]\!] \cdot [\![v]\!] \, d\gamma,\end{aligned}$$

and the functional $F : V_{hp} \to \mathbb{R}$ as

$$F(v) = \int_\Omega f v \, d\Omega - \sum_{e \in \mathcal{E}_B} \int_e \nabla v \cdot \mathbf{n}_e \, g \, d\gamma + \sum_{e \in \mathcal{E}_B} \gamma_e \int_e v g \, d\gamma,$$

The discontinuous Galerkin discrete problem reads: find $u_h \in V_{hp}$ such that

$$\mathcal{A}(u_h, v_h) = F(v_h) \quad \forall v_h \in V_{hp}, \tag{A.2}$$

which is known as symmetric interior penalty (SIP) method [Whe78; Arn82]. The following result ensures the well-posedness of (A.2), cf. [Whe78; Arn82; Arn+01], see, e.g., [PS02; HSS02; SW10; GS05] for $hp-$version error estimates.

Proposition A.1. *If $\sigma^e > \sigma_{min}$, the solution of* (A.2) *exists and is unique.*

Let $\{\varphi_j\}_{j=1}^{N_h}$ be a basis for the discrete space V_{hp}, i.e. $V_{hp} = span\{\varphi_j\}_{j=1}^{N_h}$, then (A.2) is equivalent to the following linear system of equations

$$A\mathbf{u} = \mathbf{f}, \tag{A.3}$$

where $\mathbf{u} = [u_1, \ldots, u_{N_h}]^T \in \mathbb{R}^{N_h}$ is the vector containing the unknown coefficients of the expansion of the discrete solution u_h in the chosen basis. The stiffness matrix A in (A.3) is symmetric and positive definite, provided that σ^e is large enough.

Next we describe the choice of the shape functions employed to span the discontinuous finite element space. We point out that, since in the DG framework

the shape functions are supported on a single mesh element, we trivially fit the smoothed aggregation AMG framework of Vaněk et al. [VMB96] requiring that the support of each basis function is bounded. To span the discrete space V_{hp} we require that a nodal basis is employed, i.e. $v_h \in V_{hp}$ is characterized by the values it takes at the points $P_i = (x_i, y_i)$, with $i = 1, \ldots, N_h$, and consequently the shape functions associated to the finite element space V_{hp} are defined as the Lagrangian functions associated to these interpolation nodes with support on a single element.

Remark A.1. We point out that our AMG method is developed assuming that a nodal basis associated to suitable (stable) interpolation points is employed to span the discrete space. The extension to modal, e.g. tensor product of Legendre polynomials, requires a completely different algorithm to identify connections and build the interpolation operator, such an extension is under development and will be the subject of further research.

To specify the interpolation points, on the reference triangle $\widehat{T}$ we define therein the Fekete points [TWV00; BSV12]; on the reference square $\widehat{Q}$ we consider the Gauss-Legendre-Lobatto (GLL) points [Can+06]. Then, for any $K \in \mathcal{T}_h$, K being a shape-regular triangle or quad, those points are mapped, through the linear map $F_K : \widehat{K} \to K$, $K \in \mathcal{T}_h$, $\widehat{K} = \widehat{T}, \widehat{Q}$. We point out that the choice of Fekete and GLL interpolation points is dictated by the fact that we are interested in high-order approximations, where it is known that equidistributed interpolation points lead to numerical instabilities. In Figure A.1 we show the Fekete/GLL points on the reference triangle/square for $p = 4, 7$.

Remark A.2. We point out that other choices of interpolation points for the reference triangle could be employed. Among them we mention the warped interpolation points of Warburton and Hesthaven, cf. [Hes98; War06]. We tested our AMG also employing the warped interpolation points [Hes98; War06] and from the numerical results it seems to be robust also for this choice of interpolation points; for brevity these results have been omitted.

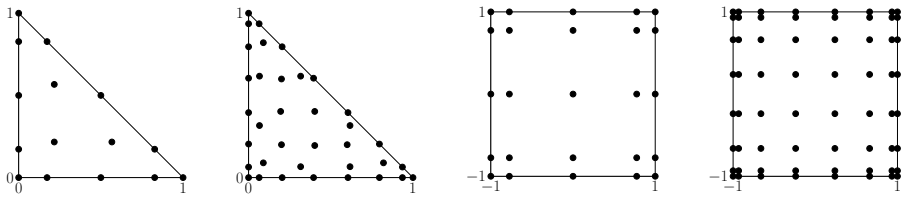

(a) $p = 4$, $\widehat{K} = \widehat{T}$ (b) $p = 7$, $\widehat{K} = \widehat{T}$ (c) $p = 4$, $\widehat{K} = \widehat{Q}$ (d) $p = 7$, $\widehat{K} = \widehat{Q}$

Figure A.1: Fekete (left) and GLL (right) points on the reference triangle/square for different choices of p (a, c) $p = 4$, (b, d) $p = 7$.

Remark A.3 (Condition number of A). It is of our interest considering the condition number $K_2(A)$ of the matrix A stemming from the DG approximation of problem

(A.2). We observe that, with the above choice of interpolation points, the condition number $K_2(A)$ of A, defined as the ratio of its extreme eigenvalues, seems to behave as $K_2(A) = \mathcal{O}(p^3/h^2)$, if the underlying grid is made of triangles and $K_2(A) = \mathcal{O}(p^3/h^2)$ if the underlying grid is made of quads, as shown in Figure A.2.

These results seem to show that, at least on triangular meshes in two-dimensions, a set of Lagrangian basis functions associated with Fekete points seems to lead to an improvement of the condition number as a function of p. Indeed, in [AH11] it is proved that, whenever a modal basis based on Legendre polynomials is employed, the condition number of the resulting stiffness matrix behaves as $K_2(A) = \mathcal{O}(p^4/h^2)$. On the other hand the results obtained for quadrilateral meshes in two-dimension are in agreement with the literature on spectral-element methods, cf. [BM92].

We point out that, in the conforming setting for triangular grids, i.e. continuous triangular spectral element methods, Pasquetti and Rapetti [PR04; PR06] observed that the condition number is of order p^4/h^2, whenever Fekete points are employed, whereas Toselli and Widlund [TW05] and Bernardi and Maday [BM92] proved a behaviour of order p^3/h^2 if the interpolation points are obtained based on mapping, through the Dubiner map, the classical Gauss-Legendre points defined on the reference square onto the reference triangle.

The issue of proving sharp bounds on the condition number of A, stemming from DG methods when the discrete space is spanned based on employing Lagrangian functions associated to Fekete points is under investigation and will be the subject of further research.

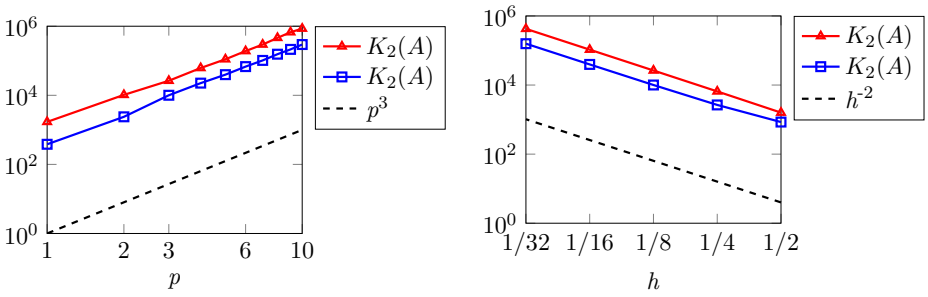

Figure A.2: Condition number $K_2(A)$ as function of p (left) and h (right), unstructured triangular grids —▲— and quadrilateral meshes —□—, $\sigma^e = 10\ \forall e \in \mathcal{E}$.

A.3 Smoothed-block aggregation algebraic multigrid

In this section, we introduce the main ingredients for the AMG algorithm. We assume to have a sequence of successively coarser matrices $A_k \in \mathbb{R}^{N_k \times N_k}$, $k =$

$1, \dots K$, with the convention that $A_1 = A$, $N_k > N_{k+1}$, and

$$A_{k+1} = I_k^{k+1} A_k I_{k+1}^k \quad k = 1, \dots, K-1.$$

Here, $I_k^{k+1} : \mathbb{R}^{N_k} \to \mathbb{R}^{N_{k+1}}$ is a linear operator to be properly defined and $I_{k+1}^k = (I_k^{k+1})^T$, see [MMB87; BHM00; XZ17], for example.

By considering a suitable smoother (e.g. damped Jacobi, symmetrized Gauss-Seidel,...), one iteration of the algebraic μ-cycle scheme, $\mu = 1, 2$, is shown in Algorithm 2, cf. also [BM87; XZ17]. More precisely given $\mathbf{u}_k^l$, $\mathbf{u}_k^{l+1}$=AMG-μCycle$(\dots, \mathbf{u}_k^l, \dots)$ returns the $(l+1)-$th iteration to solve $A_k \mathbf{u}_k = \mathbf{f}_k$. If we have a μ-cycle scheme with $\mu = 1$ we refer to it as a V-cycle, whereas for $\mu = 2$ we call the method W-cycle. In particular we denote with V(ν_1,ν_2)-cycle and W(ν_1,ν_2)-cycle the two methods above with ν_1 pre-smoothing and ν_2 post-smoothing iterations [BHM00]. Algebraic multigrid can be used as a stand-alone solver or as a preconditioner to accelerate the convergence of Krylov-based iterative schemes, such as conjugate gradient method.

Algorithm 2 One Iteration of AMG-μCycle to solve $A_k \mathbf{u}_k = \mathbf{f}_k$

function $\mathbf{u}_k^{l+1}$=AMG-μCycle(ν_1,ν_2,A_k,$\mathbf{u}_k^l$,$\mathbf{f}_k$,I_k^{k+1},I_{k+1}^k)
  if $k = K$ **then**
    $\mathbf{u}_K = A_K^{-1} \mathbf{f}_K$ ▷ Coarsest level
    return $\mathbf{u}_K$
  else
    Relax ν_1 times on $A_k \mathbf{u}_k = \mathbf{f}_k$ with initial guess $\mathbf{u}_k^0$ ▷ Pre-smoothing
    $\mathbf{f}_{k+1} = I_k^{k+1} \left(\mathbf{f}_k - A_k \mathbf{u}_k^{\nu_1} \right)$ ▷ Restriction of the residual
    $\mathbf{e}_{k+1}^0 = \mathbf{0}_{k+1}$
    for $\lambda = 1 : \mu$ **do**
      $\mathbf{e}_{k+1}^\lambda$ = AMG-μCycle(ν_1,ν_2,A_{k+1},$\mathbf{e}_{k+1}^{\lambda-1}$,$\mathbf{f}_{k+1}$,$I_{k+1}^{k+2}$,$I_{k+2}^{k+1}$)
    end for
    $\mathbf{u}_k^{\nu_1+1} = \mathbf{u}_k^{\nu_1} + I_{k+1}^k \mathbf{e}_{k+1}^\mu$ ▷ Interpolation and Correction
    Relax ν_2 times on $A_k \mathbf{u}_k = \mathbf{f}_k$ with initial guess $\mathbf{u}_k^{\nu_1+1}$ ▷ Post-smoothing
    return $\mathbf{u}_k^{\nu_1+\nu_2+1}$
  end if
end function

Our method is based on smoothed aggregation [VMB96], and extends the results of Olson and Schroder [OS11] to high-order DG methods. The main challenge in the DG setting is the redundancy of the degrees of freedom associated to the same grid points. A similar issue occurs, for example, for systems of partial differential equations where there exists multiple unknowns at the same grid point. This difficulty can be solved with strategies known as "point" or "block" approaches [RS87; VMB96]: these techniques are based on local aggregation of variables associated to

the same grid point. Here we extend this idea to deal with the multiple unknowns associated to the same grid point typical of DG methods. It is based on the use of the local aggregation for the first level coarsening, then for all the other levels different aggregation schemes can be used.

In the next sections we detail the main steps at the basis of our AMG solvers.

A.3.1 Algebraic block-aggregation algorithm

In the literature we can find different algorithms of the aggregation techniques for AMG methods applied to problem with DG discretizations that exploit the idea of the local aggregation, but all are based on the knowledge of geometric or topological information, cf. [JV01; PLMH09; OS11].
Here we propose a new purely algebraic block-aggregation coarsening strategy based on block-aggregation. Our approach differs from the ones proposed in the works by Prill et al. [PLMH09] or by Olson and Schroder [OS11] because it selects coinciding nodes typical of DG discretizations by employing only the entries of the stiffness matrix, whereas in [PLMH09; OS11] this step is made based on employing the knowledge of the mesh information. On the other hand the classical smoothed aggregation proposed by Vaněk et al. [VMB96] is not able to deal with the redundancy of degrees of freedom associated to the same grid point, therefore we modify their aggregation technique in order to take into account of this characteristic of DG methods and we employ our block-aggregation approach for the first level of coarsening. The algorithm that we present is built through to the analysis of the matrix entries associated with each degree of freedom, as described in the following.

Given the matrix $A_k \in \mathbb{R}^{N_k \times N_k}$, its entries a_{ij}, $i, j = 1, \ldots, N_k$, and its set of unknowns $\mathcal{V} = \{1, \ldots, N_k\}$, namely the degrees of freedom of the problem, we split the set of points in a disjoint covering such that $\mathcal{V} = \bigcup_{j=1}^{N_{k+1}} \mathcal{V}_j$, $N_{k+1} \leq N_k$, and $\mathcal{V}_l \cap \mathcal{V}_j = \emptyset$ for $l \neq j$. In particular, the algorithm aims at providing suitable disjoint sets such that each one of them contains the multiple variables associated to the same physical grid point, cf. Algorithm 3.

Algorithm 3 is made of three steps: startup singleton or aggregation, enlargement of the decomposition sets, and cancellation of the empty sets. First, for each $i \in \mathcal{V}$, the function find_strongest_connection(i) chooses the node $I \in \mathcal{V}$ to which the unknown i has the strongest connection, cf. Section A.3.3 below. If the strongest connection between i and I is negative, i.e. $a_{iI} < 0$, then the nodes i and I are grouped together (startup aggregation), otherwise the node i is processed alone (startup singleton). Once the startup phase is concluded, the algorithm proceeds with the enlargement of the decomposition sets, based on joining sets with at least one node in common. Finally, empty sets are deleted from the disjoint covering. Algorithm 3 is based on the function find_strongest_connection, that is detailed in the following. We introduce a symmetric, positive strength function $s(i, j)$ that

Algorithm 3 Algebraic Block-Aggregation Algorithm

$h = 0$
for all $i \in \mathcal{V}$ **do**
  I=find_strongest_connection(i)
  if $a_{iI} \geq 0$ **then**
    if $\forall h : \mathcal{V}_h \cap \{i\} = \emptyset$ **then** ▷ Startup Singleton
      $h = h + 1$, $\mathcal{V}_h = \{i\}$
    end if
  else
    if $\forall h : \mathcal{V}_h \cap \{i, I\} = \emptyset$ **then** ▷ Startup Aggregation
      $h = h + 1$, $\mathcal{V}_h = \{i, I\}$
    else ▷ Enlarging the Decomposition Sets
      if $\exists \tilde{h} : \mathcal{V}_{\tilde{h}} \cap \{i\} \neq \emptyset$ & $\forall h : \mathcal{V}_h \cap \{I\} = \emptyset$ **then**
        $\mathcal{V}_{\tilde{h}} = \mathcal{V}_{\tilde{h}} \cup \{I\}$
      else if $\exists \tilde{h} : \mathcal{V}_{\tilde{h}} \cap \{I\} \neq \emptyset$ & $\forall h : \mathcal{V}_h \cap \{i\} = \emptyset$ **then**
        $\mathcal{V}_{\tilde{h}} = \mathcal{V}_{\tilde{h}} \cup \{i\}$
      else if $\exists \tilde{h}_1 : \mathcal{V}_{\tilde{h}_1} \cap \{i\} \neq \emptyset$ & $\exists \tilde{h}_2 : \mathcal{V}_{\tilde{h}_2} \cap \{I\} \neq \emptyset$ & $\tilde{h}_1 \neq \tilde{h}_2$ **then**
        $\mathcal{V}_{\tilde{h}_1} = \mathcal{V}_{\tilde{h}_1} \cup \mathcal{V}_{\tilde{h}_2}$, $\mathcal{V}_{\tilde{h}_2} = \emptyset$
      end if
    end if
  end if
end for
$j = 0$ ▷ Deleting the Empty Sets
for all h **do**
  if $\mathcal{V}_h \neq \emptyset$ **then**
    $j = j + 1$, $\mathcal{V}_j = \mathcal{V}_h$
  end if
end for

quantifies the "amount" of connection between nodes i and j. Hereafter, we focus on strength functions $s(i, j) \geq 1$ such that small values of $s(i, j)$ indicate "strong" connections, whereas large values of $s(i, j)$ indicate "weak" connections. With this framework, we assume that the strongest connected points to i are given by

$$\mathcal{S}_i = \{j : s(i, j) \leq \vartheta\}, \tag{A.4}$$

where $\vartheta \geq 1$ is a given user-defined threshold. Next, by fixing ϑ the function find_strongest_connection(i) returns a point in the set $\mathcal{S}_i$.

A.3.2 Interpolation operator $I_k^{k+1} : \mathbb{R}^{N_k} \to \mathbb{R}^{N_{k+1}}$

Given the disjoint partition $\mathcal{V} = \bigcup_{j=1}^{N_{k+1}} \mathcal{V}_j$, $N_{k+1} \leq N_k$ given by Algorithm 3, it is natural to construct the interpolation operator in a similar manner as done for the smoothed aggregation algebraic multigrid by Vaněk et al. [VMB96].

In particular, we modify the scheme of Vaněk et al. [VMB96] in an energy-minimization framework as follows. We define algebraically smooth error modes to be grid functions with a small Rayleigh quotient, cf. [MR82] and therefore equivalent to the near null-space or low energy modes. Hence, a tentative interpolation operator is constructed in such a way that it preserves the near null-space mode vector $\mathbf{w}_k \in \mathbb{R}^{N_k}$, cf. [MBV99; WCS99; XZ04; Bre+05; Bra+06; OST11]. More precisely, the vector $\mathbf{w}_k$ is the numerical solution of $A_k \mathbf{w}_k = \mathbf{0}_k$ obtained after η smoothing steps with initial guess $\mathbf{w}_k^0 = \mathbf{1}_k$.

We first set

$$[\tilde{I}_{k+1}^k]_{ij} = \begin{cases} w_i & i \in \mathcal{V}_j \\ 0 & otherwise \end{cases}, \quad i = 1, \ldots, N_k,\ j = 1, \ldots, N_{k+1},$$

where w_i is the $i-$th component of vector $\mathbf{w}_k$, and apply the Gram-Schmidt orthonormalization algorithm to each column of $\tilde{I}_{k+1}^k$ to improve conditioning. Then, the interpolation operator is defined by a classical damped-Jacobi smoothing step, i.e.,

$$I_{k+1}^k = (I_k - \omega D_k^{-1} A_k) \tilde{I}_{k+1}^k,$$

where $\omega = 2/3$, D_k is the diagonal of A_k and I_k is the identity matrix.

Remark A.4. Other approaches can be employed to construct the interpolation matrix. For example, since our problem is symmetric and positive definite, we can employ the Krylov-based framework, cf. [OST11; OS11], where we substitute the simple damped Jacobi smoothing step with a fixed number of iterations of the conjugate gradient method.

A.3.3 Evolution measure

In this section we recall the evolution measure proposed by Olson et al. [OST10], which combines the local knowledge of both algebraic smooth error and the behaviour of the interpolation. In the DG framework this measure is necessary to define the strongest connections in Algorithm 3 and in the aggregation scheme, cf. [VMB96; OS11]. This choice is motivated by the fact that most of strength measures proposed in the literature so far are not well suited to take into account the connections between the degrees of freedom typical of DG methods as outlined in [OS11].

In order to take into account the algebraic smooth error, we define $\mathbf{z}_k \in \mathbb{R}^{N_k}$ as

$$\mathbf{z}_k = (I_k - \omega_k D_k^{-1} A_k)^m \mathbf{e}_k(i),$$

where $\mathbf{e}_k(i) \in \mathbb{R}^{N_k}$ is the unit vector centered at $i \in \mathcal{V}$, $\omega_k = 1/\rho(D_k^{-1}A_k)$ and m is an integer that has to be properly chosen.
Then we have to consider the local knowledge of the interpolation. Assume that the interpolation operator is defined as in Section A.3.2. Given a point $i \in \mathcal{V}$ we would like to be able to measure the ability of each column of the tentative interpolation operator $\tilde{I}_{k+1}^k$ to interpolate $\mathbf{z}_k$ for all points j in the algebraic neighborhood of i, i.e. $j \in N_i$, where $N_i = \{j : a_{ij} \neq 0\}$. Therefore this quantity is measured only for points $j \in N_i$, in particular with exact interpolation enforced at point i.

We define the evolution measure as

$$e(i,j) = \left| 1 - \frac{w_j z_i}{w_i z_j} \right| \quad i,j = 1,\dots,N_k,$$

where w_j and z_j are the $j-$th components of vectors $\mathbf{w}_k$, defined in Section A.3.2, and $\mathbf{z}_k$, respectively. Since our problem is symmetric, we define the symmetrized version of the evolution measure as

$$e_S(i,j) = e(i,j) + e(j,i).$$

Finally the symmetric evolution strength function is defined as

$$s(i,j) = \frac{e_S(i,j)}{\min_{k \neq i} e_S(i,k)}. \tag{A.5}$$

The symmetric evolution measure defined above is employed to identify the connections in our algorithm, cf. Section A.4 below. Our algorithm makes use of the following two steps that are the block- and classical aggregations, respectively. On the finest level, we employ Algorithm 3 with the choice of evolution strength function (A.5) and $\vartheta = 1$ in (A.4). On the coarser levels we use the aggregation scheme of Vaněk et al. [VMB96] with still evolution strength function (A.5) but with $\vartheta \in [2,4]$, cf. (A.4).

This choice is guided by the following properties that hold in the DG framework: we employ our block-aggregation for the finest level because it is suited to aggregate the multiple degrees of freedom associated to each grid point, on the other hand we use the classical aggregation for the coarser levels because it builds larger agglomerates and this is better to have less unknowns associated to these levels.

In Figure A.3 we show some examples of block-aggregation for matrices stemming from linear DG discretizations on structured/unstructured triangular and Cartesian meshes and with penalty parameter $\sigma^e = 5, 10, 20, 30$, cf. Section A.2. For $\sigma^e = 30$, we obtain the same aggregations as for $\sigma^e = 20$. For simplicity, these results have been omitted. Moreover, when we compute the evolution measure, we fix $\mathbf{w}_k = \mathbf{1}_k$. Each aggregate set is represented with a distinct number as mark.

We notice that, as expected, our block-aggregation algorithm seems to be fairly insensitive on the value of the penalty parameter.

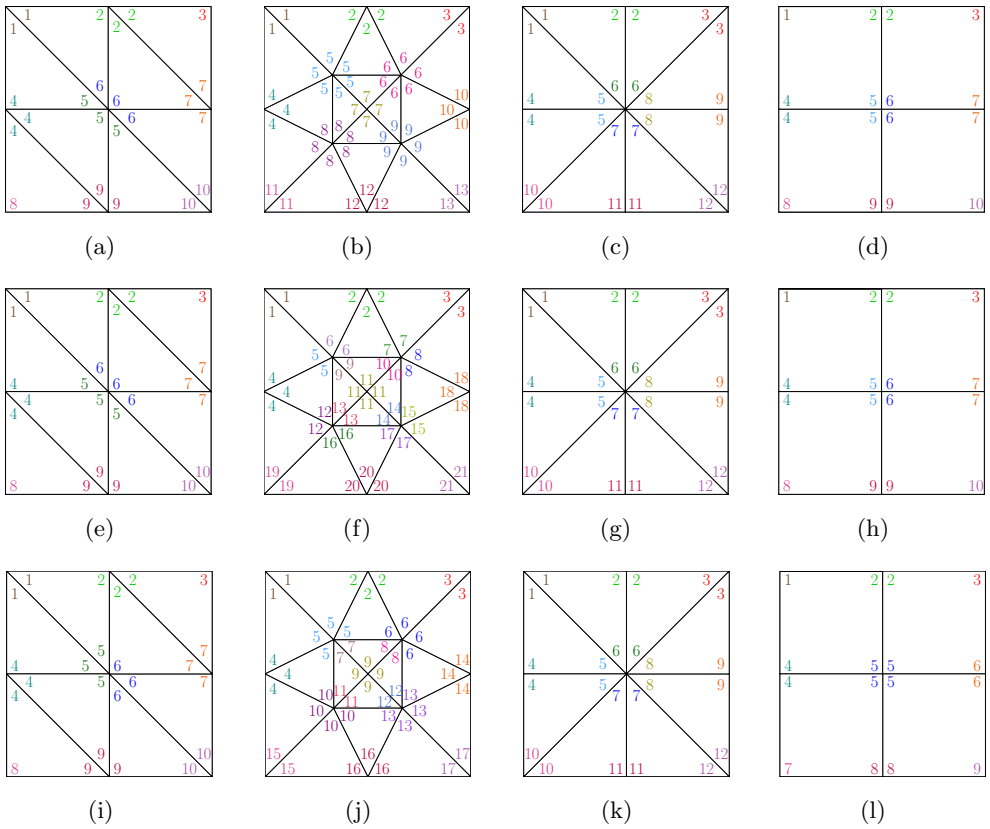

Figure A.3: Examples of block-aggregation for different meshes with $p = 1$, $h \cong 1/2$ and $\sigma^e = 5$ (top), $\sigma^e = 10$ (middle) and $\sigma^e = 20$ (bottom).

A.4 Numerical experiments

In this section we test the robustness and the efficiency of our algebraic multigrid method in solving the linear system of equations stemming from high-order discontinuous finite element discretizations of problem (A.1). We consider a sequence of structured/unstructured triangular and Cartesian meshes with granularity $h = 2^{-l}$, $l = 1, \ldots, 5$, and let the polynomial approximation degree p vary from 1 to 10. Moreover we also take into consideration $l = 6, 7$ when $p = 1$. For each h and p, we obtain a linear system of equations that we solve with our smoothed block-aggregation AMG, cf. Section A.3. At the first step of coarsening, i.e. $k = 1$, we use the block-aggregation algorithm, cf. Algorithm 3 with the strongest evolution connection defined in (A.5) and with $\vartheta = 1$, cf. (A.4). For the coarser levels, i.e. $k = 2, \ldots, K$, we use the classical aggregation of Vaněk et al. [VMB96] with still the evolution strength function in (A.5) and $\vartheta = 2$ in (A.4), cf. also [OS11]. In our numerical experiments we compute the evolution measure with $m = 4$ and $m = 2$ when we solve the problem on triangular and quadrilateral grids, respectively, cf. Section A.3.3 and [OST10; OS11].

For any multigrid level k, the associated interpolation operator is the one proposed in Section A.3.2 with $\eta = 0$ and $\eta = p$ smoothing iterations of classical Gauss-Seidel, where p is the polynomial degree, when the problem is discretized on triangular and quadrilateral meshes, respectively. For the smoothing interpolation we compare both the Jacobi iteration and the Krylov-based framework with 2 and 4 iterations of conjugate gradient method whenever triangular and quadrilateral grids are employed, respectively, cf. Remark A.4. We remark that for moderate values of p, one iteration of CG is enough. In our numerical results we denote by J-smoother/CG-smoother the smoothed block-aggregation algebraic multigrid with Jacobi/CG smoothing interpolation step, cf. Remark A.4.

In our numerical tests we test the W(ν_1,ν_2)-cycle with the classical Gauss-Seidel relaxation as a stand-alone AMG solver. Moreover, we also consider a PCG method with a preconditioner given by the the W(ν_1,ν_2) iteration with a symmetric Gauss-Seidel smoother. We refer to the preconditioned conjugate gradient with W(ν_1,ν_2)-cycle preconditioner as PCG W(ν_1,ν_2)-cycle. We point out that in each step of the proposed algebraic multigrid we employ Jacobi, Gauss-Seidel and conjugate gradient as pointwise-smoothers.

Let N be the iteration counts needed to reduce the initial relative residual below a tolerance $tol = 10^{-8}$, we compute the convergence factor ρ defined by

$$\rho = \exp\left(\frac{1}{N}\log\frac{||\mathbf{r}_N||}{||\mathbf{r}_0||}\right),$$

where $\mathbf{r}_N$ and $\mathbf{r}_0$ are the final and initial residuals, respectively.
In Sections A.4.1 and A.4.2 we report the results when employing the W-cycle algorithm as iterative scheme and as preconditioner for the conjugate gradient method, respectively. We first present results obtained with the W-cycle iteration; in Section A.4.3 we report a comparison between the V- and W-cycle in terms of convergence factor and computational costs. All the proposed solver components are summarized in Figure A.4.

Remark A.5. In case of triangular grids we can employ different sets of interpolation points as degrees of freedom to span the discrete space such as Fekete [TWV00; BSV12], Warburton [War06] and Hesthaven [Hes98] points. Here, for the sake of brevity, we present the results obtained based on employing Fekete nodes. We have tested our AMG algorithm also by using the Warburton [War06] and Hesthaven [Hes98] nodes and our schemes provides the same performance; for the sake of brevity these results have been omitted.

Remark A.6. Algorithm 3 has been tested based on employing different ordering of the degrees of freedom (DOFs). For example on triangular meshes we order DOFs in the two following ways:

1. first we number the DOFs associated with the vertices, then DOFs associated with the internal edges and finally interior DOFs;

2. first we order DOFs associated with the edges in anticlockwise order and then the interior DOFs.

On quadrilateral grids we order DOFs based on employing the lexicographic order. For all the cases our AMG algorithms exhibit the same performance and get consistent results suggesting that Algorithm 3 seems to be robust w.r.t. DOFs ordering. For brevity such a comparison has been omitted.

Remark A.7. The choice of parameters m and ϑ in the aggregation strategy follows from the considerations in work [OS11] together with additional empirical tests.

A.4.1 W-cycle algorithm as iterative scheme

In this section we present some numerical results to investigate the performance of the W-cycle AMG algorithm as iterative scheme. In Figures A.5 and A.6 we compare the W-cycle AMG with J- and CG-smoother in terms of p- and h-scalability, respectively, when employing $\nu_1 = \nu_2 = \nu = 1, 3$ pre- and post-smoothing iterations. We note that if we employ the AMG method with the CG- rather than the J-smoother we obtain better results both in terms of convergence factor and scalability.
We remark that in our tests the W-cycle AMG with J-smoother does not converge for $p = 4, \ldots, 10$ and for $p = 10$ in case of Cartesian and triangular grids, respectively, therefore in Figure A.6 these results have been omitted.

Concerning the h- and p-scalability we observe that the J-smoother AMG method seems to be scalable only if the number of smoothing steps is sufficiently large. Whenever we employ the J-smoother AMG with smaller values of smoothing steps (e.g. $\nu = 1, 2, 3$), we observe in any case hp-weak-scalability for $p = 1, \ldots, p_{max}$ and all tested configurations with $p_{max} = 7$ on triangular and $p_{max} = 3$ on quadrilateral meshes. On the other hand, for both triangular and quadrilateral grids, we have that the CG-smoother AMG method is hp-quasi-scalable for $\nu = 1, 2$ and hp-scalable for $\nu = 3$ for all considered h and p. The difference in h- and p-scalability when varying $\nu = 1, 2, 3$ for AMG method with CG-smoother is small, so it is worth considering the method with $\nu = 1$ because it has lower computational costs. For brevity, in the following we focus on the results obtained on triangular meshes.

In Table A.1 we report the computed convergence factors for the J- and CG-smoother AMG methods on both structured and unstructured triangular grids when varying the number of smoothing iterations $\nu_1 = \nu_2 = \nu = 1, 2, 3$. From the results reported in Table A.1 we can conclude that, as expected, the AMG algorithms performs better for larger number of smoothing iterations.
In Table A.2 we report the results obtained for the J- and CG-smoother AMG methods when varying the number of coarsening levels $K = 2, \ldots, 10$ and solving the problem discretized on structured and unstructured grids, respectively. From the results reported in Table A.2, it seems that all the proposed methods converge

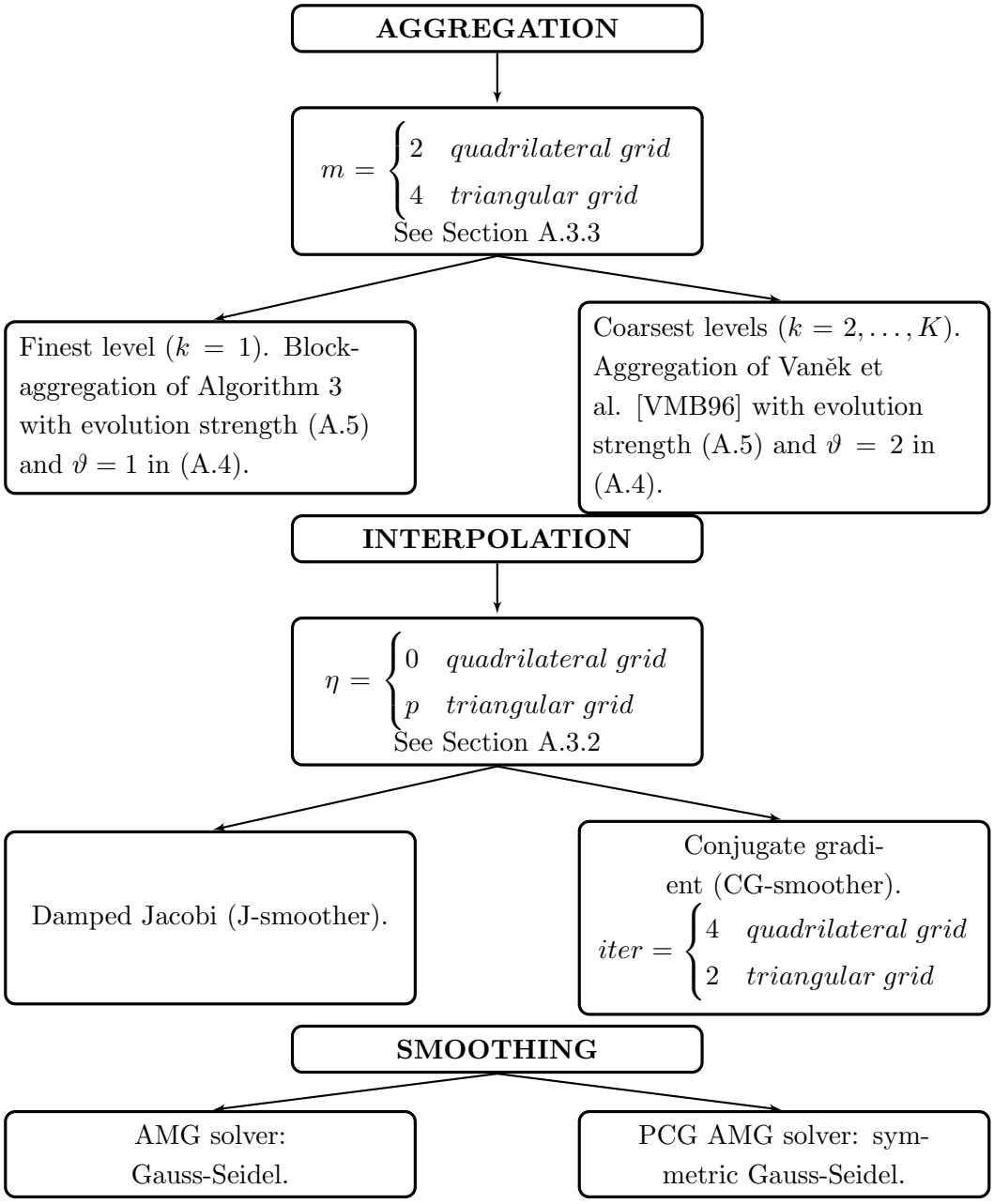

Figure A.4: Aggregation, interpolation and smoothing steps in our AMG algorithm.

uniformly with respect to the number of levels K. As already observed we can summarize the following considerations:

- the J-smoother AMG method seems to be scalable w.r.t. both the discretization parameters h and p, and the number of multigrid levels provided that the number ν of smoothing steps is chosen large enough ($\nu \gg 3$). It seems to be hp-weak-scalable for $p = 1, \ldots, 7$ and all tested h for smaller values of ν;
- the CG-smoother AMG method seems to be scalable w.r.t. both the dis-

cretization parameters h and p, and the number of levels provided that the number of smoothing steps is large enough (in our computations $\nu = 3$);

- the J-smoother AMG method, even if it seems to be only hp-weak-scalable, features lower computational costs compared to the CG-smoother AMG one.

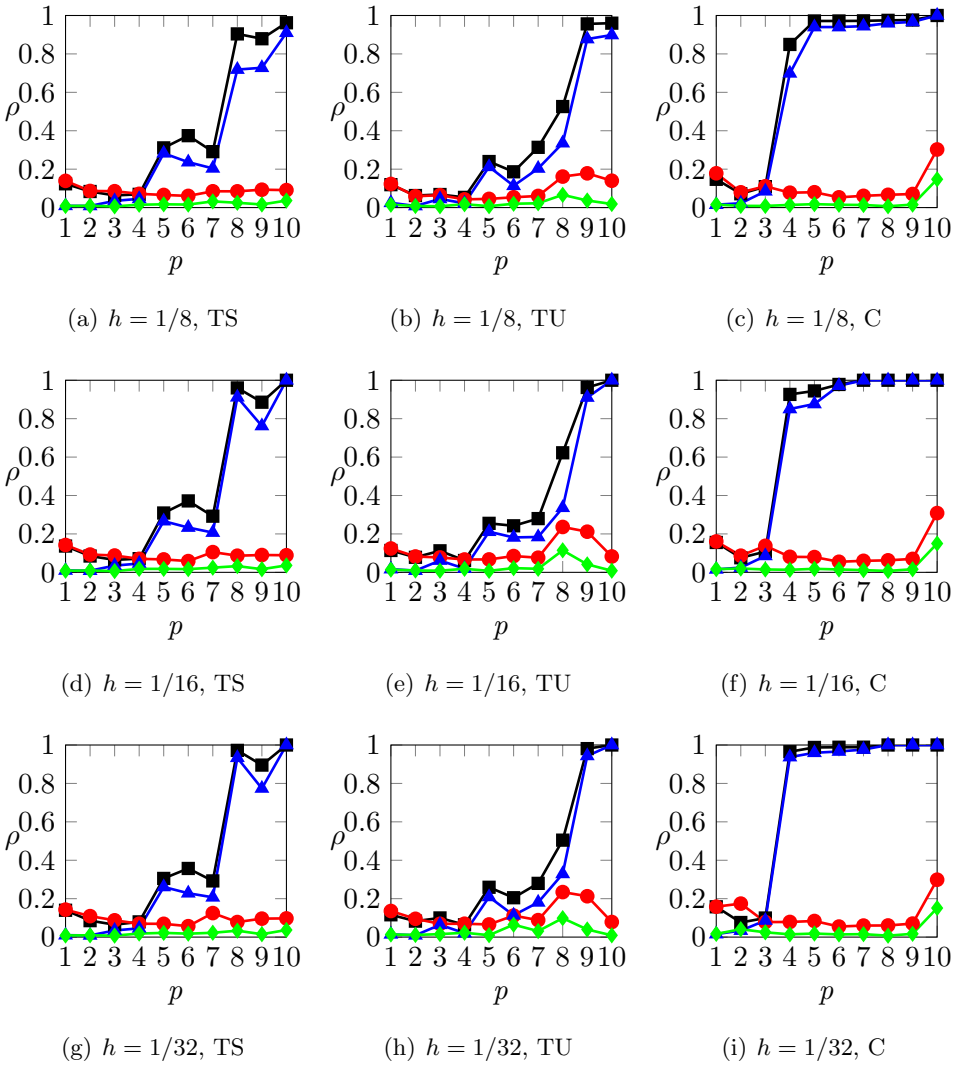

(a) $h = 1/8$, TS (b) $h = 1/8$, TU (c) $h = 1/8$, C

(d) $h = 1/16$, TS (e) $h = 1/16$, TU (f) $h = 1/16$, C

(g) $h = 1/32$, TS (h) $h = 1/32$, TU (i) $h = 1/32$, C

Figure A.5: Convergence factor of the W-cycle algorithm as a function of p for different values of $h = 1/8, 1/16, 1/32$ on structured triangular (TS, left), unstructured triangular (TU, center) and Cartesian (C, right) meshes: J-smoother, $\nu = 1$ (—■—); J-smoother, $\nu = 3$ (—▲—); CG-smoother, $\nu = 1$ (—●—); CG-smoother, $\nu = 3$ (—◆—).

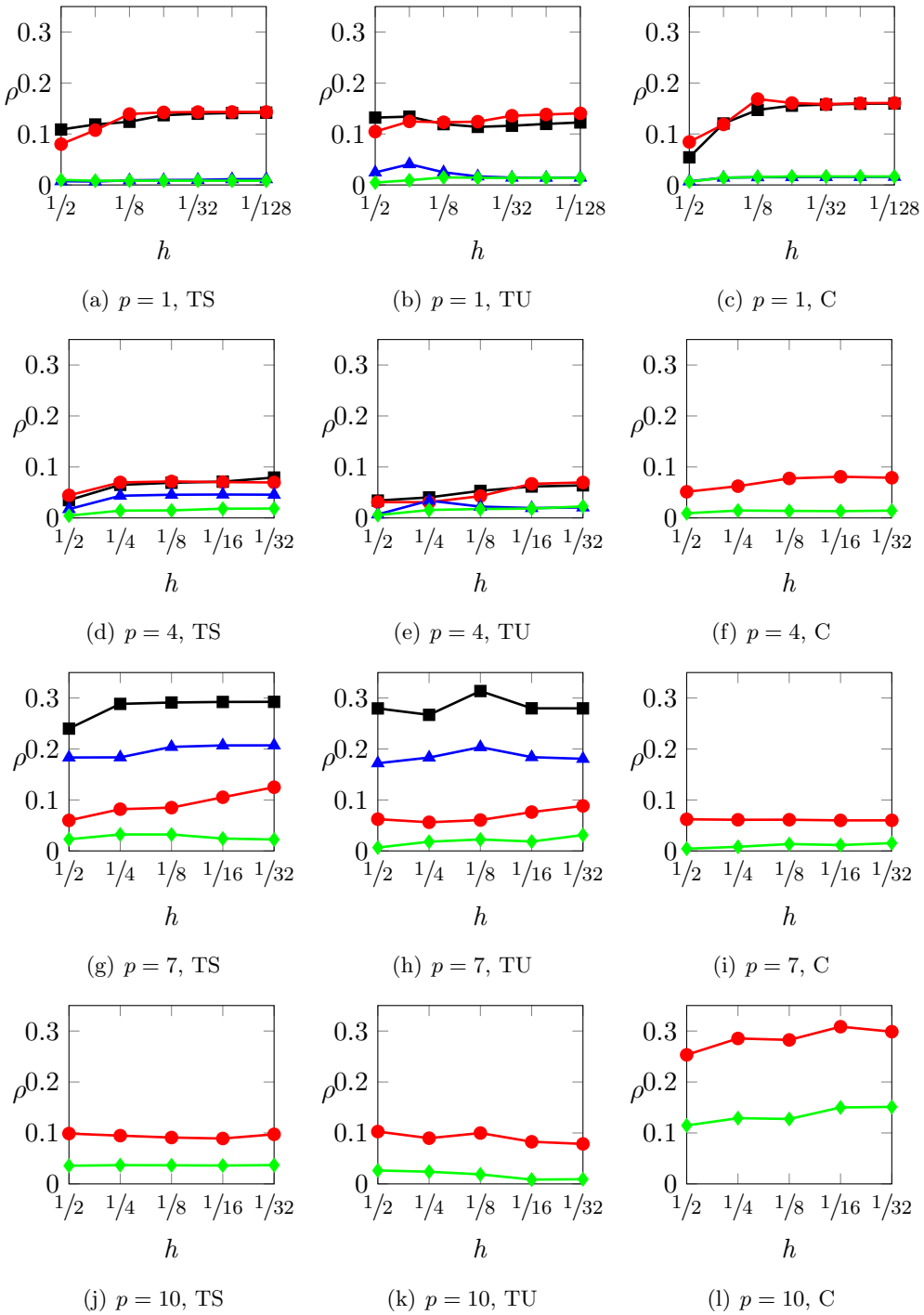

Figure A.6: Convergence factor of the W-cycle algorithm as a function of h for different values of $p = 1, 4, 7, 10$ on structured triangular (TS, left), unstructured triangular (TU, center) and Cartesian (C, right) meshes: J-smoother, $\nu = 1$ (—■—); J-smoother, $\nu = 3$ (—▲—); CG-smoother, $\nu = 1$ (—●—); CG-smoother, $\nu = 3$ (—◆—).

Table A.1: Convergence factor of the W-cycle algorithm as a function of ν, $K = 4$.

Structured Triangular Grids				
	ν	$p = 1$ $h = 1/128$	$p = 4$ $h = 1/32$	$p = 7$ $h = 1/16$
J-smoother	1	0.1418	0.0792	0.2923
	2	0.0282	0.0587	0.2342
	3	0.0113	0.0456	0.2070
CG-smoother	1	0.1432	0.0696	0.1053
	2	0.0228	0.0245	0.0346
	3	0.0082	0.0224	0.0243
Unstructured Triangular Grids				
	ν	$p = 1$ $h = 1/128$	$p = 4$ $h = 1/32$	$p = 7$ $h = 1/16$
J-smoother	1	0.1226	0.0639	0.2798
	2	0.0257	0.0225	0.2096
	3	0.0143	0.0206	0.1840
CG-smoother	1	0.1405	0.0796	0.0762
	2	0.0277	0.0249	0.0217
	3	0.0136	0.0226	0.0184

A.4.2 W-cycle algorithm as preconditioner for preconditioned conjugate gradient method

In this section we repeat the numerical tests presented in Section A.4.1, and we present some numerical results to test the efficiency of the W-cycle algorithm as preconditioner for the PCG method.

In Figures A.7 and A.8 we report the computed convergence factors based on employing the J- and CG-smoother AMG as preconditioners for PCG method in terms of p- and h-scalability, respectively, when employing $\nu_1 = \nu_2 = \nu = 1, 3$ pre- and post-smoothing iterations. We remark that in our tests the J-smoother PCG method does not converge for $p = 4, \dots, 10$ and for $p = 10$ in case of Cartesian and triangular grids, respectively, therefore in Figure A.8 these results have been omitted. For sake of brevity, in the following we report the results obtained with triangular grids.

In Table A.3 we report the convergence factor for the J- and CG-smoother PCG methods both on structured and unstructured triangular grids, respectively, when varying the number of smoothing iterations $\nu_1 = \nu_2 = \nu = 1, 2, 3$.
In Table A.4 we report the results obtained for the J- and CG-smoother PCG methods when varying the number of coarsening levels $K = 2, \dots, 10$ and solving the problem discretized on structured and unstructured triangular grids, respectively.

Table A.2: Convergence factor of the W(1,1)-cycle algorithm as a function of the number of levels K.

Structured Triangular Grids				
	K	$p=1$ $h=1/128$	$p=4$ $h=1/32$	$p=7$ $h=1/16$
J-smoother	2	0.1418	0.0718	0.2853
	3	0.1418	0.0792	0.2919
	5	0.1418	0.0792	0.2924
	7	0.1418	0.0792	0.2924
	10	0.1418	0.0792	0.2924
CG-smoother	2	0.1432	0.0695	0.1053
	3	0.1432	0.0695	0.1053
	5	0.1432	0.0696	0.1053
	7	0.1432	0.0696	0.1053
	10	0.1432	0.0696	0.1053
Unstructured Triangular Grids				
	K	$p=1$ $h=1/128$	$p=4$ $h=1/32$	$p=7$ $h=1/16$
J-smoother	2	0.1225	0.0639	0.2784
	3	0.1226	0.0639	0.2798
	5	0.1226	0.0639	0.2798
	7	0.1226	0.0639	0.2798
	10	0.1226	0.0639	0.2798
CG-smoother	2	0.1405	0.0796	0.0719
	3	0.1405	0.0796	0.0762
	5	0.1405	0.0796	0.0762
	7	0.1405	0.0796	0.0762
	10	0.1405	0.0796	0.0762

For the sake of comparison, in Tables A.3 and A.4 we also report the computed converge factor when we employ the unpreconditioned conjugate gradient (CG) method. In particular we specify that the "–" notation indicates that the CG method does not satisfy the stopping criteria within 1500 iterations.

As before, we observe that the J-smoother seems to be scalable w.r.t. all the discretization parameters and the number of multigrid levels provided that the number of smoothing iterations is sufficiently large and the CG-smoother AMG seems to be scalable for smaller values of ν (in our computations $\nu = 3$). In addition we notice that when we employ the two algorithms as preconditioner for the conjugate gradient method we obtain better values of the convergence factor.

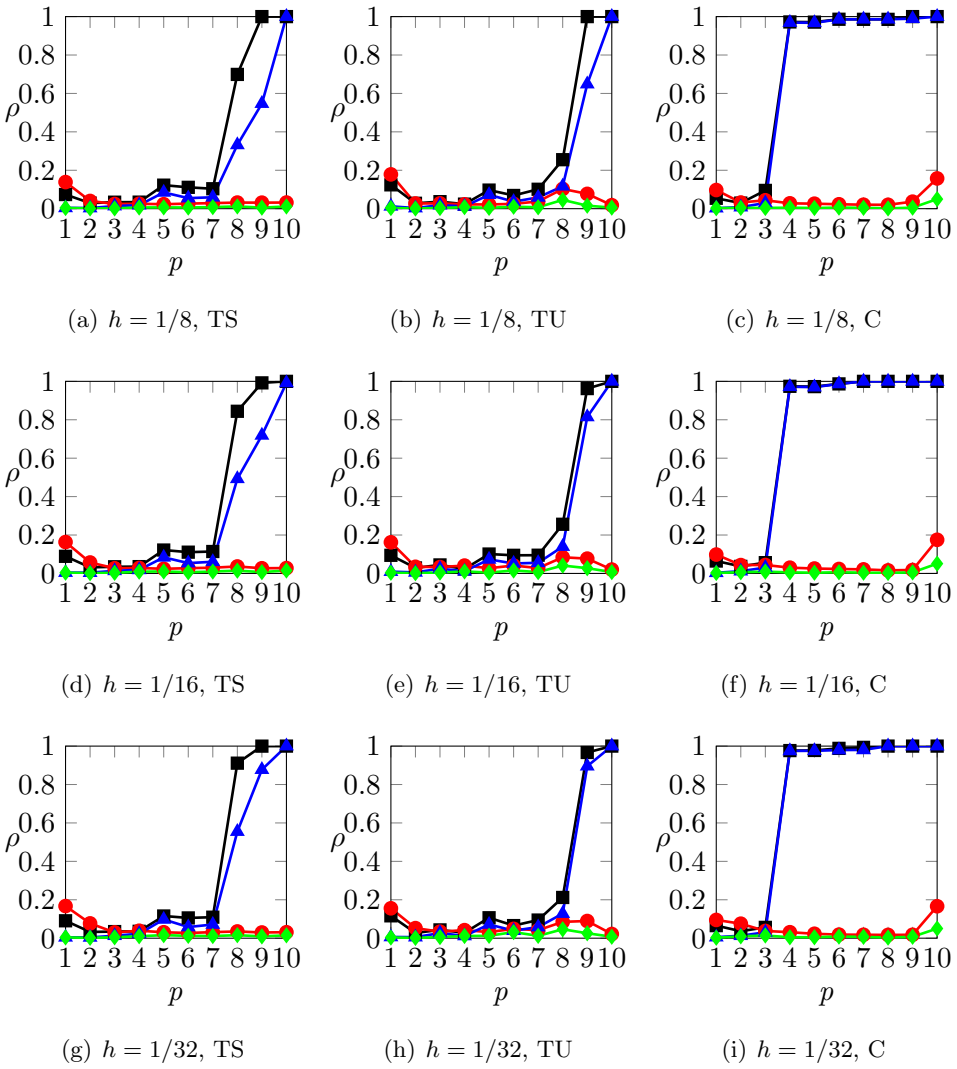

(a) $h = 1/8$, TS (b) $h = 1/8$, TU (c) $h = 1/8$, C

(d) $h = 1/16$, TS (e) $h = 1/16$, TU (f) $h = 1/16$, C

(g) $h = 1/32$, TS (h) $h = 1/32$, TU (i) $h = 1/32$, C

Figure A.7: Convergence factor of the PCG W-cycle algorithm as a function of p for different values of $h = 1/8, 1/16, 1/32$ on structured triangular (TS, left), unstructured triangular (TU, center) and Cartesian (C, right) meshes: J-smoother, $\nu = 1$ (—■—); J-smoother, $\nu = 3$ (—▲—); CG-smoother, $\nu = 1$ (—●—); CG-smoother, $\nu = 3$ (—◆—).

A.4.3 Comparison between V-cycle and W-cycle algorithms

In this section we compare the performance of V- and W-cycle algorithms based on employing both J-smoother and CG-smoother AMG method with $\nu = 1$ pre- and post-smoothing iterations. In this set of experiments the V-cycle and W-cycle AMG algorithm are employed both as iterative scheme and preconditioner for the conjugate gradient to solve the linear system (A.3). We test the V- and W-cycle iterations in case of structured/unstructured triangular and Cartesian grids and we

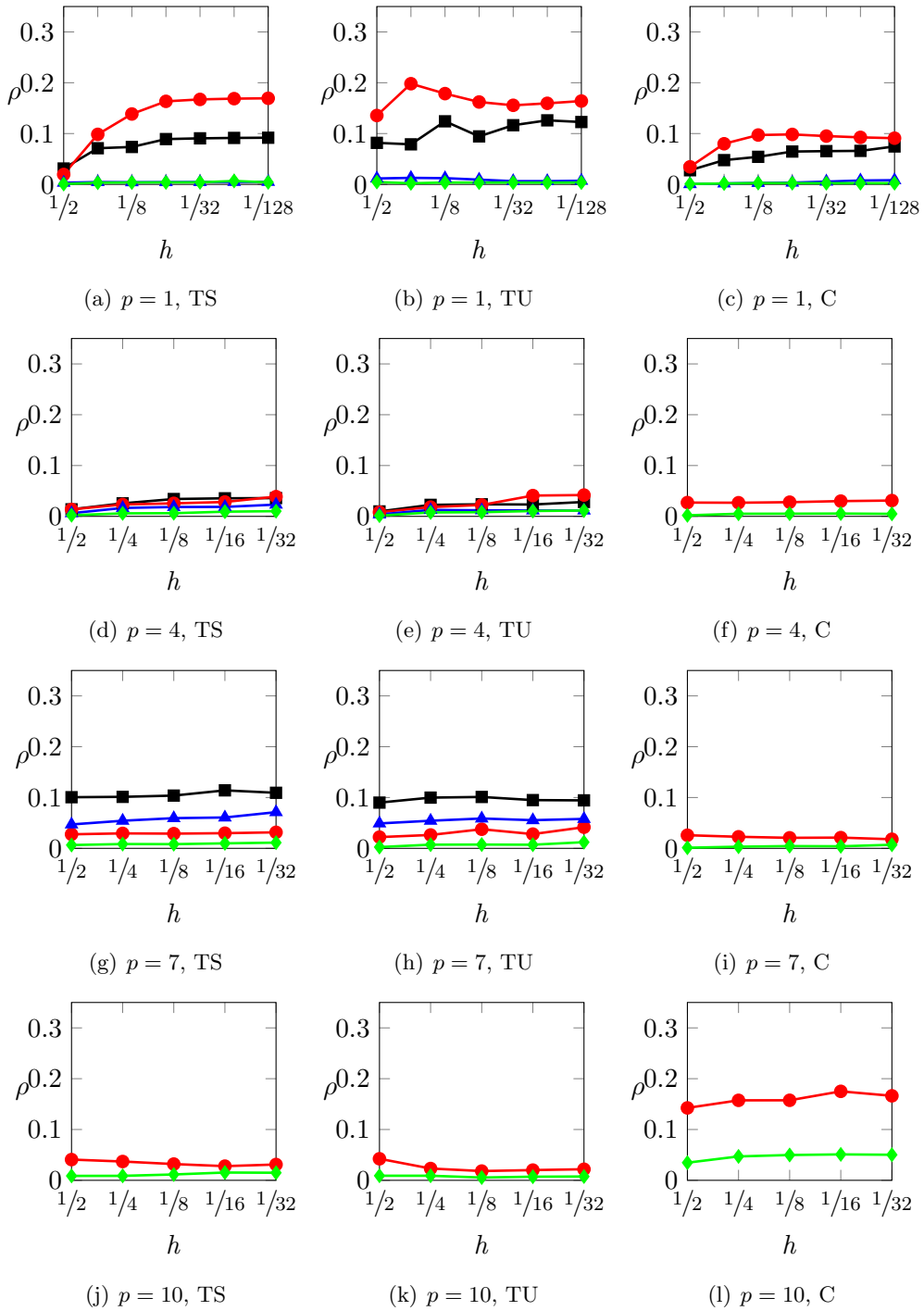

(a) $p = 1$, TS (b) $p = 1$, TU (c) $p = 1$, C

(d) $p = 4$, TS (e) $p = 4$, TU (f) $p = 4$, C

(g) $p = 7$, TS (h) $p = 7$, TU (i) $p = 7$, C

(j) $p = 10$, TS (k) $p = 10$, TU (l) $p = 10$, C

Figure A.8: Convergence factor of the PCG W-cycle algorithm as a function of h for different values of $p = 1, 4, 7, 10$ on structured triangular (TS, left), unstructured triangular (TU, center) and Cartesian (C, right) meshes: J-smoother, $\nu = 1$ (—■—); J-smoother, $\nu = 3$ (—▲—); CG-smoother, $\nu = 1$ (—●—); CG-smoother, $\nu = 3$ (—◆—).

Table A.3: Convergence factor of the PCG W-cycle algorithm as a function of ν, $K = 4$ and comparison with CG.

Structured Triangular Grids				
	ν	$p = 1$ $h = 1/128$	$p = 4$ $h = 1/32$	$p = 7$ $h = 1/16$
J-smoother	1	0.0918	0.0359	0.1141
	2	0.0110	0.0260	0.0773
	3	0.0049	0.0231	0.0607
CG-smoother	1	0.1694	0.0388	0.0298
	2	0.0128	0.0127	0.0126
	3	0.0040	0.0102	0.0098
CG		0.9862	–	–
Unstructured Triangular Grids				
	ν	$p = 1$ $h = 1/128$	$p = 4$ $h = 1/32$	$p = 7$ $h = 1/16$
J-smoother	1	0.1227	0.0283	0.0949
	2	0.0132	0.0137	0.0626
	3	0.0071	0.0115	0.0554
CG-smoother	1	0.1640	0.0419	0.0280
	2	0.0092	0.0143	0.0114
	3	0.0036	0.0114	0.0071
CG		0.9814	0.9836	0.9841

obtain similar performance. For sake of brevity we only report the results for unstructured triangular meshes.

In Figure A.9 and A.10 we compare the V- and W-cycle AMG methods with J- and CG-smoother in terms of p- and h-scalability, respectively, when employed as a standalone iterative scheme and as a preconditioner for the conjugate gradient method with $\nu_1 = \nu_2 = \nu = 1$ pre- and post-smoothing iterations. In both cases we note that if we employ the V- and W-cycle AMG method with the CG- rather than the J-smoother we obtain better results both in terms of convergence factor and scalability. In particular we observe a similar performance for V- and W-cycle, but for large values of p we can appreciate a more robust behavior of the W-cycle. We remark that in our tests the J-smoother AMG does not converge for $p = 10$ in case of triangular grids, therefore in Figure A.10 we report only the results for the CG-smoother AMG when $p = 10$.

In Figure A.11 we compare our CG-smoother AMG with the classical smoothed aggregation scheme by Vaněk et al. [VMB96]. We can conclude that our scheme seems to be both h- and p-scalable, whereas the standard smoothed aggregation

Table A.4: Convergence factor of the PCG W(1,1)-cycle algorithm as a function of the number of levels K and comparison with CG.

Structured Triangular Grids				
	K	$p=1$ $h=1/128$	$p=4$ $h=1/32$	$p=7$ $h=1/16$
J-smoother	2	0.0916	0.0358	0.0953
	3	0.0918	0.0359	0.1127
	5	0.0918	0.0359	0.1146
	7	0.0918	0.0359	0.1146
	10	0.0918	0.0359	0.1146
CG-smoother	2	0.1693	0.0385	0.0298
	3	0.1694	0.0388	0.0298
	5	0.1694	0.0388	0.0298
	7	0.1694	0.0388	0.0298
	10	0.1694	0.0388	0.0298
CG		0.9862	–	–
Unstructured Triangular Grids				
	K	$p=1$ $h=1/128$	$p=4$ $h=1/32$	$p=7$ $h=1/16$
J-smoother	2	0.1227	0.0215	0.0930
	3	0.1228	0.0283	0.0949
	5	0.1227	0.0283	0.0949
	7	0.1227	0.0283	0.0949
	10	0.1227	0.0283	0.0949
CG-smoother	2	0.1640	0.0419	0.0277
	3	0.1640	0.0419	0.0280
	5	0.1640	0.0419	0.0280
	7	0.1640	0.0419	0.0280
	10	0.1640	0.0419	0.0280
CG		0.9814	0.9836	0.9841

seems to be only h-scalable.

In Figure A.12 we compare the V-cycle AMG algorithm employed as iterative scheme when we the damped-Jacobi (J), symmetric successive over-relaxation (SSOR) and conjugate gradient (CG) methods are used for the smoothing interpolation step. Similar performance have been obtained in case of W-cycle AMG iteration, for the sake of brevity these results have been omitted. We observe a worsening of the convergence factor and scalability as we increase the number of Jacobi iterations, whereas we note that the SSOR smoother seems to be efficient only in case where

the number of coarse levels is kept small. Instead the CG-smoother seems to be competitive both in terms of *hp*-scalability and overall efficiency. For the sake of presentation, in the previous sections we report only the results obtained with the J-smoother with 1 iteration and with the CG-smoother.
In Figure A.13 we investigate the AMG setup cost (measured in terms of CPU time) to perform the evaluation of the evolution measure (see Section A.3.3), the aggregation operation (see Section A.3 and Section A.3.1), the interpolation step (see Section A.3.2) and the sum of all runtime. To make a fair comparison we have measured the relative CPU time normalized with respect to the maximum CPU time (obtained with the total runtime of the test with $p = 1$, $h = 1/128$). For sake of brevity, we show only the results when the CG-smoother is employed in the smoothing interpolation step. We observe that the most expensive operation is the computation of the strength measure. We next investigate the memory requirements of our AMG algorithm.
In Figure A.14 we report the dimension and the sparsity pattern (number of non-zero entries in the matrix) of the fine and coarser matrices (left, center) and a comparison of the computational costs between the V- and W-cycle in terms of runtime per iteration as a function of the number of coarse levels (right). We focus the discussion on the computational costs by considering only CG-smoother AMG since from the results reported in Sections A.4.1 and A.4.2 it seems to have a better behavior in terms of scalability. For sake of brevity we only show the results for the AMG method employed as iterative scheme, similar performance were observed if the AMG method is employed as preconditioner for CG method.
Concerning the overall efficiency, we can conclude that the W-cycle algorithm seems to be more robust than the V-cycle at least for high values of p, but it is more expensive in terms of overall runtime.

A.5 Concluding remarks

We have presented a new algebraic multigrid method for solving the linear systems of equations stemming from high-order discontinuous Galerkin finite element discretizations of second order elliptic problems.
We have extended the standard algebraic multigrid approach of Vaněk et al. [VMB96], by proposing a new algebraic block-aggregation scheme that suitably handles the redundancy of the degrees of freedom associated to the same grid point. In addition, we have employed a different definition of strength function of connections and an adaptive smoothed aggregation method, following the ideas of Olson and Schroder [OS11]. In particular we modified the first step of geometric coarsening within an algebraic framework leading our schemes to be purely AMG methods for high-order DG discretizations. A set of numerical experiments carried out on both triangular and quadrilateral grids suggest that the proposed AMG methods are scalable with

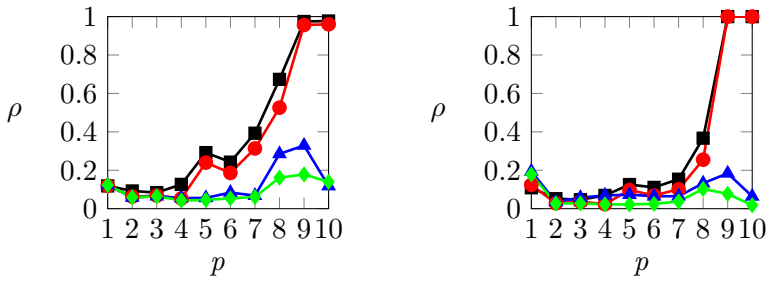

(a) $h = 1/8$

(b) $h = 1/8$

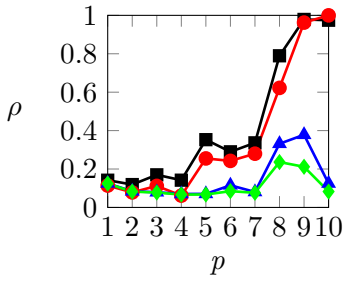

(c) $h = 1/16$

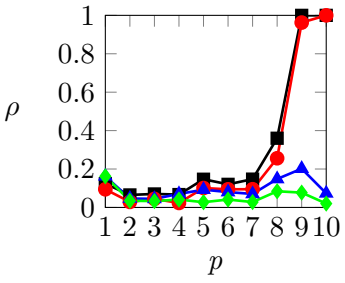

(d) $h = 1/16$

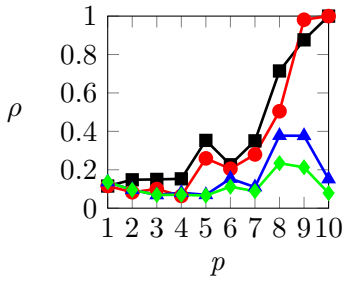

(e) $h = 1/32$

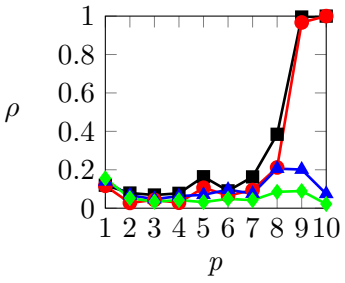

(f) $h = 1/32$

Figure A.9: Convergence factor of the V- and W-cycle algorithms with $\nu = 1$ as a function of p for different values of $h = 1/8, 1/16, 1/32$ as iterative scheme (left) and as preconditioner for CG method (right): V-cycle, J-smoother (—■—); V-cycle, CG-smoother (—▲—); W-cycle, J-smoother (—●—); W-cycle, CG-smoother (—◆—).

respect to the mesh-size h, the polynomial degree p and the number of multigrid levels.

Possible further developments include the testing for time-stepping solutions and in 3D problems. In addition we will expand the proposed methods to variable diffusion coefficient, cf. [Sch12]. We could also deepen new algebraic multigrid methods whenever modal shape functions are employed to span the discrete DG space. Finally, concerning the computational aspects we point out that for higher values of p the construction of the coarser matrices and interpolation operators becomes more expensive, therefore we should develop a new implementation based on massively

parallel strategies. These are some of the many goals to be achieved to possibly apply AMG methods to elastodynamics equations.

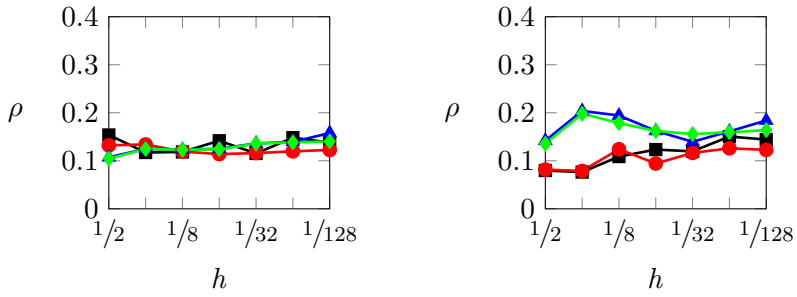

(a) $p = 1$

(b) $p = 1$

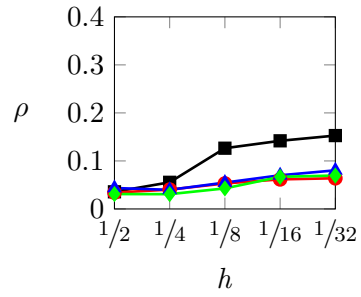

(c) $p = 4$

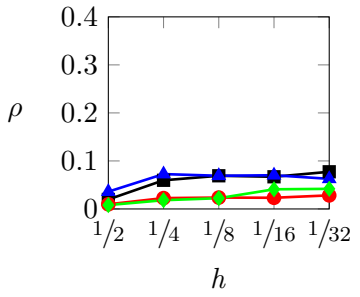

(d) $p = 4$

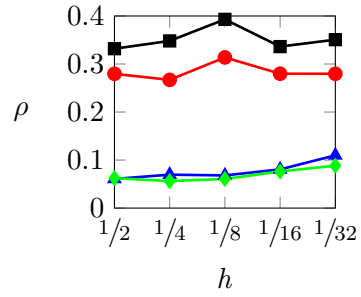

(e) $p = 7$

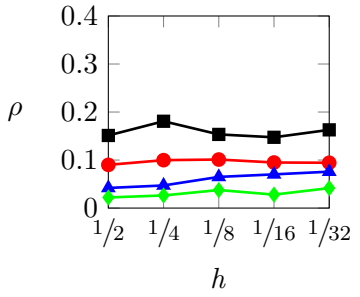

(f) $p = 7$

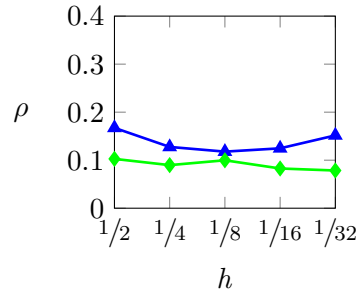

(g) $p = 10$

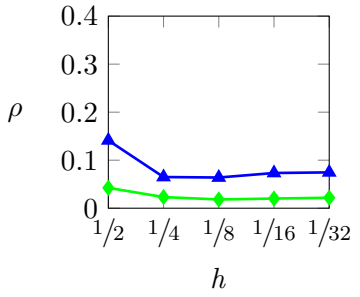

(h) $p = 10$

Figure A.10: Convergence factor of the V- and W-cycle algorithms with $\nu = 1$ as a function of h for different values of $p = 1, 4, 7, 10$ as iterative scheme (left) and as preconditioner for CG method (right): V-cycle, J-smoother (—■—); V-cycle, CG-smoother (—▲—); W-cycle, J-smoother (—●—); W-cycle, CG-smoother (—◆—).

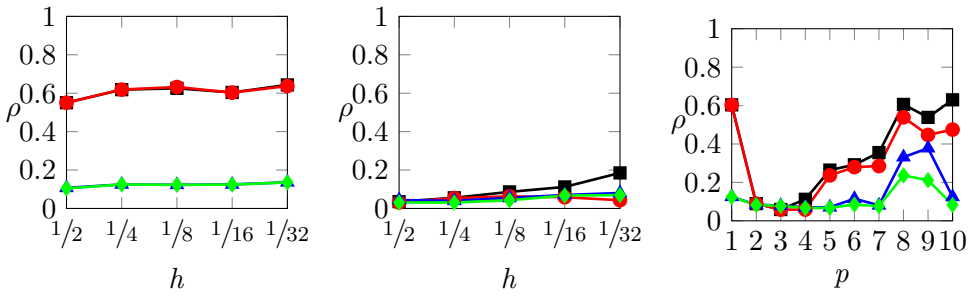

(a) $p = 1$ (b) $p = 4$ (c) $h = 1/16$

Figure A.11: Convergence factor of the V- and W-cycle algorithms as iterative scheme with $\nu = 1$ as a function of h (left, center) and p (right) : V-cycle, SA (—■—); V-cycle, CG-smoother (—▲—); W-cycle, SA (—●—); W-cycle, CG-smoother (—◆—)

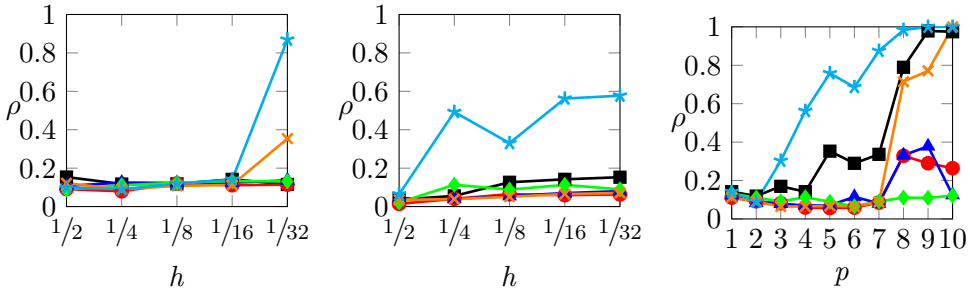

(a) $p = 1$ (b) $p = 4$ (c) $h = 1/16$

Figure A.12: Convergence factor of the V-cycle algorithm as iterative scheme with $\nu = 1$ as a function of h (left, center) and p (right) : J-smoother, $iter = 1$ (—■—); J-smoother, $iter = 3$ (—×—), J-smoother, $iter = 8$ (—✳—), CG-smoother, $iter = 2$ (—▲—); SSOR-smoother, $iter = 1$ (—●—); SSOR-smoother, $iter = 3$ (—◆—)

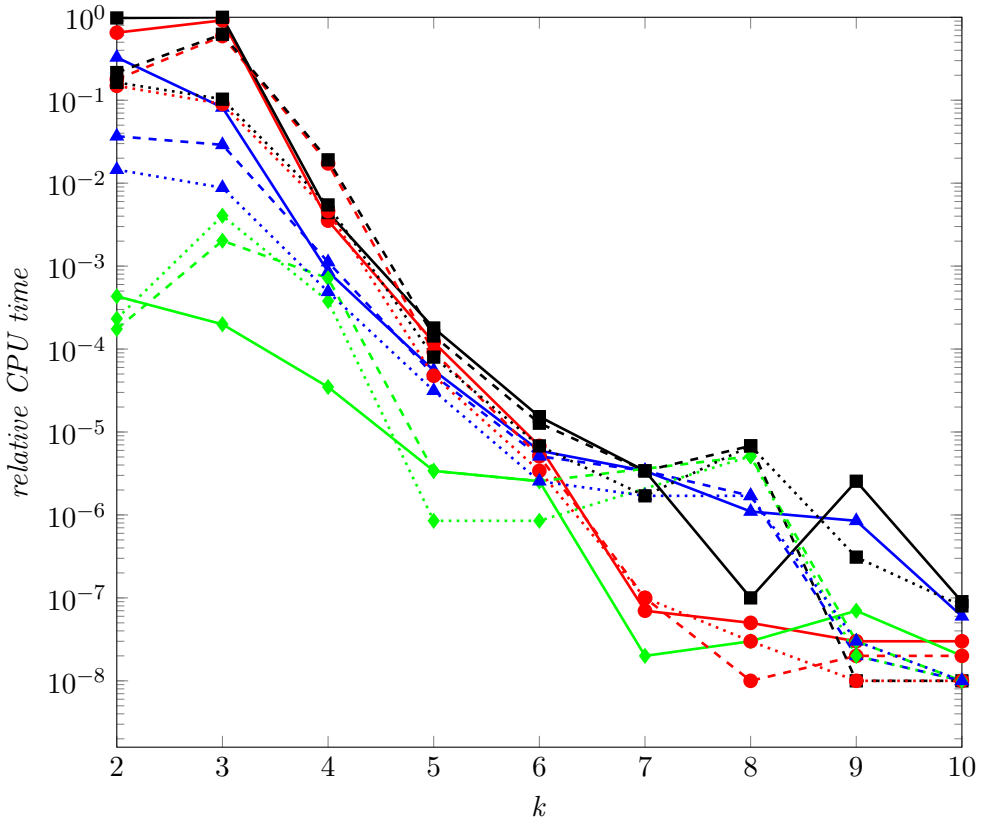

Figure A.13: Relative CPU time (normalized with respect to the maximum CPU time) of the setup phase of the AMG algorithms as a function of the number of coarse levels $k = 2, \ldots, K$, CG-smoother. $p = 1$, $h = 1/128$: total (—■—), evolution (—●—); aggregation (—▲—); interpolation (—♦—) cost. $p = 4$, $h = 1/32$: total (- ■ -), evolution (- ● -); aggregation (- ▲ -); interpolation (- ♦ -) cost. $p = 7$, $h = 1/16$: total (···■···), evolution (···●···); aggregation (···▲···); interpolation (···♦···) cost.

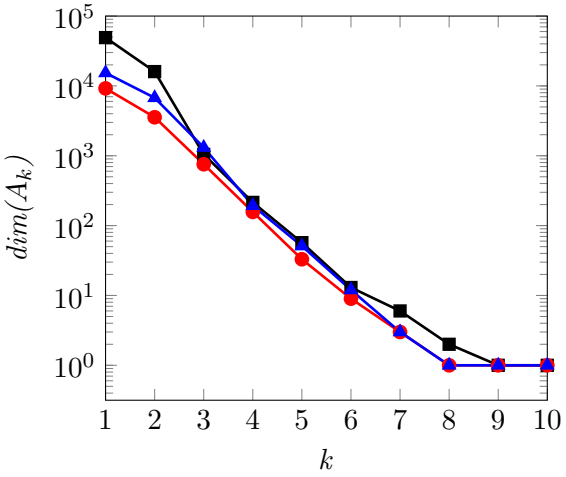

(a)

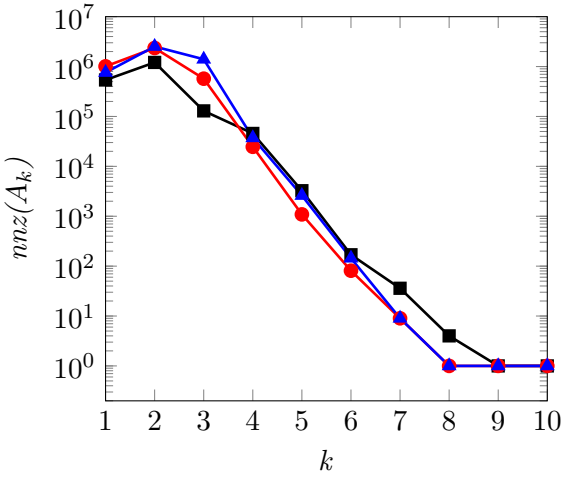

(b)

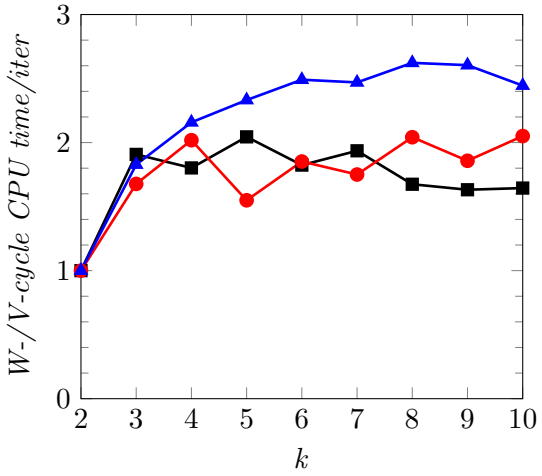

(c)

Figure A.14: Dimension (top), number of non-zero entries of the matrices A_k (middle) and ratio of the CPU time per iteration of the V- and W-cycle algorithms with $\nu = 1$ (bottom) as a function of the number of coarser levels $k = 1, \ldots, K$, CG-smoother: $p = 1$, $h = 1/128$ (—■—); $p = 4$, $h = 1/32$ (—▲—); $p = 7$, $h = 1/16$ (—●—).

Bibliography

[AA+10] L. Al Atik, N. Abrahamson, J. Bommer, F. Scherbaum, F. Cotton, and N. Kuehn. "The variability of ground-motion prediction models and its components". In: *Seismol. Res. Lett.* 81.5 (2010), pp. 794–801.

[ABM19] P. Antonietti, F. Bonaldi, and I. Mazzieri. "Simulation of 3D elasto-acoustic wave propagation based on a Discontinuous Galerkin Spectral Element method". In: *MOX report, 26/2019* (2019).

[ABM20] P. F. Antonietti, F. Bonaldi, and I. Mazzieri. "A high-order discontinuous Galerkin approach to the elasto-acoustic problem". In: *Comput. Methods Appl. Mech. Engrg.* 358 (2020), pp. 112634, 29.

[Abr+08] N. Abrahamson, G. Atkinson, D. Boore, Y. Bozorgnia, K. Campbell, B. Chiou, I. Idriss, W. Silva, and R. Youngs. "Comparisons of the NGA ground-motion relations". In: *Earthq. Spectra* 24.1 (2008), pp. 45–66.

[Ada75] R. A. Adams. *Sobolev spaces*. Pure and Applied Mathematics, Vol. 65. Academic Press, New York-London, 1975, pp. xviii+268.

[AFV20] P. F. Antonietti, C. Facciolà, and M. Verani. "Unified analysis of discontinuous Galerkin approximations of flows in fractured porous media on polygonal and polyhedral grids". In: *Math. Eng.* 2.2 (2020), pp. 340–385.

[Agm65] S. Agmon. *Lectures on elliptic boundary value problems*. Prepared for publication by B. Frank Jones, Jr. with the assistance of George W. Batten, Jr. Van Nostrand Mathematical Studies, No. 2. D. Van Nostrand Co. Inc. Princeton N.J.-Toronto-London, 1965, pp. v+291.

[AH11] P. F. Antonietti and P. Houston. "A class of domain decomposition preconditioners for *hp*-discontinuous Galerkin finite element methods". In: *J. Sci. Comput.* 46.1 (2011), pp. 124–149.

[AHH01] B. T. Aagaard, T. H. Heaton, and J. F. Hall. "Dynamic earthquake ruptures in the presence of lithostatic normal stresses: Implications for friction models and heat production". In: *B. Seismol. Soc. Am.* 91.6 (2001), pp. 1765–1796.

[AKJ68] Z Alterman and F. Karal Jr. "Propagation of elastic waves in layered media by finite difference methods". In: *B. Seismol. Soc. Am.* 58.1 (1968), pp. 367–398.

[AM18] P. F. Antonietti and I. Mazzieri. "High-order Discontinuous Galerkin methods for the elastodynamics equation on polygonal and polyhedral meshes". In: *Comput. Methods Appl. Mech. Engrg.* 342 (2018), pp. 414–437.

[AM20] P. F. Antonietti and L. Melas. "Algebraic multigrid schemes for high-order nodal discontinuous Galerkin methods". In: *SIAM J. Sci. Comput.* 42.2 (2020), A1147–A1173.

[AMM20] P. F. Antonietti, I. Mazzieri, and F. Migliorini. "A space-time discontinuous Galerkin method for the elastic wave equation". In: *J. Comput. Phys.* 419 (2020), pp. 109685, 26.

[Amp02] J.-P. Ampuero. "Etude physique et numérique de la nucléation des séismes". In: *PhD Thesis, University of Paris VII, France* (2002).

[AMR14] S. Amdouni, M. Moakher, and Y. Renard. "A stabilized Lagrange multiplier method for the enriched finite-element approximation of Tresca contact problems of cracked elastic bodies". In: *Comput. Methods Appl. Mech. Engrg.* 270 (2014), pp. 178–200.

[Ana+99] A. Anastasiadis, M Demosthenous, C. Karakostas, N Klimis, B Lekidis, B. Margaris, C. Papaioannou, C Papazachos, and N. Theodulidis. *The Athens (Greece) earthquake of September 7, 1999: preliminary report on strong motion data and structural response.* Multidisciplinary Center for Earthquake Engineering Research, 1999.

[And73] D. Andrews. "A numerical study of tectonic stress release by underground explosions". In: *B. Seismol. Soc. Am.* 63.4 (1973), pp. 1375–1391.

[And76] D. Andrews. "Rupture propagation with finite stress in antiplane strain". In: *J. Geophys. Res.* 81.20 (1976), pp. 3575–3582.

[And99] D. Andrews. "Test of two methods for faulting in finite-difference calculations". In: *B. Seismol. Soc. Am.* 89.4 (1999), pp. 931–937.

[Ant+ a] P. F. Antonietti, P. Houston, G. Pennesi, and E Suli. "An agglomeration-based massively parallel non-overlapping additive Schwarz preconditioner for high-order discontinuous Galerkin methods on polytopic grids". In: *Math. Comp.* (to appear).

[Ant+12] P. F. Antonietti, I. Mazzieri, A. Quarteroni, and F. Rapetti. "Non-conforming high order approximations of the elastodynamics equation". In: *Comput. Methods Appl. Mech. Engrg.* 209/212 (2012), pp. 212–238.

[Ant+16] P. F. Antonietti, B. Ayuso de Dios, I. Mazzieri, and A. Quarteroni. "Stability analysis of discontinuous Galerkin approximations to the elastodynamics problem". In: *J. Sci. Comput.* 68.1 (2016), pp. 143–170.

[Ant+17] P. F. Antonietti, P. Houston, X. Hu, M. Sarti, and M. Verani. "Multigrid algorithms for *hp*-version interior penalty discontinuous Galerkin methods on polygonal and polyhedral meshes". In: *Calcolo* 54.4 (2017), pp. 1169–1198.

[Ant+18a] P. F. Antonietti, A. Ferroni, I. Mazzieri, R. Paolucci, A. Quarteroni, C. Smerzini, and M. Stupazzini. "Numerical modeling of seismic waves by discontinuous Spectral Element methods". In: *ESAIM: Proceedings and Surveys* 61 (2018), pp. 1–37.

[Ant+18b] P. Antonietti, N. Dal Santo, I. Mazzieri, and A. Quarteroni. "A high-order discontinuous Galerkin approximation to ordinary differential equations with applications to elastodynamics". In: *IMA J. Numer. Anal.* 38.4 (2018), pp. 1709–1734.

[Ant+20] P. F. Antonietti, I. Mazzieri, M. Muhr, V. Nikolić, and B. Wohlmuth. "A high-order discontinuous Galerkin method for nonlinear sound waves". In: *J. Comput. Phys.* 415 (2020), pp. 109484, 27.

[Ant+21] P. F. Antonietti, I. Mazzieri, L. Melas, R. Paolucci, A. Quarteroni, C. Smerzini, and M. Stupazzini. "Three-dimensional physics-based earthquake ground motion simulations for seismic risk assessment in densely populated urban areas". In: *Math. Eng.* 3.2 (2021), pp. 1–31.

[AP18] P. F. Antonietti and G. Pennesi. "V-cycle multigrid algorithms for discontinuous Galerkin methods on non-nested polytopic meshes." In: *J. Sci. Comput.* (2018).

[AR02] K. Aki and P. G. Richards. *Quantitive Seismology: Theory and Methods*. Vol. 1. Freeman, San Francisco, California, 2002.

[Arg+13] A. Argyraki, E. Kelepertzis, G. Fligos, E. Athanasiou, K. Gardiakos, and V. Kourgia. "Geochemical mapping of urban soils in Athens, Greece - Preliminary results". In: *Bull. Geol. Soc. Greece* 47.2 (2013), pp. 901–909.

[Arn+01] D. N. Arnold, F. Brezzi, B. Cockburn, and L. D. Marini. "Unified analysis of discontinuous Galerkin methods for elliptic problems". In: *SIAM J. Numer. Anal.* 39.5 (2001/02), pp. 1749–1779.

[Arn82] D. N. Arnold. "An interior penalty finite element method with discontinuous elements". In: *SIAM J. Numer. Anal.* 19.4 (1982), pp. 742–760.

[ASV15] P. F. Antonietti, M. Sarti, and M. Verani. "Multigrid algorithms for *hp*-discontinuous Galerkin discretizations of elliptic problems". In: *SIAM J. Numer. Anal.* 53.1 (2015), pp. 598–618.

[AW09] T. I. Allen and D. J. Wald. "On the use of high-resolution topographic data as a proxy for seismic site conditions (VS30)". In: *B. Seismol. Soc. Am.* 99.2A (2009), pp. 935–943.

[Bas+12] F. Bassi, L. Botti, A. Colombo, D. A. Di Pietro, and P. Tesini. "On the flexibility of agglomeration based physical space discontinuous Galerkin discretizations". In: *J. Comput. Phys.* 231.1 (2012), pp. 45–65.

[Bay+86] A. Bayliss, K. Jordan, B. LeMesurier, and E Turkel. "A fourth-order accurate finite-difference scheme for the computation of elastic waves". In: *B. Seismol. Soc. Am.* 76.4 (1986), pp. 1115–1132.

[BBC14] F. Bassi, L. Botti, and A. Colombo. "Agglomeration-based physical frame dG discretizations: an attempt to be mesh free". In: *Math. Models Methods Appl. Sci.* 24.8 (2014), pp. 1495–1539.

[BBS12] P. Bastian, M. Blatt, and R. Scheichl. "Algebraic multigrid for discontinuous Galerkin discretizations of heterogeneous elliptic problems". In: *Numer. Linear Algebra Appl.* 19.2 (2012), pp. 367–388.

[BC08] J. W. Baker and C. A. Cornell. "Uncertainty propagation in probabilistic seismic loss estimation". In: *Struct. Saf.* 30.3 (2008), pp. 236–252.

[BCS09] S. C. Brenner, J. Cui, and L.-Y. Sung. "Multigrid methods for the symmetric interior penalty method on graded meshes". In: *Numer. Linear Algebra Appl.* 16.6 (2009), pp. 481–501.

[BD18] M. Barboteu and S. Dumont. "A primal-dual active set method for solving multi-rigid-body dynamic contact problems". In: *Math. Mech. Solids* 23.3 (2018), pp. 489–503.

[BeHW07] S. Brunß en, S. Hüeber, and B. Wohlmuth. “Contact dynamics with Lagrange multipliers”. In: *IUTAM Symposium on Computational Methods in Contact Mechanics*. Vol. 3. IUTAM Bookser. Springer, Dordrecht, 2007, pp. 17–32.

[BHM00] W. L. Briggs, V. E. Henson, and S. F. McCormick. *A multigrid tutorial*. Second. Society for Industrial and Applied Mathematics (SIAM), Philadelphia, PA, 2000, pp. xii+193.

[Biz+01] A Bizzarri, M Cocco, D. Andrews, and E. Boschi. “Solving the dynamic rupture problem with different numerical approaches and constitutive laws”. In: *Geophys. J. Int.* 144.3 (2001), pp. 656–678.

[BM87] W. Briggs and S. McCormick. “Introduction”. In: *Multigrid methods*. Vol. 3. Frontiers Appl. Math. SIAM, Philadelphia, PA, 1987, pp. 1–30.

[BM92] C. Bernardi and Y. Maday. *Approximations spectrales de problèmes aux limites elliptiques*. Vol. 10. Mathématiques & Applications (Berlin) [Mathematics & Applications]. Springer-Verlag, Paris, 1992, pp. ii+242.

[BO07] S. C. Brenner and L. Owens. “A W-cycle algorithm for a weakly overpenalized interior penalty method”. In: *Comput. Methods Appl. Mech. Engrg.* 196.37-40 (2007), pp. 3823–3832.

[Boo72] D. M. Boore. “Finite difference methods for seismic wave propagation in heterogeneous materials”. In: *Seismology: Surface Waves and Earth Oscillations*. Vol. 11. Methods in Computational Physics: Advances in Research and Applications. Academic Press Inc, 1972, pp. 1–37.

[Bra+06] J. Brannick, M. Brezina, S. MacLachlan, T. Manteuffel, S. McCormick, and J. Ruge. “An energy-based AMG coarsening strategy”. In: *Numer. Linear Algebra Appl.* 13.2-3 (2006), pp. 133–148.

[Bra18] B. Bradley. “On-going challenges in physics-based ground motion prediction and insights from the 2010–2011 Canterbury and 2016 Kaikoura, New Zealand earthquakes”. In: *Soil Dyn. Earthq. Eng.* (2018).

[Bre04] S. C. Brenner. “Korn’s inequalities for piecewise H^1 vector fields”. In: *Math. Comp.* 73.247 (2004), pp. 1067–1087.

[Bre+05] M. Brezina, R. Falgout, S. MacLachlan, T. Manteuffel, S. McCormick, and J. Ruge. “Adaptive smoothed aggregation (αSA) multigrid”. In: *SIAM Rev.* 47.2 (2005), pp. 317–346.

[Bre+11] S. C. Brenner, J. Cui, T. Gudi, and L.-Y. Sung. “Multigrid algorithms for symmetric discontinuous Galerkin methods on graded meshes”. In: *Numer. Math.* 119.1 (2011), pp. 21–47.

[BS08] S. Banerjee and M. Shinozuka. "Mechanistic quantification of RC bridge damage states under earthquake through fragility analysis". In: *Probabilist. Eng. Mech.* 23.1 (2008), pp. 12–22.

[BS87a] I. Babuška and M. Suri. "The *hp* version of the finite element method with quasiuniform meshes". In: *ESAIM: Mathematical Modelling and Numerical Analysis-Modélisation Mathématique et Analyse Numérique* 21.2 (1987), pp. 199–238.

[BS87b] I. Babuška and M. Suri. "The *h-p* version of the finite element method with quasi-uniform meshes". In: *RAIRO Modél. Math. Anal. Numér.* 21.2 (1987), pp. 199–238.

[BSV12] M. Briani, A. Sommariva, and M. Vianello. "Computing Fekete and Lebesgue points: simplex, square, disk". In: *J. Comput. Appl. Math.* 236.9 (2012), pp. 2477–2486.

[BZ05] S. C. Brenner and J. Zhao. "Convergence of multigrid algorithms for interior penalty methods". In: *Appl. Numer. Anal. Comput. Math.* 2.1 (2005), pp. 3–18.

[Cal+06] G. M. Calvi, R. Pinho, G. Magenes, J. J. Bommer, L. F. Restrepo-Vélez, and H. Crowley. "Development of seismic vulnerability assessment methodologies over the past 30 years". In: *ISET Journal of Earthquake Technology* 43.3 (2006), pp. 75–104.

[Can+06] C. Canuto, M. Y. Hussaini, A. Quarteroni, and T. A. Zang. *Spectral methods – Fundamentals in single domains*. Scientific Computation. Springer-Verlag, Berlin, 2006, pp. xxii+563.

[Can+07] C. Canuto, M. Y. Hussaini, A. Quarteroni, and T. A. Zang. *Spectral methods – Evolution to complex geometries and applications to fluid dynamics*. Scientific Computation. Springer, Berlin, 2007, pp. xxx+596.

[Cas+02] F. Casadei, E. Gabellini, G. Fotia, F. Maggio, and A. Quarteroni. "A mortar spectral/finite element method for complex 2D and 3D elastodynamic problems". In: *Comput. Methods Appl. Mech. Engrg.* 191.45 (2002), pp. 5119–5148.

[Cau+08] M. Causse, F. Cotton, C. Cornou, and P.-Y. Bard. "Calibrating Median and Uncertainty Estimates for a Practical Use of Empirical Green's Functions Technique". In: *B. Seismol. Soc. Am.* 98.1 (Feb. 2008), pp. 344–353.

[Cau+15a] C. Cauzzi, E. Faccioli, M. Vanini, and A. Bianchini. "Updated predictive equations for broadband (0.01–10 s) horizontal response spectra and peak ground motions, based on a global dataset of digital acceleration records". In: *B. Earthq. Eng.* 13.6 (2015), pp. 1587–1612.

[Cau+15b] C. Cauzzi, I. Kalogeras, N. Melis, M. Stupazzini, I. Mazzieri, and J. Clinton. "Preliminary Results on the Seismic Response of the Acropolis of Athens (Greece) through Recorded Earthquake Data and Numerical Simulations". In: *Proceedings of the 6th International Conference of Earthquake Geotechnical Engineering (ICEGE)*. Paper 637, 2015.

[CCR09] A. Capatina, M. Cocou, and M. Raous. "A class of implicit variational inequalities and applications to frictional contact". In: *Math. Methods Appl. Sci.* 32.14 (2009), pp. 1804–1827.

[CEP20] F. Chouly, A. Ern, and N. Pignet. "A Hybrid High-Order Discretization Combined with Nitsche's Method for Contact and Tresca Friction in Small Strain Elasticity". In: *SIAM J. Sci. Comput.* 42.4 (2020), A2300–A2324.

[CGH14] A. Cangiani, E. H. Georgoulis, and P. Houston. "hp-version discontinuous Galerkin methods on polygonal and polyhedral meshes". In: *Math. Methods Appl. Sci.* 24.10 (2014), pp. 2009–2041.

[Cha+07] E. Chaljub, D. Komatitsch, J.-P. Vilotte, Y. Capdeville, B. Valette, and G. Festa. "Spectral-element analysis in seismology". In: *Adv. Geophys.* 48 (2007), pp. 365–419.

[Cha+10] E. Chaljub, P. Moczo, S. Tsuno, P.-Y. Bard, J. Kristek, M. Käser, M. Stupazzini, and M. Kristekova. "Quantitative comparison of four numerical predictions of 3D ground motion in the Grenoble Valley, France". In: *B. Seismol. Soc. Am.* 100.4 (2010), pp. 1427–1455.

[Cho14] F. Chouly. "An adaptation of Nitsche's method to the Tresca friction problem". In: *J. Math. Anal. Appl.* 411.1 (2014), pp. 329–339.

[Cho+17] F. Chouly, M. Fabre, P. Hild, R. Mlika, J. Pousin, and Y. Renard. "An overview of recent results on Nitsche's method for contact problems". In: *Geometrically unfitted finite element methods and applications*. Vol. 121. Lect. Notes Comput. Sci. Eng. Springer, Cham, 2017, pp. 93–141.

[Cho+19] F. Chouly, P. Hild, V. Lleras, and Y. Renard. "Nitsche-based finite element method for contact with Coulomb friction". In: *Numerical mathematics and advanced applications—ENUMATH 2017*. Vol. 126. Lect. Notes Comput. Sci. Eng. Springer, Cham, 2019, pp. 839–847.

[CMR18] F. Chouly, R. Mlika, and Y. Renard. "An unbiased Nitsche's approximation of the frictional contact between two elastic structures". In: *Numer. Math.* 139.3 (2018), pp. 593–631.

[Coh02] G. C. Cohen. *Higher-order numerical methods for transient wave equations*. Scientific Computation. With a foreword by R. Glowinski. Springer-Verlag, Berlin, 2002, pp. xviii+348.

[COK82] L. T. Campos, J. T. Oden, and N. Kikuchi. “A numerical analysis of a class of contact problems with friction in elastostatics”. In: *Comput. Methods Appl. Mech. Engrg.* 34.1-3 (1982). FENOMECH ”81, Part III (Stuttgart, 1981), pp. 821–845.

[Cou97] B. S. S. Council. “NEHRP guidelines for the seismic rehabilitation of buildings”. In: *FEMA-273, Federal Emergency Management Agency, Washington, DC* (1997).

[CPB04] H. Crowley, R. Pinho, and J. Bommer. “A probabilistic displacement-based vulnerability assessment procedure for earthquake loss estimation”. In: *B. Earthq. Eng.* 2.2 (2004), pp. 173–219.

[DA08] J. Douglas and H. Aochi. “A survey of techniques for predicting earthquake ground motions for engineering purposes”. In: *Surv. Geophys.* 29.3 (2008), p. 187.

[DA77] S. Das and K. Aki. “A numerical study of two-dimensional spontaneous rupture propagation”. In: *Geophys. J. Int.* 50.3 (1977), pp. 643–668.

[Dab86] M. Dablain. “The application of high-order differencing to the scalar wave equation”. In: *Geophysics* 51.1 (1986), pp. 54–66.

[Dal12] L. A. Dalguer. “Numerical algorithms for earthquake rupture dynamic modeling”. In: *The mechanics of faulting: from laboratory to real earthquakes* (2012), pp. 93–124.

[Day+05] S. M. Day, L. A. Dalguer, N. Lapusta, and Y. Liu. “Comparison of finite difference and boundary integral solutions to three-dimensional spontaneous rupture”. In: *J. Geophys. Res. - Sol. Ea.* 110.B12 (2005).

[Day77] S. M. Day. “Finite element analysis of seismic scattering problems”. PhD thesis. University of California, San Diego.(Ph. D. in Oceanography), 1977.

[Day82] S. M. Day. “Three-dimensional finite difference simulation of fault dynamics: rectangular faults with fixed rupture velocity”. In: *B. Seismol. Soc. Am.* 72.3 (1982), pp. 705–727.

[DD06] L. A. Dalguer and S. M. Day. “Comparison of fault representation methods in finite difference simulations of dynamic rupture”. In: *B. Seismol. Soc. Am.* 96.5 (2006), pp. 1764–1778.

[DD07] L. A. Dalguer and S. M. Day. “Staggered-grid split-node method for spontaneous rupture simulation”. In: *J. Geophys. Res. - Sol. Ea.* 112.B2 (2007).

[DE16] J. Douglas and B. Edwards. “Recent and future developments in earthquake ground motion estimation”. In: *Earth-Sci. Rev.* 160 (2016), pp. 203–219.

[Din+04] Z. Ding, F. Romanelli, Y. Chen, and G. Panza. "Realistic modeling of seismic wave ground motion in Beijing City". In: *Pure Appl. Geophys.* 161.5-6 (2004), pp. 1093–1106.

[DK06] M. Dumbser and M. Käser. "An arbitrary high-order discontinuous Galerkin method for elastic waves on unstructured meshes—II. The three-dimensional isotropic case". In: *Geophys. J. Int.* 167.1 (2006), pp. 319–336.

[DL76] G. Duvaut and J.-L. Lions. *Inequalities in mechanics and physics.* Translated from the French by C. W. John, Grundlehren der Mathematischen Wissenschaften, 219. Springer-Verlag, Berlin-New York, 1976, pp. xvi+397.

[Dob+06] V. A. Dobrev, R. D. Lazarov, P. S. Vassilevski, and L. T. Zikatanov. "Two-level preconditioning of discontinuous Galerkin approximations of second-order elliptic equations". In: *Numer. Linear Algebra Appl.* 13.9 (2006), pp. 753–770.

[Dou03] J. Douglas. "Earthquake ground motion estimation using strong-motion records: a review of equations for the estimation of peak ground acceleration and response spectral ordinates". In: *Earth-Sci. Rev.* 61.1-2 (2003), pp. 43–104.

[DPE12] D. A. Di Pietro and A. Ern. *Mathematical aspects of discontinuous Galerkin methods.* Vol. 69. Mathématiques & Applications (Berlin) [Mathematics & Applications]. Springer, Heidelberg, 2012, pp. xviii+384.

[DW17] S. Detweiler and A. Wein. "The HayWired earthquake scenario–Earthquake Hazards". In: *Scientific Investigations Report* 2017–5013.A–H (2017). 126 p., U.S Geological Survey.

[DW18] S. Detweiler and A. Wein. "The HayWired earthquake scenario–Engineering implications". In: *Scientific Investigations Report* 2017–5013.I–Q (2018). 429 p., U.S Geological Survey.

[EDM09] G. P. Ely, S. M. Day, and J.-B. Minster. "A support-operator method for 3-D rupture dynamics". In: *Geophys. J. Int.* 177.3 (2009), pp. 1140–1150.

[EJK05] C. Eck, J. Jarusek, and M. Krbec. *Unilateral contact problems: variational methods and existence theorems.* Vol. 270. CRC Press, 2005.

[Ell01] B. R. Ellingwood. "Earthquake risk assessment of building structures". In: *Reliab. Eng. Syst. Safe.* 74.3 (2001), pp. 251–262.

[ER07] Y. Epshteyn and B. Rivière. “Estimation of penalty parameters for symmetric interior penalty Galerkin methods”. In: *J. Comput. Appl. Math.* 206.2 (2007), pp. 843–872.

[Erd17] M. Erdik. “Earthquake risk assessment”. In: *B. Earthq. Eng.* 15.12 (2017), pp. 5055–5092.

[Eva+17] L. Evangelista, S. del Gaudio, C. Smerzini, A. d’Onofrio, G. Festa, I. Iervolino, L. Landolfi, R. Paolucci, A. Santo, and F. Silvestri. “Physics-based seismic input for engineering applications: a case study in the Aterno river valley, Central Italy”. In: *B. Earthq. Eng.* 15.7 (2017), pp. 2645–2671.

[Fac+97] E. Faccioli, F. Maggio, R. Paolucci, and A. Quarteroni. “2D and 3D elastic wave propagation by a pseudo-spectral domain decomposition method”. In: *J. Seismol.* 1.3 (1997), pp. 237–251.

[Fer+17] A Ferroni, P. F. Antonietti, I Mazzieri, and A Quarteroni. “Dispersion-dissipation analysis of 3-D continuous and discontinuous spectral element methods for the elastodynamics equation”. In: *Geophys. J. Int.* 211.3 (2017), pp. 1554–1574.

[FM10] L Faenza and A Michelini. “Regression analysis of MCS intensity and ground motion parameters in Italy and its application in ShakeMap”. In: *Geophys. J. Int.* 180 (2010), pp. 1138–1152.

[Fra93] A. Frankel. “Three-dimensional simulations of ground motions in the San Bernardino Valley, California, for hypothetical earthquakes on the San Andreas fault”. In: *B. Seismol. Soc. Am.* 83.4 (1993), pp. 1020–1041.

[FV05] G. Festa and J.-P. Vilotte. “The Newmark scheme as velocity–stress time-staggering: an efficient PML implementation for spectral element simulations of elastodynamics”. In: *Geophys. J. Int.* 161.3 (2005), pp. 789–812.

[Gal+14] P. Galvez, J.-P. Ampuero, L. A. Dalguer, S. N. Somala, and T. Nissen-Meyer. “Dynamic earthquake rupture modelled with an unstructured 3-D spectral element method applied to the 2011 M 9 Tohoku earthquake”. In: *Geophys. J. Int.* 198.2 (2014), pp. 1222–1240.

[Gan+04] A. Ganas, S. Pavlides, S. Sboras, S. Valkaniotis, S. Papaioannou, G. Alexandris, A. Plessa, and G. Papadopoulos. “Active fault geometry and kinematics in Parnitha Mountain, Attica, Greece”. In: *J. Struct. Geol.* 26.11 (2004), pp. 2103 –2118.

[Gao+04] M Gao, Y Yu, X Zhang, and J Wu. “Three-dimensional finite-difference modeling of ground motions in Beijing form a Mw 7 scenario earthquake”. In: *Proceedings of the 13th World Conference on Earthquake Engineering*. Paper 581, 2004.

[Gaz01] G Gazetas. “The 1999 Parnitha (Athens) Earthquake: soil effects on distribution of damage”. In: *Lessons Learned from Recent Strong Earthquakes* (2001), pp. 5–18.

[GB04] F. Gallovič and J. Brokešová. “The k-2 Rupture Model Parametric Study: Example of the 1999 Athens Earthquake”. In: *Stud. Geophys. Geod.* 48 (2004), pp. 589–613.

[GES08] B. Gencturk, A. S. Elnashai, and J. Song. “Fragility relationships for populations of woodframe structures based on inelastic response”. In: *J. Earthq. Eng.* 12.S2 (2008), pp. 119–128.

[GHH07] E. H. Georgoulis, E. Hall, and P. Houston. “Discontinuous Galerkin methods for advection-diffusion-reaction problems on anisotropically refined meshes”. In: *SIAM J. Sci. Comput.* 30.1 (2007/08), pp. 246–271.

[GK03] J. Gopalakrishnan and G. Kanschat. “A multilevel discontinuous Galerkin method”. In: *Numer. Math.* 95.3 (2003), pp. 527–550.

[GLS83] G. Gu, T. Lin, and Z. Shi. “Catalogue of earthquakes in China (1831AD–1969BC).” In: *Science Press, Beijing (in Chinese)* (1983).

[GM13] S. Günay and K. M. Mosalam. “PEER performance-based earthquake engineering methodology, revisited”. In: *J. Earthq. Eng.* 17.6 (2013), pp. 829–858.

[GMK08] M. Galis, P. Moczo, and J Kristek. “A 3-D hybrid finite-difference—finite-element viscoelastic modelling of seismic wave motion”. In: *Geophys. J. Int.* 175.1 (2008), pp. 153–184.

[Gra+11] R. Graves, T. Jordan, S. Callaghan, E. Deelman, E. Field, G. Juve, C. Kesselman, P. Maechling, G. Mehta, K. Milner, D. Okaya, P. Small, and K. Vahi. “CyberShake: A Physics-Based Seismic Hazard Model for Southern California”. In: *Pure and Applied Geophysics* 168.3-4 (2011), pp. 367–381.

[Gra96] R. W. Graves. “Simulating seismic wave propagation in 3D elastic media using staggered-grid finite differences”. In: *B. Seismol. Soc. Am.* 86.4 (1996), pp. 1091–1106.

[GS05] E. H. Georgoulis and E. Süli. “Optimal error estimates for the *hp*-version interior penalty discontinuous Galerkin finite element method”. In: *IMA J. Numer. Anal.* 25.1 (2005), pp. 205–220.

[Gue13] P. Gueguen. *Seismic vulnerability of structures*. John Wiley & Sons, 2013.

[Gui+11] R. Guidotti, M. Stupazzini, C. Smerzini, R. Paolucci, and P. Ramieri. "Numerical study on the role of basin geometry and kinematic seismic source in 3D ground motion simulation of the 22 February 2011 MW 6.2 Christchurch earthquake". In: *Seismol. Res. Lett.* 82.6 (2011), pp. 767–782.

[HA06] B. T. Helenbrook and H. L. Atkins. "Application of p-Multigrid to Discontinuous Galerkin Formulations of the Poisson Equation". In: *AIAA Journal* 44 (3 Mar. 2006).

[HA08] B. T. Helenbrook and H. L. Atkins. "Solving Discontinuous Galerkin Formulations of Poisson's Equation using Geometric and p Multigrid". In: *AIAA Journal* 46 (4 Apr. 2008).

[Har+04] R. Harris, R Archuleta, B Aagaard, J Ampuero, D. Andrews, L Dalguer, S Day, E Dunham, G Ely, Y Kase, et al. "The source physics of large earthquakes-Validating spontaneous rupture methods". In: *AGUFM* 2004 (2004), S12A–05.

[Har78] S. H. Hartzell. "Earthquake aftershocks as Green's functions". In: *Geophys. Res. Lett.* 5.1 (1978), pp. 1–4.

[Hes98] J. S. Hesthaven. "From electrostatics to almost optimal nodal sets for polynomial interpolation in a simplex". In: *SIAM J. Numer. Anal.* 35.2 (1998), pp. 655–676.

[HH06] P. Heintz and P. Hansbo. "Stabilized Lagrange multiplier methods for bilateral elastic contact with friction". In: *Comput. Methods Appl. Mech. Engrg.* 195.33-36 (2006), pp. 4323–4333.

[Hla+88] I. Hlaváček, J. Haslinger, J. Nečas, and J. Lovíšek. *Solution of variational inequalities in mechanics*. Vol. 66. Applied Mathematical Sciences. Translated from the Slovak by J. Jarník. Springer-Verlag, New York, 1988, pp. x+275.

[HMW07] S. Hüeber, A. Matei, and B. I. Wohlmuth. "Efficient algorithms for problems with friction". In: *SIAM J. Sci. Comput.* 29.1 (2007), pp. 70–92.

[Hou52] G. W. Housner. "Intensity of ground motion during strong earthquakes". In: *California Institute of Technology* (1952). Second technical report.

[HSS02] P. Houston, C. Schwab, and E. Süli. "Discontinuous hp-finite element methods for advection-diffusion-reaction problems". In: *SIAM J. Numer. Anal.* 39.6 (2002), pp. 2133–2163.

[HSW08] S. Hüeber, G. Stadler, and B. I. Wohlmuth. "A primal-dual active set algorithm for three-dimensional contact problems with Coulomb friction". In: *SIAM J. Sci. Comput.* 30.2 (2008), pp. 572–596.

[Hug+76] T. J. Hughes, R. L. Taylor, J. L. Sackman, A. Curnier, and W. Kanoknukulchai. "A finite element method for a class of contact-impact problems". In: *Comput. Methods Appl. Mech. Engrg.* 8.3 (1976), pp. 249–276.

[Hug87] T. J. R. Hughes. *The finite element method*. Linear static and dynamic finite element analysis, With the collaboration of Robert M. Ferencz and Arthur M. Raefsky. Prentice Hall Inc. Englewood Cliffs NJ, 1987, pp. xxviii+803.

[HW05] S. Hüeber and B. I. Wohlmuth. "A primal-dual active set strategy for non-linear multibody contact problems". In: *Comput. Methods Appl. Mech. Engrg.* 194.27-29 (2005), pp. 3147–3166.

[HW08] J. S. Hesthaven and T. Warburton. *Nodal discontinuous Galerkin methods*. Vol. 54. Texts in Applied Mathematics. Algorithms, analysis, and applications. Springer, New York, 2008, pp. xiv+500.

[HW12] S. Hüeber and B. Wohlmuth. "Equilibration techniques for solving contact problems with Coulomb friction". In: *Comput. Methods Appl. Mech. Engrg.* 205/208 (2012), pp. 29–45.

[Ida72] Y. Ida. "Cohesive force across the tip of a longitudinal-shear crack and Griffith's specific surface energy". In: *J. Geophys. Res.* 77.20 (1972), pp. 3796–3805.

[II02] I. R. Ionescu and Q.-L. Ionescu. "Dynamic contact problems with slip-dependent friction in viscoelasticity". In: vol. 12. 1. Mathematical modelling and numerical analysis in solid mechanics. 2002, pp. 71–80.

[Inf+19] M. Infantino, I. Mazzieri, A. Özcebe, R. Paolucci, and M. Stupazzini. "Physics-based Probabilistic Seismic Hazard Assessment in Istanbul, Part 1: 3D numerical modelling and simulated earthquake ground motions". In: *submitted* (2019).

[JB09] N. Jayaram and J. Baker. "Correlation model for spatially distributed ground-motion intensities". In: *Earthquake Engng. Struct. Dyn.* 38.15 (2009), pp. 1687–1708.

[JME12] S.-H. Jeong, A. M. Mwafy, and A. S. Elnashai. "Probabilistic seismic performance assessment of code-compliant multi-story RC buildings". In: *Eng. Struct.* 34 (2012), pp. 527–537.

[JV01] J. E. Jones and P. S. Vassilevski. "AMGe based on element agglomeration". In: *SIAM J. Sci. Comput.* 23.1 (2001), pp. 109–133.

[Kal79] J. Kalker. “The computation of three-dimensional rolling contact with dry friction”. In: *Int. J. Numer. Meth. Eng.* 14.9 (1979), pp. 1293–1307.

[Kap+06] A. J. Kappos, G. Panagopoulos, C. Panagiotopoulos, and G. Penelis. “A hybrid method for the vulnerability assessment of R/C and URM buildings”. In: *B. Earthq. Eng.* 4.4 (2006), pp. 391–413.

[Käs+07] M. Käser, M. Dumbser, J. De La Puente, and H. Igel. “An arbitrary high-order discontinuous Galerkin method for elastic waves on unstructured meshes—III. Viscoelastic attenuation”. In: *Geophys. J. Int.* 168.1 (2007), pp. 224–242.

[Kaz+14] A. Kazantzi, D. Vamvatsikos, K. Porter, and I. H. Cho. “Analytical vulnerability assessment of modern highrise RC moment-resisting frame buildings in the Western USA for the Global Earthquake Model”. In: *Proceedings of the 2nd European Conference on Earthquake Engineering and Seismology*. 2014.

[KD06] M. Käser and M. Dumbser. “An arbitrary high-order discontinuous Galerkin method for elastic waves on unstructured meshes–I. The two-dimensional isotropic case with external source terms”. In: *Geophys. J. Int.* 166.2 (2006), pp. 855–877.

[KE13] I. Kalogeras and D Egglezos. “Strong motion record processing for the Athenian Acropolis seismic response assessment”. In: *Geotechnical Engineering for the Preservation of Monuments and Historic Sites* (2013), pp. 483–492.

[KHP08] M. Käser, V. Hermann, and J. d. l. Puente. “Quantitative accuracy analysis of the discontinuous Galerkin method for seismic wave propagation”. In: *Geophys. J. Int.* 173.3 (2008), pp. 990–999.

[KI05] M. Käser and A. Iske. “ADER schemes on adaptive triangular meshes for scalar conservation laws”. In: *J. Comput. Phys.* 205.2 (2005), pp. 486–508.

[KIP98] K. Kamae, K. Irikura, and A. Pitarka. “A technique for simulating strong ground motion using hybrid Green’s function”. In: *B. Seismol. Soc. Am.* 88.2 (1998), pp. 357–367.

[KL18] G. Karanikoloudis and P. B. Lourenço. “Structural assessment and seismic vulnerability of earthen historic structures. Application of sophisticated numerical and simple analytical models”. In: *Eng. Struct.* 160 (2018), pp. 488–509.

[KLA08] Y. Kaneko, N. Lapusta, and J.-P. Ampuero. “Spectral element modeling of spontaneous earthquake rupture on rate and state faults: Effect of velocity-strengthening friction at shallow depths”. In: *J. Geophys. Res. - Sol. Ea.* 113.B9 (2008).

[KM03] J. Kristek and P. Moczo. “Seismic-wave propagation in viscoelastic media with material discontinuities: A 3D fourth-order staggered-grid finite-difference modeling”. In: *B. Seismol. Soc. Am.* 93.5 (2003), pp. 2273–2280.

[KMD07] M Käser, P Mai, and M Dumbser. “On the accurate treatment of finite source rupture models using ADER-DG on tetrahedral meshes”. In: *Bull. Seism. Soc. Am* 97.5 (2007), pp. 1570–1586.

[KO88] N. Kikuchi and J. T. Oden. *Contact problems in elasticity: a study of variational inequalities and finite element methods*. Vol. 8. SIAM Studies in Applied Mathematics. Society for Industrial and Applied Mathematics (SIAM), Philadelphia, PA, 1988, pp. xiv+495.

[Kra96] S. Kramer. *Earthquake geotechnical engineering*. 1996.

[KS00] G Koukis and N Sabatakakis. “Engineering geological environment of Athens, Greece”. In: *Bull. Eng. Geol. Environ.* 59.2 (2000), pp. 127–135.

[KS13] G. Karniadakis and S. Sherwin. *Spectral/hp element methods for computational fluid dynamics*. Oxford University Press, 2013.

[KS81] N. Kikuchi and Y. J. Song. “Penalty/finite-element approximations of a class of unilateral problems in linear elasticity”. In: *Quarterly of Applied Mathematics* 39.1 (1981), pp. 1–22.

[KT02a] D. Komatitsch and J. Tromp. “Spectral-element simulations of global seismic wave propagation—I. Validation”. In: *Geophys. J. Int.* 149.2 (2002), pp. 390–412.

[KT02b] D. Komatitsch and J. Tromp. “Spectral-element simulations of global seismic wave propagation—II. Three-dimensional models, oceans, rotation and self-gravitation”. In: *Geophys. J. Int.* 150.1 (2002), pp. 303–318.

[KT99] D. Komatitsch and J. Tromp. “Introduction to the spectral element method for three-dimensional seismic wave propagation”. In: *Geophys. J. Int.* 139.3 (1999), pp. 806–822.

[KV98] D. Komatitsch and J.-P. Vilotte. “The spectral element method: an efficient tool to simulate the seismic response of 2D and 3D geological structures”. In: *B. Seismol. Soc. Am.* 88.2 (1998), pp. 368–392.

[KZ67] C. Y. Kai and O. C. Zienkiewicz. *The finite element method in structural and continuum mechanics, numerical solution of problems in structural and continuum mechanics*. McGraw-Hill, 1967.

[Lau02] T. A. Laursen. *Computational contact and impact mechanics*. Fundamentals of modeling interfacial phenomena in nonlinear finite element analysis. Springer-Verlag, Berlin, 2002, pp. xvi+454.

[LC07] N. Luco and C. Cornell. "Structure-specific scalar intensity measures for near-source and ordinary earthquake ground motions". In: *Earthq. Spectra* 23.2 (2007), pp. 357–392.

[LD72] J. Lysmer and L. A. Drake. "A finite element method for seismology". In: *Seismology: Surface Waves and Earth Oscillations*. Vol. 11. Methods in Computational Physics: Advances in Research and Applications. Academic Press Inc, 1972, pp. 181–216.

[LK79] J. Lee and K Kamemura. "Analysis of elastodynamics with unilateral supports". In: *Engineering Mechanics*. ASCE. 1979, pp. 777–780.

[Lu+19] X. Lu, X. Zeng, Z. Xu, and H. Guan. "Improving the accuracy of near real-time seismic loss estimation using post-earthquake remote sensing images". In: *Earthq. Spectra* 34.3 (2019), pp. 1219–1245.

[MA86] A. Mosleh and G. Apostolakis. "The assessment of probability distributions from expert opinions with an application to seismic fragility curves". In: *Risk Anal.* 6.4 (1986), pp. 447–461.

[Mad76] R. Madariaga. "Dynamics of an expanding circular fault". In: *B. Seismol. Soc. Am.* 66.3 (1976), pp. 639–666.

[Mas03] A. Masi. "Seismic vulnerability assessment of gravity load designed R/C frames". In: *B. Earthq. Eng.* 1.3 (2003), pp. 371–395.

[Maz12] I. Mazzieri. "Non-conforming high order methods for the elastodynamics equation". PhD thesis. Italy, 2012.

[Maz+13] I. Mazzieri, M. Stupazzini, R. Guidotti, and C. Smerzini. "SPEED: SPectral Elements in Elastodynamics with Discontinuous Galerkin: a non-conforming approach for 3D multi-scale problems". In: *Internat. J. Numer. Methods Engrg.* 95.12 (2013), pp. 991–1010.

[MBV99] J. Mandel, M. Brezina, and P. Vaněk. "Energy optimization of algebraic multigrid bases". In: *Computing* 62.3 (1999), pp. 205–228.

[MDL89] K. Makropoulos, J. Drakopoulos, and J. Latousakis. "A revised and extended earthquake catalogue for Greece since 1900". In: *Geophys. J. Int.* 98.2 (1989), pp. 391–394.

[MHA10] B. S. Mascarenhas, B. T. Helenbrook, and H. L. Atkins. "Coupling p-multigrid to geometric multigrid for discontinuous Galerkin formulations of the convection-diffusion equation". In: *J. Comput. Phys.* 229.10 (2010), pp. 3664–3674.

[MKG14] P. Moczo, J. Kristek, and M. Gális. *The finite-difference modelling of earthquake motions: Waves and ruptures.* Cambridge University Press, 2014.

[MKH00] P. Moczo, J. Kristek, and L. Halada. "3D fourth-order staggered-grid finite-difference schemes: Stability and grid dispersion". In: *B. Seismol. Soc. Am.* 90.3 (2000), pp. 587–603.

[MKS17] C. Mai, K. Konakli, and B. Sudret. "Seismic fragility curves for structures using non-parametric representations". In: *Front. Struct. Civ. Eng.* 11.2 (2017), pp. 169–186.

[MMB87] J. Mandel, S. McCormick, and R. Bank. "Variational multigrid theory". In: *Multigrid methods.* Vol. 3. Frontiers Appl. Math. SIAM, Philadelphia, PA, 1987, pp. 131–177.

[MO83] J. A. C. Martins and J. T. Oden. "A numerical analysis of a class of problems in elastodynamics with friction". In: *Comput. Methods Appl. Mech. Engrg.* 40.3 (1983), pp. 327–360.

[MOA98] R Madariaga, K Olsen, and R Archuleta. "Modeling dynamic rupture in a 3D earthquake fault model". In: *B. Seismol. Soc. Am.* 88.5 (1998), pp. 1182–1197.

[Moc+07] P. Moczo, J. Kristek, M Galis, P Pazak, and M Balazovjech. "The finite-difference and finite-element modeling of seismic wave propagation and earthquake motion". In: *Acta Phys. Slovaca* 57.2 (2007).

[Moe+11] J. Moehle, Y. Bozorgnia, N. Jayaram, P. Jones, M. Rahnama, N. Shome, Z. Tuna, J. Wallace, T. Yang, and F. Zareian. "Case studies of the seismic performance of tall buildings designed by alternative means". In: *Pacific Earthquake Engineering Research Center College of Engineering University of California, Berkeley PEER Report* 5 (2011).

[MR12] I. Mazzieri and F. Rapetti. "Dispersion analysis of triangle-based spectral element methods for elastic wave propagation". In: *Numer. Algorithms* 60.4 (2012), pp. 631–650.

[MR82] S. F. McCormick and J. W. Ruge. "Multigrid methods for variational problems". In: *SIAM J. Numer. Anal.* 19.5 (1982), pp. 924–929.

[MV12] A. Masi and M. Vona. "Vulnerability assessment of gravity-load designed RC buildings: evaluation of seismic capacity through non-linear dynamic analyses". In: *Eng. Struct.* 45 (2012), pp. 257–269.

[Nit71] J. Nitsche. "Über ein Variationsprinzip zur Lösung von Dirichlet-Problemen bei Verwendung von Teilräumen, die keinen Randbedingungen unterworfen sind". In: *Abh. Math. Sem. Univ. Hamburg* 36 (1971), pp. 9–15.

[OA96] K. B. Olsen and R. J. Archuleta. "Three-dimensional simulation of earthquakes on the Los Angeles fault system". In: *B. Seismol. Soc. Am.* 86.3 (1996), pp. 575–596.

[OAN00] D. D. Oglesby, R. J. Archuleta, and S. B. Nielsen. "The three-dimensional dynamics of dipping faults". In: *B. Seismol. Soc. Am.* 90.3 (2000), pp. 616–628.

[OAN98] D. D. Oglesby, R. J. Archuleta, and S. B. Nielsen. "Earthquakes on dipping faults: the effects of broken symmetry". In: *Science* 280.5366 (1998), pp. 1055–1059.

[OK79] J. Oden and N Kikuchi. "Contact problems in elasticity, TICOM Rep." In: (1979).

[OK82a] J. T. Oden and S. J. Kim. "Interior penalty methods for finite element approximations of the Signorini problem in elastostatics". In: *Comput. Math. Appl.* 8.1 (1982), pp. 35–56.

[OK82b] J. Oden and N Kikuchi. "Finite element methods for constrained problems in elasticity". In: *Int. J. Numer. Meth. Eng.* 18.5 (1982), pp. 701–725.

[OS11] L. N. Olson and J. B. Schroder. "Smoothed aggregation multigrid solvers for high-order discontinuous Galerkin methods for elliptic problems". In: *J. Comput. Phys.* 230.18 (2011), pp. 6959–6976.

[OST10] L. N. Olson, J. Schroder, and R. S. Tuminaro. "A new perspective on strength measures in algebraic multigrid". In: *Numer. Linear Algebra Appl.* 17.4 (2010), pp. 713–733.

[OST11] L. N. Olson, J. B. Schroder, and R. S. Tuminaro. "A general interpolation strategy for algebraic multigrid using energy minimization". In: *SIAM J. Sci. Comput.* 33.2 (2011), pp. 966–991.

[PAK09] J. de la Puente, J.-P. Ampuero, and M. Käser. "Dynamic rupture modeling on unstructured meshes using a discontinuous Galerkin method". In: *J. Geophys. Res. - Sol. Ea.* 114.B10 (2009).

[Pan77] P. D. Panagiotopoulos. "On the unilateral contact problem of structures with a non quadratic strain energy density". In: *Internat. J. Solids Structures* 13.3 (1977), pp. 253–261.

[Pan79] P. Panagiotopoulos. "A variational inequality approach to the dynamic unilateral contact problem of elastoplastic foundations". In: *Proc. 3rd Int. Conf. Num. Methods in Geomechanics, Aachen.* 1979, pp. 2–6.

[Pao+14] R. Paolucci, I. Mazzieri, C. Smerzini, and M. Stupazzini. "Physics-based earthquake ground shaking scenarios in large urban areas". In: *Perspectives on European earthquake engineering and seismology.* Springer, 2014, pp. 331–359.

[Pao+16] R. Paolucci, L. Evangelista, I. Mazzieri, and E. Schiappapietra. "The 3D numerical simulation of near-source ground motion during the Marsica earthquake, Central Italy, 100 years later". In: *Soil Dyn. Earthq. Eng.* 91 (2016), pp. 39–52.

[Pao+18] R. Paolucci, M. Infantino, I. Mazzieri, A. G. Özcebe, C. Smerzini, and M. Stupazzini. "3D physics-based numerical simulations: advantages and current limitations of a new frontier to earthquake ground motion prediction. The Istanbul case study". In: *Recent Advances in Earthquake Engineering in Europe: 16th European Conference on Earthquake Engineering-Thessaloniki 2018.* Springer. 2018, pp. 203–223.

[Pap+00a] P. Papadimitriou, N. Voulgaris, I. Kassaras, G. Kaviris, N. Delibasis, and K. Makropoulos. "The September 7, 1999 Athens Earthquake Sequence recorded by the Cornet Network: Preliminary Results of Source Parameters Determination of the mainshock." In: *Ann. Geol. Pays Hellen* XXXVII (2000), pp. 29–39.

[Pap+00b] G. Papadopoulos, G Drakatos, D Papanastassiou, I Kalogeras, and G Stavrakakis. "Preliminary results about the catastrophic earthquake of 7 September 1999 in Athens, Greece". In: *Seismol. Res. Lett.* 71.3 (2000), pp. 318–329.

[Pap+97] V. Papazachos, B. Papazachos, C. Papazachou, and K. Papazachou. *The earthquakes of Greece.* Editions Ziti, 1997.

[Pav+00] R. Pavic, M. G. Koller, P.-Y. Bard, and C. Lacave-Lachet. "Ground motion prediction with the empirical Green's function technique: an assessment of uncertainties and confidence level". In: *J. Seismol.* 4.1 (2000), pp. 59–77.

[PBB07] J. Park, P. Bazzurro, and J. Baker. "Modeling spatial correlation of ground motion Intensity Measures for regional seismic hazard and portfolio loss estimation". In: *Applications of Statistics and Probability in Civil Engineering - Proceedings of the 10th International Conference on Applications of Statistics and Probability, ICASP10.* 2007.

[Pel+10] C. Pelties, M. Käser, V. Hermann, and C. E. Castro. “Regular versus irregular meshing for complicated models and their effect on synthetic seismograms”. In: *Geophys. J. Int.* 183.2 (2010), pp. 1031–1051.

[Pel+12] C. Pelties, J. De la Puente, J.-P. Ampuero, G. B. Brietzke, and M. Käser. “Three-dimensional dynamic rupture simulation with a high-order discontinuous Galerkin method on unstructured tetrahedral meshes”. In: *J. Geophys. Res. - Sol. Ea.* 117.B2 (2012).

[PF09] I. Peruš and P. Fajfar. “How reliable are the ground motion prediction equations”. In: *Proceedings of the 20th International Conference on Structural Mechanics in Reactor Technology (SMiRT 20), Espoo.* Vol. 9. Paper 1662, 2009.

[PKB07] K. Porter, R. Kennedy, and R. Bachman. “Creating Fragility Functions for Performance-Based Earthquake Engineering”. In: *Earthq. Spectra* 23.2 (2007), pp. 471–489.

[PLMH09] F. Prill, M. Lukáčová-Medvidová, and R. Hartmann. “Smoothed aggregation multigrid for the discontinuous Galerkin method”. In: *SIAM J. Sci. Comput.* 31.5 (2009), pp. 3503–3528.

[PMS15] R. Paolucci, I. Mazzieri, and C. Smerzini. “Anatomy of strong ground motion: Near-source records and three-dimensional physics-based numerical simulations of the Mw 6.0 2012 May 29 Po plain earthquake, Italy”. In: *Geophys. J. Int.* 203.3 (2015), pp. 2001–2020.

[Por+11] K. Porter, L. Jones, D. Cox, J. Goltz, K. Hudnut, D. Mileti, S. Perry, D. Ponti, M. Reichle, A. Rose, C. Scawthorn, H. Seligson, K. Shoaf, J. Treiman, and A. Wein. “The ShakeOut scenario: A hypothetical Mw7.8 earthquake on the Southern San Andreas Fault”. In: *Earthq. Spectra* 27.2 (2011), pp. 239–261.

[Pow+08] M. Power, B. Chiou, N. Abrahamson, Y. Bozorgnia, T. Shantz, and C. Roblee. “An overview of the NGA project”. In: *Earthq. Spectra* 24.1 (2008), pp. 3–21.

[PPG02] S. Pavlides, G Papadopoulos, and A Ganas. “The fault that caused the Athens September 1999 Ms= 5.9 earthquake: Field observations”. In: *Natural Hazards* 27.1-2 (2002), pp. 61–84.

[PR04] R. Pasquetti and F. Rapetti. “Spectral element methods on triangles and quadrilaterals: comparisons and applications”. In: *J. Comput. Phys.* 198.1 (2004), pp. 349–362.

[PR06] R. Pasquetti and F. Rapetti. “Spectral element methods on unstructured meshes: comparisons and recent advances”. In: *J. Sci. Comput.* 27.1-3 (2006), pp. 377–387.

[PR73] A. C. Palmer and J. R. Rice. "The growth of slip surfaces in the progressive failure of over-consolidated clay". In: *Proceedings of the Royal Society of London. A. Mathematical and Physical Sciences* 332.1591 (1973), pp. 527–548.

[PS02] I. Perugia and D. Schötzau. "An *hp*-analysis of the local discontinuous Galerkin method for diffusion problems". In: *J. Sci. Comput.* 17.1-4 (2002), pp. 561–571.

[PSZ07] C. di Prisco, M. Stupazzini, and C. Zambelli. "Nonlinear SEM numerical analyses of dry dense sand specimens under rapid and dynamic loading". In: *Int. J. Numer. Anal. Met.* 31.6 (2007), pp. 757–788.

[Pue+07] J. de la Puente, M. Käser, M. Dumbser, and H. Igel. "An arbitrary high-order discontinuous Galerkin method for elastic waves on unstructured meshes-IV. Anisotropy". In: *Geophys. J. Int.* 169.3 (2007), pp. 1210–1228.

[Pue+08] J. de la Puente, M. Dumbser, M. Käser, and H. Igel. "Discontinuous Galerkin methods for wave propagation in poroelastic media". In: *Geophysics* 73.5 (2008), T77–T97.

[Qua14] A. Quarteroni. *Numerical models for differential problems*. Second. Vol. 8. MS&A. Modeling, Simulation and Applications. Translated from the fifth (2012) Italian edition by Silvia Quarteroni. Springer, Milan, 2014, pp. xx+656.

[QV94] A. Quarteroni and A. Valli. *Numerical approximation of partial differential equations*. Vol. 23. Springer Series in Computational Mathematics. Springer-Verlag, Berlin, 1994, pp. xvi+543.

[RE03] T Rossetto and A Elnashai. "Derivation of vulnerability functions for European-type RC structures based on observational data". In: *Eng. Struct.* 25.10 (2003), pp. 1241–1263.

[RE05] T. Rossetto and A. Elnashai. "A new analytical procedure for the derivation of displacement-based vulnerability curves for populations of RC structures". In: *Eng. Struct.* 27.3 (2005), pp. 397–409.

[RH05] M. H. van Raalte and P. W. Hemker. "Two-level multigrid analysis for the convection-diffusion equation discretized by a discontinuous Galerkin method". In: *Numer. Linear Algebra Appl.* 12.5-6 (2005), pp. 563–584.

[Riv08] B. Rivière. *Discontinuous Galerkin methods for solving elliptic and parabolic equations*. Vol. 35. Frontiers in Applied Mathematics. Theory and implementation. Society for Industrial and Applied Mathematics (SIAM), Philadelphia, PA, 2008, pp. xxii+190.

[Rob96] J. O. Robertsson. "A numerical free-surface condition for elastic/viscoelastic finite-difference modeling in the presence of topography". In: *Geophysics* 61.6 (1996), pp. 1921–1934.

[Roj+08] O. Rojas, S. Day, J. Castillo, and L. A. Dalguer. "Modelling of rupture propagation using high-order mimetic finite differences". In: *Geophys. J. Int.* 172.2 (2008), pp. 631–650.

[Rou+03] Z. Roumelioti, D Dreger, A Kiratzi, and N Theodoulidis. "Slip distribution of the 7 September 1999 Athens earthquake inferred from an empirical Green's function study". In: *B. Seismol. Soc. Am.* 93.2 (2003), pp. 775–782.

[RS87] J. W. Ruge and K. Stüben. "Algebraic multigrid". In: *Multigrid methods*. Vol. 3. Frontiers Appl. Math. SIAM, Philadelphia, PA, 1987, pp. 73–130.

[RT83] P.-A. Raviart and J.-M. Thomas. *Introduction à l'analyse numérique des équations aux dérivées partielles*. Collection Mathématiques Appliquées pour la Maîtrise. [Collection of Applied Mathematics for the Master's Degree]. Masson, Paris, 1983, p. 224.

[SAL12] J. Schmedes, R. J. Archuleta, and D. Lavallée. "A kinematic rupture model generator incorporating spatial interdependency of earthquake source parameters". In: *Geophys. J. Int.* 192.3 (Dec. 2012), pp. 1116–1131.

[Sch12] J. B. Schroder. "Smoothed aggregation solvers for anisotropic diffusion". In: *Numer. Linear Algebra Appl.* 19.2 (2012), pp. 296–312.

[Sch98] C. Schwab. *p- and hp-finite element methods*. Numerical Mathematics and Scientific Computation. Theory and applications in solid and fluid mechanics. The Clarendon Press, Oxford University Press, New York, 1998, pp. xii+374.

[Seo+12] J. Seo, L. Dueñas-Osorio, J. I. Craig, and B. J. Goodno. "Metamodel-based regional vulnerability estimate of irregular steel moment-frame structures subjected to earthquake events". In: *Eng. Struct.* 45 (2012), pp. 585–597.

[Sew69] M. J. Sewell. "On dual approximation principles and optimization in continuum mechanics". In: *Philos. Trans. Roy. Soc. London Ser. A* 265 (1969/70), pp. 319–351.

[Sey+10] D. Seyedi, P. Gehl, J. Douglas, L. Davenne, N Mezher, and S Ghavamian. "Development of seismic fragility surfaces for reinforced concrete buildings by means of nonlinear time-history analysis". In: *Earthquake Engng. Struct. Dyn.* 39.1 (2010), pp. 91–108.

[She09] P. M. Shearer. *Introduction to Seismology*. Cambridge University Press, 2009.

[Shi+00] M. Shinozuka, M. Q. Feng, J. Lee, and T. Naganuma. "Statistical analysis of fragility curves". In: *J. Eng. Mech.* 126.12 (2000), pp. 1224–1231.

[SK95] S. J. Sherwin and G. E. Karniadakis. "A new triangular and tetrahedral basis for high-order (hp) finite element methods". In: *Int. J. Numer. Meth. Eng.* 38.22 (1995), pp. 3775–3802.

[SK96] A. Singhal and A. S. Kiremidjian. "Method for probabilistic evaluation of seismic structural damage". In: *J. Struct. Eng.* 122.12 (1996), pp. 1459–1467.

[Smo+04] A. Smolka, A. Allmann, D. Hollnack, and H. Thrainsson. "The Principle of Risk Partnership and the Role of Insurance in Risk Mitigation". In: *Proceedings of the 13th World Conference on Earthquake Engineering*. Paper 2020, 2004.

[SP18] C. Smerzini and K. Pitilakis. "Seismic risk assessment at urban scale from 3D physics-based numerical modeling: the case of Thessaloniki". In: *B. Earthq. Eng.* 16.7 (2018), pp. 2609–2631.

[SPH17] C. Smerzini, K. Pitilakis, and K. Hashemi. "Evaluation of earthquake ground motion and site effects in the Thessaloniki urban area by 3D finite-fault numerical simulations". In: *B. Earthq. Eng.* 15.3 (2017), pp. 787–812.

[SPI09] M. Stupazzini, R. Paolucci, and H. Igel. "Near-Fault Earthquake Ground-Motion Simulation in the Grenoble Valley by a High-Performance Spectral Element Code". In: *Bull. seism. Soc. Am.* 99.1 (2009), pp. 286–301.

[Sta88] R. Stacey. "Improved transparent boundary formulations for the elastic-wave equation". In: *B. Seismol. Soc. Am.* 78.6 (1988), pp. 2089–2097.

[Stu+20] M. Stupazzini, M. Infantino, A. Allmann, and R. Paolucci. "Physics-based probabilistic seismic hazard and loss assessment in large urban areas: A simplified application to Istanbul". In: *Earthquake Engng. Struct. Dyn.* (2020), pp. 1–17.

[STW11] J. Shen, T. Tang, and L.-L. Wang. *Spectral methods*. Vol. 41. Springer Series in Computational Mathematics. Algorithms, analysis and applications. Springer, Heidelberg, 2011, pp. xvi+470.

[SW10] B. Stamm and T. P. Wihler. "*hp*-optimal discontinuous Galerkin methods for linear elliptic problems". In: *Math. Comp.* 79.272 (2010), pp. 2117–2133.

[SWW15] S. Sitzmann, K. Willner, and B. I. Wohlmuth. "A dual Lagrange method for contact problems with regularized frictional contact conditions: modelling micro slip". In: *Comput. Methods Appl. Mech. Engrg.* 285 (2015), pp. 468–487.

[TP82] D Talaslidis and P. Panagiotopoulos. "A linear finite element approach to the solution of the variational inequalities arising in contact problems of structural dynamics". In: *Int. J. Numer. Meth. Eng.* 18.10 (1982), pp. 1505–1520.

[Tri76] M. Trifunac. "Preliminary analysis of the peaks of strong earthquake ground motion—dependence of peaks on earthquake magnitude, epicentral distance, and recording site conditions". In: *B. Seismol. Soc. Am.* 66.1 (1976), pp. 189–219.

[TT02] V. A. Titarev and E. F. Toro. "ADER: Arbitrary high order Godunov approach". In: *J. Sci. Comput.* 17.1-4 (2002), pp. 609–618.

[TW05] A. Toselli and O. Widlund. *Domain decomposition methods—algorithms and theory*. Vol. 34. Springer Series in Computational Mathematics. Springer-Verlag, Berlin, 2005, pp. xvi+450.

[TWV00] M. A. Taylor, B. A. Wingate, and R. E. Vincent. "An algorithm for computing Fekete points in the triangle". In: *SIAM J. Numer. Anal.* 38.5 (2000), pp. 1707–1720.

[TZ00] G.-A. Tselentis and J. Zahradnik. "The Athens earthquake of 7 September 1999". In: *B. Seismol. Soc. Am.* 90.5 (2000), pp. 1143–1160.

[VFA06] J Vilotte, G Festa, and J Ampuero. "Dynamic fault rupture propagation using nonsmooth spectral element method". In: *AGUFM* 2006 (2006), S52B–05.

[Vil+14] M. Villani, E. Faccioli, M. Ordaz, and M. Stupazzini. "High resolution seismic hazard analysis in a complex geological configuration: The case of the Sulmona basin in Central Italy". In: *Earthq. Spectra* 30.4 (2014), pp. 1801–1824.

[Vir86] J. Virieux. "P-SV wave propagation in heterogeneous media: Velocity-stress finite-difference method". In: *Geophysics* 51.4 (1986), pp. 889–901.

[VMB96] P. Vaněk, J. Mandel, and M. Brezina. “Algebraic multigrid by smoothed aggregation for second and fourth order elliptic problems”. In: *Computing* 56.3 (1996). International GAMM-Workshop on Multi-level Methods (Meisdorf, 1994), pp. 179–196.

[War06] T. Warburton. “An explicit construction of interpolation nodes on the simplex”. In: *J. Engrg. Math.* 56.3 (2006), pp. 247–262.

[WC94] D. L. Wells and K. J. Coppersmith. “New empirical relationships among magnitude, rupture length, rupture width, rupture area, and surface displacement”. In: *B. Seismol. Soc. Am.* 84.4 (Aug. 1994), pp. 974–1002.

[WCS99] W. L. Wan, T. F. Chan, and B. Smith. “An energy-minimizing interpolation for robust multigrid methods”. In: *SIAM J. Sci. Comput.* 21.4 (1999), pp. 1632–1649.

[Wea+15] G. Weatherill, V. Silva, H. Crowley, and P. Bazzurro. “Exploring the impact of spatial correlations and uncertainties for portfolio analysis in probabilistic seismic loss estimation”. In: *B. Earthq. Eng.* 13.4 (2015), pp. 957–981.

[WH03] T. Warburton and J. S. Hesthaven. “On the constants in *hp*-finite element trace inverse inequalities”. In: *Comput. Methods Appl. Mech. Engrg.* 192.25 (2003), pp. 2765–2773.

[Whe78] M. F. Wheeler. “An elliptic collocation-finite element method with interior penalties”. In: *SIAM J. Numer. Anal.* 15.1 (1978), pp. 152–161.

[Woh11] B. Wohlmuth. “Variationally consistent discretization schemes and numerical algorithms for contact problems”. In: *Acta Numer.* 20 (2011), pp. 569–734.

[WWY13] F. Wu, M. Wang, and X. Y. Yang. “Building Seismic Vulnerability Study for China High Rises”. In: *Appl. Mech. Mater.* 353 (2013), pp. 2301–2304.

[Xio+19] C. Xiong, X. Lu, J. Huang, and H. Guan. “Multi-LOD seismic-damage simulation of urban buildings and case study in Beijing CBD”. In: *B. Earthq. Eng.* 17.4 (2019), pp. 2037–2057.

[Xu+19] Z. Xu, X. Lu, X. Zeng, Y. Xu, and Y. Li. “Seismic loss assessment for buildings with various-LOD BIM data”. In: *Adv. Eng. Inform.* 39 (2019), pp. 112–126.

[XXL14] P. Xu, C. Xiao, and J. Li. “Relationship between natural vibration periods and structural heights for high-rise buildings in China”. In: *Int. J. High-rise Buildings* 3.1 (2014), pp. 49–64.

[XZ04] J. Xu and L. Zikatanov. “On an energy minimizing basis for algebraic multigrid methods”. In: *Comput. Vis. Sci.* 7.3-4 (2004), pp. 121–127.

[XZ17] J. Xu and L. Zikatanov. “Algebraic multigrid methods”. In: *Acta Numer.* 26 (2017), pp. 591–721.

[Zen10] I Zentner. “Numerical computation of fragility curves for NPP equipment”. In: *Nucl. Eng. Des.* 240.6 (2010), pp. 1614–1621.